

JAERI-M

88-181

JAERI TANDEM, LINAC & V.D.G.

ANNUAL REPORT

1987

April 1, 1987—March 31, 1988

October 1988

Department of Physics

日本原子力研究所  
Japan Atomic Energy Research Institute

JAERI-Mレポートは、日本原子力研究所が不定期に公刊している研究報告書です。  
入手の間合わせは、日本原子力研究所技術情報部情報資料課（〒319-11茨城県那珂郡東海村）  
あて、お申しこしてください。なお、このほかに財団法人原子力弘済会資料センター（〒319-11茨城  
県那珂郡東海村日本原子力研究所内）で複写による実費頒布をおこなっております。

JAERI-M reports are issued irregularly.  
Inquiries about availability of the reports should be addressed to Information Division, Department  
of Technical Information, Japan Atomic Energy Research Institute, Tokai-mura, Naka-gun,  
Ibaraki-ken 319-11, Japan.

© Japan Atomic Energy Research Institute, 1988

---

編集兼発行	日本原子力研究所
印刷	日立高速印刷株式会社

JAERI TANDEM, LINAC & V.D.G.  
Annual Report  
1987

April 1, 1987 - March 31, 1988

Department of Physics  
Tokai Research Establishment  
Japan Atomic Energy Research Institute  
Tokai-mura, Naka-gun, Ibaraki-ken

(Received September 1, 1988)

This annual report describes research activities which have been performed with the JAERI tandem accelerator, the electron linear accelerator and the Van de Graaff accelerator from April 1, 1987 to March 31, 1988. Summary reports of 49 papers, and list of publications, personnel and cooperative researches with universities are contained.

Keywords: JAERI TANDEM, e-LINAC, V.D.G., Atomic Physics, Radiation Chemistry Solid State Physics, Material Science, Nuclear Chemistry, Nuclear Physics, Neutron Physics, Annual Report

Editors: Naomoto Shikazono  
Mitsuhiko Ishii  
Yuuki Kawarasaki  
Yukio Kazumata  
Chiaki Kobayashi  
Yohta Nakai  
Yoichi Suto

原研タンデム、リニアック、バンデグラフ加速器 1987 年度年次報告

日本原子力研究所東海研究所  
物理部

(1988 年 9 月 1 日受理)

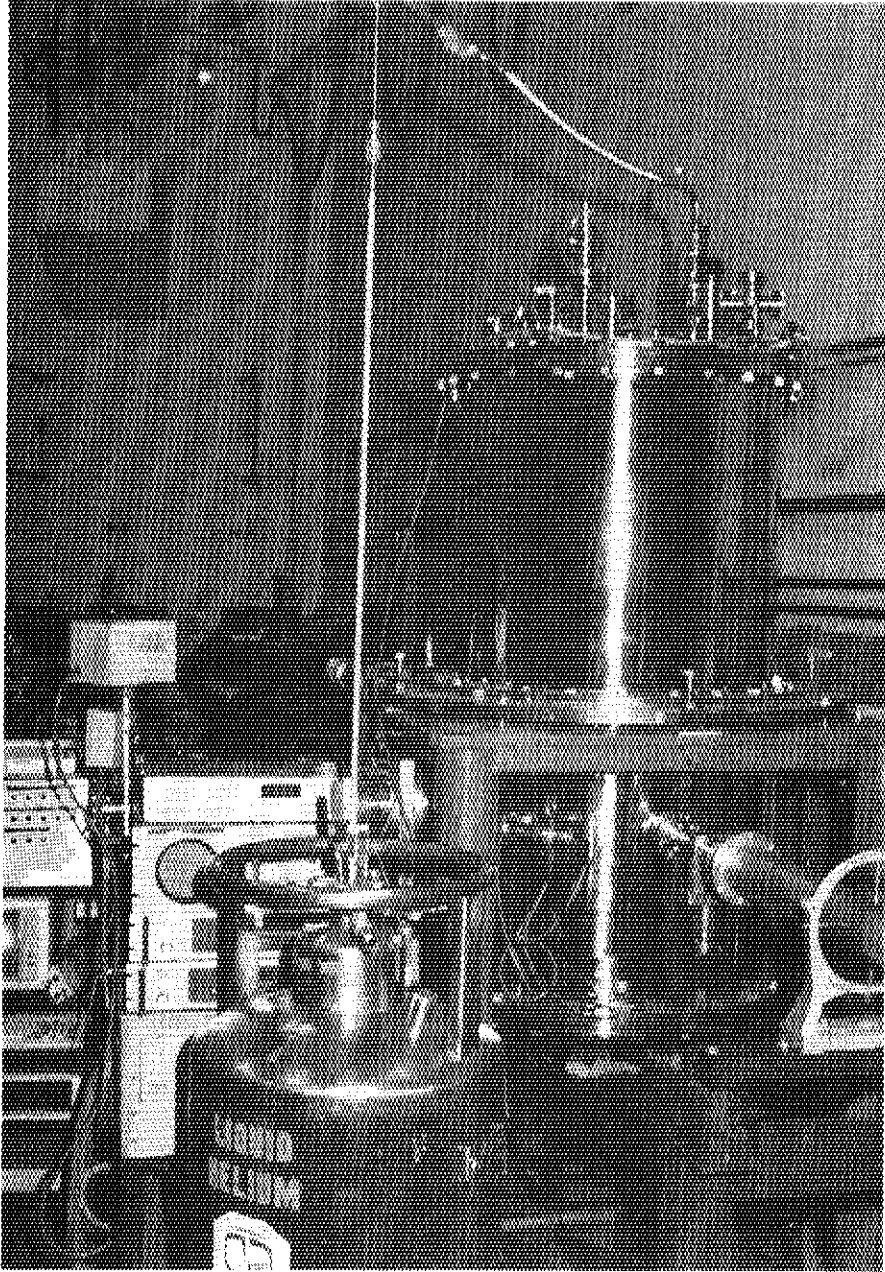
本年次報告は、原研タンデム、リニアック及びバンデグラフ加速器で、1987 年 4 月 1 日から 1988 年 3 月 31 日までの間に東海研で行われた研究活動を取りまとめたものである。

1) 加速器運転と開発研究 2) 原子分子及び化学 3) 固体物理及び材料の放射線効果 4) 核化学 5) 核物理及び 6) 中性子物理の 6 部門にまたがる 49 編の研究報告、公表された文献、関与した職員及び大学等との協力研究のリストを収録している。

---

東海研究所：〒319-11 茨城県那珂郡東海村白方字白根 2-4

(編集者) 鹿園直基・石井三彦・河原崎雄紀・数又幸生・小林千明  
中井洋太・須藤洋一



Superconducting buncher going up for its beam test.

## PREFACE

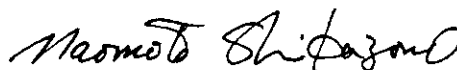
This report covers activities of research and development carried out by means of accelerators of Department of Physics JAERI during the period from April 1 1987 through march 31 1988.

All the accelerators, i. e. the tandem accelerator, the electron linear accelerator and the Van de Graaff accelerator, have been operated satisfactorily throughout the period. The tandem accelerator, with which a majority of the research activities have been done, operated on a regular schedule in accordance with the cycle of three months operation for research activities and the one month for the maintenance. A project of constructing a post accelerator to boost the energy of the heavy ion beams have progressed remarkably in the period. A superconducting quater wave resonator was repeatedly tested and found to work excellently. Our plan is to obtain a 30 MV of accelerating voltage by using the 40 quater wave resonators. The electron linear accelerator and the Van de Graaff accelerator have been used for some of the research works of neutron physics and solid state physics, respectively. A design study of superconducting electron linear accelerator for free electron laser has been performed in this period. In particular, injection system was studied in every detail.

Main subjects of our research activities contains; 1) atomic physics and chemistry, 2) solid state physics and radiation effects in materials, 3) nuclear chemistry, 4) nuclear physics, and 5) neutron physics.

During the period, more than 60 staff members of JAERI have worked in the above mentioned fields of researches, and about 100 colleagues have joined from universities and institutes outside JAERI for colaboration in these studies.

A joint seminar on heavy iion nuclear physics and nuclear chemistry in the energy region of tandem accelerators was held at Tokai Research Establishment of JAERI, January 7 - 9, 1988. Some of the experimental results presented in the seminar are included in this annual report.



Naomoto Shikazono  
Director  
Department of Physics

## CONTENTS

I	ACCELERATOR OPERATION AND DEVELOPMENT .....	1
1.1	Tandem Accelerator Operation .....	3
1.2	Electron Linac Operation and Improvements .....	6
1.3	Production and Acceleration of Alkaline Metal Ions using an Inverted Sputter Ion Source .....	10
1.4	Slackened Carbon Stripper Foils .....	13
1.5	Superconducting Booster .....	15
1.6	Superconducting Resonators for JAERI Tandem Booster .....	19
1.7	Linac for a Free-Electron-Laser Oscillator .....	23
1.8	Beam Optics of a Superconducting Booster for the JAERI Tandem Accelerator .....	28
II	ATOMIC PHYSICS AND CHEMISTRY .....	31
2.1	Production of Multiply Charged Recoil Ions in Collisions of 50-kev/u and 100-kev/u C and Ne Ions with Ne .....	33
2.2	Radiative Electron Capture in Heavy Ion and H <sub>2</sub> Collisions .....	37
2.3	X-Ray Emission from Foil-Excited Silicon Beams .....	40
2.4	Beam-Foil Spectra of Chlorine Ions in High Energy Region (V) .....	44
2.5	Microhole Formation in Polymethyl Methacrylate Film by Heavy Ion Irradiation .....	47
III	SOLID STATE PHYSICS AND RADIATION EFFECTS IN MATERIALS .....	51
3.1	Radiation Annealing in Nickel and Copper by 100 MeV Iodine Ion Irradiation .....	53
3.2	Depth Dependence of Isochronal Annealing Process in Fe irradiated by Cl Ions .....	57
3.3	Calculation of Damage Depth Profiles for 2-7.5 MeV/amu Heavy Ions on Pure Metals with Experimental Comparisons .....	61
3.4	Microstructure and Mechanical Properties of Ion Irradiated Fe-12%Cr-15 to 30%Mn Alloys .....	65
3.5	Volume Change of Lithium Oxide by Lithium Ion Irradiation .....	68
3.6	Effect of Irradiation Damage on Ion Conductivity of Li <sub>2</sub> O .....	72
3.7	Irradiation Damage Studies of Ceramic Materials .....	76
3.8	Effect of Heavy Ion Irradiation on Negative Thermal Expansion	

	in Gap Single Crystal.....	80
3.9	X-Ray Diffraction Topographic Observation of Silicon Single Crystals Irradiated with Energetic Heavy Ions (6).....	84
3.10	Electron Energy Loss Spectroscopy Analysis of Damage Structure in Alumina Irradiated with He-ions.....	88
3.11	Effect of High-Energy Ion Irradiation on Superconducting Properties of $\text{YBa}_2\text{Cu}_3\text{O}_{7-x}$ .....	92
3.12	Surface Analysis of $\text{YBa}_2\text{Cu}_3\text{O}_x$ Compound Irradiated with 100 MeV Bromine Ions.....	96
IV	NUCLEAR CHEMISTRY.....	101
4.1	$^{12}\text{C}$ Induced Fission of $^{233}\text{U}$ , $^{235}\text{U}$ and $^{238}\text{U}$ .....	103
4.2	Complex Fragment Emission From the Compound Nucleus $^{105}\text{Ag}$ .....	107
4.3	Mass Distributions of the Fission Fragments of $^{233}\text{U}+p$ , $^{237}\text{Np}+p$ and $^{239}\text{Pu}+p$ .....	110
4.4	Excitation Functions of $^{95}\text{Mo}(p,n)$ Reaction For the Production $^{95m}\text{Tc}$ .....	114
4.5	Identification of A New Isotope of $^{121}\text{La}$ by Means of Element-Selective Mass Separation.....	117
4.6	Decays of $^{122,124,126}\text{La}$ and $^{128,130}\text{Pr}$ and Properties of the Low-Lying States of Their Daughter Nuclei.....	121
4.7	Isolation of Short-Lived Nuclides with a Helium-Jet Recoil-Transport System and SISAK.....	124
V	NUCLEAR PHYSICS.....	129
5.1	Nuclear Structure of $^{106}\text{Sn}$ .....	131
5.2	G-factor of the $10^+$ Isomer in $^{134}\text{Nd}$ .....	132
5.3	Electromagnetic Transition Probabilities for Natural-Parity Rotational Bands in $^{173}\text{Yb}$ and $^{157}\text{Gd}$ .....	134
5.4	Multiple Coulomb Excitation of $^{148,150}\text{Nd}$ .....	137
5.5	Quasi-Elastic Scattering for $^{16}\text{O}+^{144,148,152}\text{Sm}$ Near The Coulomb Barrier.....	138
5.6	Mass Distributions of Fission Fragments in the $^{19}\text{F} + ^{197}\text{Au}$ Reaction.....	142
5.7	A Two-Dimensional Position-Sensitive Detection System for the $^8\text{Be}$ Nuclei from Heavy Ion Reactions.....	146



5.8	Effect of the Shell Structure on the Potential Barrier for the Subbarrier Fusion Reactions .....	150
5.9	Alpha Decay in Actinide Nuclei and the SPDF Boson Model .....	153
5.10	Proton-Neutron SDG Boson Model and Spherical-Deformed Phase Transition .....	155
5.11	Davydov-Filippov Limit of the IBM .....	156
VI	NEUTRON PHYSICS .....	157
6.1	A Preliminary Measurement of the Kinematically-Collimated Neutron Sources Using the $^1\text{H}(^{10}\text{B},\text{N})^{10}\text{C}$ and $^1\text{H}(^{11}\text{B},\text{N})^{11}\text{C}$ Reactions .....	159
6.2	Scattering of 13 MeV Neutrons from $^{11}\text{B}$ .....	163
6.3	Analysis of the Neutron Scattering Cross Sections of $^{118}\text{Sn}$ at 14.9 and 18.0 MeV .....	166
6.4	Measurements of Gamma-Ray Production Cross Sections .....	170
6.5	Nondestructive Elemental Analysis by the Method of Neutron Resonance Absorption .....	174
6.6	Construction of a Stabilization System for Photomultipliers' Gain Using a Regulated Light-Emitting Diode .....	177
VII	PUBLICATIONS .....	181
VIII	PERSONNEL AND COMMITTEES .....	207
IX	CO-OPERATIVE RESEARCHES .....	217

I ACCELERATOR OPERATION AND DEVELOPMENT

## 1.1 TANDEM ACCELERATOR OPERATION

Tandem Accelerator Group

Department of physics, JAERI

Accelerator operation

During the year from April 1, 1987 to March 31, 1988, the tandem accelerator has been operated for many kinds of experimental programs. In this period, the accelerator ran almost under the arranged schedule. However, some experiments were canceled by unexpected troubles, which occurred four times on the inside of the tank and once on the negative ion injector. The following are summary of the operation and the maintenance.

## 1) Time distribution by terminal voltage

>16 MV	18 days	10.2 %		11-12 MV	0 days	0.0 %
15-16	66	37.5		10-11	5	2.8
14-15	55	31.3		9-10	0	0.0
13-14	5	2.8		8-9	2	1.1
12-13	9	5.1		< 8	16	9.1

## 2) Time distribution by projectile

H	15 days	8.5 %		Si	11 days	6.3 %
D	7	4.0		S	37	21.0
Li	4	2.3		Cl	21	11.9
B	2	1.1		Ni	15	8.5
C	20	11.4		Cu	3	1.7
N	2	1.1		Br	3	1.7
O	20	11.4		I	6	3.4
F	10	5.7				

## 3) Time distribution by activity

Operation for research	179 days	49.0 %
Atomic and solid state physics	( 51 days )	
Radiation effects in materials	( 13 )	
Nuclear chemistry	( 27 )	
Nuclear physics	( 61 )	

Fast neutron physics	( 21 )	
Accelerator development	( 6 )	
Voltage conditioning	27	7.4 %
Operation training	2	0.6
Scheduled maintenance	92	25.2
Unexpected repair	19	5.2
Holidays and vacation	45	12.3

### Tank openings

The scheduled maintenance and major troubles, requiring seven tank openings, were as follows.

1) April 4 - 19, 1987 (scheduled opening)

Renewal of all the corona needles for both tubes and the columns.  
Renewal of the rotating shafts bearings on the lower seven column units.

2) June 28 - July 4

The trouble of the rotating shaft.

3) July 13 - 17

The trouble of the 180° magnet's power supply on the terminal.

4) September 16 - October 6 (scheduled opening)

Renewal of 1 to 3 MV low and high energy acceleration tubes.  
Renewal of the rotating shafts bearings on the middle six column units.

Replacement of the vacuum isolation valves, at the top end of the high energy tube and at the upper dead section of the high energy tube, by newly designed type.

Installation of new vacuum pump station at the entrance of the low energy tube.

5) October 9 - 12

Vacuum leakage on the high energy tube.

6) January 7 - 8, 1988

The trouble of the terminal electrostatic quadrupole lens' power supply.

7) February 17 - March 7 (scheduled opening)

Replacement of the terminal stripper foil changer and reload of the foils.

Renewal of the rotating shafts bearings on the upper seven column

units.

Regular maintenance for the components of the inside of the tank.

#### Other major troubles

- 1) Instability of the switching magnet flux.

The layer insulator deterioration on the upper coil of switching magnet occurred on end of December 1987.

- 2) Breakdown of the high voltage isolation transformer for the injector. The high voltage isolation transformer for the negative ion injector has been used instead of motor-generator system to eliminate the mechanical vibrations. A big spark across the high voltage platform to the ground attacked the isolation transformer. Some insulation layers of the primary coil (three phase 200V 50HZ) were broken by the spark energy.

#### Improvement and development

In order to obtain practically usable intensity of the Li ion beam ( $\sim \mu A$  order at the target) for the material research program, an inverted type sputter ion source was installed on the injector. The ion source, purchased from National Electrostatics Corporation, was somewhat modified in JAERI. The ion source is being used reliably for the routine operation not only for the Li beam but also many species of the ions.

In order to keep stable operation of the injector system and safety maintenance, now we are constructing a second negative injector which is placed next to the first injector.

Development of new control system, which consist of parallel processing computer by means of the Transputer, has started. The present control system, two set of 32 bit mini computers and CAMAC has been using over ten years and is already insufficient for the speed and the memory capacity. We intend to complete the new system within three years.

## 1.2 ELECTRON LINAC OPERATION AND IMPROVEMENTS

## Electron Linac Group

Department of Physics, JAERI

Operation

The operation of the 120 MeV JAERI electron linear accelerator (linac) have been carried out smoothly with a repetition rate of less than 150 pps. The total beam time was summed up to 929 hours for various experimental researches.

A summary of the linac conditions during the period between April, 1987 and March, 1988 is listed in Table 1 for each experimental program. The linac machine times were used as follows; (1) the study of the neutron guide mirror for the JRR-3 (Japan Research Reactor-3) facility, (2) the neutron cross section measurements, (3) the mono-energetic positron emission and its applications for material researches, (4) the neutron radiography, (5) the study of the irradiation damage in solid at the liquid helium temperature and (6) the radioisotope production.

The total machine time was decreased compared to the previous year, because it took three months to construct the measuring station for positron experiments and to repair the roof and outside-wall of the linac building. The machine time for neutron cross section measurements was

Table 1 Machine Time and Output Beam for Research Programs in 1987

Research Program	Time (h)	Ratio (%)	Energy (MeV)	Rate (pps)	Length ( $\mu$ s)	Current Ave. ( $\mu$ A)
Development of Research Reactor (Development of Neutron Mirror)	533.5	57.5	100	50	1	24
Neutron Radiography	216.6	23.3	120	150	1	12
Neutron Cross Section (Time of Flight Method)	116.3	12.5	120	150	0.025	12
Positron Experiment (Emission of Mono-Energetic Positron)	37.5	4.0	100	50	1	12
Solid State Physics (Low Temperature Electron Irradiation)	15.0	1.6	55	50	1	2
Tuning and Test Operation	10.2	1.1	100~180	50~150	1	30
<u>Total</u>	<u>929.1</u>	<u>100.0</u>				

considerably decreased during the last fiscal year because the number of the members of the low energy neutron experiments was decreased.

### Maintenance

The unscheduled shut-down was only due to the breakdown of an assembly for the electron gun cathode.

Several parts of the linac components were replaced as the scheduled maintenance. Those replaced parts were as follows ;(1) the eleven stabilized power supplies for focusing coils, that is, four sets of quadruple magnet power supplies for the #4 and #5 accelerating structures and five sets of quadruple magnets power supplies for the Tl beam transport line and two quadruple magnet for the Tlr beam transport line.

(2) the beam transport tubes of stainless steel for the Tl and Tr line were replaced with those of aluminum. By this replacements, residual activities in the beam transport tube were reduced significantly to 1/10 ~ 1/20.

### Improvements

#### (1) Trigger pulse transmission system

In order to lower the noises from the pulse modulators for the klystrons, the coaxial cables for eight sets of the trigger pulse transmission systems were replaced with the light fiber cables. The light fiber cable was Toshiba TOCP100Q (single signal line) with an out-side radius of 2.2 mm and photo couplers attached to the cable at both ends. Eight sets of cables were wired with a total length of 40 m. Two kinds of electronic apparatuses were used ;pulse transmitter (TOJX170) and receiver (TORX170). Electronic signals with a 2  $\mu$ sec and 5 V are converted to light signals by the transmitter and inversely restored to electronic signals by the receiver. The output signals from the receiver are directly used to operate the SCR drivers of large thyratrons with a pulse width of 2  $\mu$ sec and a voltage of 2 kV.

#### (2) Accelerated beam monitor systems

The 9 sets of beam monitors were prepared at each output of accelerating structure and the beam transport line. The coaxial cables (5D2W) were used from the each monitor position to the control room with a total length of 25 m ~ 35 m. This system with coaxial cables has been exchanged for the one with the semi-rigid cable (MX50-3.6) which was expected to reduce the noises significantly. The noises were reduced by 20 db compared to the

previous system.

(3) Grid-cathod assembly for the electron gun.

The grid-cathod assembly for the electron gun was replaced with the new model Y-796 produced by Eimac. The structure of the electron gun assembly was modified in order to mount the model Y-796 at the part of stem. The modified gun was fabricated after baking for 10 days at a temperature of 150 degree. The vacuum inside the gun was reached to  $3 \times 10^{-9}$  Torr and the beam test is now being carried out using the test bench.

#### The JAERI Storage Ring (JSR) to be Constructed at Linac

Fig. 1 shows the expected layout of the JSR facility in the linac building. The specification and dimensions of the facility are also listed in Table 2. The research team for the project of the intense photon source was assembled in Department of Physics in October, 1987. The decision was

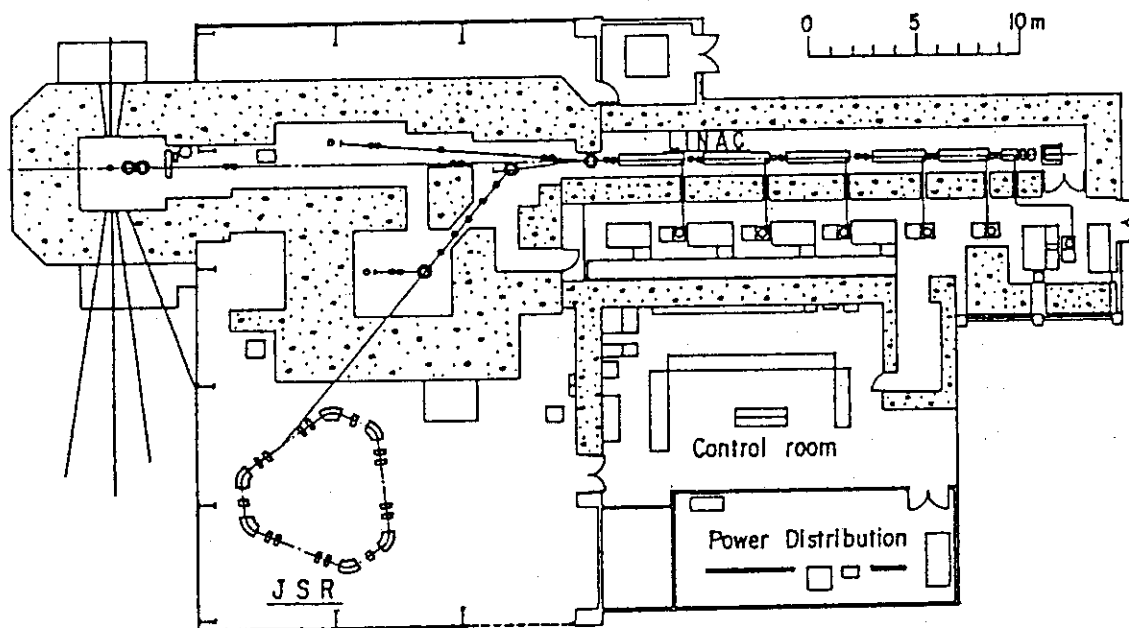


Fig. 1 Layout of the linac building.

made to design and fabricate the JSR, which will use the presently existing JAERI linac as an electron injector and accumulate experiences for the next coming large scale photon source. For this JSR facility, the high quality of the linac electron beam is required with an electron energy of 150 MeV and an energy resolution of 1 %.

In December, 1987, the preliminary test has been performed for the JSR injection and the beam energy resolution of  $150 \pm 1.55$  % with a peak current



Table 2 List of Parameters

Stored energy	300 MeV	of 38 mA and a beam radius of 5 mm
(Injection energy)	150 MeV)	was obtained. In order to inject
Circumference	20.546 m	more stable electron beam into
Average radius	3.27 m	JSR, further improvement has to be
Revolution time	68.5 nsec	made to achieve the overall stabi-
Available straight section	1.45 m	lities for all the electric power
Number of bending magnets	6	supplies. Under the present con-
Property of bending magnet	sector magnet	dition, the usage of the MG (Motor
Bending radius	0.835 m	Electric Power Generator) would be
Bending magnet field	1.2 T	more efficient choice which do not
Number of quadrupoles	15	need improvements and modifica-
Strength of quadrupole field	6.8 m <sup>-2</sup>	tions to the linac structure and
	4.1 m <sup>-2</sup>	parts.
	-5.6 m <sup>-2</sup>	
Natural emittance	1.1 x 10 <sup>-7</sup> m·rad	
Natural chromaticity	x -1.81	
	y -4.54	
Tune	x 2.25	
	y 1.25	
Damping time constant	x 58 msec	
	y 48 msec	
	s 22 msec	
Momentum compaction factor	0.044	
Energy loss per turn	0.86 keV/turn	
RF frequency	116.7 MHz	
Harmonic number	8	
Peak voltage	30 kV	
Synchrotron phase	8.8 degree	
Phase oscillation frequency	34.6 kHz	
RF power	2 kW	
Natural bunch length	1.6 cm	
Touschek lifetime	~2 hours	

#### The 12th Linear Accelerator Meeting in Japan

In August 1987, The 12th Linear Accelerator Meeting was held by the joint cooperation between Nuclear Engineering Research Laboratory, Faculty of Engineering, University of Tokyo and the JAERI Linac Laboratory. The information of the current linac technology for actively operating accelerators including proton and heavy ion linacs as well as electron linacs has been exchanged among more than 150 participants through the 70 presented papers.

#### Reference

H. Yokomizo et al. : Design of a Small Storage Ring in JAERI (1988).

### 1.3 PRODUCTION AND ACCELERATION OF ALKALINE METAL IONS USING AN INVERTED SPUTTER ION SOURCE

Eisuke MINEHARA, Tadashi YOSHIDA and  
Shinichi ABE

Department of Physics, JAERI

Five kinds of negative Li, Na, K, Rb, and Cs ions were tried to produce in the JAERI negative ion source test facility with an inverted sputter ion source manufactured by National Electrostatic Corporation. Tens kinds of different sputtering targets<sup>1)</sup> containing these elements were prepared, and tested to find the materials having the larger negative ion intensities.

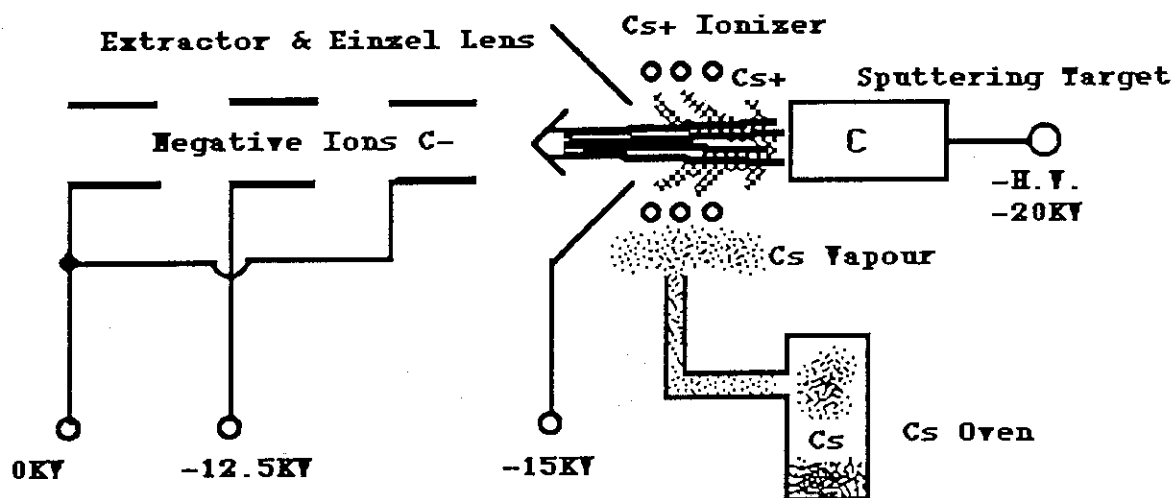


Fig.1 Inverted Sputter Ion Source.

Fig.1 shows the inverted sputter ion source, and illustrates the working mechanism. The sputtering targets were fabricated by pressing the powder materials impregnated with or without silver powder binder. Several examples of the materials and their typical current intensities of the elemental ions are shown in fig.2.

According to the several user's requests, we applied lithium oxide for producing negatively-charged lithium metal

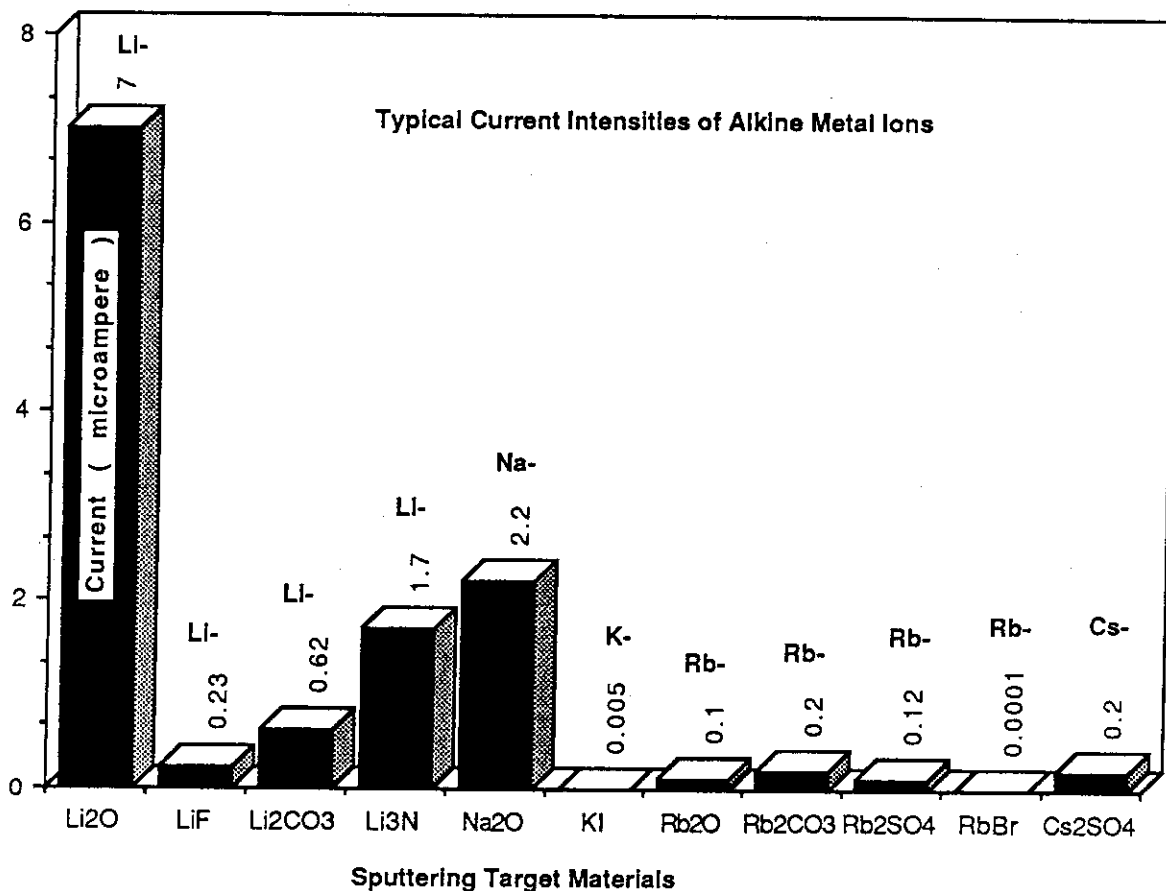


Fig.2 Several examples of the sputtering target materials and their typical current intensities of the elemental alkaline metal ions<sup>2)</sup>.

Table 1 Acceleration of Li Ions

Terminal Voltage	14.88 MV
Ion Source Voltage	20.00 KV
Preacceleration Voltage	198.40 KV
Final Energy	59.70 MV
Final Charge State	3+
Beam Current at Injector	4.7 microampere
Beam Current at Injection Line	0.6 microampere
Beam Current before Foil Stripper	0.3 microampere
Beam Current after Foil Stripper	0.7 microampere
Beam Current after Analyzer	0.7 microampere

ions, and accelerated them to check the feasibility for the actual operation.

Lithium beam current intensities, which were measured at several Faraday cups along the beam line, are summarized in Table 1. Parameters of the accelerator are also listed briefly

in the table. After the acceleration test were performed successfully in early stage of the 1987 fisical year, Li ions have been available for all users.

References

- 1) E.Minehara: Proc.of the Workshop on Negative Ion Sources, Negative Ions and their Applications, Tsukuba, National Laboratory for High Energy Physics, April 1988, to be published.
- 2) S.Abe et al.:Proc. of the Workshop on Tandem Accelerators and Related Technologies, JAERI Tokyo, July 1988, to be published.

## 1.4 SLACKENED CARBON STRIPPER FOILS

Shuhei KANAZAWA and Suehiro TAKEUCHI

Department of Physics, JAERI

We need thin and long-lived carbon stripper foils to have a good heavy ion beam transmission through a tandem accelerator. A good beam transmission is going to be more significant for beam injection into a post acceleration booster which will be constructed for the JAERI tandem accelerator.

It has been shown <sup>1)</sup> that the lifetimes of JAERI type super stripper foils strongly depend on their thicknesses: foils of  $5 \mu\text{g}/\text{cm}^2$  had only one-fourth of the lifetimes that foils of  $10 \mu\text{g}/\text{cm}^2$  had. The reason is that beam-irradiated areas shrink faster in thinner foils.

As a way to improve their lives against heavy ions, we introduced foil slackening into our preparation method of the super stripper foils. Foils of  $3 - 5 \mu\text{g}/\text{cm}^2$  were coated with thin collodion films, holded on aluminum rings of 16 mm in inner diameter and slackened by contracting the rings to 14 mm in inner diameter.

These foils were set at the tandem terminal foil stripper position. Their lives were tested with destructive ion beams of iodine. A beam energy was 15 MeV, that is, the tandem terminal voltage was set at a usually available voltage of 15 MV. The beam current was measured at the Faraday cups in front of the stripper foils(FC-TL-1) and at the image point of the analyzing magnet(FC-04-1). The charge state of the analyzed ions was + 11.

The result is shown in Table 1. The lifetimes were determined when the beam current at FC-04-1 decayed to a half of the initial value. Current ratios of FC-04-1 to FC-TL-1 are shown also. Foils of  $10 \mu\text{g}/\text{cm}^2$  were also tested for a comparison. As a result, the slackened 3 or 5  $\mu\text{g}/\text{cm}^2$  foils lived as long as the non-slackened  $10 \mu\text{g}/\text{cm}^2$  super stripper foils did. The beam transmission was apparently improved in use of 3 or 5  $\mu\text{g}/\text{cm}^2$  foils. Another beam test was done for slackened and non-slackened 5  $\mu\text{g}/\text{cm}^2$  foils. Slackened foil's lifetimes were twice and half as much as non-slackened ones.

Table. 1 Lifetimes of carbon stripper foils and current ratios of analyzed ions to initial ions for iodine.

Foils	Average Lifetime	Average Current Ratio of FC-04-1 to FC-TL-1.
3 $\mu\text{g}/\text{cm}^2$ slackened	30 min.	105 %
5 $\mu\text{g}/\text{cm}^2$ slackened	29 min.	90 %
10 $\mu\text{g}/\text{cm}^2$ non-slackened, self-suport	33 min.	55 %

Reference

- 1) S. Takeuchi and S. Kanazawa, Proc. of The 11th World Conf. of the International Nuclear Target Development Society, Seattle, Wa, USA Oct. 6-8, 1982, ppi-17.

## 1.5 SUPERCONDUCTING BOOSTER

Booster Project Group

Department of Physics, JAERI

1. Accelerating structure

For the accelerating structure of the JAERI tandem superconducting booster, a superconducting quarter wave resonator has been fully developed as is reported elsewhere in this report.

A buncher composed of two 130 MHz superconducting quarter wave resonators was built in 1987 by Mitsubishi Electric Corp., Kobe Works. Accelerating field levels of 5 to 6.2 MV/m were obtained at an rf loss less than 4 watts with the buncher resonators. A mechanical frequency tuner was developed and confirmed to work well. Prototype rf control circuits were fabricated and worked well with a superconducting resonator. Further work is, however, necessary to fully control resonators and cryostats. A test with beams from the tandem accelerator will be performed in 1988 at a beam line, H-3.

A prototype acceleration unit composed of two 130MHz superconducting quarter wave resonators is under construction at Mitsubishi Electric Corp. in Kobe. This unit is a testing unit for developing booster modules and will be used for a de-buncher at the end of the booster. We ordered a set of booster control satellite with four resonator boards from Applied Superconductivity Inc. for the de-buncher (and the buncher) since it was found to fit perfectly to our booster modules, buncher and de-buncher from its specification. Use of the ASI's control satellites reduces our developing work on the booster control system.

The initial part of the booster which will be composed of 16 resonators and four cryostats, that is, four modules having four resonators in each cryostat, is going to be funded in the fiscal years of 1988 and 1989. The design is proceeding. A schematic view is shown in Fig.1.

As a result of considerations on beam bunching, we decided to add a 260MHz superconducting sub-buncher in front of the buncher in place of having pre-tandem low frequency buncher.

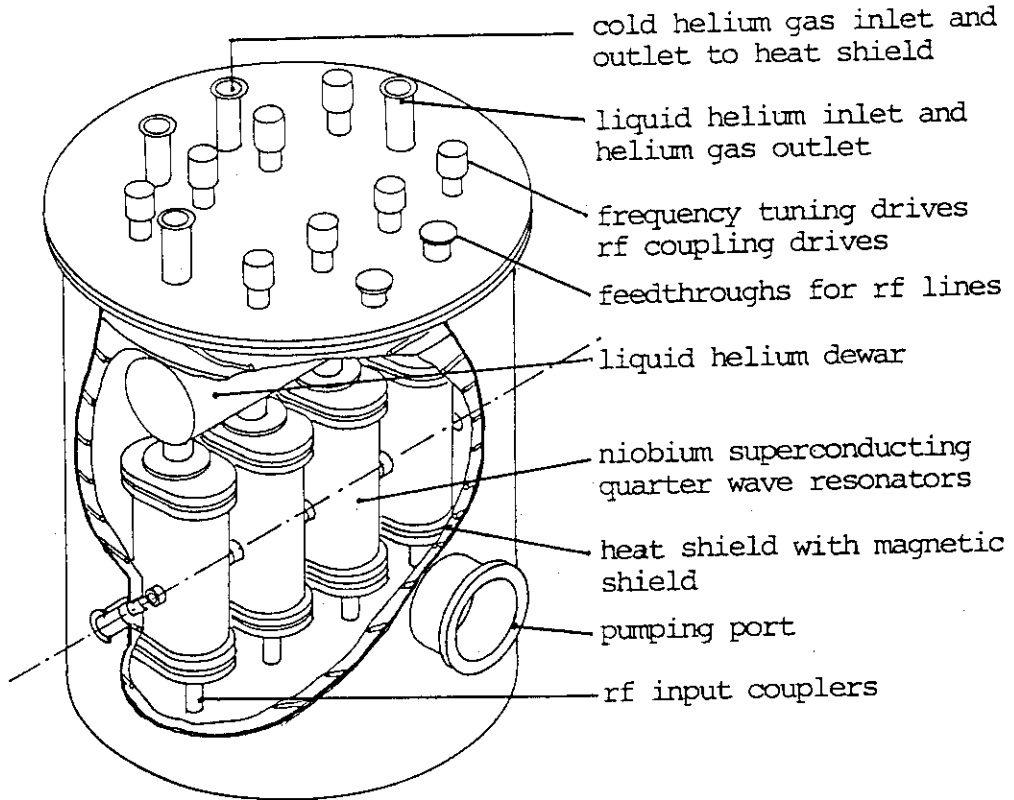


Fig. 1 Schematic of a booster module.

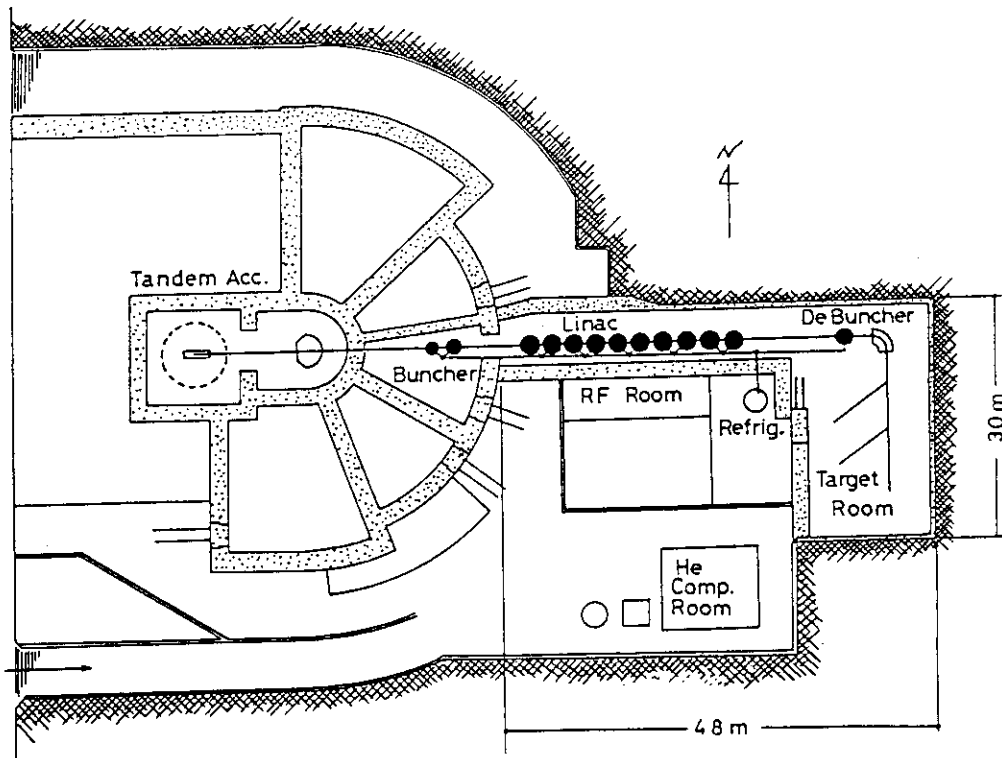


Fig. 2 Layout of JAERI Tandem Superconducting Booster



## 2. Layout plan

The booster construction site has been decided to be on the east side of the tandem accelerator. As is shown in Fig. 2, the booster modules will be lined up along the straight line extended from the 0 degree course from the tandem switching magnet. The bunchers will be put in the existing target room, Heavy Ion Target Room No. 1. A new target room of about 15 m x 20 m and rooms for rf controls, a refrigerator and utilities will be constructed on the south side. There will be no thick radiation shield from the bunchers to the new target room, so that the Heavy Ion Target Room No. 1, the booster room and the new target room are regarded as one room on radiation security. A helium compressor room, helium gas reservoirs and a water cooler will be put apart from the booster building.

## 3. Beam dynamics study

Our beam dynamics group has been calculating the beam dynamics from the bunching system composed of 130 MHz and 260 MHz resonators, through ten modules, each of which consists of 4 quarter wave resonators and a quadrupole doublet lens, and through a de-buncher, down to an analyzing magnet. As a result, the group has a prospect that the bunching system will work well without a pre-tandem bunching system and that 50 to 62 percent of incident continuous heavy ion beams from the tandem accelerator can be bunched and accelerated on a right rf phase through the booster. A buffer aperture is necessary at each module entrance to prevent some of out-of-phase beams from hitting resonators. A beam diagnostic system for resonator rf phase tuning is under study in addition to a way to tune resonator phases one by one from the first resonator to the end by measuring beam energy v.s. phase variations at the booster exit .

## 4. Cryogenic system plan

A 350 watts refrigerator without liquid nitrogen assist is considered for supplying liquid helium to the booster resonators. A consumption of about 100 watts out of 350 watts is estimated for transfer lines to all modules and about 20 watts for each modules. We are not going to use liquid nitrogen for helium gas pre-cooling in the refrigerator and for the heat shields of booster modules because of the

reasons below. We have a hope to run the booster under the high pressure gas safety regulations for refrigerators and coolers, rather than the general regulations for high pressure gas equipments. To realize it, the helium refrigerator and the booster modules must compose a closed circuit like a popular cooler and must not contain a heat exchanger with high pressure gas, liquid nitrogen in this case. A liquid nitrogen assisted system requires huge amount of supplies or consumption of liquid nitrogen week after week and a lot of expence. It is more economical and convenient to us in this laboratory to buy and use a system which runs fully by electric power than to buy liquid nitrogen.

## 1.6 SUPERCONDUCTING RESONATORS FOR JAERI TANDEM BOOSTER

Suehiro TAKEUCHI, Tetsuro ISHII and Hiroshi IKEZOE

Department of Physics, JAERI

Development of niobium superconducting quarter wave resonators for the booster of the JAERI tandem accelerator went forward to the construction of the beam bunching and de-bunching resonators after finishing the test with the first-fabricated prototype resonator.

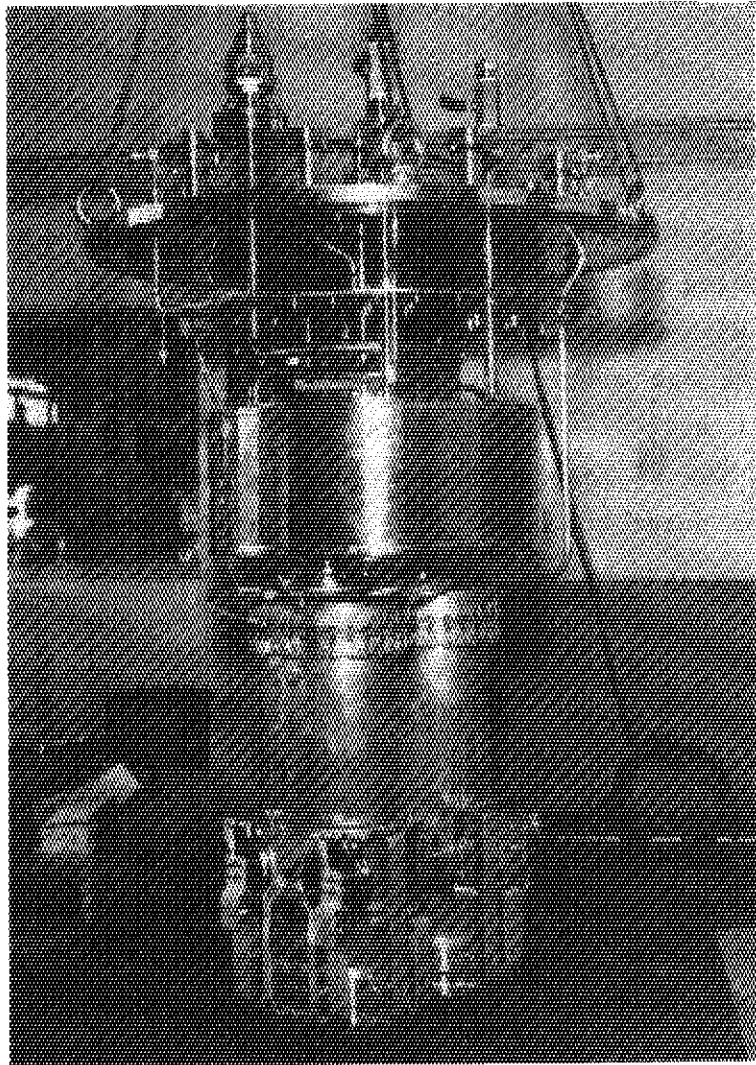
With the prototype resonator, a maximum acceleration field level of 5 MV/m was eventually obtained at an rf loss of 6 watts<sup>1-4)</sup>. This result satisfies our requirement on the field level but not on the rf loss. The rf loss was partly due to niobium weld defects at the top end of the outer conductor. Weld failures should be prevented or followed by a perfect repair work in the construction of the resonators for the booster. The prototype resonator did not have heavy electron multi-pactoring barriers nor a heavy rf loss due to electron field emission. These facts promise that we will get a high field level quickly without tedious conditioning in starting the booster.

A superconducting buncher composed of two quarter wave resonators was constructed at Mitsubishi Electric Corp., Kobe in 1987. The design of the resonators is essentially the same as the prototype one except the following changes: a) The outer conductors were given eight vertical straight grooves 4 mm deep and 9 mm wide on the copper surface and demountable stainless steel franges at their bottom ends in place of copper ones welded on. These changes provide an easy deformation to the outer conductor for frequency course tuning. b) The top copper franges and the top niobium end plates were changed thicker in order to satisfy high pressure gas safety regulations. The fabrication proceeded successfully. There happened no failures in machining, welding, annealing, electropolishing and etc. The electro-polishing was done at an electroplating company in Kobe. The resonators equipped with frequency tuners and a liquid helium dewar are shown in Fig.1.

However, helium leaked in a cryogenic test. The top niobium end plates were found to be deformed by bolting with copper franges which had gasket grooves about 12 mm smaller in diameter than the prototype

resonator's one. The end plates were reformed. New top copper franges were made, of which gas-ket grooves were designed to press the outermost rigid end of the niobium end plates. And, the leaks were abolished.

Fig. 1 A super-conducting buncher composed of two quarter wave resonators made of niobium and copper.



The buncher resonators were tested in a test cryostat after slight electropolishing as a final surface treatment and a rinse with de-ionized water in a clean room. Their results are shown in Fig. 2 a) and b). Two results obtained firstly with a resonator (labeled No. 2) are shown in Fig. 2 a). The field level of the first result, curve A, was unexpectedly high but the Q was smaller than expected. After the test, we found that the cryostat inside had not been properly shielded to about 200 mG against the earth's magnetic field. The second result, curve B, was obtained after reducing the magnetic field in the cryostat

to 25 mG level. The difference of Q between the two curves at lower field region indicates that the frozen-in-magnetic flux affects significantly on the resonator Q. A sharp decrease in Q of the second result at higher field region is probably due to electron field emission. The Q would be improved if pulse conditioning was applied. A result for the other resonator(labeled No. 1) is shown in Fig. 2 b). There were two changes from the No.2 resonator in its rinse process. We used 10% H<sub>2</sub>O<sub>2</sub> in place of HF for the rinse just after the final electropolishing. Fresh de-ionized water from a de-ionizer was directly sprayed onto the resonator surface instead of pre-de-ionized water from a polyethylene reservoir. The resistance would be improved by this from 1 megaohm\*cm to 18 megaohm\*cm. The Q was as high as expected. A sharp decrease in Q due to electron field emission observed at higher field in curve A was easily cured and a higher field level was obtained by pulse conditioning(see curve B). Curve C is the result after more pulse

Fig. 2 a) Resonator Q v.s. accelerating field level of a superconducting quarter wave resonator at 4.2K. Q A:The resonator was cooled in the external magnetic field of about 200 mG, B:in about 25 mG.

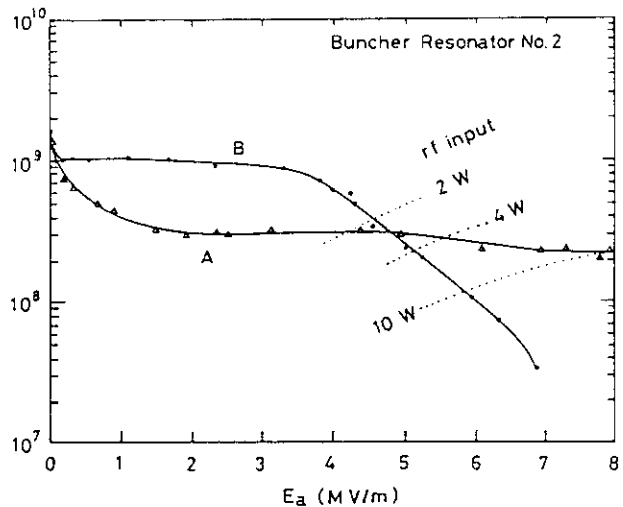
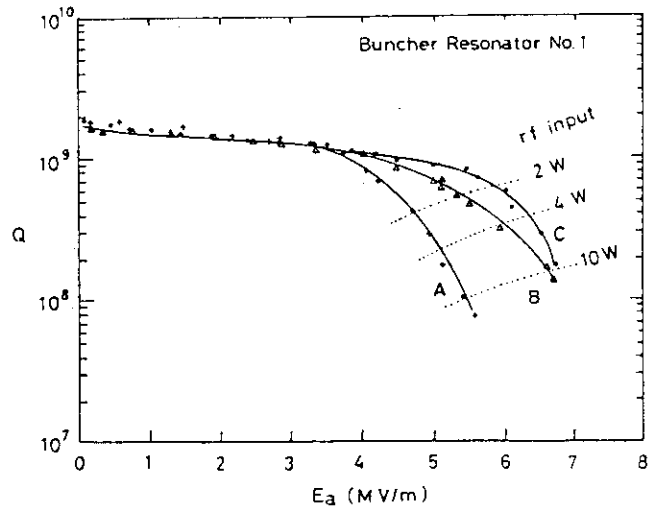


Fig. 2 b) Resonator Q v.s. accelerating field level of a superconducting resonator at 4.2K cooled in the external magnetic field of about 25 mG. A:before conditioning. B:after pulse conditioning. C:after additional pulse conditioning with helium gas.



conditioning with introducing helium gas into the resonator.

As a result, we learned that a maximum field level of 6MV/m (or an acceleration voltage of 900 kV) is available at an rf loss of 4 watts and that the magnetic shield is crucial on Q of our niobium quarter wave resonators. Rinse with 10% H<sub>2</sub>O<sub>2</sub> and fresh de-ionized water is promising.

On the other hand, a slow frequency tuner has been re-designed. The tuners seen in Fig. 1 employed a pneumatic control with helium gas and bellows. We gave up to proceed with them because of several reasons and finally chose a fully mechanical frequency tuner schematically

illustrated in Fig. 3. A prototype tuner was made and tested with the No.2 resonator at the helium temperature. The frequency was tunable within a Hz. There was a back rush of about 5 Hz, which is small enough for operation. Appreciable frequency instability was not observed during the test. The tuning range designed is 40 KHz. The tuner will be driven from outside the cryostat with stepping motors. An advantage to use such a mechanical tuner is that operation is rarely necessary once a resonator is tuned.

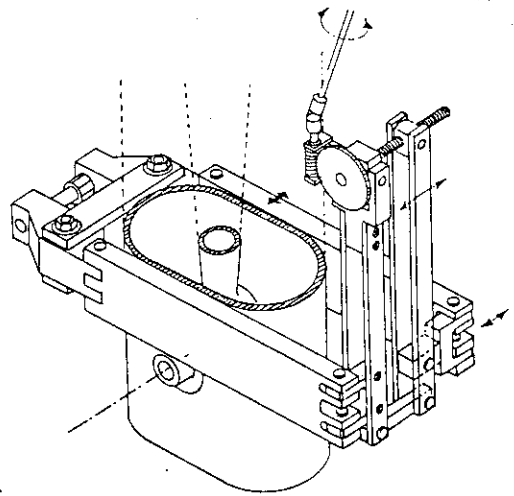


Fig. 3 A frequency tuner.

#### References

- 1) S. Takeuchi, T. Ishii, H. Ikezoe and M. Ohkubo: Proc. of the 12th Linear Acc. Meeting in Japan, Tokai(1987)36.
- 2) S. Takeuchi: Proc. of The Third Workshop on RF Superconductivity, Argonne, 1987, ANL-PHY-88-1 2(1988)429.
- 3) S. Takeuchi: Symposium of North Eastern Acc. Personnel, Florida, 1987(World Scientific, Singapore, Newjersey and Hongkong, 1988)pp333-342.
- 4) S. Takeuchi:Proc. of Japan-China Joint Symposium, Wako, 1987, to be published.

## 1.7 LINAC FOR A FREE-ELECTRON-LASER OSCILLATOR

Yuuki KAWARASAKI, Makio OHKUBO,  
Katsuo MASHIKO and Naomoto SHIKAZONO

Department of Physics, JAERI

The choice of accelerator types for a free-electron-laser(FEL) oscillator is discussed. A superconducting radio-frequency(RF) linac is found out to be the most suited one for our case. Specification of the linac is given with an R&D schedule.

### 1. Introduction

Laser beam from FEL can be obtained, in principle, by oscillating relativistic electron beams through adequate wigglers or undulators<sup>1)</sup>. As practical electron-beam sources, candidates may actually be: pulse-diode devices charged up by e.g. Marx generators, Van de Graaff accelerators, induction linacs, RF linacs and storage rings.

The aim of our project is to produce infrared through ultraviolet laser beam by FEL, because these lasers can be possibly used for various fields of research and application. Though the laser wavelength depends on the design of the undulator magnet, the electron beam energy, ranging from a few of tens of MeV to several hundred MeV, is considered to be suitable for those purposes. This requirement immediately lead us to adopt a linear accelerator(linac) as the first stage machine of our project.

We are now continuing the operation of a 120MeV normal conducting RF(S-band) linac<sup>2)</sup> for neutron nuclear data measurements and other research purposes. This will be used as the injector of a small(300MeV) storage ring and as a positron source in near future. The required beam quality, however, cannot be easily achieved from the simple modification of the present linac. It seems preferable to design a completely new machine dedicated only to the FEL project.

### 2. Considerations on linac types.

Three normal conducting linacs have been newly built or greatly

modified for the FEL projects and succeeded in oscillation: the first one is the 20MeV standing wave mode L-band(1300MHz) linac at LANL<sup>3)</sup> in oscillation at an infrared wavelength, the second the Boeing Aerospace Company's(BAC's) 120MeV traveling wave mode L-band linac<sup>4)</sup> at a visible wavelength and the last the modified Stanford Mark III (traveling, S-band(2856MHz)) linac<sup>5)</sup> an infrared wave-length.

The former two linacs operate in longer pulse duration( $\sim 100\mu s$ ), being provided by specially prepared components; klystrons and their pulse power supplies. The last linac is the old Mark III, the conventional gun and buncher being replaced by a so-called RF-gun and a momentum filter, by which high quality beam can eventually be injected into one unit of Mark III waveguide.

The first FEL oscillation at Stanford<sup>6)</sup> has reasonably been succeeded using HEPL's superconducting linac(SCL), which can accelerate high quality beams in long macropulses. Thus a SCL is attractive if greater field gradient( $>5MV/m$ ) in cavity is achievable. In recent years, the remarkable progresses of this matter ( $\sim 10MV/m$ ) have been reported from TRISTAN's at KEK<sup>7)</sup> and from CEBAF's<sup>8)</sup>. At JAERI, a project of a heavy ion boosting linac<sup>9)</sup> for the Tandem Accelerator is now in progress, using a niobium quarter-wave coaxial resonator. The various techniques of the cryogenics and high Q cavities developed there will be helpful.

In the RF-linac based FEL operation, an energy-recovery configuration is desirable and forthcoming for high-power oscillation, because the FEL efficiency(laser power vs. beam power) is still order of few to several percents and the remaining beam power is dumped out unless it is reused. The tests of this configuration have been successfully performed both at LANL and at HEPL. The LANL's uses two structures: one accelerator and another decelerator, while the HEPL's SCL uses a technique of beam recirculation. The recirculation is also applicable as an energy doubler. Furthermore, solid-state RF amplifiers can hopefully be used, because the cavity wall losses in SCL are negligible. New finding of high  $T_c$  superconductor may somewhat influence the choice, because the project period will span over several years.

### 3. Superconducting Linac

The choice of SCL's frequency is important: e.g., HEPL's at 1300MHz, CEBAF's at 1500MHz, TRISTAN's at 508MHz and CERN's at 350MHz. Use of



lower frequency is fit to higher quality and current beam without extra cooling below liquid H<sub>2</sub> boiling point, 4.2° K, at 1 atm. Thus the same cavity structure as TRISTAN's is satisfactorily applicable for a main part of the linac. TRISTAN's one cryostat module contains two 5-cell units, i.e., being capable to accelerate beams of 15MeV (5MeV/m) to 30MeV (10MeV/m).

The injector design is another key point, because its performance governs strongly the output beam quality. Higher injection-gun voltage can well prevent from emittance growth. A photocathode gun can actually produce micropulseformatted beams of enough current density, however, its adoption here seems yet premature. A thermoionic cathode gun must accordingly be followed by bunchers. Furthermore, a micropulse formatter (e.g., chopper) is necessary anywhere in their vicinity. A gridded gun is expected to work with an elaborated pulsing circuit. Two single superconducting cavities for pre-acceleration (1~4MeV) seem more neat than a normal conducting one. The geometrical  $\beta$  of the first cavity, can effectively be chosen less than unity (~0.9) for further longitudinal bunching. The above considerations allow us to depict the conceptual FEL scheme shown in fig.1.

#### 4. Schedule

The FEL system will finally incorporate with the beam recirculation both for energy doubling and for energy recovery. The whole project period is accordingly divided into three phases. The Phase-I is basically devoted to the fundamental R&D of the simplest FEL feature, aiming at an infrared (10.6  $\mu$ m) lasing. In Phase-II, the addition of one more SCL module with recirculation as an energy doubling (~100MeV) will work lasing at a visible or ultraviolet wavelength and the increase of output power by means of an energy recovery will be attempted in Phase-III. The injector gun will be improved in later phases by replacement of a mode-locked photocathode gun.

#### 5. Specification in Phase-I

< Main Part of the Linac >

---

Type	superconducting 2(unit) × 5(cavity)
frequency	508MHz

Effective Length  $2 \times 1.5\text{m}$

< Gun (Injector-I) >

---

Type	Thermoionic Gridded Pierce ( $2 \sim 3\text{mm } \phi$ )
Applied voltage	$>200\text{kV}$
Pulsing format	$2 \sim 4\text{ns}$ width every $80\text{ns}$ ( $127\text{MHz}$ ) separation during $1\text{ms}$ (macropulse)
Repetition	$10\text{Hz}$ (macropulse)

< Sub- and harmonic Buncher (Injector-II) >

---

Type	$\lambda/4$ coaxial resonator (normal conducting)
Frequency	$127\text{MHz}$ ( $1/4$ ) or $87\text{MHz}$ ( $1/6$ )
Gap Voltage	$30 \sim 60\text{kV}$

< Harmonic buncher >

---

Type	re-entrant cavity (normal conducting)
Frequency	$508\text{MHz}$
Gap Voltage	$10 \sim 40\text{kV}$

< Pre-accelerator (Injector-III) >

---

Type	Two superconducting single cavities
Geometrical $\beta$	the 1st's $\sim 0.9(\beta)$ 2nd's $1.0$

### References

- 1) For example, review articles or textbooks on FEL
- 2) H. TAKEKOSHI, ed., JAERI-1238 (1975) ( in Japanese)
- 3) J.M. WATSON, Nucl. Instr. and Methods A250 (1986) 1
- 4) J.L. ADAMSKI et al., IEEE NS-32 (1985) 3397
- 5) S.V. BENSON et al., Nucl. Instr. and Methods A250 (1986) 39
- 6) D.A.G. DEACON et al., Phys. Rev. Lett 38 (1977) 892
- 7) Y. KOJIMA, OHM, No.1 (1988) p38 ( in Japanese)
- 8) H. A. GRUNDER et al., CEBAF-PR-87-017
- 9) S. TAKEUCHI et al., JAERI-M 87-115, p16

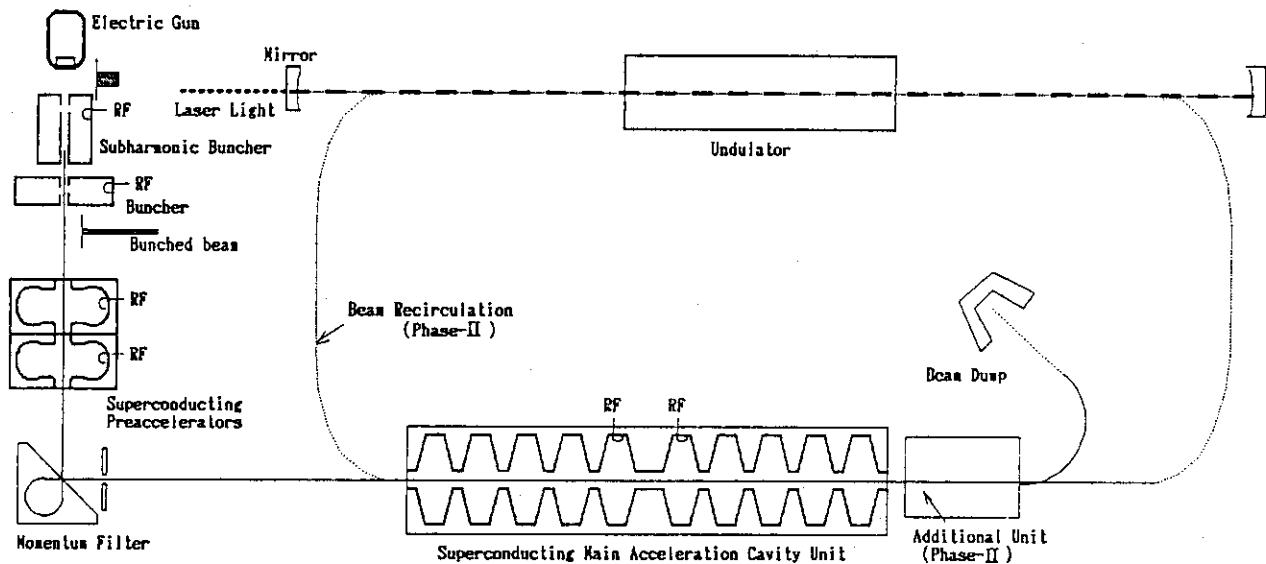


Fig.1 Free Electron Laser Scheme

In Phase-I, an experiment for FEL oscillation at an infrared wavelength(10.6 $\mu$ m) will be performed in 1991. In Phase-II, the increase of the beam energy will be attempted to a visible wavelength oscillation with one more of the main acceleration unit and by means of the beam recirculation (dotted figures). A new building (Phase-II) for the FEL system with application facilities will be prepared. This figure corresponds to an energy-recovery configuration using the same beam-recirculation path.

## 1.8 BEAM OPTICS OF A SUPERCONDUCTING BOOSTER FOR THE JAERI TANDEM ACCELERATOR

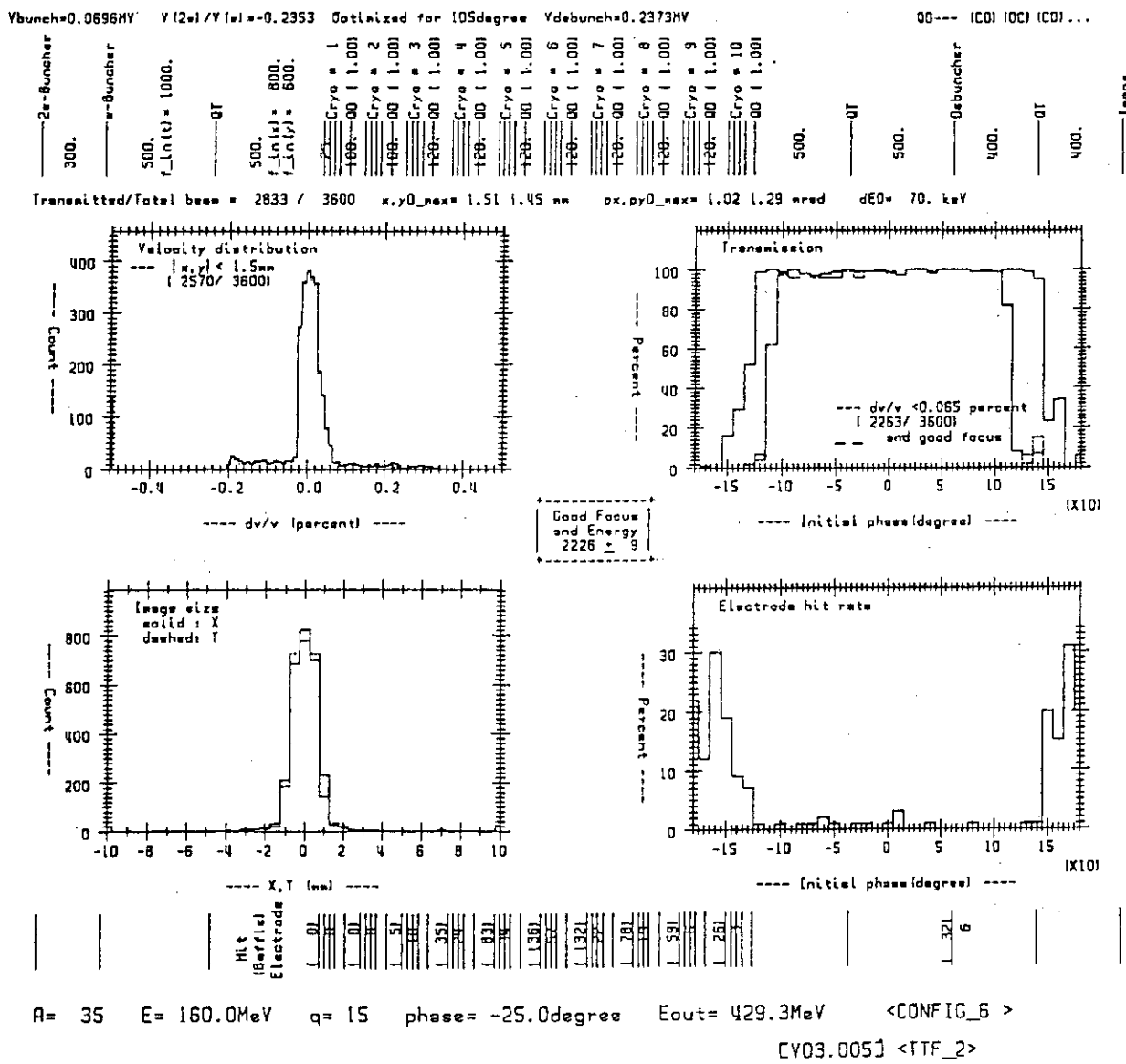
Yoshiaki TOMITA, Tetsuro ISHII, Suehiro TAKEUCHI,  
Shiro KIKUCHI and Eisuke MINEHARA

Department of Physics, JAERI

In order to investigate beam optics of a superconducting booster for the JAERI tandem accelerator, a computer program has been written which calculates beam trajectories in the booster. This program runs on a DEC VAX and can display beam trajectories, phase bunching, velocity-time correlation and final distributions of velocity and position using a E&S MPS graphic display. By using this program various configurations has been examined and a configuration has been chosen as a "good" candidate. Calculation has been made for  $^{12}\text{C}$ ,  $^{35}\text{Cl}$  and  $^{127}\text{I}$  beams and the results are summerized in Table 1. As is shown in the table, 50-60 % of continuous beam can be accelerated even without a prebuncher, if control of the beam/resonators can be accomplished as intended. Results of calculation for 3600 incident beams of 160 MeV  $^{35}\text{Cl}$  are shown in Fig. 1. Used configuration is shown by vertical lines at the top: from left to right, 2 bunchers, a triplet Q-lens, 10 sets of 4 resonators in a cryostat and a doublet Q-lens, a triplet Q-lens, a debuncher, a triplet Q-lens and final image point. Distances between devices are indicated in cm. Upper left histogram is the final velocity distribution. Lower left histogram shows beam size. Upper right histogram is the beam transmission ratio versus initial phase. It can be seen that nearly all beam of initial phase between  $-105^{\circ}$  and  $110^{\circ}$  can be used with a velocity spread of  $\pm 0.065\%$  and a beam size of 3mm. Lower right histogram is the ratio of beam stopped inside the resonators versus initial phase. A baffle is placed before each resonator. The case shown in Fig. 1 uses baffles with a bore 12 mm in radius. By reducing this radius to 8 mm, the ratio of beam stopped inside the resonators becomes negligible without significantly reducing the output beam.

Table 1 Typical results of calculation.

Beam	$^{12}\text{C}$	$^{35}\text{Cl}$	$^{127}\text{I}$
<b>Injection</b>			
Energy (MeV)	96.2	160.0	203.0
Charge	6	15	31
<b>Emittance</b>			
x (mm)	0.88	1.51	1.31
y (mm)	1.06	1.45	1.47
x' (mrad)	0.95	1.02	0.91
y' (mrad)	0.92	1.29	1.51
$\Delta E$ (MeV)	0.014	0.070	0.250
<b>Output</b>			
Energy (MeV)	197	429	770
$\Delta E$ (MeV)	0.13	0.56	1.77
Available beam (%)	50	62	55



Dump file:cl35\_6 [V03.002] Date:22-APR-1988 12:55:42.91 Baffle radius=12.0mm

Fig. 1 Calculated distributions for 3600 incident beams of <sup>35</sup>Cl.

II ATOMIC PHYSICS AND CHEMISTRY

## 2.1 PRODUCTION OF MULTIPLY CHARGED RECOIL IONS IN COLLISIONS OF 50-keV/u AND 100-keV/u C AND Ne IONS WITH Ne

Yasuaki SUGIZAKI, Masao SATAKA, Toshizo SHIRAI,  
kiyoshi KAWATSURA and Yohta NAKAI

Department of Physics, JAERI

### Introduction

Multiple ionization processes in ion-atom collisions are interesting subjects not only in atomic physics and astrophysics but also in accelerator technology and nuclear fusion research. In the last decade, many investigations have reported the net ionization cross sections (NI),  $\sigma_+$  ( $=\sum_i i\sigma_i$ ), and partial ionization cross sections (PI),  $\sigma_i$ , where  $\sigma_i$  is the cross section for production of target recoil ions  $i$ -times ionized.

In this paper, we present the partial ionization cross sections of multiply charged recoil  $\text{Ne}^{i+}$  ions produced by impact of highly charged C and Ne ions at the incident energies of 50 and 100 keV/u. We have systematically examined the  $i$ -dependence of the PI in the asymmetric ( $\text{C}^{q+} + \text{Ne}$ ) and the symmetric ( $\text{Ne}^{q+} + \text{Ne}$ ) collision systems.

### Experimental procedure

The present experiment was performed at the 2 MV Van de Graaff accelerator at JAERI. The experimental apparatus is schematically shown in Fig. 1. The partial ionization cross sections (PI) for production of multiply charged recoil Ne ions were measured by means of a coincidence and a time of flight (TOF) method. Figure 2 shows a typical TOF spectrum of recoil  $\text{Ne}^{i+}$  ions produced by impact of  $\text{Ne}^{3+}$  ions at 100 keV/u. The detail of experimental method was described elsewhere.<sup>1,2)</sup>

In this experiment, the projectiles such as  $\text{C}^+$ ,  $\text{Ne}^+$  and  $\text{Ne}^{2+}$  are extracted directly from the PIG ion source and then accelerated. The higher charge state ions are obtained by post-stripping the primary beam in the gas cell.



### Results and discussion

Figures 3 and 4 show the experimental PI for production of recoil target Ne ions in collisions with the projectile  $C^{q+}$  and  $Ne^{q+}$  ions at 50 and 100 keV/u, respectively. The PI decreases steeply with the increase of the charge state of the recoil ions. While, the PI for the same charge state of the recoil ions increase smoothly with the increase the projectile charge state. Figure 5 shows the NI as a function of the initial charge state of the projectiles. The solid curves show the least-squares fitted results of the cross section  $\sigma_+$  to the equation  $\sigma_+ = Cq^n$  ( $C$  is a constant). We have obtained  $n=1.2$  ( $C = 5.9 \times 10^{-16} \text{ cm}^2$ ) and  $n=1.3$  ( $C = 3.6 \times 10^{-16} \text{ cm}^2$ ) at 50 keV/u and 100 keV/u, respectively. The experimental results are compared with the calculation of the classical trajectory Monte-Carlo (CTMC) model<sup>3)</sup> in connection with the independent-electron approximation (IEA).<sup>4)</sup> The present measurement is in good agreement with the theoretical calculations within a factor of 2.

### References

- 1) Y. Sugizaki, M. Sataka, K. Kawatsura and Y. Nakai: JAERI-M 87-115 (1987) 27.
- 2) Y. Sugizaki, M. Sataka, K. Kawatsura, T. Shirai and Y. Nakai: to be published.
- 3) R.E. Olson and A. Salop: Phys. Rev. A16 (1977) 531.
- 4) J.H. McGuire and L. Weaver: Phys. Rev. A16 (1977) 41.

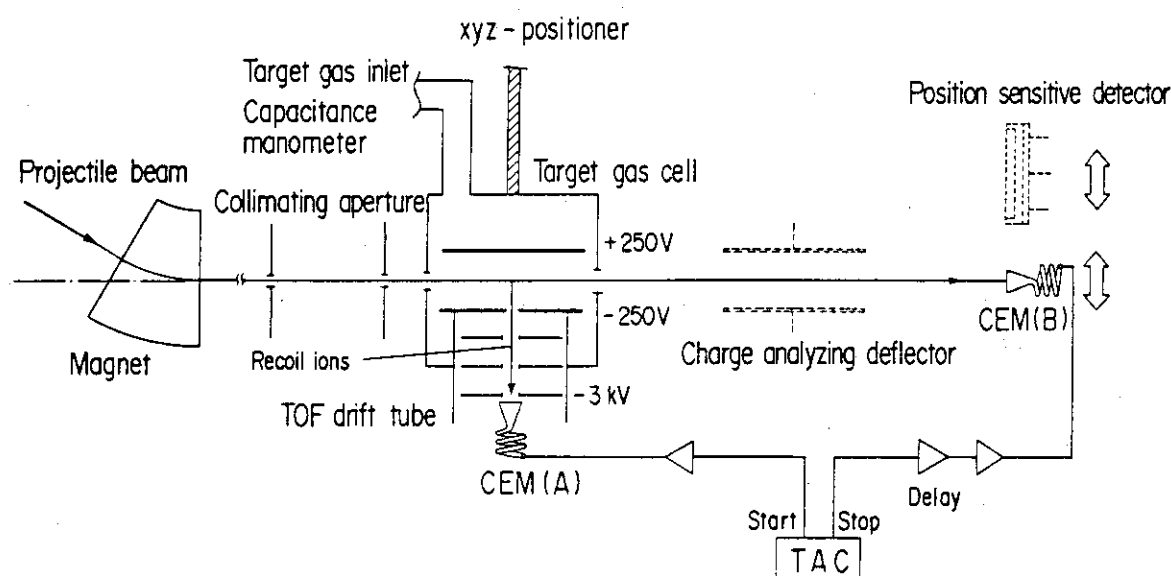


Fig. 1 Schematic illustration of the experimental apparatus.

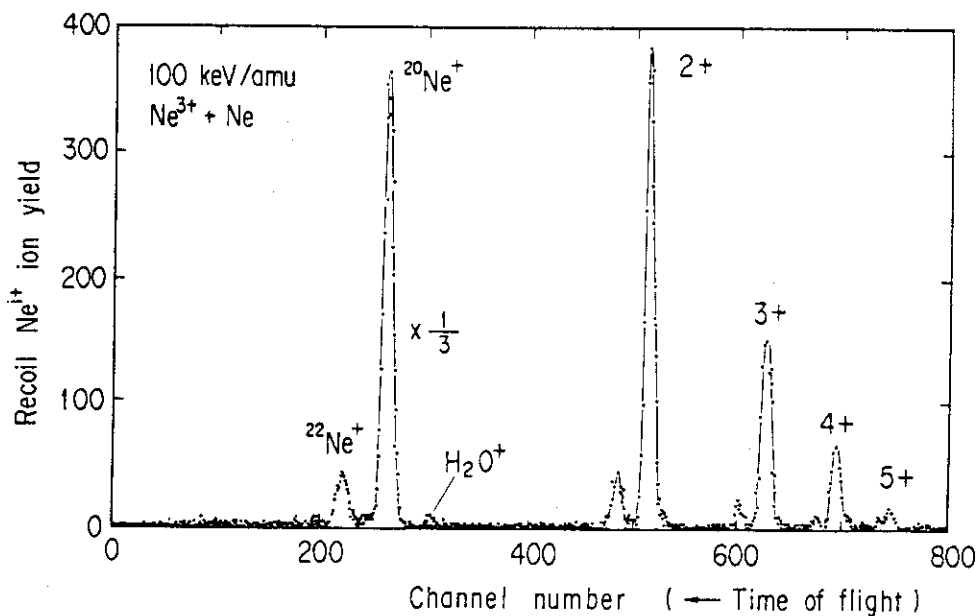


Fig. 2 A typical time-of-flight spectrum.

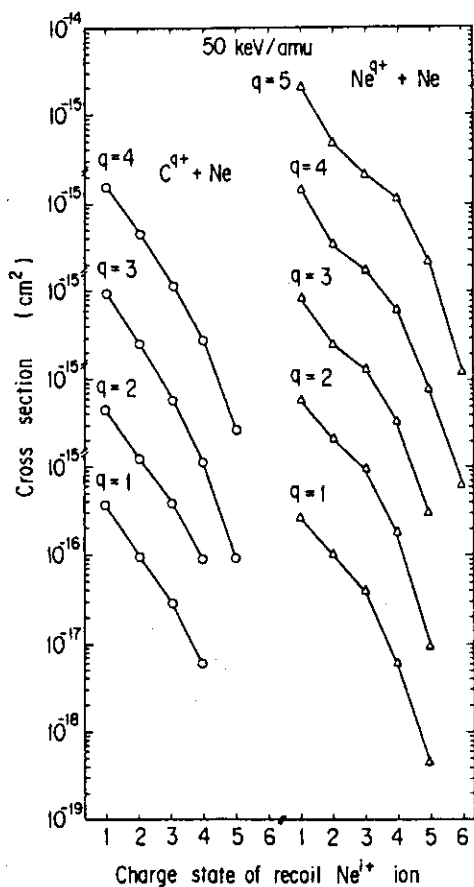


Fig. 3 Partial ionization cross sections at 50 keV/u.

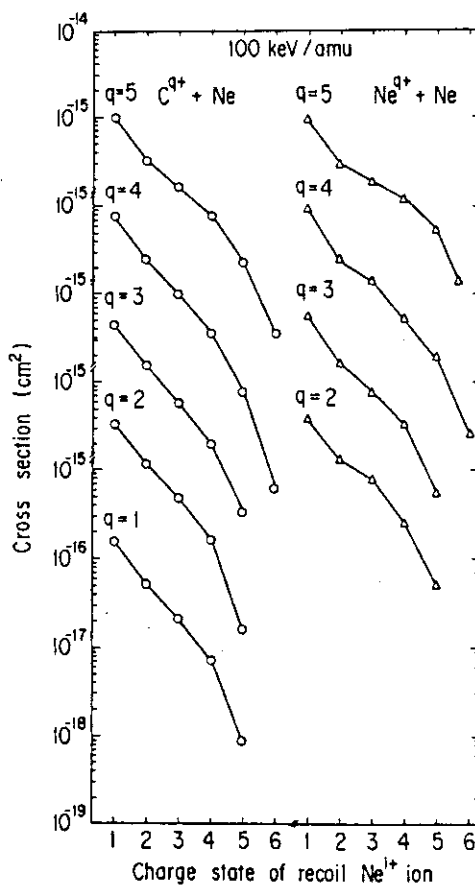


Fig. 4 Partial ionization cross sections at 100 keV/u.

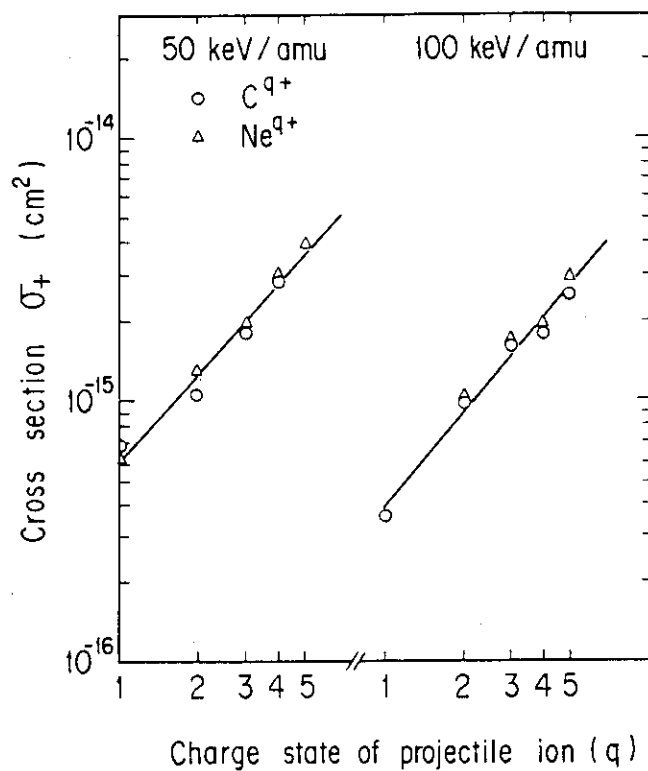


Fig. 5 Net ionization cross sections.

Solid lines are the fitting results.

2.2 RADIATIVE ELECTRON CAPTURE IN HEAVY ION AND H<sub>2</sub> COLLISIONS

Kiyoshi KAWATSURA, Akio Ootuka,<sup>\*</sup> Ken-ichiro KOMAKI,<sup>\*</sup>  
 Masao SATAKA, Yasuaki SUGIZAKI, Hiroshi NARAMOTO,  
 Fuminori FUJIMOTO,<sup>\*</sup> Yohta NAKAI and Kunio OZAWA<sup>\*\*</sup>

Department of Physics, JAERI,<sup>\*</sup> College of Arts and Sciences,  
 University of Tokyo,<sup>\*\*</sup> Energy Research Laboratory, Hitachi  
 Ltd.

Introduction

Radiative electron capture (REC) in fast heavy ion-atom collisions was first observed by Schnopper et al.<sup>1)</sup> Most of the experimental REC data has been accumulated by using either a solid target or a gas cell with an entrance window. Therefore, the observed data should be corrected to obtain the real REC x-ray spectra. The experiments should be carried out under single collision conditions to compare directly experimental data with the theoretical calculations. This work was done in order to extend our data<sup>2-4)</sup> to the different target. We report measurements and analyses of the x rays produced in the radiative electron-capture process in Si<sup>13+</sup> and Si<sup>14+</sup>, S<sup>15+</sup> and S<sup>16+</sup>, Cl<sup>16+</sup> and Cl<sup>17+</sup> ions incident on a H<sub>2</sub> gas target at energies of 4.0-5.5 MeV/amu.

Experiments

The present experiment was performed using the tandem accelerator at JAERI. Beams of highly ionized silicone, sulfur and chlorine were accelerated to the energy of 4.0-5.5 MeV/amu. The 0- and 1-electron projectiles were obtained by post-stripping the primary beams in a carbon foil (15-30 μg/cm<sup>2</sup>). A collision chamber contained a single nozzle for the target gas jet and was connected to the H-2 beam line through the differential pumping system. The characteristic K x rays and the broad K-REC x rays were observed with a Horiba Si(Li) x-ray detector which was placed at 90° to the beam direction. The energy resolution was about 170 eV FWHM at 5.9 keV. The experimental procedure has been described in a previous paper.<sup>4)</sup>

### Results and discussion

Figure 1 shows the x-ray spectra for  $\text{Cl}^{16+}$  and  $\text{Cl}^{17+}$  ions incident on a  $\text{H}_2$  gas target at an energy of 175 MeV (5.0 MeV/amu). The broad peaks between 6 keV and 7 keV correspond to the radiative capture of bound electrons from a H atom into the K-shell of the bare or one-electron ions (K-REC x rays). The centroid energy of the REC x rays which changes with the projectile energy is given as<sup>5)</sup>

$$h\omega = \epsilon_f - \epsilon_i + (1/2)mv_0^2 = \epsilon_f - \epsilon_i + (m/M)E_0. \quad (1)$$

In present measurement,  $\epsilon_f$  and  $\epsilon_i$  correspond to the binding energies of the 1s electrons of the projectile ions and H atoms (13.6 eV). The experimental results are in good agreement with the calculated ones.

The full width at half maximum of the REC x rays is given as<sup>6)</sup>

$$\Gamma_{\text{REC}}(\text{FWHM}) = 2.04(T_0 T_i)^{1/2}. \quad (2)$$

$T_0$  is  $(1/2)mv_0^2$  and  $T_i$  the kinetic energy average of the target electron. The experimental results seem to be in agreement with the theoretical calculations. The more detailed analyses are in progress now.

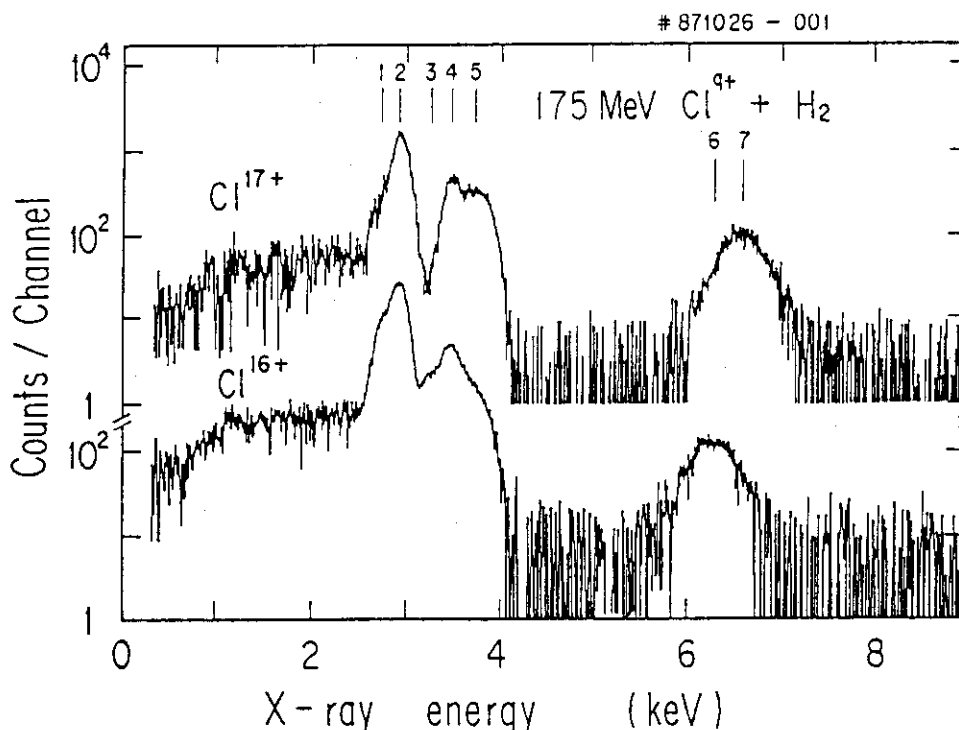


Fig. 1 The x-ray spectra obtained from 175 MeV  $\text{Cl}^{16+}$  and  $\text{Cl}^{17+}$  ions incident on a  $\text{H}_2$  gas target. 1,  $\text{K}\alpha(1s2p \rightarrow 1s^2)$ ; 2,  $\text{Ly}\alpha(2p \rightarrow 1s)$ ; 3,  $\text{K}\beta(1s3p \rightarrow 1s^2)$ ; 4,  $\text{Ly}\beta(3p \rightarrow 1s)$ ; 5,  $4p \rightarrow 1s$ ; 6, helium-like REC (final state  $1s^2$ ); 7, hydrogen-like REC (final state  $1s$ ).

References

- 1) H.W. Schnopper, H.D. Betz, J.P. Delvaille, K. Kalata, A.R. Sohval, K.W. Jones and H.E. Wegner: Phys. Rev. Lett. 29 (1972) 898.
- 2) K. Kawatsura, H. Tawara and P. Richard: IEEE Trans. Nucl. Sci. NS-28 (1981) 1053.
- 3) H. Tawara, P. Richard and K. Kawatsura: Phys. Rev. A26 (1982) 154.
- 4) K. Kawatsura, A. Ootuka, M. Sataka, K. Komaki, H. Naramoto, K. Ozawa, Y. Nakai and F. Fujimoto: Nucl. Instrum. & Methods A262 (1987) 33.
- 5) M. Kleber and D.H. Jakubassa: Nucl. Phys. A252 (1975) 152.
- 6) A.R. Sohval, J.P. Delvaille, K. Kalata, K. Kirby-Docken and H.W. Schnopper: J. Phys. B9 (1976) L25.

## 2.3 X-RAY EMISSION FROM FOIL-EXCITED SILICON BEAMS

Ken-ichiro KOMAKI,<sup>\*</sup> Kiyoshi KAWATSURA, Akio OOTUKA,<sup>\*</sup>  
 Masao SATAKA, Yasuaki SUGIZAKI, Hiroshi NARAMOTO,  
 Kunio OZAWA,<sup>\*\*</sup> Yohta NAKAI and Fuminori FUJIMOTO<sup>\*</sup>

Department of Physics, JAERI,<sup>\*</sup> College of Arts and Sciences,  
 University of Tokyo,<sup>\*\*</sup> Energy Research Laboratory, Hitachi,  
 Ltd.

Introduction

The precise measurements of the transition energies and probabilities of highly ionized atoms can provide an important information of the relativistic effects and quantum-electrodynamics. They are also very useful in the fields of nuclear fusion research and astrophysics. Especially, forbidden decays in few-electron systems for the low Z atoms show too small rate to be observable. They, however, become observable at the higher Z atoms.

In the previous paper,<sup>1,2)</sup> we have presented the results of experimental measurements of the Cl K x-ray transition energies and the lifetimes for the metastable states in He-like and Li-like Cl atoms. In this report, we present the experimental results of Si atoms obtained by the Bragg crystal x-ray spectrometer and the Doppler-tuned x-ray absorption edge spectrometer (DTS).

Experimental

The measurement of the Si K x-ray spectra was carried out using 50 to 60 MeV Si<sup>7+</sup> ions from the JAERI tandem accelerator. In order to obtain the transition energies of the highly ionized Si ions, the Si K x-ray spectra were measured for 50 MeV Si<sup>7+</sup> ions incident on a carbon foil target using a 12.7 cm, curved crystal x-ray spectrometer. The Si K x rays were analyzed with a PET crystal, 2d spacing of 8.742 Å. The lifetime measurement was performed using the DTS which was similar to that described by Cocke et al.<sup>3)</sup> In this experiment, we have used 50 MeV Si ions as the incident projectiles, a carbon foil of 15 µg/cm<sup>2</sup> thickness as an exciter of the projectile beams and a 18 µm SiO<sub>2</sub> foil or a 20 µm Si foil as an

absorber. The detail of these spectrometers has been described elsewhere.<sup>1,2)</sup>

### Results and discussion

Figure 1 shows the K x-ray spectrum of the 60 MeV  $\text{Si}^{7+}$  ions incident on a  $15 \mu\text{g}/\text{cm}^2$  C foil target. It involves most of the Si K x rays ranging from four-electron (Be-like) to one-electron (H-like) ions. This spectrum also reveals lines from multiply excited states. The present measurement is in good agreement with the similar measurements for 35-45 MeV Si ions incident on a C foil target by Trabert et al.<sup>4)</sup>

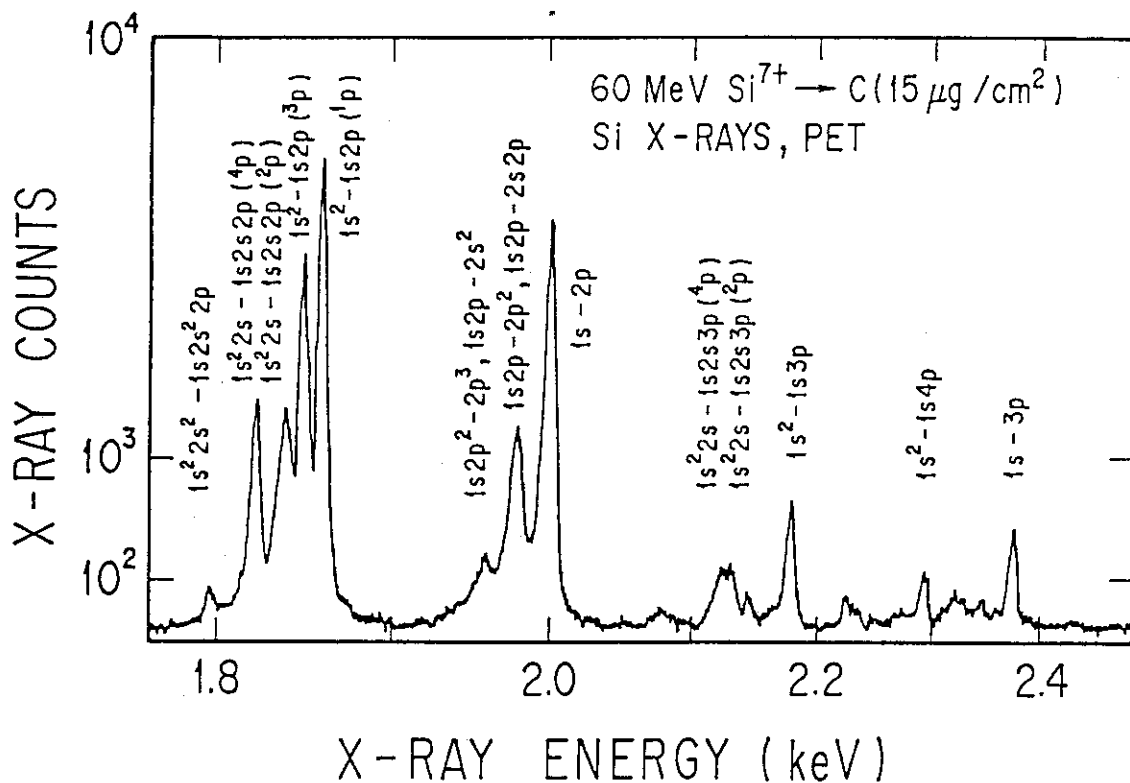


Fig. 1 High resolution Si K x-ray spectrum resulting from 60 MeV  $\text{Si}^{7+}$  ions incident on a carbon foil target.



Another high resolution study of the x-ray emission from the foil-excited beams was performed using the DTS. A typical DTS spectrum from 50 MeV  $\text{Si}^{7+}$  beams is shown in Fig. 2. In upper of the figure, the integral spectrum is shown as a function of the detector angle. Three steps are clearly found in this spectrum. A differential spectrum is shown at the bottom part of the figure. Three peaks are also found at the same positions, which correspond  $78.8^\circ$ ,  $92.7^\circ$  and  $98.3^\circ$ . These lines are compared with Fig. 1 and the results of Trabert et al.<sup>4)</sup> It is concluded that the line at  $78.8^\circ$  correspond to the overlapping of the transitions of  $1s2p\ ^3P_{1,2} - 1s^2\ ^1S_0$  Si XIII (1854.15, 1855.7 eV), the line at  $92.7^\circ$  to the overlapping of the transitions of  $1s2s2p\ ^4P_j - 1s^22s\ ^2S_j$  Si XII (1826.8 eV) and  $1s2p^2\ ^4P_j - 1s^22p\ ^2P_j$  Si XII (1828.15 eV). The line at  $98.3^\circ$  corresponds to the transition of  $1s2p\ ^1P_1 - 1s^2\ ^1S_0$  Si XIII (1860.0 eV).

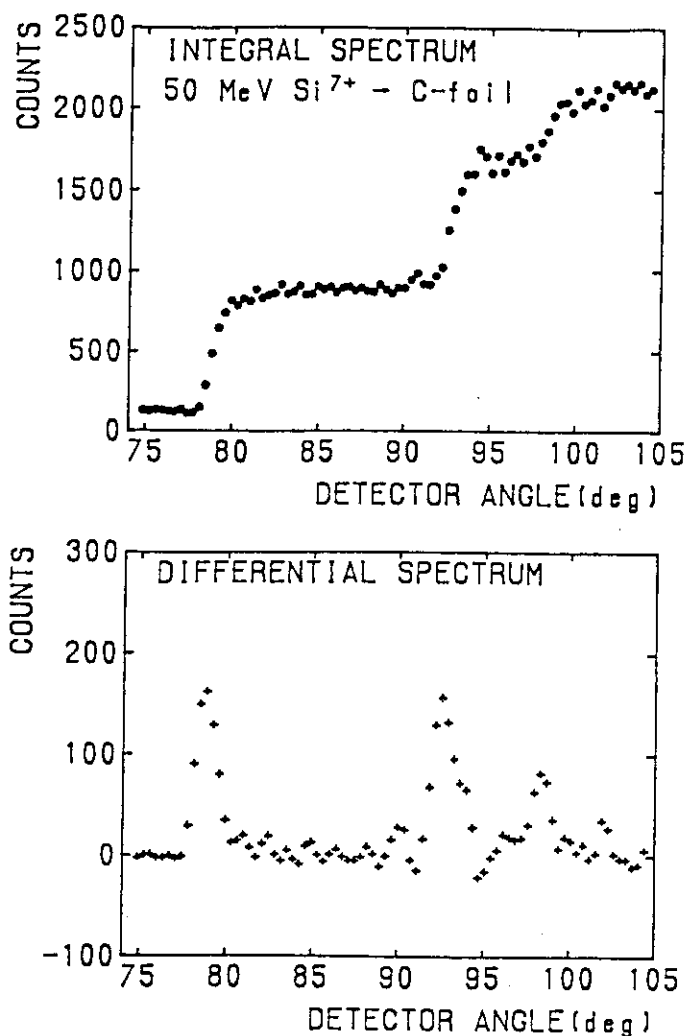


Fig. 2 Typical DTS spectrum resulting from 50 MeV  $\text{Si}^{7+}$  ions incident on a carbon foil target. The integral spectrum (upper) and its differential one (bottom).

We have tried to measure the radiative lifetimes of the metastable states in highly ionized Si ions using the TOF method. The measured lifetime for the decay of  $1s2p^3P_2$  level is  $4.42 \pm 0.08$  ns, which is in good agreement with the theoretical calculations. The measured lifetime for the decay of the  $1s2s2p^4P_{5/2}$  level is  $1.93 \pm 0.10$  ns, which is in good agreement with the theoretical results of 1.84 ns and 2.05 ns and the experimental result of 2.1 ns.

#### References

- 1) K. Kawatsura, M. Sataka, Y. Sugizaki, H. Naramoto, Y. Nakai, K. Komaki, A. Ootuka, F. Fujimoto and K. Ozawa: JAERI-M 87-115 (1987) 36.
- 2) K. Kawatsura, M. Sataka, A. Ootuka, K. Komaki, H. Naramoto, K. Ozawa, Y. Nakai and F. Fujimoto: Nucl. Instrum. & Method A262 (1987) 150.
- 3) C.L. Cocke, B. Curnutte, J.R. Macdonald and R. Randall: Phys. Rev. A9 (1974) 57.
- 4) E. Trabert, I.A. Armour, S. Bashkin, N.A. Jelley, R. O'Brien and J.D. Silver: J. Phys. B12 (1979) 1665.

## 2.4 BEAM-FOIL SPECTRA OF CHLORINE IONS IN HIGH ENERGY REGION (V)

Masao SATAKA, Kiyoshi KAWATSURA, Yasuaki SUGIZAKI,  
 Hiroshi NARAMOTO, Yohta NAKAI, Kunio OZAWA\*, Akio OOTUKA\*\*,  
 Ken-ichiro KOMAKI\*\*, Fuminori FUJIMOTO\*\* and Keishi ISHII\*\*\*

Department of Physics, JAERI, \* Energy Research Laboratory,  
 Hitachi Ltd., \*\* College of Arts and Sciences, University of  
 Tokyo, \*\*\* Faculty of Engineering, Kyoto University

In order to study the transition energies and the lifetimes of excited states in highly ionized Cl atoms, a beam-foil investigation has started using the tandem accelerator at JAERI in 1982.<sup>1)</sup> A number of beam-foil studies of Cl ions have been reported. the previous measurements were performed at lower energies than 50 MeV. In the present experiment, the beam energy is varied from 80 to 150 MeV. The wavelength range of beam-foil spectra is covered 30 to 470 Å. The experimental apparatus has been described in detail in references.<sup>1-3)</sup>

Figure 1 shows a typical beam-foil spectrum between 30 and 390 Å of highly ionized Cl ions at an energy of 120 MeV. The strong lines were easily identified with the use of the results of the previous works. In order to identify complicated or weak lines, we have measured the beam-foil spectra at different energies from 80 to 150 MeV, and we have performed some calculations. Most of the lines are attributed to the  $\Delta n = 0$  transitions of the type  $2s^2 2p^k - 2s2p^{k+1}$  and  $2s2p^{k+1} - 2p^{k+2}$  in Cl XII - Cl XV. Several lines are newly identified as high nl transitions in Cl XIII - Cl XVII in this wavelength region.

We have also measured the radiative lifetimes of the  $\Delta n = 0$  transition. In Fig. 2 the normalized intensity decay curve of the  $(1s^2 2p)^2 P_{3/2} - (1s^2 2s)^2 S_{1/2}$  transition is shown as a function of the distance of the foil. After background subtraction, the decay curve was least-squared fitted to a single exponential function. The line blending with 380.4 Å (Cl XIV,  $n = 5-6$ ) is negligible. The observed lifetime of  $0.76 \pm 0.01$  ns is in good agreement with the previous ones of  $0.76 \pm 0.04$  ns from Forester et al.<sup>4)</sup> and  $0.71 \pm 0.03$  ns from Ishii et al.<sup>5)</sup> It is found that the present value is most accurate among all of the experimental values. Part

of the energy and lifetime data obtained in the present work is summarized in the Table 1. The detailed results and discussion of the present experiment will be reported elsewhere.<sup>3,6)</sup>

### References

- 1) M. Sataka, K. Ozawa, K. Kawatsura, H. Yamaguchi, K. Ishii, T. Kitahara, K. Masai, A. Ootuka, K. Komaki, F. Fujimoto and K. Kikuchi: JAERI-M 85-125 (1985) 58.
- 2) K. Kawatsura, M. Sataka, A. Ootuka, K. Komaki, H. Naramoto, K. Ozawa, Y. Nakai and F. Fujimoto: Nucl. Instrum. & Methods A262 (1987) 150.
- 3) M. Sataka, K. Ozawa, K. Kawatsura, A. Ootuka, K. Komaki, H. Naramoto, F. Fujimoto, Y. Nakai and K. Ishii: J. Phys. Soc. Jpn. (1988) in press.
- 4) J.P. Forester, D.J. Pegg, P.M. Griffin, G.D. Alton, S.B. Elston, H.C. Hayden, R.S. Thoe, C.R. Vane and J.J. Wright: Phys. Rev. A18 (1978) 1476.
- 5) K. Ishii, E. Alvarez, R. Hallin, J. Lindskog, A. Marelius, J. Pihl, R. Sjodin, B. Denne, L. Engstrom, S. Huldt and I. Martinson: Physica Scripta 18 (1978) 57.
- 6) M. Sataka, K. Ozawa, A. Ootuka, K. Ishii, K. Kawatsura, K. Komaki, H. Naramoto, Y. Nakai and F. Fujimoto: in preparation.

Table 1 Radiative lifetimes in Cl XIII - Cl XV

Ion	Wavelength (A)	Transition	Lifetime (ns)		
			Present	Forester[4]	Ishii[5]
XV	415.6	2s <sup>2</sup> S <sub>1/2</sub> - 2p <sup>2</sup> P <sub>1/2</sub>	0.96 ±0.02	0.95 ±0.05	1.0 ±0.1
XV	384.0	2s <sup>2</sup> S <sub>1/2</sub> - 2p <sup>2</sup> P <sub>3/2</sub>	0.76 ±0.01	0.76 ±0.04	0.71 ±0.03
XIV	458.4	2s2p <sup>1</sup> P <sub>1</sub> - 2p <sup>2</sup> <sup>1</sup> D <sub>2</sub>	0.63 ±0.02	0.60 ±0.06	0.54 ±0.01
XIV	294.9	2s2p <sup>3</sup> P <sub>2</sub> - 2p <sup>2</sup> <sup>3</sup> P <sub>1</sub>	0.17 ±0.01		
XIV	286.2	2s2p <sup>3</sup> P <sub>2</sub> - 2p <sup>2</sup> <sup>3</sup> P <sub>2</sub>	0.16 ±0.01	0.16 ±0.01	
XIV	284.3	2s2p <sup>3</sup> P <sub>1</sub> - 2p <sup>2</sup> <sup>3</sup> P <sub>1</sub>	0.16 ±0.01		
XIV	277.9	2s2p <sup>1</sup> P <sub>1</sub> - 2p <sup>2</sup> <sup>1</sup> S <sub>0</sub>	0.084±0.005	0.067±0.010	
XIV	276.1	2s2p <sup>3</sup> P <sub>1</sub> - 2p <sup>2</sup> <sup>3</sup> P <sub>2</sub>	0.16 ±0.01		
XIV	237.8	2s <sup>2</sup> <sup>1</sup> S <sub>0</sub> - 2s2p <sup>1</sup> P <sub>1</sub>	0.14 ±0.01	0.15 ±0.03	
XIII	302.2	2s2p <sup>2</sup> <sup>2</sup> P <sub>3/2</sub> - 2p <sup>3</sup> <sup>2</sup> D <sub>3/2</sub>	0.63 ±0.02		

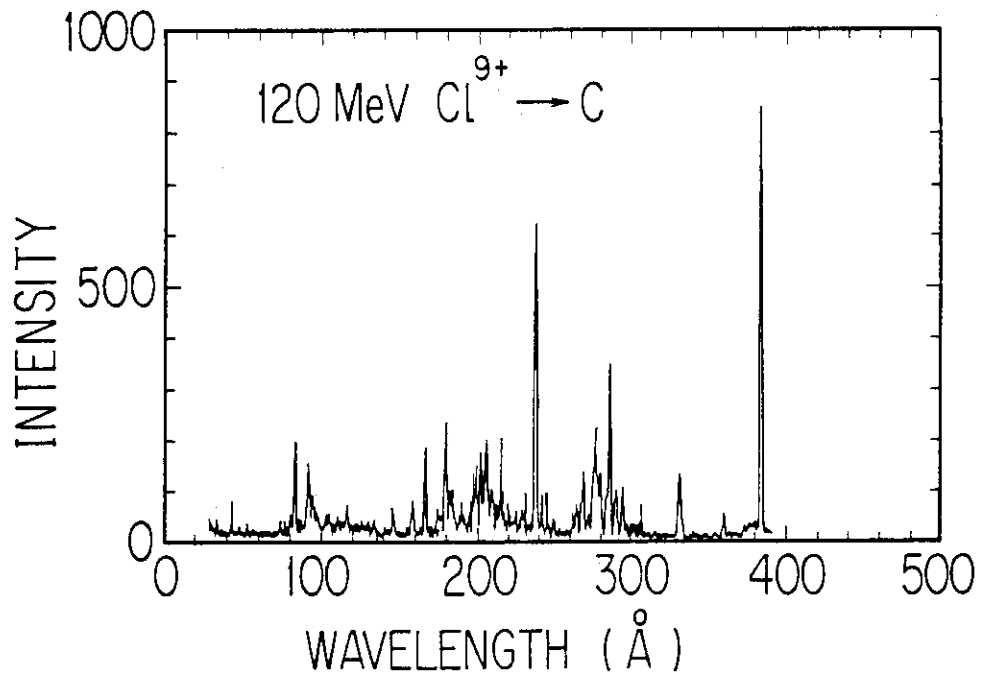


Fig. 1 Beam-foil spectrum of Cl ions.

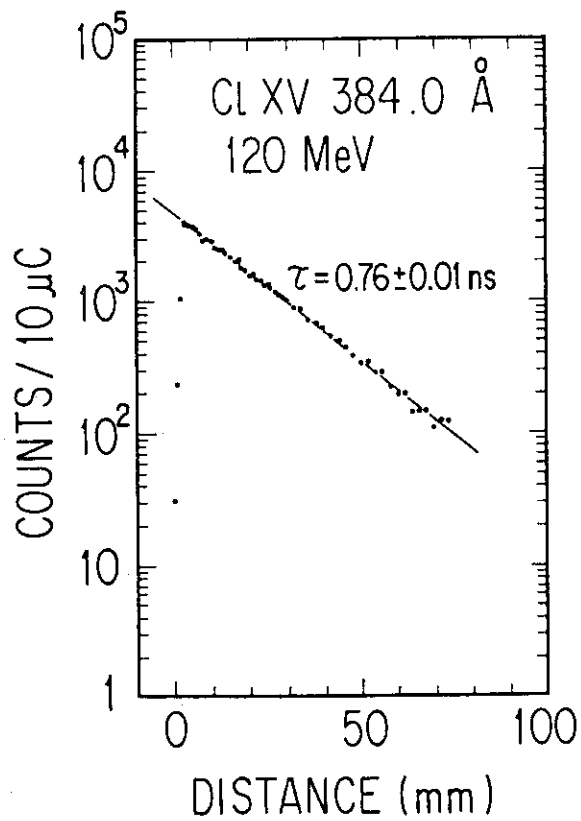


Fig. 2 Intensity decay curve.

## 2.5 MICROHOLE FORMATION IN POLYMETHYL METHACRYLATE FILM BY HEAVY ION IRRADIATION

Minoru KUMAKURA, Hideo KOHYAMA, Isao KAETSU,  
Yoshihide KOMAKI\*, Ni-ro ISHIKAWA\*, Tsutomu SAKURAI\*,  
Katsutoshi FURUKAWA\*, and Shinichi OHNO\*.

Takasaki Radiation Chemistry Research Establishment and

\* Department of Chemistry, Japan Atomic Energy Research  
Institute.

### Introduction

Formation of microporous structure in polymer films by heavy ion irradiation has been studied by many workers.<sup>1-5)</sup> Heavy ion track technique is noticed as a practical tool for producing functional materials and changing their properties, not as a method for track detectors.

Polymethyl methacrylate (PMMA) has been used widely as a conventional glass material to have a transparent and hard property. In the field of ion beam technology, PMMA has been studied with the photoresist technique.<sup>6)</sup> It is called a positive resist; it consists of long chains of polymer molecules. From there it is known that well-resolved patterns with a resolution of 10 nm may be reduced.<sup>7)</sup>

In this work, microhole formation in PMMA film by heavy ion irradiation has been studied by varying etching condition.

### Experimental

PMMA films with thickness of 110  $\mu\text{m}$  and diameter of 10 mm were irradiated with scanning the beams of heavy ions ( $\text{O}^{7+}$ ). The ion energy and density in ion irradiation were 120 MeV and  $10^8$  ions/cm<sup>2</sup>. After irradiation, the etching of the irradiated films was carried out by ultrasonic etching using chlorinated acetic acid solution (monochloroacetic acid, dichloro acetic acid, and trichloro acetic acid). After washed enough in water and dried in air, the films etched were observed by a scanning electron microscopy (JSM-35C), after depositing Au in vacuum on the film. The thickness of deposition is about 10 nm. The specimen was fixed with Ag-paste on the holder of brass.

### Results and Discussion

The films irradiated with a certain condition were etched by various conditions and relationship between microhole structure and etching condition was investigated.

Figure 1 shows the effect of the concentration of etching agent (trichloro acetic acid solution) on hole density. In the films etched with trichloro acetic acid solution of 25% above, the generated holes across the film was observed, in which the average number of the holes was  $4 \times 10^7 / \text{cm}^2$ . But, the films etched with trichloro acetic acid solution of 20% below did not have a hole. Thus, it was found that the appearance of the holes was intimately related to the concentration of trichloro acetic acid solution.

Ultrasonic etching; etching with 25% trichloro acetic acid solution under ultrasonics (28 kHz, 450 W) at 20 °C, was carried out. The relationship between hole diameter and etching time in ultrasonic etching is shown in Figure 2. Etching under ultrasonics was able to decrease etching time. Hole diameter in the holes increased slightly with increasing etching time in ultrasonic etching though the deviation in hole diameter is relatively large. Etching rate is, of course, a function of etching temperature, etching time, and concentration of etching agent. Necessary etching time

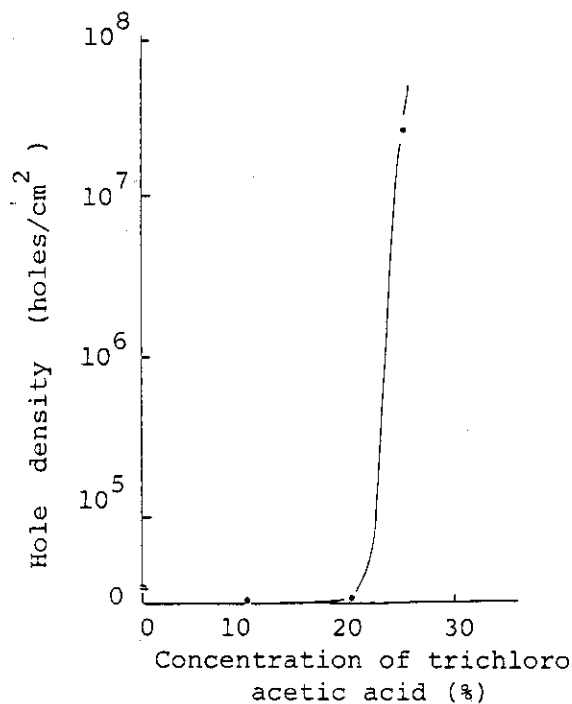


Fig. 1 Effect of concentration of trichloro acetic acid solution on hole density.

Etching temperature ; 25 °C  
Etching time ; 20 hr

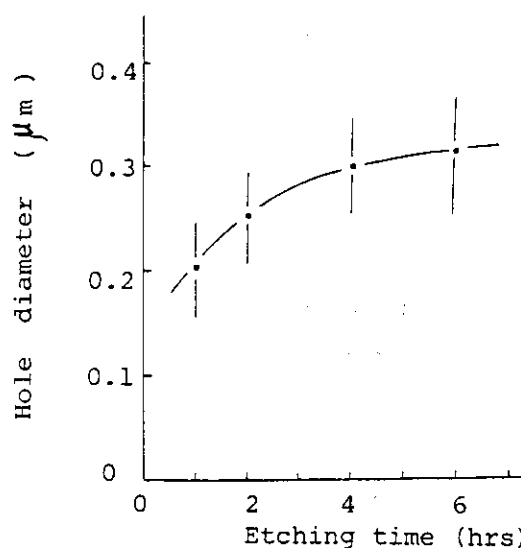


Fig. 2 Effect of etching time on hole diameter in ultrasonic etching.  
Trichloro acetic acid ; 25 %  
Etching temperature ; 20 °C

to get a perfect penetrated hole was about 5 hr in the etching with 25 % trichloro acetic acid solution at 20 °C.

Effect of etching temperature on hole density is shown in Figure 3. In this work, the etching was carried out at relatively low temperature because trichloro acetic acid which was a strong organic acid having a oxidation property was a high reactive etching agent for PMMA film. When etching was carried out at high temperature of 50 °C for 1 hr, the films were deformed and its transparent property disappeared. It was, thus, found that suitable etching temperature range for the film with thickness of 110 μm was 5 - 25 °C. Though etching at low temperature such as 5 °C needed long etching times, it is considered that etching time can be decreased by ultrasonic etching as can be seen in Figure 2.

The relationship between hole diameter and number of hole is shown in Figure 4. Though major diameter range of holes was 0.3 - 0.4 μm, the holes with the diameter from 0.1 μm to 0.6 μm were formed in the ultrasonic etching using 25% trichloroacetic acid solution at 20 °C for 6 hr. The diameter of the holes formed in this work appeared to be ununiform in comparison with other polymers, in which etching has been carried out by alkali solution such as sodium hydroxide solution. (4,5,8) This is seemed to be a characteristic of

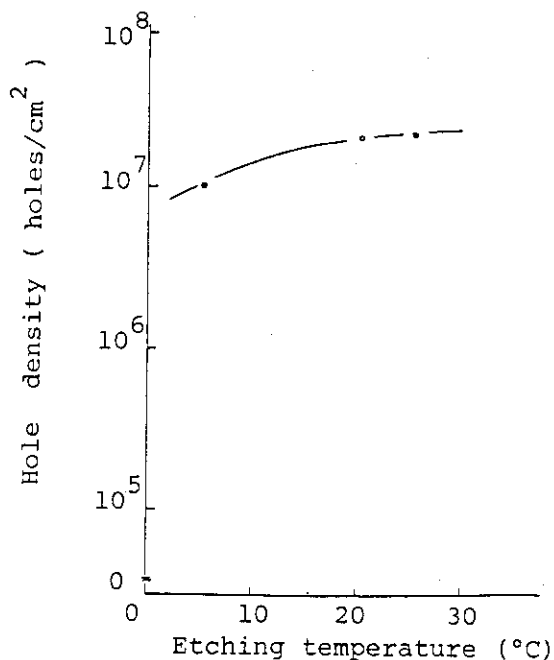


Fig. 3 Effect of etching temperature on hole density. Trichloro acetic acid ; 25 % Etching time ; 20 hr

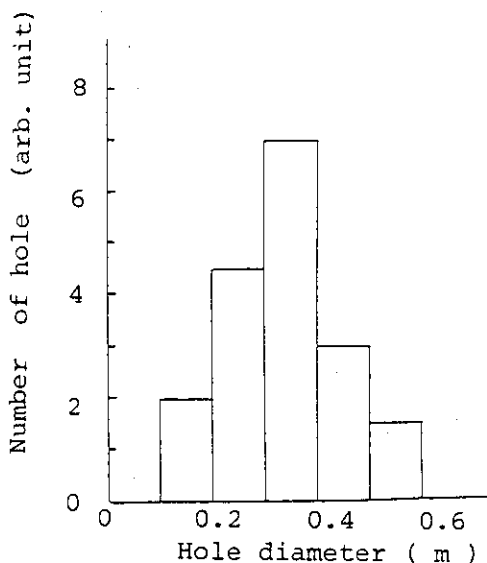


Fig. 4 Relation between number of hole and hole diameter in ultrasonic etching. Trichloro acetic acid ; 25 % Etching temperature ; 20 °C Etching time ; 6 hr



porous structure in PMMA films resulting in the ultrasonic etching using trichloro acetic acid solution.

Various chlorinated acetic acid derivatives were used as an etching agent. The relationship between hole density and number of chlorine atom in chlorinated acetic acid molecule is shown in Figure 5. Hole density increased with increasing number of chlorine atom and trichloro acetic acid was the most effective etching agent, indicating that trichloro acetic acid having three chlorine atoms has a property of strong acid and oxidation. The oxygen permeability of the film which was etched by ultrasonic etching using 25% trichloro acetic acid solution at 23 °C for 6 hr was obtained to be  $2.2 \times 10^{-9}$  cc·cm/cm<sup>2</sup>·sec·mmHg.

From these results, it was found that PMMA films irradiated with the heavy ions can be effectively etched by ultrasonic etching using trichloro acetic acid solution and the micro-holes formed were affected by etching condition.

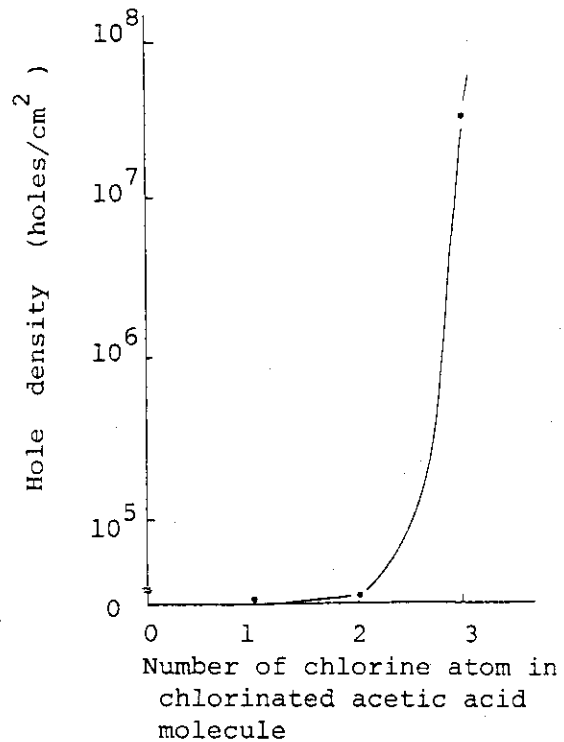


Fig. 5 Relation between hole density and number of chlorine atom in chlorinated acetic acid molecule in ultrasonic etching.

Chlorinated acetic acid ; 25 %  
Etching temperature ; 23 °C  
Etching time ; 6 hr

#### References

- 1) S. Spohr, J. Electrochem. Soc., 128, 188 (1981).
- 2) P. Yu. Apel, Nucl. Tracks, 6, 115 (1982).
- 3) H. A. Kham, R. Brandt, H. A. Khan, and K. Jamil, Nucl. Tracks, 7, 129 (1983).
- 4) Y. Komaki, S. Ohno, H. Ohtsu, H. Ito, and T. Seguchi, Nucl. Tracks, 11, 99 (1986).
- 5) M. Berndt, J. Krause, G. Siegmund, and W. Enge, Nucl. Tracks, 12, 985 (1986).
- 6) L. Karapiperis, I. Adesias, C. A. Lee, and E. D. Wolf, J. Vac. Sci. Tech., 19, 1259 (1981).
- 7) L. Karapiperis and C. A. Lee, Appl. Phys. Lett., 35, 395 (1979).
- 8) B. E. Fisher and R. Spohr, Rev. Mod. Phys., 55, 907 (1983).

III. SOLID STATE PHYSICS AND RADIATION  
EFFECTS IN MATERIALS

### 3.1 Radiation Annealing in Nickel and Copper by 100 MeV Iodine Ion Irradiation

Akihiro IWASE, Tadao IWATA, Shigemi Sasaki and Takeshi  
NIHIRA\*

Department of Physics, JAERI, \* Faculty of Engineering,  
Ibaraki University

More than 30 years ago, Seitz discussed the effect of electron excitation on the radiation damage in metals.<sup>1)</sup> Recently, we found the anomalous reduction of stage-I recovery in Ni irradiated with  $\sim 100$  MeV heavy ions and explained it as the defect annihilation due to the electron excitation by energetic heavy ions.<sup>2)</sup> In this paper, we report a quantitative study of radiation annealing in Ni and Cu during 100 MeV I-ion irradiations, and show that the electron excitation by irradiating ions enhances the radiation annealing in Ni.

The experiments were performed as follows; first, Ni and Cu thin foils, 0.27  $\mu\text{m}$  and 0.24  $\mu\text{m}$  thick respectively, were doped with relatively simple defects using 84 MeV C-ion irradiations. Subsequently, the specimens were irradiated with 100 MeV  $^{127}\text{I}$ -ions. For reference, undoped Ni and Cu specimens were also irradiated with 100 MeV I-ions. The electrical resistivity change  $\Delta\rho$  was measured as a function of C- and I-ion fluence. As the thickness of the specimens is much smaller than the projected range of C- and I-ions, ions pass completely through the specimens and the energy loss of ions in the specimens is only  $3 \times 10^{-3}$  and  $7 \times 10^{-2}$  of the incident energy for the C-ion and I-ion irradiation, respectively. The specimens were held below 10 K during irradiations.

Figures 1(a) and 1(b) illustrate the irradiation induced electrical resistivity change  $\Delta\rho$  as a function of ion fluence for Ni and Cu, respectively. The concentration of doped-in defects by C-ion irradiations is  $7.9 \times 10^{-4}$  in Ni and  $8.6 \times 10^{-4}$  in Cu. In the I-ion irradiation of pre-doped Ni, about the half of doped-in defects are annihilated at the initial stage of I-ion irradiation. On the contrary, in Cu, the defect concentration continues to increase during I-ion irradiation. In the figures are also shown the resistivity changes of undoped specimens during I-ion irradiations.

To study what kinds of defects are annealed by 100 MeV I-ion irradiation, the thermal annealing experiments were performed up to 300 K at a constant heating rate of 1.5 deg/min, after the C-ion irradiation and after the C-ion irradiation plus subsequent I-ion irradiation. Figures 2(a) and 2(b) show the recovery curves  $\Delta\rho/\Delta\rho_0$  and their temperature derivatives  $-(T/\Delta\rho_0)(d(\Delta\rho)/dT)$  as a function of annealing temperature for Ni and Cu, respectively, where  $\Delta\rho_0$  is the electrical resistivity increment due to C-ion irradiation. In Ni the peak of stage-I recovery is strongly reduced by the I-ion irradiation, and the reduction of other recovery peaks is also observed up to  $\sim 200$  K. On the contrary, in Cu only the defect recovery below  $\sim 35$  K is slightly reduced by I-ion irradiation, but the total amount of stage I recovery is little changed.

The result of the thermal annealing shows that during the I-ion irradiation some configurations of defects are preferentially annihilated and the others are not. This selective defect annihilation will dominate the present radiation annealing in Ni and Cu. Then, we assume that there are several configurations of defects produced by irradiation and that during the I-ion irradiation some kinds of defects are annihilated by the subthreshold recoil events with the respective cross sections. By analyzing the results of Fig. 1 and Fig. 2, we can determine the subthreshold recombination cross sections and the defect recovery stages which correspond to the subthreshold recombination for the respective defect configurations. The details of the data analysis will be published elsewhere.<sup>3)</sup> The results of the analysis are summarized in Table I.

We can explain the defect recovery spectra after I-ion irradiations of Figs. 2(a) and 2(b) in terms of the results in Table I. In Ni, the strong reduction of the stage-I recovery is due to a large cross section for the subthreshold recombination of stage-I defects, and the reduction of the stage-II recovery is also caused by the subthreshold recoil events. On the other hand, in Cu, as the cross section of the subthreshold recombination is not so large as in Ni, the annihilation of stage-I defects is compensated by the defect production and the concentration of stage-I defects remains nearly constant during the I-ion irradiation. For the defects recovering in stage-II and III, as the subthreshold recombination cross section is small, the defect production overcomes the defect annihilation, which causes the increase of the recovery.

Several experiments of radiation annealing have been performed so far in FCC metals by irradiation of  $\sim 0.5$ -3 MeV electrons<sup>4)</sup> and ions,<sup>5)</sup> and it

has been considered that the radiation annealing is caused by the subthreshold lattice agitations which are induced by nuclear elastic collisions. Since Ni is the next element of Cu in the periodic table, the physical parameters related with the nuclear elastic collision are not quite different between them if irradiating ions are the same. Therefore, the radiation annealing in Ni by nuclear elastic collisions is expected to be about the same as in Cu. The present result shows, however, that the radiation annealing in Ni is much larger than in Cu, and some different effect is dominant in Ni. Heavy ions with the energy of  $\sim 100$  MeV lose almost all energy by exciting the electrons in solid. The degree of the electron excitation by ions is nearly the same in Ni and Cu. Thus, the large amount of radiation annealing in Ni, as compared with Cu, can be explained as due to the effective transfer of energy from the excited electrons to the lattice atoms through the strong electron-lattice interaction. The transferred energy enhances the subthreshold lattice agitation along the ion beam path, and the agitation causes the annihilations of a large number of defects in Ni.

Only from the present experimental results, we can not say whether or not the effect of electron excitation on the radiation annealing is negligible in Cu, but can clearly say that the difference in the radiation annealing between Ni and Cu is due mainly to the effect of electron excitation.

#### References

- 1) F. Seitz and J. S. Koehler, in Solid State Physics, edited by F. Seitz and D. Turnbull (Academic, New York, 1956), Vol. 2, pp. 305-448.
- 2) A. Iwase, S. Sasaki, T. Iwata and T. Nihira, Phys. Rev. Lett. 58, 2450 (1987).
- 3) A. Iwase, T. Iwata, S. Sasaki and T. Nihira, Submitted to Phys. Rev. Lett.
- 4) For example, F. Dworschak, Chr. Lehmann, H. Schuster, H. Wollenberger and J. Wurm, in Proc. of the Intern. Conf. on Solid State Physics Research with Accelerators, 1967, BNL-50083(C-52), pp. 327-334; G. Duesing, W. Sassin, W. Schilling and H. Hemmerich, Crystal Lattice Defects 1, 55 (1969); G. Duesing, H. Hemmerich, W. Sassin and W. Schilling, Crystal Lattice Defects 1, 135 (1970).
- 5) R. S. Averback and K. L. Merkle, Phys. Rev. B 16, 3860 (1977).

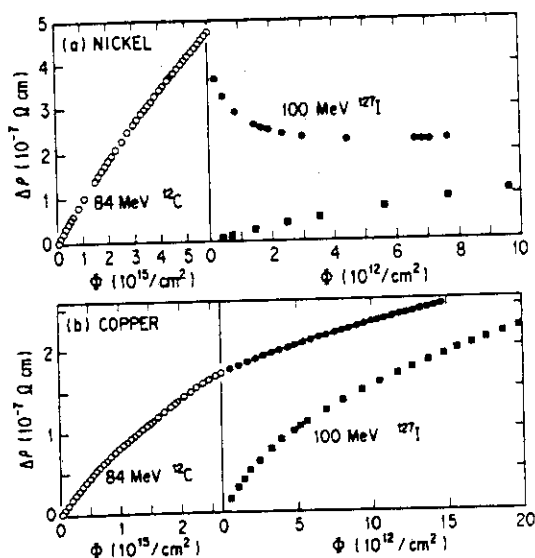


Fig.1 Electrical resistivity change versus ion fluence in (a) Ni and (b) Cu during 84 MeV <sup>12</sup>C-ion irradiation for doping (open circles) and subsequent 100 MeV <sup>127</sup>I-ion irradiation (solid circles). Solid squares present the electrical resistivity change of undoped specimens during I-ion irradiation.

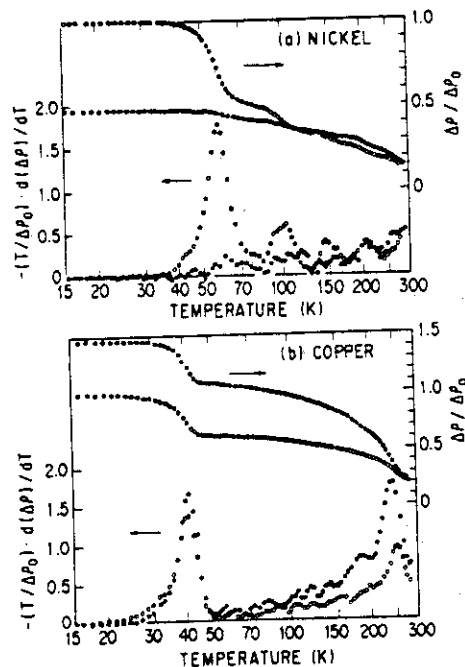


Fig.2 Recovery curves of electrical resistivity and their temperature derivatives in (a) Ni and (b) Cu after 84 MeV C-ion irradiation (open circles) and after 84 MeV C-ion irradiation plus subsequent 100 MeV I-ion irradiation (solid circles).

Table 1 Characteristic data of the radiation annealing in Ni and Cu by 100 MeV I-ion irradiation. Index j shows the type of defect configuration,  $\sigma_{rj}$  is the subthreshold recombination cross section and  $C_j(0)/C(0)$  is the fractional initial concentration of defects doped by 84 MeV C-ion irradiation. Thermal annealing stages corresponding to the radiation annealing of defects of the respective configurations are also shown.

specimen	j	$\sigma_{rj}$ ( $\text{cm}^2$ )	$C_j(0)/C(0)$ (%)	thermal annealing stage (temperature region)
Ni	1	$6.5 \times 10^{-12}$	20	stage-I <sub>B</sub> and I <sub>C</sub> (T < 55 K)
	2	$1.4 \times 10^{-12}$	24	stage-I <sub>D+E</sub> (55 K < T < 65 K)
	3	$2.2 \times 10^{-13}$	35	stage-II (65 K < T < 210 K)
Cu	1	$4.6 \times 10^{-13}$	27	stage-I (T < 42 K)
	2	* $5.3 \times 10^{-14}$	67	stage-II and III (42 K < T)

\* This value includes the spontaneous recombination cross section.

### 3.2 DEPTH DEPENDENCE OF ISOCHRONAL ANNEALING PROCESS IN Fe IRRADIATED BY Cl IONS

Saburo TAKAMURA, Kiyotomo NAKATA\*, Takeo ARUGA\*\* and Mamoru KOBIYAMA\*\*\*

Department of Physics, JAERI, \* Hitachi Research Laboratory Hitachi Ltd., \*\* Department of Fuels and Materials Research, JAERI, \*\*\* Faculty of Engineering, Ibaraki University

#### 1. Introduction

Radiation damage by ions has a strong gradient with the highly damaged region in the direction of depth in a sample. Recently in our group, the depth profiles of damage have been measured by an electrical resistivity method for several pure metals, and the experimental depth profiles obtained have been compared with theoretical predictions by using the modified EDEP-1 and TRIM codes<sup>1-3)</sup>.

The damage distribution in displacement cascades produced by ion irradiation seems to be different with the depth in target materials, and is studied by isochronal annealing processes in electrical resistivity.

In this study, Cl ions at an energy of 150 MeV are irradiated into multi-foil samples composed by pure Fe at low temperature, and electrical resistivity change caused by isochronal annealings of each foil are measured.

#### 2. Experimental procedure

Foils used in this study were pure Fe(99.85 %) with about 5  $\mu\text{m}$  in thickness, which were obtained from Goodfellow Metals Ltd.; ratio of resistivity at 4.2 K to that at room temperature was about 10. The foil thickness was precisely determined by an weighing method for the foil of  $20 \times 20 \text{ mm}^2$ . Electric and potential leads were soldered at the ends of the foils cut to about 2 mm width. Arrangement of the samples for ion irradiation is shown in Fig. 1, schematically; the samples of #1, #2 and #3 are set at 0-5, 5-10 and 10-15  $\mu\text{m}$  in depth from the ion bombarded surface, respectively.

Ion irradiation of 150 MeV Cl ions was performed by a Tandem accelerator up to a dose of about  $2 \times 10^{18}$  ions/ $\text{m}^2$ , using a low-temperature ion-irradiation cryostat<sup>2)</sup>. The temperature of the samples was not

precisely determined during irradiation, but seems to be held at a temperature below 100 K, because electrical resistivity of the irradiated samples decreased above 100 K anneals in isochronal curves. After the irradiation, the samples were removed from the sample holder in liquid nitrogen.

The electrical resistivity was always measured in liquid helium by the conventional four-probe potentiometric method. The uncertainty in resistivity variations was 0.5 pΩm. Isochronal annealing for 300 s in steps of 20 K from 100 to 360 K was carried out by using the copper box with an electrical heater.

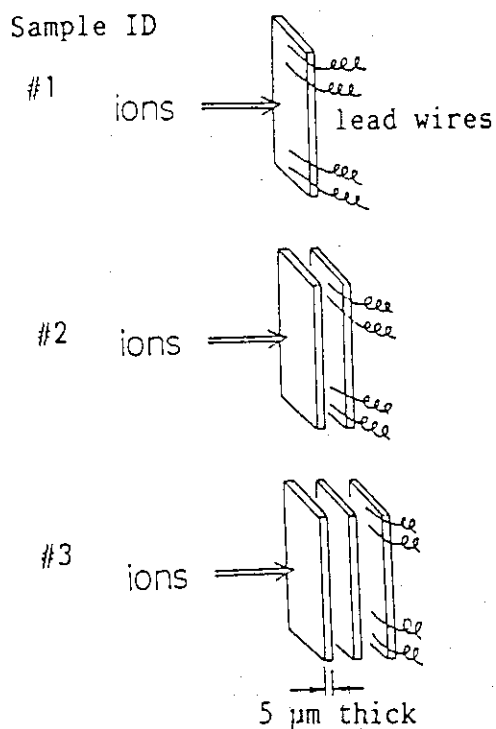


Fig.1 Arrangement of foils for ion irradiation.

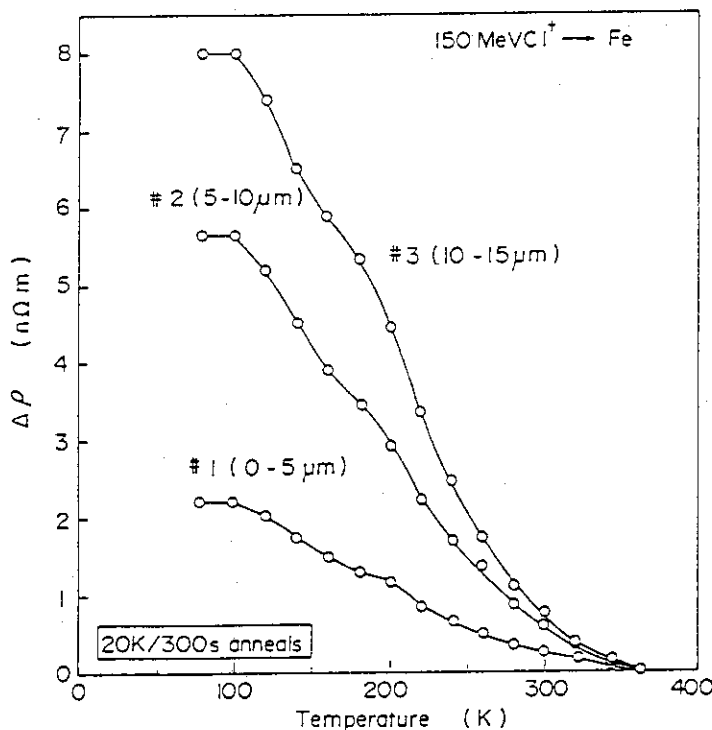


Fig.2 The isochronal annealing curves in the samples located at different depth from ion bombarded surface after the Cl ion irradiation.



### 3. Results and discussion

Damage peak for Fe irradiated by 150 MeV Cl ions appeared at 15.8  $\mu\text{m}$  in depth, and half-value width of damage distribution was about 3  $\mu\text{m}$ , which almost agreed with the calculated values. The samples for isochronal annealing experiment, #1, #2 and #3, are located in front of the highly damaged region.

The radiation-induced resistivity of the samples was successively increased in the sequence #1, #2 and #3. The resistivity was annihilated by the annealing at 360 K for 300 s. The isochronal annealing curves in resistivity of #1, #2 and #3 are shown in Fig. 2, where  $\Delta\rho$  means the difference between the resistivity after annealing at a temperature and that after annealing at 360 K. Mainly two annealing stages of 80 to 150 K and above 150 K are found in all the samples. The stages are correspond to stage I, and stages II and III, respectively, which have been found in the annealing curves of neutron irradiated samples<sup>5)</sup>. Fig. 3 shows the annealing curves normalized by the radiation-induced resistivity  $\Delta\rho_0$ .

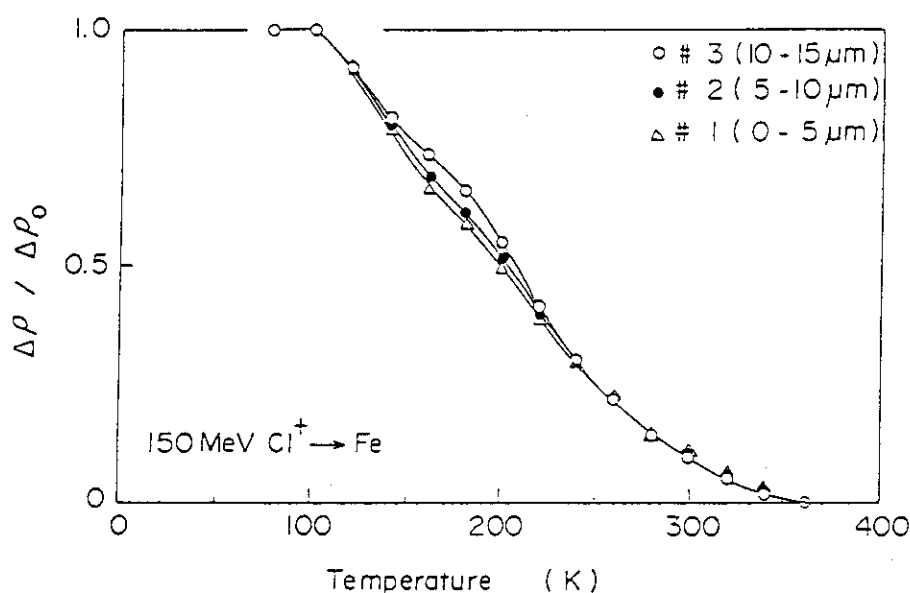


Fig.3 The annealing curves normalized by the radiation-induced resistivity  $\Delta\rho_0$ .

While temperature ranges of the stages are strictly the same in the three samples, the fraction of recovery in the stage above 150 K, stage II-III, to  $\Delta\rho_0$  increases with depth of the samples. A computer calculation using the TRIM 85 code<sup>4)</sup> was performed to know the average PKA (primary knock-on atom) energy in each depth of a sample; the result for Fe

irradiated with 150 MeV Cl ions is given in Fig. 4, together with the damage depth profile. According to the calculation, since the PKA energy is almost independent of the depth from the ion bombarded surface, the defect cluster structure and/or size produced directly by the ion irradiation, seem not to be different among the samples #1, #2 and #3. As the large amount of defects is produced in the sample at deep positions (Fig. 2), large defect clusters, to be annealed in stage II-III, is considered to be formed in the samples. Therefore, the difference of the fraction of stage II-III seems to be attributed to the formation of large cluster in the samples at deeper positions during isochronal annealing. Further study on depth dependence of the damage structure caused by the high energy irradiation will be required.

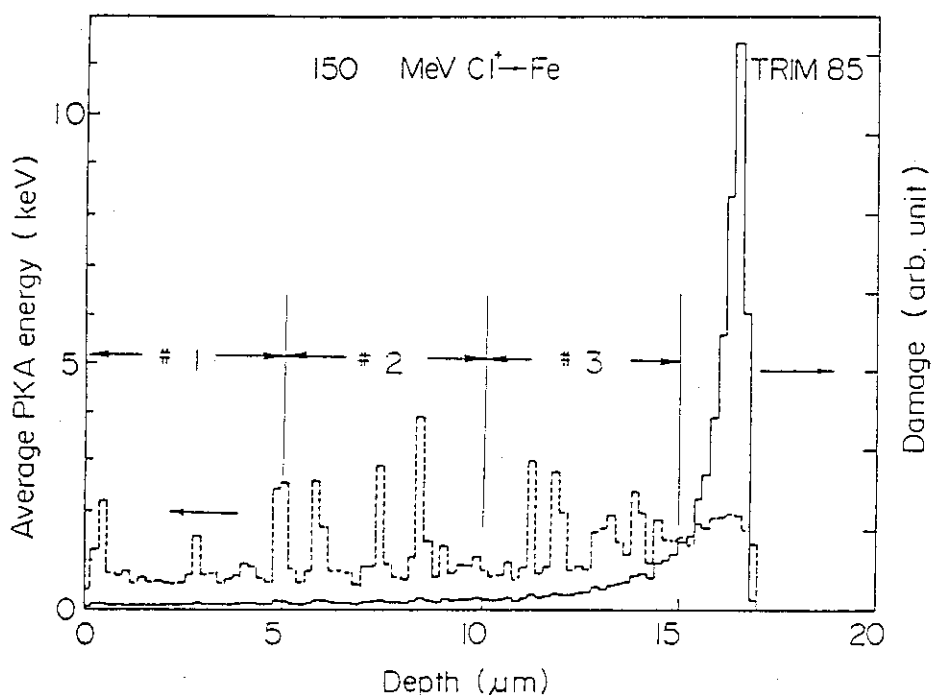


Fig.4 Depth dependent average PKA energy(dotted line) and damage (solid line); calculation for Fe irradiated by 150 MeV Cl ions. The sample positions are also indicated.

#### References

- 1) S. Takamura, K. Nakata, M. Kobiyama and T. Aruga: JAERI-M 87-134 (1987) pp. 224.
- 2) K. Nakata, S. Takamura, T. Aruga and M. Kobiyama: J. Nucl. Mater. 151 (1988) 301.
- 3) T. Aruga, K. Nakata and S. Takamura: Nucl. Instru. & Methods, in press.
- 4) J. F. Ziegler, J. P. Biersack and U. Littmark: The Stopping and Range of Ions in Solids, vol. 1 (Pregamon Press, New York, 1985).
- 5) S. Takamura, H. Maeta and S. Okuda: J. Phys. Soc. Jpn., 26 (1969) 1125.

### 3.3 CALCULATION OF DAMAGE DEPTH PROFILES FOR 2-7.5 MeV/amu HEAVY IONS ON PURE METALS WITH EXPERIMENTAL COMPARISONS

Takeo ARUGA, Kiyotomo NAKATA\* and Saburo TAKAMURA\*\*

Department of Fuels and Materials Research, JAERI,  
\*Hitachi Research Laboratory, Hitachi Ltd., \*\*Department  
of Physics, JAERI

For ion irradiation techniques utilized in fields of material science and engineering, a precise knowledge of the damage distribution is vital. Computer codes of EDEP-1<sup>1,2)</sup>, Brices's code<sup>3)</sup> and TRIM<sup>4)</sup> have been frequently used as standards to calculate the depth profile of damage and of the implanted ions. These codes are, however, limited either in lower energy(LSS) region, or in available stopping powers or in consumption of computer resources. It is highly desirable to develop a standardized code with universally available stopping formulas and data for the damage distribution of ion irradiation. Presently, the applicability of the EDEP-1 code extended to the high energy region, EDEP-1(ext.), was examined for predicting the damage depth profiles of highly energetic heavy ions<sup>5)</sup>.

The extension to the high energy region was made for the second version of EDEP-1<sup>2)</sup>. The code calculates the depth profile of energy deposited into elastic collision based on the approximation that a distribution of ion energies at any depth can be related to the range straggling and that the primary knock-on atom ranges are small. Below  $E_{lim}=25Z^{1/3}$  keV/amu, the LSS stopping power with the revised  $k$  of Land and Brennan<sup>6)</sup> is used. The electronic stopping power by Ziegler<sup>7)</sup> is adopted for energies higher than 1.5 MeV/amu. In the intermediate energy region from  $E_{lim}$  to 1.5 MeV/amu, the semi-empirical electronic stopping power by Sugiyama<sup>8)</sup> is used. The electronic stopping powers for three energy regions are smoothly connected by matching interpolation around the boundary energies and are here designated as  $S_e(LBSZ)$  or  $S_e$  of Land-Brennan-Sugiyama-Ziegler. The nuclear energy loss and relevant energy straggling are calculated by the stopping cross section of Wilson et al.(WHB)<sup>9)</sup> in stead of previous one of Lindhard et al.(LNS). In the present extension, electronic range straggling is

taken into consideration and is added to the nuclear range straggling.

The calculated parameters for the damage depth profiles are given in table 1, and are compared with our experimental parameters already reported<sup>10)</sup>, as well as those obtained by TRIM85<sup>11)</sup> calculations. The discrepancies between the calculated and measured depths for the peak damage are compared in fig. 1 for C- and Cl-ions as a function of the target atomic number. The discrepancies for C- and Cl-ions lie within a respective band, as shown in fig. 1. This means that the presently adopted electronic stopping power still have to include  $Z_1, Z_2$ -dependence in the energy region up to 7.5 MeV/amu. The damage straggling calculated by EDEP-1(ext.) or by TRIM85 are considerably smaller, even if the electronic straggling is included in the former, compared with the experimental values (table 1). Inclusion of electronic straggling in EDEP-1(ext.) calculation gives slightly larger straggling values for the lighter ions.

In summary, the depth profiles calculated for pure metals of Al, Fe Ni, Cu, Ag and Ta irradiated with 2-7.5 MeV/amu heavy ions of C, Cl and Br show that the extended code gives nearly similar profiles and depths of peak damage to those obtained by a Monte Carlo calculation code, TRIM85. The discrepancies from the experimental peak depths are less than 15 %. The damage straggling around the peak, however, are calculated to be much smaller than the experimental values. The present discrepancies in damage stragglings suggest that the damage produced by recoils, which would be created by the ions with considerable energy straggling after long path lengths, must be properly evaluated for highly energetic ions.

#### References

1. I. Manning and G.P. Mueller: Comp. Phys. Commun. 7 (1974) 85.
2. C. M. Davisson and G.P. Mueller: Comp. Phys. Commun. 42 (1986) 137.
3. D. K. Brice: Ion Implantation Range and Energy Deposition Distributions vol 1. (Plenum press, Newyork, 1975).
4. J. P. Biersack and L. G. Haggmark: Nucl. Instr. and Meth. 174 (1980) 257.
5. T. Aruga, K. Nakata and S. Takamura: Nucl. Instr. and Meth. B, in press.

6. D. J. Land and J. G. Brennan: Atomic Data and Nuclear Data Tables 22 (1978) 235.
7. J. F. Ziegler: The Stopping and Ranges of Ions in Matter, vol. 5, ed., J. F. Ziegler (Pergamon, New York, 1980).
8. H. Sugiyama: Bull. Electrotech. Lab. (1974) no. 181.
9. W. D. Wilson, L. G. Haggmark and J. P. Biersack: Phys. Rev. B 15 (1977) 2458.
10. Kiyotomo Nakata, Saburo Takamura, Takeo Aruga and Mamoru Kobiyama: J. Nucl. Mater. 151 (1988) 301.
11. J. F. Ziegler, J. P. Biersack and U. Littmark: The stopping and Ranges of Ions in Matter, vol. 1 (Pergamon, New York, 1985)

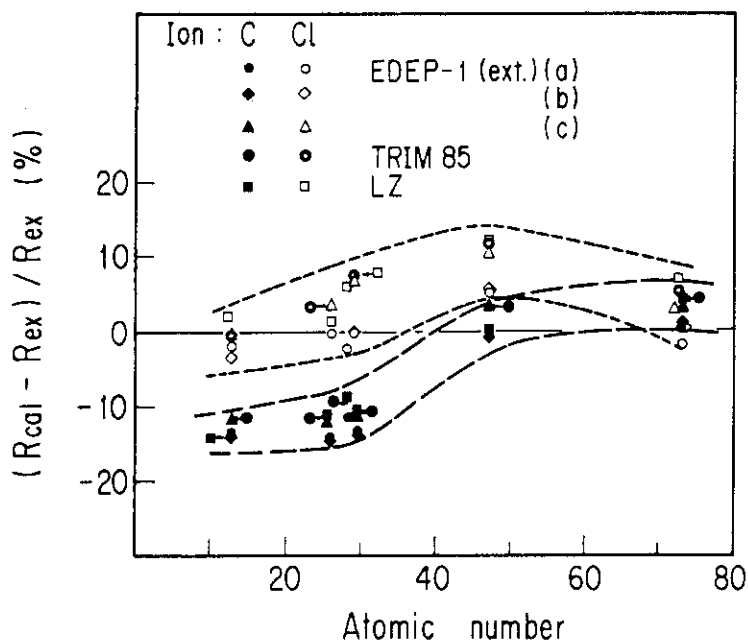


Fig. 1 Comparisons of differences between the calculated and measured depths of peak damage,  $R_{cal}$  and  $R_{ex}$ , to  $R_{ex}$  as a function of the target atomic number. EDEP-1(ext.) (a), (b) and (c) stand for the calculation with (a)  $S_e(LSS-k, Sugiyama, Ziegler)$  or  $S_e(LSSSZ)$ , (b)  $S_e(LBSZ)$  and (c)  $S_e(RSTOP)$ . Comparisons with the results obtained by TRIM85 and with the tabulated range data in Ref. (7) : LZ are also shown.

Table 1

Comparisons of the calculated parameters with the experimental ones for the investigated ion-target combinations. Rd, ΔRd, Dp, SD and Df are the depth of peak damage, FWHM for the peak damage, peak dpa for 1 x 10<sup>20</sup> ions/m<sup>2</sup>, total damage energy and the Frenkel defect concentration estimated from the measured resistivity changes of the peak foil for a normalized dose of 1 x 10<sup>18</sup> ions/m<sup>2</sup>. The values in brackets are obtained by the calculation with electronic range straggling taken into account.

Ion Energy (MeV)	Target	EDEP-1(ext.)				EDEP-1(ext.)				TRIM85				Exp.	
		Rd (μm)	ΔRd (μm)	Dp (dpa)	Se(LSS2)	Rd (μm)	ΔRd (μm)	Dp (dpa)	Se(RSTOP in TRIM85)	Rd (μm)	ΔRd (μm)	Dp (dpa)	SD(MeV)		WHB
90.3	Al	140.0	2.4	0.60	0.46	0.075	0.076	142.0	2.4	0.50	0.085	0.087	0.42	161.2	5
			(3.8)	(0.29)	(0.077)	(0.079)		(3.8)	(0.31)	(0.084)	(0.086)				
89.2	Fe	57.6	1.2	0.55				59.0	1.2				0.55	67.1	5
			(2.4)	(0.29)	(0.105)	(0.106)		(2.4)	(0.31)	(0.115)	(0.116)				
91.4	Ni	53.6	1.2	0.74				56.8	1.2	0.95	0.142	0.145	0.48	60.5	4
			(2.8)	(0.42)	(0.119)	(0.120)		(2.8)	(0.49)	(0.141)	(0.143)				
90.3	Cu	55.3	1.2	0.86				58.6	1.5	0.76	0.133	0.133	0.62	63.8	2
			(4.2)	(0.30)	(0.121)	(0.121)		(4.2)	(0.31)	(0.131)	(0.131)				
	Ag	56.7	1.5	0.84				47.1	1.3	0.41	0.146	0.145	0.51	56.8	5
			(5.5)	(0.105)	(0.120)	(0.119)		(5.5)	(0.12)	(0.143)	(0.142)				
150.6	Al	36.7	1.2	5.1				37.3	1.2	5.0	0.32	0.39	4.0	37.4	3
			(1.2)	(4.4)	(0.38)	(0.39)		(1.2)	(4.5)	(0.38)	(0.39)				
	Fe	15.8	0.7	4.6				16.4	0.7				3.4	15.8	2.5
			(0.9)	(4.3)	(0.59)	(0.61)		(0.9)	(4.5)	(0.58)	(0.58)				
149.7	Ni	14.1	0.7	6.0				15.9	0.8	8.4	0.74	0.77	4.6	14.4	2.5
			(1.0)	(7.1)	(0.69)	(0.71)		(1.0)	(7.5)	(0.74)	(0.77)				
150.6	Cu	14.9	0.8	7.2				16.6	1.0	7.6	0.72	0.73	7.4	14.9	1.5
			(1.4)	(6.0)	(0.73)	(0.75)		(1.4)	(6.4)	(0.72)	(0.73)				
	Ag	15.8	1.0	6.6				13.9	1.3	3.8	0.83	0.84	7.5	15.0	6
			(1.6)	(3.0)	(0.77)	(0.78)		(1.6)	(2.9)	(0.83)	(0.85)				
160.0	Al	19.7	1.6	11.0				20.3	1.6	10.8	1.36	1.39	12.0	21.2	2.5
			(1.7)	(10.7)	(1.31)	(1.33)		(1.7)	(10.8)	(1.36)	(1.39)				
	Fe	8.9	1.0	12.0				9.1					11.0	8.9	2
			(1.2)	(12.2)	(1.2)	(13.0)		(1.2)	(13.0)	(2.2)	(2.2)				

### 3.4 MICROSTRUCTURE AND MECHANICAL PROPERTIES OF ION IRRADIATED FE-12%CR-15 TO 30%MN ALLOYS

Shozo HAMADA\*, Akimichi HISHINUMA\*, Kazuya MIYAHARA\*\*  
Yuzo HOSOI\*\* and Hideo KAYANO\*\*\*

\* Department of Fuels and Materials Research, JAERI,

\*\* Department of Iron and Steel Engineering, Nagoya University,

\*\*\* Research Institute of Iron and Steels, Tohoku University.

#### 1. Introduction

The potentiality of Fe-Cr-Mn alloys as substitutes for Fe-Cr-Ni austenitic stainless steels or Fe-Cr-Mo ferritic stainless steels is explored under much effort<sup>(1,2)</sup>, because this substitution is desired to achieve a reduced level of radioactivity in fusion structural materials. Fusion neutron irradiation is known to cause several kinds of degradation of mechanical properties of materials, that is, irradiation embrittlement, helium embrittlement, hydrogen embrittlement, irradiation creep, etc. The object of the present work is, as one of these tasks, to investigate the effect of helium and hydrogen injection on microstructures and mechanical properties of Fe-Cr-Mn alloys. This time, however, as a first step of the present research, helium effect only has been investigated.

#### 2. Experimental procedures

Materials used were Fe-12Cr-15Mn and 30Mn alloys, which were melted in vacuum induction furnace. Chemical composition of these materials is shown in Table 1. After the solution treatment at 1323 to 1373K for  $3.6 \times 10^3$ s in a vacuum, the materials were water quenched, mechanically polished to the thickness of 100 to 160 $\mu$ m and then small size tensile test specimens (gauge width 1.2mm, gauge length 5mm, total length 12.5mm) and 3mm diameter discs for transmission electron microscope (TEM) were die punched.

Table 1 Chemical composition of materials used (wt%)

	C	Si	Mn	P	S	Cr	W	N	O
15Mn	0.006	0.009	14.74	<0.003	0.009	12.33	<0.01	0.0015	<0.0010
30Mn	<0.003	0.011	29.72	<0.003	0.013	12.62	<0.01	0.0016	0.011

According to the X-ray diffraction analysis and optical microscopy image analysis, Fe-12Cr-15Mn alloy was composed of 65%  $\alpha$  martensite phase, 20%  $\epsilon$  martensite phase and 15%  $\gamma$  (austenite) phase. On the other hand, Fe-12Cr-30Mn alloy is consisted of 2%  $\delta$  ferrite phase and 98%  $\gamma$  phase. Hereafter, Fe-12Cr-15Mn alloy and Fe-12Cr-30Mn alloy are designated to 15Mn alloy and 30Mn alloy, respectively. Helium injection was performed by 30MeV alpha particle irradiation to the specimens, using a SF cyclotron of University of Tokyo (INS). A sheet of stainless steel foil of 100 $\mu$ m thickness and 0 to 4 sheets of aluminum foils of 7 $\mu$ m thickness were inserted into the beam path as an energy absorber. The calculation of projected range based on the E-DEP-1 and the reported stopping powers shows that this irradiation condition makes the uniformly He-implanted region of 20 $\mu$ m width around the midst of the specimen thickness. Alpha particles were implanted up to  $3.3 \times 10^{17} \text{cm}^{-2}$  with the beam current of  $2 \mu\text{A}/\text{cm}^2$  on the specimens set on a specimen holder which was cooled by flowing water.

Tensile test (strain rate;  $1 \times 10^{-3} \text{s}^{-1}$ ) were made at room temperature. The fracture surface of each specimen was observed by a scanning electron microscope. He bubble distribution in the He deposited area was observed by a transmission electron microscope (JEM 200CX).

### 3. Experimental Results

The TEM observation shows that many helium bubbles were formed in the helium deposited area in the martensite of 15Mn alloy and in the austenitic phase of 30Mn alloy, which were irradiated to  $2 \times 10^{17} \text{cm}^{-2}$  (average He concentration in the He deposited area; 2000appm) and the number density of helium bubbles in 15Mn alloy was lower than that in 30Mn alloy. The average size of helium bubbles observed in 15Mn alloy (100nm) was smaller than in 30Mn alloy (200nm).

Both alloys show the decrease of total elongation with the helium injection. On the other hand, the strength of both alloys did not change systematically with the helium injection, that is, 0.2% proof stress and ultimate tensile strength of 15Mn alloy increased, but those of 30Mn alloy decreased with the helium injection.

The scanning electron microscope observations of the fracture surfaces in the tensile tested 15Mn and 30Mn alloys indicate that both unirradiated and irradiated ( $1.9 \times 10^{17} \text{cm}^{-2}$ , 1600appmHe) 15Mn alloys fractured by the mode



of transgranular ductile fracture. On the other hand, in 30Mn alloys, the transgranular ductile fracture was observed only in the unirradiated 30Mn alloy and the intergranular ductile fracture was observed in the helium deposited zone of the specimen of 30Mn alloy irradiated to  $2.1 \times 10^{17} \text{cm}^{-2}$  (1800appm). Moreover, the traces of helium bubbles were recognized on the intergranular ductiled fractured surfaces.

#### 4. Discussion and Conclusions

The elongation of these alloys decreased with alpha particle irradiation. Intergranular-ductile fracture was observed on the Fe-12Cr-30Mn alloy in which alpha particles had been injected up to  $2.1 \times 10^{17} \text{cm}^{-2}$  at the depth of range, whereas transgranular-ductile fracture occurred on the Fe-12Cr-15Mn alloy. These fracture modes of Fe-Cr-Mn alloys are, however, in contrast to the authors' previous results<sup>(3)</sup> of type 316 stainless steel which showed intergranular-brittle fracture in the helium deposited zone. The difference of the formation and distribution of helium bubbles among two Fe-Cr-Mn alloys and type 316 stainless steel was recognized, and this difference is considered to be an important factor to determine the fracture modes of these materials.

#### References

- (1) H.R.Brager, F.A.Garner, D.S.Gelles and M.L.Hamilton, J.Nucl.Mater. 133&134 (1985), 907.
- (2) F.A.Garner, H.R.Brager, D.S.Gelles and J.M.McCarthy, J.Nucl.Mater 133&134 (1987), 294.
- (3) N.Igata, K.Miyahara, C.Tada, D.Blasl, S.Hamada, T.Sawai, H.Kayano and Y.Hosoi, J.Nucl.Mater., 141-143 (1986), 543.

### 3.5 VOLUME CHANGE OF LITHIUM OXIDE BY LITHIUM ION IRRADIATION

Yoshinobu ISHII, Kenji NODA and Hitoshi WATANABE

Department of Fuels and Materials Research, JAERI

#### 1. Introduction

Lithium oxide ( $\text{Li}_2\text{O}$ ) is a candidate of tritium breeding blanket materials for a fusion reactor. During operation of the fusion reactor, a lot of defects will be introduced in the  $\text{Li}_2\text{O}$  by the energetic particles (neutrons, tritons and helium ions). These defects will induce swelling and cracking. The swelling of  $\text{Li}_2\text{O}$  sintered pellets was measured after high dose irradiation at high temperature using EBR-II<sup>1)</sup> and it was concluded to be mainly associated with helium bubbles. To understand the swelling of  $\text{Li}_2\text{O}$  associated with the formation of point defects or clusters, the volume change of  $\text{Li}_2\text{O}$  irradiated with the lithium ions has been measured by using a photoelastic technique.

#### 2. Experimental

Specimens were cut in rectangular shape (about 7mm in length, 4mm in width, 0.264 mm in thickness) from the single crystal. These were annealed at 1270 K for 10 hours in high vacuum ( $1 \times 10^{-3}$  Pa) to remove the residual stress induced by cutting and to eliminate LiOH or  $\text{Li}_2\text{CO}_3$  formed on the surface. After these treatments, the specimen was mounted on a circular polarimeter which was equipped in a high vacuum chamber. One half of the specimen was irradiated with lithium ions (60 MeV) by using a tandem accelerator at JAERI. By such irradiation an irradiated part expands, but an unirradiated part remains unchanged. Then a strain field is introduced into the specimen. The strain field was measured by using the circular polarimeter. The schematic illustration of the circular polarimeter used in this experiment is shown in Fig.1.

The measurement of the volume change of the specimen was intermittently carried out after irradiation for the several hours at room temperature. Further experimental procedure is described elsewhere<sup>2)</sup>.

After irradiation, the recovery of the volume change of the specimen was investigated by isochronal annealing experiments. The

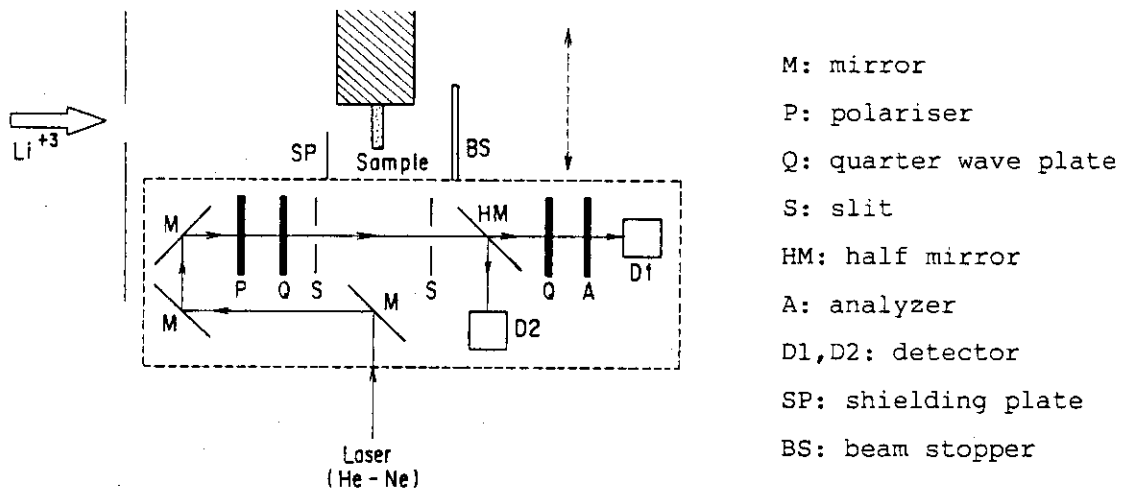


Fig.1 Schematic illustration of circular polarimeter.

irradiated specimen was heated for 30 min. at each annealing temperature from 323K to 873K.

3. Results and discussion

In Fig.2, the displacement per atom ( D.P.A ) is shown schematically as a function of the distance from surface of Li<sub>2</sub>O irradiated by lithium ions with an energy of 60MeV. The hatched part in Fig.2 shows the specimen in the direction of the thickness in our experiments. The penetration depth of lithium ions ( 60MeV ) is about 0.36 mm for the Li<sub>2</sub>O. The bombarded lithium ion dose not stay in the specimen and causes the uniform volume expansion in the direction of the depth.

A typical strain profile of irradiated Li<sub>2</sub>O is shown in Fig.3 as a function of the dis-

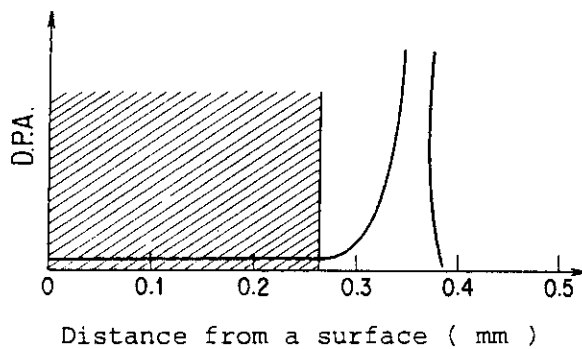


Fig.2 Displacement per an atom ( D.P.A ) versus the distance from the surface of Li<sub>2</sub>O irradiated by lithium ions with the energy of 60MeV. The hatched part shows the specimen in the direction of the thickness.

tance from the boundary between the unirradiated and the irradiated part. Longitudinal axis indicates rotation angle which is proportional to induced strain. In the unirradiated part, the rotation angle increases rapidly with the distance from the boundary and have a maximum value at about  $x=-0.9$  mm, then it decreases gradually toward the specimen edge. To get the fractional volume change, the value of rotation angle at  $X=-0.9$  mm was used and analysis conducted by the same way as described in our previous report<sup>2)</sup>.

The fluence dependence of the fractional volume change of  $\text{Li}_2\text{O}$  irradiated with lithium ions is shown in Fig.4. The fractional volume change increases rapidly with the ion fluence up to a value of  $2.5 \times 10^{19}$  ions/m<sup>2</sup>. Above this value they increase very slowly. This dependence is similar to that of the oxygen-ion irradiation<sup>2)</sup>.

The recovery behavior of fractional volume change is shown in Fig.5 as a function of annealing temperature. Two stages appeared in examined temperature range i.e., one was in the temperature range from 350 to 600 K, the other was about

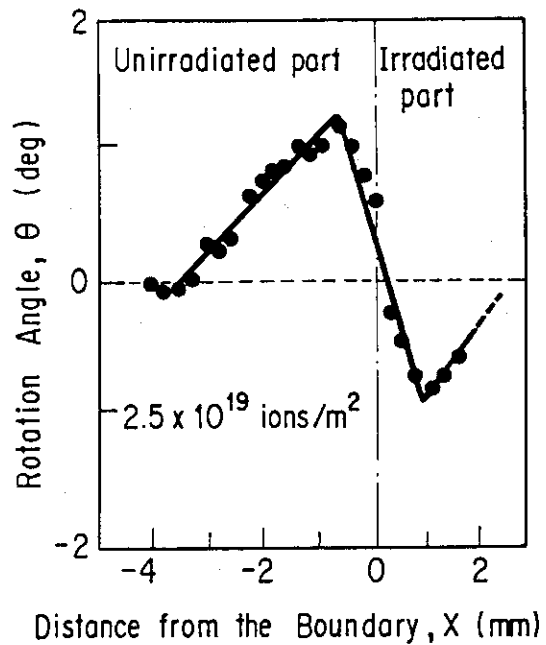


Fig.3 Strain profile irradiated to  $2.5 \times 10^{19}$  lithium ions/m<sup>2</sup> as a function of the distance from the boundary.

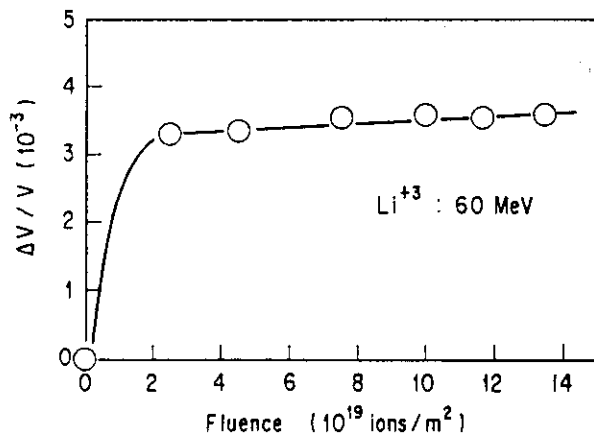


Fig. 4 Fluence dependence of the fractional volume change.

700 to 870K. It is known by our ESR and optical absorption experiments that  $F^+$  centers and the lithium colloid recovers at temperature about 500 K and about 780 K, respectively. From these facts, it is understood that the first stage in these experiments is related with the recovering of the  $F^+$  centers and the second stage is related with the lithium colloid.

To clarify mechanisms of this macroscopic volume expansion of  $Li_2O$  irradiated with lithium ions, information about the concentration of  $F^+$  centers and the lithium colloid and the volume change due to each of them is required. Furthermore,

a microscopic volume change ( lattice parameter change ) measurement is useful to understand the volume change related with the elementary defects. ESR and optical absorption studies and measurements of lattice constant of  $Li_2O$  irradiated with lithium ions will be carried out.

#### Acknowledgment

Authors thanks to Dr. T.Aruga for the computation of D.P.A by using EDEP-1 computer code.

#### References

- (1) G.W.Hollenberg : J.Nucl.Mater. 122/123 (1984) 896
- (2) Y.Ishii, K.Noda, H.Watanabe : JAERI-M 87-115 96

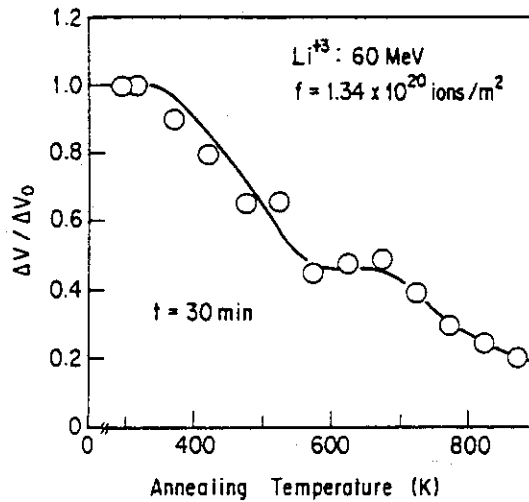


Fig. 5 Isochronal annealing of irradiated specimen. Annealing time is 30 minutes.  $\Delta V_0$  is a increased volume of the specimen irradiated up to  $1.34 \times 10^{20}$  ions/m<sup>2</sup>.

3.6 EFFECT OF IRRADIATION DAMAGE ON ION CONDUCTIVITY OF  $\text{Li}_2\text{O}$ 

Kenji NODA, Yoshinobu ISHII, Hisayuki MATSUI\*,  
Mikio HORIKI\*, Kenji NAKAYA\*, Kouji NEZAKI\*, Naomi OBATA\*  
and Hitoshi WATANABE

Department of Fuels and Materials Research, JAERI,

\*Faculty of Engineering, Nagoya University

### 1. Introduction

In lithium oxide ( $\text{Li}_2\text{O}$ ) as a solid breeder material of D-T fusion reactors, a large number of irradiation defects will be introduced by the high energetic neutrons (up to 14 MeV), tritons (2.7 MeV) and helium ions (2.1 MeV) produced from  ${}^6\text{Li}(n,\alpha){}^3\text{H}$  reactions. These defects will not only induce swelling but also have a large influence on migration of tritium and the composing atoms of the materials.

Defects in  $\text{Li}_2\text{O}$  irradiated with thermal neutrons and oxygen ions have been investigated by electron spin resonance (ESR) and optical absorption methods, to understand fundamental properties<sup>1-3</sup>.

In the present study, the ion conductivity of  $\text{Li}_2\text{O}$  irradiated with oxygen ions was measured to get information of irradiation defects and irradiation effect on the migration of lithium ion.

### 2. Experimental

Specimens used were thin plates (7 to 9 mm in length, 8 to 9 mm in width, 0.3 to 0.4 mm in thickness) of  $\text{Li}_2\text{O}$  single crystals. The specimens were annealed at 1270 K for 10 h in a vacuum better than  $1 \times 10^{-3}$  Pa to eliminate  $\text{OH}^-$  ions or  $\text{LiOH}$  from the specimens.

The specimens were irradiated with oxygen ions (120 MeV) by using a tandem accelerator at JAERI. Measurements of the ion conductivity of the specimens along the direction perpendicular to the thickness were conducted "in-situ" in an irradiation chamber at the prescribed temperatures with a two-terminal AC method using a HP Model 4194 A impedance analyzer after interrupting the irradiation at the ambient temperature.

### 3. Results and Discussion

The ion conductivity at a measurement temperature of 443 or 489 K was measured at various ion fluences using one specimen for each measurement temperature. Fig. 1 shows typical examples of relationships between the ion conductivity and measurement time at 443 K for various ion fluences. The conductivity decreased with the measurement time in each run, reaching constant values after 5000 to 10000 s. Such relationships between the conductivity and the measurement time were also observed at 489 K. The decrease of conductivity with the measurement time was assumed to be due to desorption of water from the surface of the specimen, which arose from adsorption of water vapor in the irradiation chamber at temperatures lower than the measurement temperatures. Evidence for such adsorption-desorption behavior of water on the surface of  $\text{Li}_2\text{O}$  in vacuum was provided by an experiment in which the behavior of water or  $\text{OH}^-$  ions near the surface of  $\text{Li}_2\text{O}$  single crystals in vacuum at various temperatures was studied with elastic recoil detection (ERD) using 2.0 MeV helium ions<sup>4)</sup>. The constant values of conductivity after 5000 to 10000 s can be regarded as the ion conductivity of the specimen.

Fig. 2 shows the relationships between the ion conductivity and the oxygen ion fluence at 443 and 489 K. The conductivity at 443 K increased with the fluence to attain a constant value above  $6 \times 10^{19}$  ions/m<sup>2</sup>. The conductivity at 489 K decreased continuously with fluence in the examined range (up to  $3.45 \times 10^{19}$  ions/m<sup>2</sup>).

After the irradiation, the recovery of ion conductivity was investigated by isochronal annealing experiments. The recovery behavior is shown in Fig. 3. For measurements at 489 K, the conductivity increased in the annealing temperature range from 489 to 570 K, to be completely recovered to the level before the irradiation. On the other hand, for the measurement at 443 K the conductivity decreased once with the annealing temperature in the temperature range from 443 to 498 K, and then it increased with the annealing temperature in the range from 498 to 548 K.

The temperature range in which the conductivity increased was almost the same as that for the recovery of the  $\text{F}^+$  center (an oxygen ion vacancy trapping an electron) in  $\text{Li}_2\text{O}$ <sup>2,3)</sup>. Accordingly, the increase of the conductivity at 443 and 489 K in Fig. 3 can be attributed to the recovery of  $\text{F}^+$  centers. The decrease of the conductivity at 443 K during the anneal-

ing may be due to unspecified irradiation defects which enhance the conductivity and are recovered in the range 443 to 498 K.

It is the migration of lithium ions, rather than oxygen ions, in  $\text{Li}_2\text{O}$  that leads to the ion conductivity, since lithium ions diffuse much more rapidly<sup>5)</sup>. So, the results in the present study suggest that the diffusivity of lithium ions is decreased by the  $\text{F}^+$  centers in the range from 490 K to the temperature at which the  $\text{F}^+$  centers are virtually recovered (about 570 K). Around 440 K the diffusivity of lithium ions is supposed to be increased by the unspecified irradiation defects mentioned above.

The ion conductivity of  $\text{Li}_2\text{O}$  depends on concentration of  $\text{OH}^-$  impurity. The  $\text{OH}^-$  impurities introduce lithium ion vacancies to maintain neutrality of the lattice. Consequently, lithium ions are considered to diffuse by a vacancy mechanism. The ion conductivity can be expressed by

$$\sigma = Ne \eta_{v_{\text{Li}}} \mu_{v_{\text{Li}}} \quad (1),$$

where  $N$  is the number of lithium ions,  $\eta_{v_{\text{Li}}}$  the mole fraction of lithium ion vacancies, and  $\mu_{v_{\text{Li}}}$  the mobility of lithium ion vacancies. The lithium ion vacancies have a negative charge, while the  $\text{F}^+$  centers have a positive charge. Therefore, the lithium ion vacancies are electrostatically attracted by the  $\text{F}^+$  centers. Accordingly, the decrease of ion conductivity (the decrease of diffusivity of lithium ions) at 489 K due to the irradiation can be attributed to the decrease of mobility of lithium ion vacancies due to retardation by the  $\text{F}^+$  centers, or to the decrease in number of mobile lithium ion vacancies due to trapping by the  $\text{F}^+$  centers.

In addition, the unspecified irradiation defects enhancing the ion conductivity (the diffusivity of lithium ions) at 443 K are considered to be defects which increase the number of mobile lithium ion vacancies.

#### References

- 1) K. Noda, K. Uchida, T. Tanifuji and S. Nasu: J. Nucl. Mater. 91 (1980) 234.
- 2) K. Uchida, K. Noda, T. Tanifuji, S. Nasu, T. Kirihara and A. Kikuchi: phys. stat. sol. (a) 58 (1980) 557.
- 3) K. Noda, K. Uchida, T. Tanifuji and S. Nasu: Phys. Rev. B 24 (1981) 3736.
- 4) J. A. Sawicki, L. M. Howe and K. Noda: Nucl. Instr. and Meth. B 32 (1988) 85.



5) H. Akiyama, K. Ando and Y. Oishi: Solid State Ionics 3 & 4 (1981) 469.

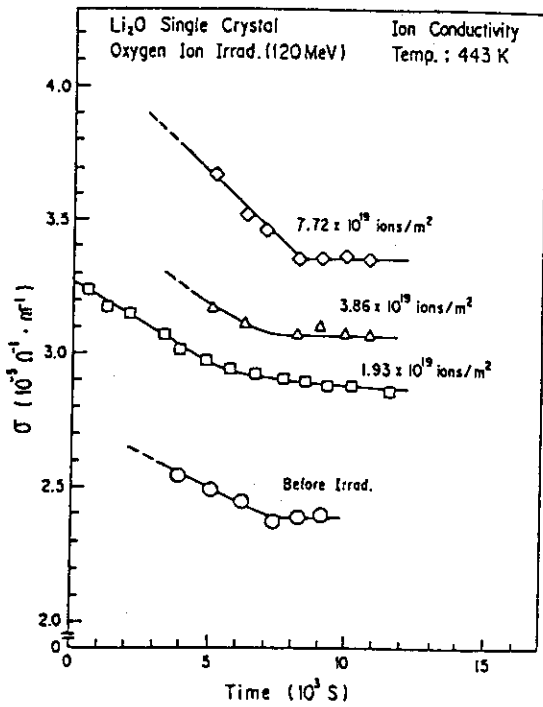


Fig.1 Relationship between ion conductivity at 443 K and measurement time for various fluences.

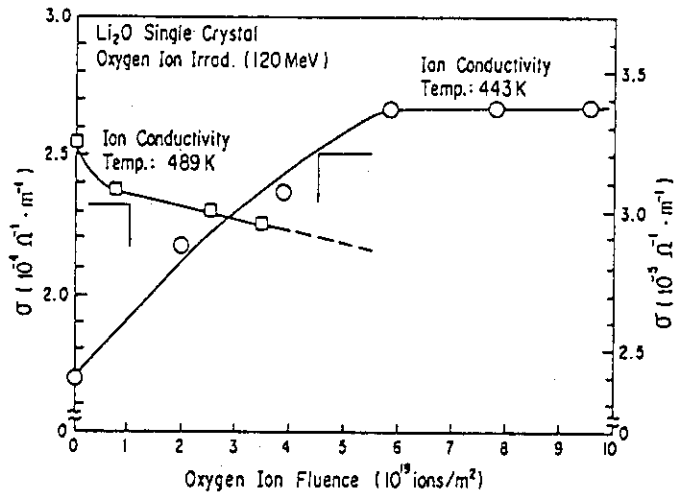
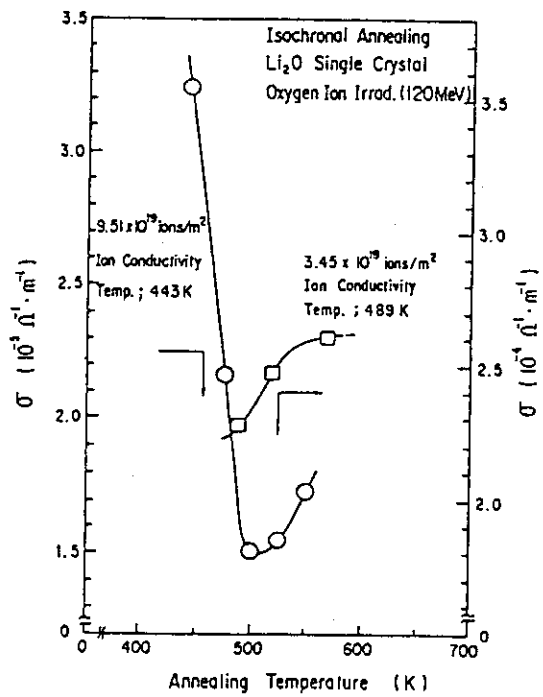


Fig.2 Ion conductivity at 443 and 489 K as a function of fluence.

Fig.3 Recovery behavior of ion conductivity at 443 and 489 K.



## 3.7 IRRADIATION DAMAGE STUDIES OF CERAMIC MATERIALS

Kenji NODA, Yoshinobu ISHII, Kotaro KURODA\*,  
Masakatsu, SASAKI\*, Makoto SUGINOSHITA\* Toru IMURA\*  
Hiroyasu SAKA\* and Hitoshi WATANABE

Department of Fuels and Materials Research, JAERI,

\* Faculty of Engineering, Nagoya University

Many kinds of ceramic materials are considered to be used in fusion reactors. Improvement of resistance to irradiation degradation of ceramic materials is desired for development of the fusion reactors. Such improvement will make application of ceramic materials in radiation circumstance (fusion and fission reactors, space, etc.) larger. In this study, radiation damage and behavior of electric resistivity of SiC and  $\text{YBa}_2\text{Cu}_3\text{O}_{7-x}$  irradiated with nitrogen or oxygen ions were studied, in order to get fundamental information for improvement of resistance to irradiation degradation.

Specimens used were SiC single crystals and sintered  $\text{YBa}_2\text{Cu}_3\text{O}_{7-x}$ . The specimens were irradiated by nitrogen ions with an energy of 400 keV or oxygen ions with an energy of 1.0 MeV using 2 MV Van de Graaff accelerator at JAERI. After the irradiation, measurements of electric resistivity and transmission electron microscope (TEM) observation of the specimens were carried out.

For SiC single crystal TEM specimens irradiated to  $1.1 \times 10^{21}$  ions/m<sup>2</sup> by nitrogen ions, whole areas being observable by TEM were found to be changed into amorphous state. As reported previously, partial amorphization due to irradiation was observed for  $\beta\text{-Si}_3\text{N}_4$  irradiated to  $2.2 \times 10^{21}$  ions/m<sup>2</sup> by argon ions with an energy of 400 keV, which introduced displacement damage more effectively than the nitrogen ions with an energy of 400 keV<sup>1,2)</sup>. So, it seems that irradiation degradation of SiC occurred more easily than that of  $\beta\text{-Si}_3\text{N}_4$ . However, systematic radiation damage studies are necessary to clarify difference of radiation damage production between SiC and  $\beta\text{-Si}_3\text{N}_4$ .

Electric resistivity of sintered  $\text{YBa}_2\text{Cu}_3\text{O}_{7-x}$  disk specimens (diameter; 6 mm, thickness; 0.6 mm) was measured using DC four-terminal method. For the irradiated specimen, the electrodes were attached on the

irradiated surface. Fig. 1 shows relationship between electric resistivity and temperature for the  $\text{YBa}_2\text{Cu}_3\text{O}_{7-x}$  specimens unirradiated and irradiated to  $1.1 \times 10^{21}$  ions/ $\text{m}^2$  by oxygen ions. The unirradiated specimen was in super conductive state below 90 K, while the irradiated specimen was not even at 77 K. After the measurements of electric resistivity, the unirradiated specimen and the irradiated region of the oxygen-ion-irradiated specimen were observed with TEM. In case of preparation of the TEM specimen for observation of the irradiated region, the irradiated specimen was thinned from only the unirradiated surface side by argon ion-milling so that only the irradiated region might be remained. Fig. 2 shows electron micrographs and diffraction patterns of the unirradiated specimen and the irradiated region of the oxygen-ion-irradiated specimen. The unirradiated specimen was found to be orthorhombic super conductive phase consisting of many twins. On the other hand, it was seen from the hallow rings that the irradiated region was changed into amorphous state by the irradiation.

#### References

- 1) K. Kuroda, K. Noda, Y. Ishii, H. Saka, T. Imura and H. Watanabe: Proc. 11th Int. Cong. on Electron Microscopy, Kyoto, 1986, p.1305-1306.
- 2) K. Noda, Y. Ishii, K. Kuroda, H. Saka, K. Sasaki, M. Sakurai, T. Imura and H. Watanabe: JAERI-M 87-115, p.100-103.

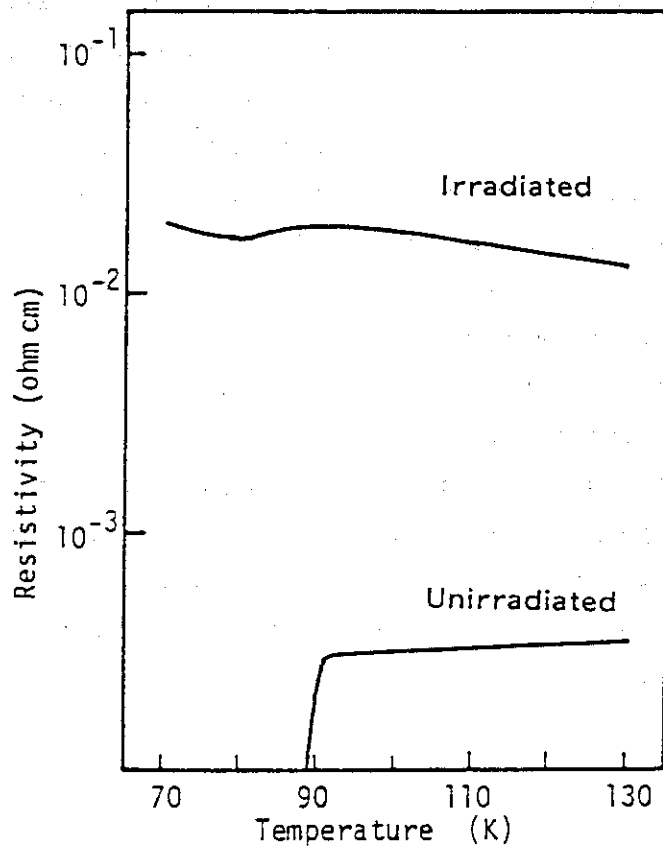


Fig.1 Electric resistivity of sintered  $\text{YBa}_2\text{Cu}_3\text{O}_{7-x}$  specimens unirradiated and irradiated to  $1.1 \times 10^{21}$  ions/m<sup>2</sup> with oxygen ions with an energy of 400 keV.

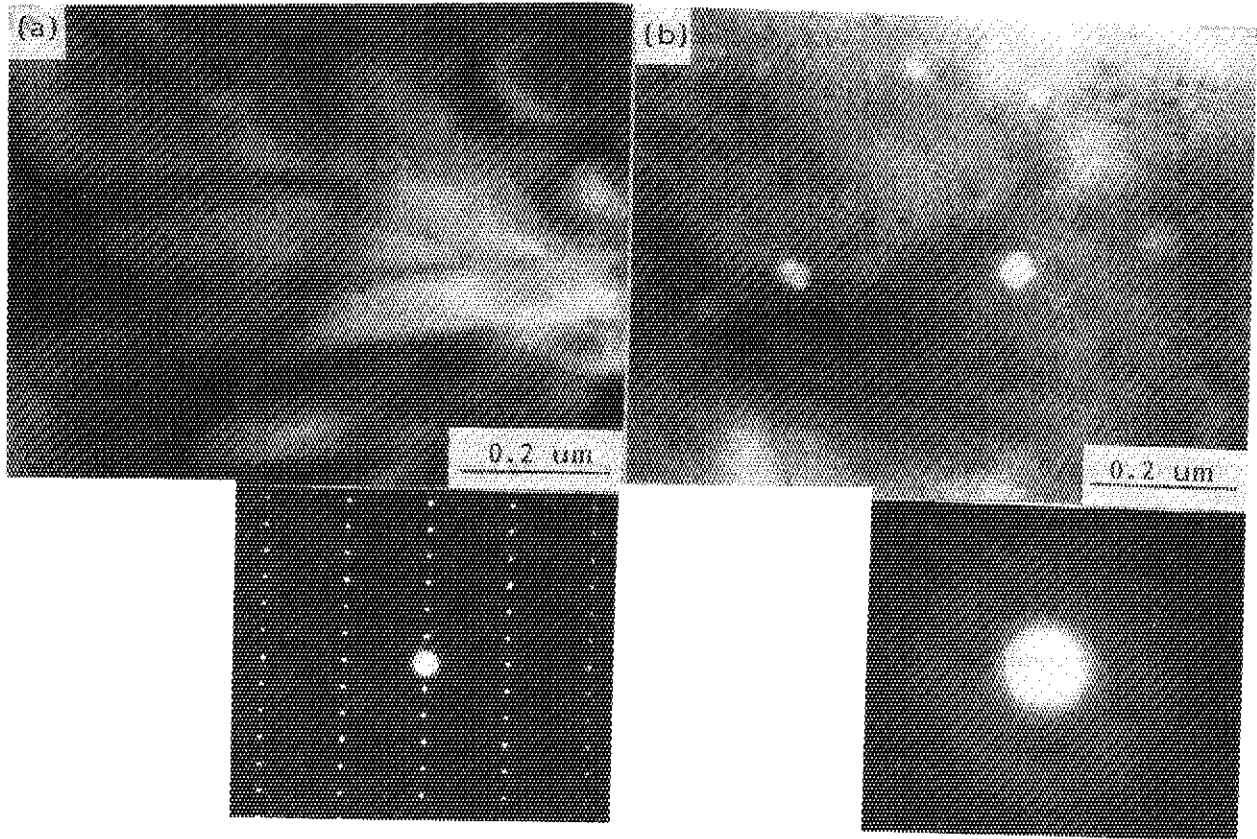


Fig.2 Electron micrographs and diffraction patterns of sintered  $\text{YBa}_2\text{Cu}_3\text{O}_{7-x}$  specimens unirradiated (a) and irradiated to  $1.1 \times 10^{21}$  ions/m<sup>2</sup> with oxygen ions with an energy of 400 keV (b).

### 3.8 EFFECT OF HEAVY ION IRRADIATION ON NEGATIVE THERMAL EXPANSION IN GAP SINGLE CRYSTAL

Hiroshi MAETA, Katsuji HARUNA\*, Kazutosi OHASHI\*,  
Takuro KOIKE\* and Fumihisa ONO\*\*

Department of Physics, JAERI, \*Faculty of Engineering,  
Tamagawa University, \*\*College of Liberal Arts and Sciences,  
Okayama University

#### Introduction

Most of semiconductors, which have tetrahedrally bonded solids, have a negative thermal expansion coefficient below approximately 100 K and a corresponding negative Gruneisen parameter.

Recently, we have studied the thermal expansion of GaP single crystal by means of measurements of lattice parameter, and found a small negative thermal expansion coefficient below 50 K.<sup>1)</sup> However, this value of GaP is very smaller than that of Si and InP. In the previous paper<sup>2)</sup>, we reported the effects of the heavy ion irradiation on negative thermal expansion coefficient in Si and InP. By the irradiation, we found remarkable changes of thermal expansion coefficients in the irradiated Si and InP crystals.

In this paper, we report the effect of heavy ion bombardment on negative thermal expansion in GaP single crystal.

#### Experimental Procedures

The specimens were prepared in thin rectangular plates of GaP single crystals with area of  $3 \times 10 \text{ mm}^2$  and thickness of 0.3 mm. These specimens were bombarded with 120 - 150 MeV  $\text{Cl}^{+10}$  ion at  $4 \times 10^{10}$  ion/cm<sup>2</sup>sec at about liquid nitrogen temperature. After the irradiation, the specimens were warmed up to room temperature. By using a  $\text{CuK}$  beam through a fine slit of 0.2 mm in width, the Bragg reflections were measured by the Bond method in which two counter were placed symmetrically. Measurements of the thermal expansion coefficients by the lattice parameter were made between at 4.2 K and room temperature.

## Results and Discussion

Typical results of this experiment are shown in figure 1 for GaP specimens bombarded with 120 MeV - 150 MeV  $\text{Cl}^{+10}$  ions. The figure shows the results of the temperature dependence of the lattice parameters in irradiated specimens and unirradiated specimen.

Characteristic features of the results are as follows : 1) Very large values of increased lattice parameters,  $\Delta a / a_0$ , with the irradiation were obtained to be about 10 %. However, the values of the lattice parameter decreased a little with the doses of Cl ions. 2) Remarkable change of negative thermal expansion of lattice parameters was found. Temperatures corresponding to the minimum values of the lattice parameters shifted to lower temperature and the minimum value of lattice parameter decreased more deeply, as shown in figure 1.

It is very surprising that the changed values of the lattice parameter after the heavy ion irradiation amount up to 10 % in GaP crystal with the Cl ion irradiation. We observed the similar result for the ion irradiated specimen of InP in which the change of lattice parameter was 7%<sup>2)</sup>.

The heavy ion irradiation is expected to produce a large number of the defects. We tried to estimate the concentration of the induced defects in the GaP crystal with  $\text{Cl}^+$  bombardments from the measured lattice parameter. There is, however, no value of the relative volume change per interstitial, so we used a value of Si crystal ( $\Delta v / \Omega$ ) = 0.55 and we got the concentration of defects in the irradiated GaP crystal to be 0.5 for the measured lattice parameter change  $\Delta a / a_0 = 0.1$  with 120 MeV Cl ion irradiation to the fluence of  $6 \times 10^{14}$  ions/cm<sup>2</sup>. Very large number of the defects would exist after the irradiation even if the defects recovered during the irradiation and warming up to the room temperature, resulting to the large change of the relative lattice parameter ( $a/a_0$ ) up to 10 %. It will be expected for these defects to change the thermal expansion coefficients remarkably.

In the case of materials which have negative thermal expansion coefficients, it has to take into account the increasing frequencies of lattice vibrations with temperatures and/or expanded volume. Barron<sup>4)</sup> has pointed out that the normal mode which satisfies the above condition must be the transverse acoustic one (so called shear mode vibrations) in the short wave length region. Most of the defects would be interstitial clusters and/or dislocation loops, and many of the bonding chains of these

atoms be cut down. So, the atoms would be able to vibrate easily and the transverse acoustic mode be enhanced at lower temperature. It is also reasonable that the temperature of the minimum values of lattice parameters shifted to lower temperature, because the shear mode vibration ( so-called TA modes ) would be easily able to occur in the cut-bonding specimen. This phenomenon has also been found for Si crystal after Cl ion irradiation, as already reported<sup>2)</sup> .

A more detailed experiment is currently in progress and will be published elsewhere.

#### References

- 1) K. Haruna, H. Maeta, H. K. Ohashi and T. Koike : J. Phys. C Solid State Phys., 19 (1986) 5149.
- 2) H. Maeta, K. Haruna, K. Ohashi, T. Koike and F. Ono, JAERI TANDEM, LINAC & V.D.G. Annual Report 1985, p 45.
- 3) T.H. Barron : Phil.Mag., 46 (1955) 720.
- 4) Point Defects in Solid, ed. by I.H. Crawhold and L.M. Slifkin, p.96.
- 5) W. Mayer and H. Peisl : J. Nuclear Materials, 108 & 109 (1982) 627.



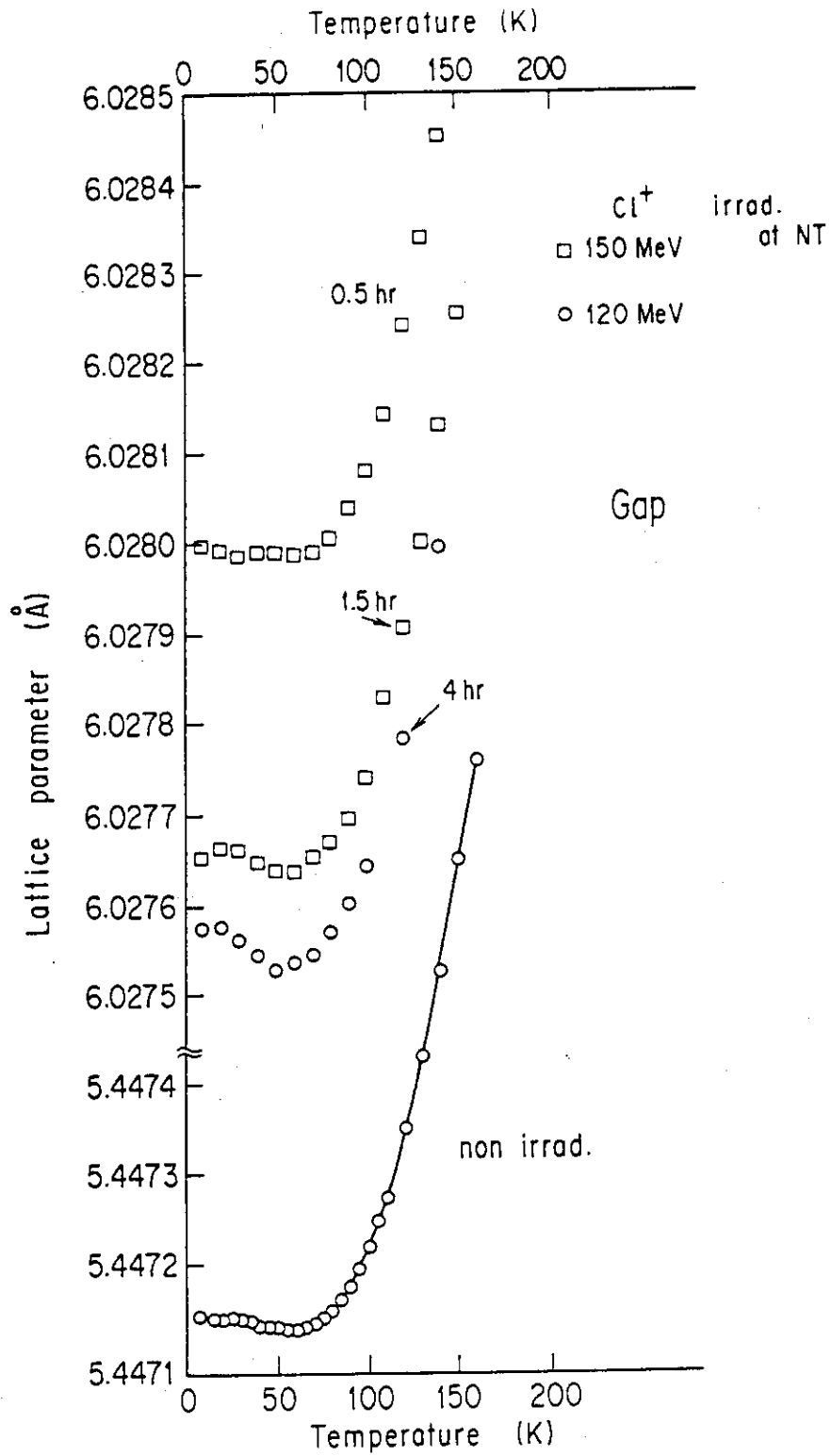


Fig. 1 Temperature dependence of the lattice parameters in GaP single crystals irradiated with 120 MeV  $\text{Cl}^{+10}$  ion at liquid nitrogen temperature.

### 3.9 X-RAY DIFFRACTION TOPOGRAPHIC OBSERVATION OF SILICON SINGLE CRYSTALS IRRADIATED WITH ENERGETIC HEAVY IONS (6)

Hiroshi TOMIMITSU

Department of Physics, JAERI

#### 1. Introduction

The lattice disorder induced by ion-irradiation has been studied by X-ray diffraction topography (XDT). Schwuttke et al<sup>1)</sup> have shown that disorders concentrate in the very thin layer corresponding to the range stragglings of projectiles, when Si single crystals were irradiated with 2 MeV  $N^+$ ,  $B^+$  and  $P^+$  ions to the doses of more than  $10^{15}$  ions/cm<sup>2</sup>, and the upper and lower parts of the specimen crystal separated by the disordered thin layer remained perfect. More refined study by Bonse, Hart and Schwuttke<sup>2)</sup> found the interference fringes arising from the two perfect regions separated by the very thin disordered layer.

The present author has also reported<sup>3)</sup> the following results by the conventional XDT-observation in Si single crystals irradiated with 150 MeV  $Ni^{9+}$  and  $Cl^{9+}$  ions; 1) the specimens were deformed as a whole, 2) they sustained heavy strains which concentrated at the irradiation boundaries, and 3) systematic fringes were observed in the irradiated areas.

In order to confirm the results mentioned above, further measurements were made on the specimens irradiated with various kinds of energetic ions. The present article briefly summarizes the results of the conventional XDT-observation on those heavy-ion-irradiated Si single crystals.

#### 2. Experimental Procedure

Si wafers used in this experiment were grown by Cz-method along  $\langle 100 \rangle$  or  $\langle 111 \rangle$  direction, cut into slices with surface indices of (100) or (111), respectively, of the thickness of 300 or 600  $\mu m$ , and finished with chemical-etching or mechanical-polishing.

The ion-irradiations were carried out with the tandem accelerator of this institute, operated with terminal accelerating voltage of about 15MV, on which ions were accelerated up to several tens of MeV or up to about 200 MeV depending on their respective charge states as listed in Table 1, where

typical conditions of the ion-irradiation are summarized for all the specimens including those examined in the fiscal year 1987(\*), together with the observation-results to be mentioned in the next section. All of the specimens were partially covered with specially designed masks made of Al or Mo foils of around 30 $\mu$ m thickness, to examine whether any special crystal-imperfection such as dislocations are generated or not through the irradiation. During the irradiation period, the wafers were cooled with liquid nitrogen via Cu-supporter.

In order to examine the effect of the beam-homogeneity on the irradiation-caused lattice-imperfection, around 40% of the all specimen was irradiated with the horizontally-scanning beam of the vertically-elongated cross section. The comparison will be mentioned in section 3.4.

The XDT-observation was carried out with a fine focus x-ray generator, mostly with the Mo-K $\alpha$ 1 radiation.

### 3. Results and Discussions

#### 3.1 Macroscopic Deformation of Irradiated Crystal

In more than 50% of the specimen examined, macroscopic deformation was, more or less, recognized because the angular position of the reflection maximum in the rocking curve moved as the position of the incident X-rays on the specimen surface was moved and because a topograph taken at an angular position showed only partial images of the whole specimen crystal. The crystal deformation in the specimen irradiated with 150MeV  $^{35}\text{Cl}^{9+}$  (Dose:  $6 \times 10^{14}$  ions/cm $^2$ ) was concluded to be convexed towards the irradiated surface, the estimated value of the radius of the surface curvature being about 33m.

#### 3.2 Lattice Strains at Irradiation-Boundaries

In almost all specimens examined, the so-called "black-and-white" contrasts were observed at the boundaries between the irradiated- and non-irradiated areas separated with the specially designed hollow of the mask foil. This fact indicates that the heavy lattice-strains concentrate at the boundaries. The lattice-strain at the irradiation boundaries was concluded to be perpendicular to the boundary, because the black-and-white contrasts were clearly observed at the parts of the boundary perpendicular to the reflection vector and, on the other hand, they were only faint at the parts parallel to it. Furthermore, it was confirmed that boundary-lattice-strain

Table 1 Summary of Experimental Conditions and Results

Spec. No.	Projectile Ion	Thick. ( $\mu\text{m}$ )	Surface Index	Energy (MeV)	Dose ( $\times 10^{14}/\text{cm}^2$ )	Beam Scan.	Results <sup>2,3)</sup>			
							①	②	③	④
* 70201	${}^7\text{Li}^{3+}$	300	100	20	14.8	No	Yes	No	Yes	Yes
* 70202	${}^7\text{Li}^{3+}$	300	100	20	5.1	Yes	Yes	No	Yes	No
110201	${}^{11}\text{B}^{3+}$	610	111	20	4.1	No	Yes	No	Yes	Yes
110301	${}^{11}\text{B}^{4+}$	610	111	30	1.6	Yes	Yes	No	Yes	Yes
110401	${}^{11}\text{B}^{4+}$	610	111	40	1.3	Yes	Yes	No	Yes	No
* 110601	${}^{11}\text{B}^{4+}$	610	111	60	8	No	Yes	No	Yes	Yes
* 110602	${}^{11}\text{B}^{4+}$	340	100	60	7	Yes	Yes	No	No	Yes
* 120301	${}^{12}\text{C}^{4+}$	600	111	30	4.9	No	Yes	Yes	Yes	Yes
* 120302	${}^{12}\text{C}^{4+}$	600	111	30	6.4	Yes	Yes	No	Yes	Yes
* 120601	${}^{12}\text{C}^{4+}$	600	111	60	18.3	No	Yes	No	Yes	Yes
* 120602	${}^{12}\text{C}^{5+}$	600	111	60	35.3	Yes	Yes	No	Yes	Yes
121002	${}^{12}\text{C}^{5+}$	360	100	100	43.2	No	Yes	Yes	No	No
121003	${}^{12}\text{C}^{6+}$	605	111	100	15	No	Yes	No	Yes	No
121004	${}^{12}\text{C}^{5+}$	600	111	100	135.4	Yes	Yes	No	Yes	No
* 140401	${}^{14}\text{N}^{4+}$	610	111	40	3	Yes	Yes	No	No	No
* 140402	${}^{14}\text{N}^{4+}$	610	111	40	4.7	No	Yes	No	No	No
140801	${}^{14}\text{N}^{5+}$	610	111	80	2.4	No	Yes	No	Yes	Yes
140802	${}^{14}\text{N}^{5+}$	605	111	80	2.2	Yes	Yes	No	No	Yes
* 160601	${}^{16}\text{O}^{6+}$	360	100	60	10.7	No	Yes	Yes	Yes	Yes
160801	${}^{16}\text{O}^{6+}$	600	111	80	8	No	Yes	Yes	Yes	Yes
161201	${}^{16}\text{O}^{7+}$	470	100	120	6.9	No	Yes	Yes	No	Yes
190601	${}^{19}\text{F}^{6+}$	370	100	60	2	No	Yes	Yes	No	Yes
191201	${}^{19}\text{F}^{7+}$	340	100	120	3.2	No	Yes	Yes	No	Yes
281001	${}^{28}\text{Si}^{8+}$	355	100	100	4.1	No	Yes	Yes	Yes	Yes
281501	${}^{28}\text{Si}^{9+}$	470	100	150	1.2	No	Yes	Yes	Yes	Yes
320501	${}^{32}\text{S}^{7+}$	370	100	50	0.1	No	Yes	Yes	Yes	Yes
321001	${}^{32}\text{S}^{8+}$	370	100	100	0.9	No	Yes	Yes	Yes	Yes
321501	${}^{32}\text{S}^{9+}$	340	100	150	28.5	Yes	Yes	Yes	Yes	Yes
321651	${}^{32}\text{S}^{10+}$	370	100	165	1.1	No	Yes	Yes	Yes	Yes
351201	${}^{35}\text{Cl}^{8+}$	340	100	120	1	No	Yes	No	Yes	No
351202	${}^{35}\text{Cl}^{8+}$	340	100	120	51.7	Yes	Yes	Yes	No	Yes
351401	${}^{35}\text{Cl}^{8+}$	330	100	140	0.7	Yes	Yes	No	Yes	No
351402	${}^{35}\text{Cl}^{8+}$	330	100	140	6.1	Yes	Yes	Yes	Yes	No
351403	${}^{35}\text{Cl}^{8+}$	370	111	140	6.1	Yes	Yes	Yes	Yes	No
351501	${}^{35}\text{Cl}^{9+}$	420	100	150	5.7	No	Yes	Yes	Yes	Yes
351502	${}^{35}\text{Cl}^{10+}$	350	100	150	8	No	Yes	Yes	No	No
351651	${}^{35}\text{Cl}^{10+}$	340	100	165	1	Yes	Yes	Yes	No	Yes
351652	${}^{35}\text{Cl}^{10+}$	350	100	165	4	Yes	Yes	No	No	No
581651	${}^{58}\text{Ni}^{9+}$	420	100	165	0.5	No	Yes	Yes	Yes	Yes
581901	${}^{58}\text{Ni}^{12+}$	605	111	190	0.4	No	Yes	No	Yes	Yes
581921	${}^{58}\text{Ni}^{11+}$	365	100	192	0.7	Yes	Yes	Yes	Yes	No
631801	${}^{63}\text{Cu}^{11+}$	640	111	180	3.1	Yes	Yes	No	Yes	No
* 631802	${}^{63}\text{Cu}^{11+}$	610	111	180	2.6	No	Yes	Yes	Yes	Yes
800901	${}^{80}\text{Br}^{6+}$	470	100	90	10	No	Yes	No	No	No
801201	${}^{80}\text{Br}^{10+}$	370	100	120	3	Yes	Yes	Yes	No	No
1971691	${}^{197}\text{Au}^{13+}$	470	100	169	0.9	No	Yes	Yes	No	Yes
1972101	${}^{197}\text{Au}^{13+}$	370	100	210	1	Yes	Yes	Yes	Yes	No

Notice: \*) The irradiation was made during the fiscal year 1987.

- \*\*\*) ① Macroscopic Deformation of the Specimen Crystal  
 ② Lattice-Strain Concentrated at the Irradiation Boundaries  
 ③ Defect Images Caused by the Ion-Irradiation  
 ④ Interference Fringes within the Irradiated Area

reaches at the other surface far from the irradiated surface, because both of the strain images, i.e. the black-and-white contrasts, at the irradiation boundaries were very similar to each other in the topographs taken on the irradiated surface and on the other surface, in the topographs taken with the reflection vector perpendicular to the specimen surface.

In spite of those heavy lattice-strains observed at the irradiation boundaries, however, there was not observed any particular lattice defect like dislocations generated around the irradiation boundary.

### 3.3 Irradiation-Caused Damages

In more than 60% of the specimens examined, irregular contrasts were observed within the irradiated areas, which seemed to indicate the damaged lattice caused by the ion-irradiation.

### 3.4 Interference Fringes

Regularly arrayed systematic fringes were observed in more than 70% of the specimen irradiated without beam-scanning, while in more than 60% of the specimens irradiated rather homogeneously with beam-scanning, they were not observed. The origin of such interference fringes, thus, seems to be attributed to the inhomogeneous distribution of the projectile ions, which causes the lens-like damaged zone just at the depth of the ion range in the wafer separating two perfect layers shallower- and deeper than the ion range, just as assumed by Bonse, Hart and Schwuttke<sup>2)</sup>. It would be emphasized, however, that several of the specimen are not the case, because they show the interference fringes even in the topograph taken with the reflection vector perpendicular to the specimen surface, which apparently contradicts with their assumption<sup>2)</sup>.

The author is much indebted to Drs. Abe and Masui of Shinetsu-Handotai Co. for their kind offering him the Si wafers used in this experiment.

### References

- 1) G.H.Schwuttke, K.Brack, E.E.Gardner and H.M.DeAngelis: Proc. Santa Fe Conf. Radiation Effects in Semiconductors, ed. F.Vook, (Plenum Press, N.Y., 1968) pp.406.
- 2) U.Bonse, M.Hart and G.H.Schwuttke: Phys.Stat.Solidi **33** (1969) 361.
- 3) H.Tomimitsu: Jpn.J.Appl.Phys. **22** (1983) L674.

### 3.10 ELECTRON ENERGY LOSS SPECTROSCOPY ANALYSIS OF DAMAGE STRUCTURE IN ALUMINA IRRADIATED WITH He-IONS

Yoshio KATANO, Hisayoshi MITAMURA\* and Hideo OHNO

Department of Fuels and Materials Research, JAERI,

\*Department of Environmental Safety Research, JAERI

#### 1. Introduction

Alumina is a candidate material for such insulators as RF windows of future fusion reactors because of its generally good structural and electrical properties. Although much work on radiation effects of alumina has been done by irradiations with fission neutron(1), the structural stability and microstructural development of alumina which contains a large amount of helium have not yet been well studied. Helium is calculated to be produced in alumina at a level of 500 appm per 1MW/m<sup>2</sup> through (n, $\alpha$ ) reaction with fusion neutrons(2). Therefore, it is of practical importance to elucidate the behavior of helium in alumina and the influences on microstructural development. In the present work, damage structures of single crystal alumina irradiated with energetic helium ions were investigated.

#### 2. Experimental procedure

The material used in this study was single crystal alumina of high purity supplied by Rare Metallic Co., Ltd. Disk sample of 0.2 mm thick 3 mm in diameter with the basal plane parallel to the foil surface were thinned to 15  $\mu$ m by both mechanical grinding and polishing with diamond paste. The thinned specimens were irradiated with 0.4MeV He-ions at temperature of 1023K using a Van de Graaff accelerator in JAERI. The current density was 1 mA/m<sup>2</sup> and dose was 1 x 10<sup>20</sup> He/m<sup>2</sup>.

The irradiations are estimated to inject helium to a peak concentration of 4 x 10<sup>3</sup> appm and to produce a displacement damage of 0.3 dpa at peak around 1.0 $\mu$ m. The front surface of the irradiated samples was carefully removed by about 0.8 $\mu$ m by ion-thinning and then the samples were back-thinned to an electron-transparency by ion-thinning. The ion-thinning was carried out with 6 keV Ar-ions incident on the surface at an angle of 20°. The microstructural examinations were made with an H-800 transmission

electron microscope operated at 200 kV and an electron energy loss spectroscopy (EELS). The diameter of the electron beam used in the analysis was about 150nm. The thickness of the observed area was about 20 to 100nm.

### 3. Results and discussions

Microstructures of alumina annealed for 1h at 1223K after He<sup>-</sup>ion irradiation at 1023K are shown in Fig.1. The average size and number density of the cavities were 7nm and  $2 \times 10^{22}/\text{m}^3$ , respectively. In addition, the size of the cavities is seen to be larger in regions near to the ion-range as observed by using a stereo-microscopy technique. However, around the ion-range which was exposed to the foil surface, cavities coalesced into large cavity channels of 300nm long and 30nm in diameter at maxima. Then, the cavity sizes are seen to have a bimodal distribution. Other distinguished features are small and large sized spherical precipitates, which were considered to be aluminum metal colloids from the morphology in the previous study (3). These precipitates, however, have not yet been examined by analytical methods such as EELS.

The examined region in the irradiated and annealed alumina sample in the EELS analysis is shown in Fig.2. The region was around the depths of ion-range and the microstructural change was prominent. The EELS spectra of the non-irradiated sample and the sample annealed after the irradiation are compared in Fig.3. From Fig.3(b), a plasmon excitation peak of about 30 eV is noticed to be overlapped with the main plasmon peak of bulk alumina at 24 eV. The energy of 30 eV almost coincides with twice the plasmon energy of metallic aluminum, e.g., 15.3eV. The fact confirms that the observed precipitates of black features are colloids of metallic aluminum. Moreover, the other peak observed at around 78.5eV in the irradiated and annealed sample can be identified to be  $L_{2,3}$  absorption of aluminum. Another peak observed around 40 to 50eV, however, can not be identified clearly.

### 4. Summary

The precipitates observed in the He-ion irradiated and annealed sample were revealed to be Al metal colloids from the EELS analysis. The Al metal colloids in the present sample were formed during annealing at 1223K after He-ion irradiation at 1023K: both temperatures were much higher than the Al

melting point. The present results seem to confirm the strong influence of highly injected helium atoms and radiation-induced defects on forming and stabilizing the Al metal precipitates on alumina.

References

- 1) F. W. Clinard, Jr., G. F. Hurley and L. W. Hobbs: J. Nucl. Mater. 108/109 (1982) 655.
- 2) G. P. Pelles: J. Nucl. Mater. 122/123 (1984) 1338.
- 3) Y. Katano, H. Ohno and H. Katsuta: J. Nucl. Mater. 154/156 (1988) in press.

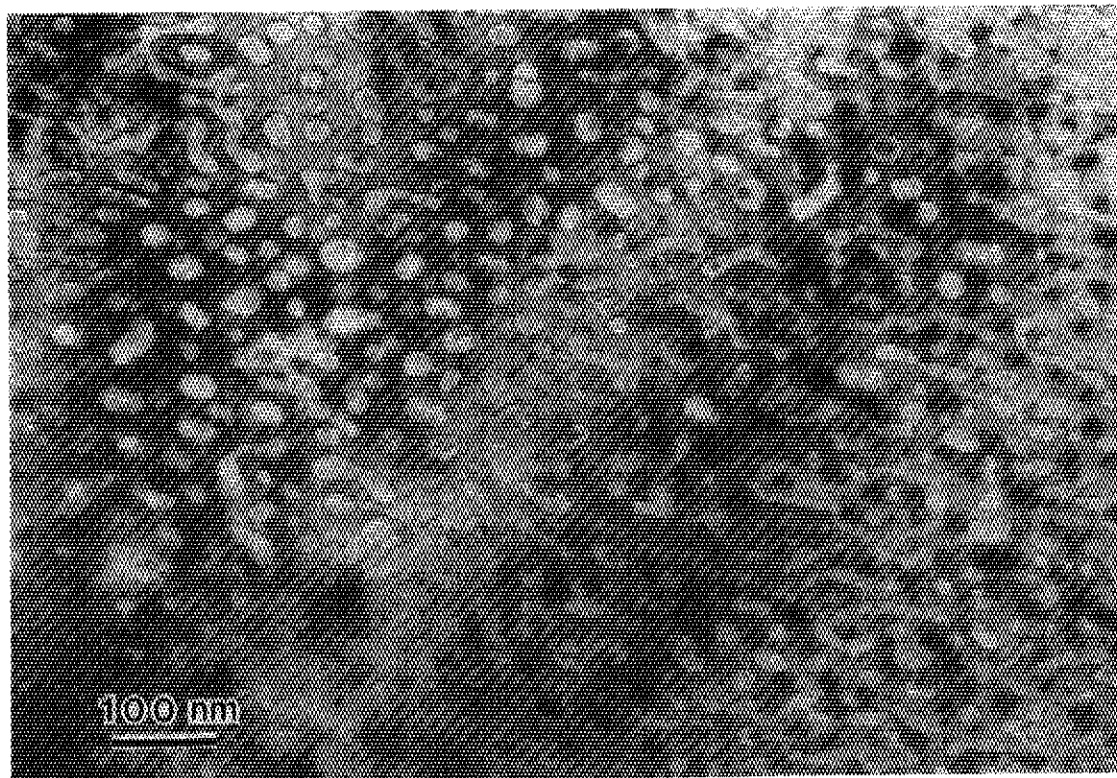


Fig. 1 Damage structure in single crystal alumina annealed for 1 h at 1223 K after He-irradiation at 1023 K.



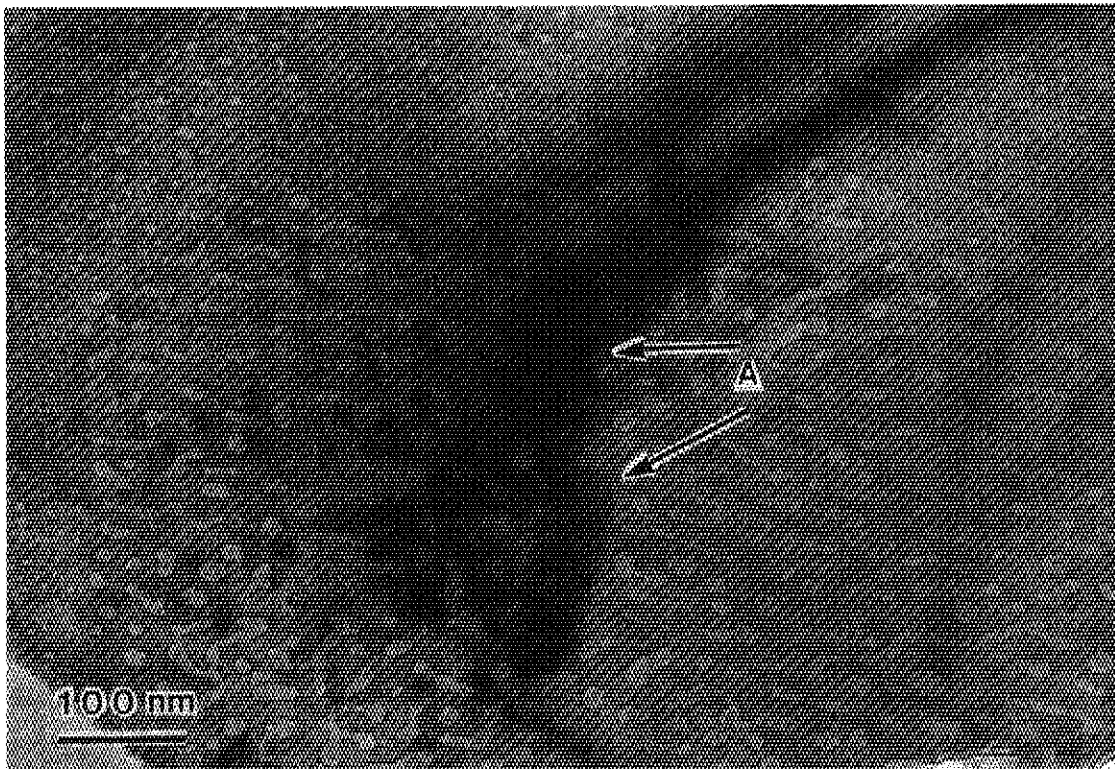


Fig. 2 A micrograph showing the examined region (A) of EELS analysis of He-irradiated and annealed alumina.

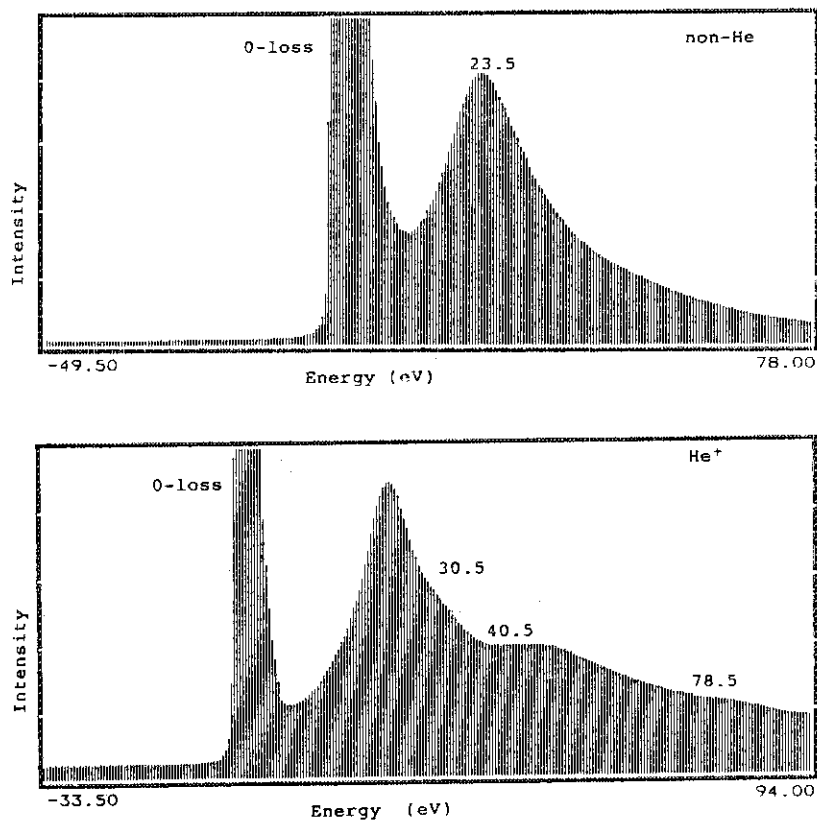


Fig. 3 EELS spectra from (a) non-irradiated alumina and (b) He-irradiated and annealed alumina.

3.11 EFFECT OF HIGH-ENERGY ION IRRADIATION ON SUPERCONDUCTING  
PROPERTIES OF  $\text{YBa}_2\text{Cu}_3\text{O}_{7-x}$ 

Akihiro IWASE, Norio MASAKI, Tadao IWATA and Shigemi SASAKI

Department of Physics, JAERI

After the discoveries of high- $T_c$  superconductors,<sup>1,2)</sup> many studies of irradiation damage in these materials have already been performed. Irradiation-induced defects are, however, expected to move rapidly in the materials, and are annihilated or are transformed to other complex configurations, unless the irradiations are performed at low temperatures. On the other hand, there is a prospect of technological uses of high- $T_c$  superconductors, such as magnet materials in fusion reactors. In these technological uses, the superconductors will be exposed to some kinds of irradiations below the transition temperature  $T_c$ . Therefore, both for the fundamental research of irradiation damage in high- $T_c$  superconductors, and for the technological data acquisition, performances of low-temperature irradiation experiment are necessary. So far, however, a few irradiation experiments have been performed at low temperatures.<sup>3,4)</sup> In this paper, we report the effects of 120 MeV  $^{16}\text{O}$ -ion irradiations at liquid nitrogen temperature on the superconducting properties of  $\text{YBa}_2\text{Cu}_3\text{O}_{7-x}$ .

The specimen used in the experiment was carefully prepared from aqueous solutions of Y-, Ba-, and Cu-nitrate in their appropriate ratios. The sheet-shaped specimen of  $10 \times 1 \times 0.1 \text{ mm}^3$  was cut from the disc for electrical resistance measurement. A standard four-probe method was used to measure the electrical resistance as a function of temperature. The measuring current density was about  $1.0 \text{ A/cm}^2$ . The accuracy of the electrical resistance measurement is  $10^{-4} \Omega$ . Before the irradiation, the electrical resistance of the specimen was measured up to 300 K. The irradiations of 120 MeV  $^{16}\text{O}$ -ions up to the fluence of  $1.6 \times 10^{15} / \text{cm}^2$  were performed at liquid nitrogen temperature. The intermediate measurements of electrical resistance up to 100 K were carried out several times, and after the irradiation to the fluence of  $1.6 \times 10^{15} / \text{cm}^2$ , the electrical resistance was measured up to 300 K. In all the electrical resistance measurements, the specimen temperatures were raised at a constant heating rate of about

1.5 deg/min. The specimen temperature during the irradiation was held at liquid nitrogen temperature.

Figure 1 shows the electrical resistance of the specimen before and after O-ion irradiation to the fluence of  $1.6 \times 10^{15} / \text{cm}^2$  as a function of temperature from 77.3 K to 300 K. The effects of O-ion irradiation appears as (1) a decrease of  $T_c$ , (2) an increase of electrical resistance above the transition, and (3) the anomalous temperature dependence of electrical resistance in higher temperature region. Figure 2 shows the electrical resistance of the specimen around  $T_c$  for several O-ion fluences. As can be seen in Fig.2, the temperature at which the resistance becomes zero decreases and the resistance above the transition increases monotonically with increasing the O-ion fluence. There is, however, very little change in the onset of the transition temperature. In this paper, therefore, we define the transition temperature  $T_c$  by the temperature at which the resistance becomes zero. Figure 3 shows the  $T_c$  and the electrical resistance at 100 K as a function of O-ion fluence. The decrease of  $T_c$  and the increase of the electrical resistance at 100 K tend to be saturated at higher ion-fluence. The decrease rate of  $T_c$  obtained from the initial several data points is about  $1.0 \text{ K} / 10^{14} \text{ O cm}^{-2}$ . This is to be compared with  $2.6 \text{ K} / 10^{18} \text{ n cm}^{-2}$  and  $3 \text{ K} / 10^{18} \text{ n cm}^{-2}$  for fission neutron irradiations.<sup>5,6</sup>

The behavior of electrical resistance in higher temperature region in the irradiated specimen is interesting, but there remains possibility that this behavior is caused by the instability of the electrodes of the specimen. Then, after warm up to 300 K, we cooled the specimen to liquid nitrogen temperature, and performed the resistance measurement up to 300 K again. After warm up to 300 K, the anomalous behavior of electrical resistance vanished. Therefore the above mentioned possibility can be discarded. In the present experiment, as the range of O-ions is smaller than the specimen thickness, the irradiating O-ions accumulate in the specimen. The number of accumulating ions are, however, much smaller than the number of O-atoms originally included in the specimen. Therefore, we can conclude that the behavior of electrical resistance in higher temperature region is the recovery of electrical resistance that is attributed to the thermally activated motions of irradiation-induced defects. Figure 4 shows that this resistance recovery leads to the recovery of  $T_c$  from 78 K to 81 K. In Fig. 5,  $\Delta R / \Delta R_0$  and the temperature derivative are plotted as a function of temperature for two measurements after

irradiations, where  $\Delta R$  the difference of the electrical resistances between before and after irradiation at a given temperature, and  $\Delta R_0$  the value of  $\Delta R$  at 100 K. The figure clearly shows that the main recovery of electrical resistance appears from  $\sim 160$  K, and that the recovery of about 30 % of irradiation-induced electrical resistance increment occurs during annealing up to 300 K.

Figure 6 shows the linear correlation between  $T_c$  and the electrical resistance at 100 K. The result after annealing up to 300 K lies on the same straight line. The similar correlation have been found in another irradiation experiment.<sup>3)</sup>

References

- 1) J. G. Bednorz and K. A. Muller, Z. Phys. B64, 189 (1986).
- 2) M. K. Wu, J. R. Ashburn, C. J. Torng, P. H. Hor, R. L. Meng, L. Gao, Z. J. Huang, Y. Q. Wang and C. W. Chu, Phys. Rev. Lett. 58, 908 (1987).
- 3) P. Muller, H. Gerstenberg, M. Fischer, W. Schindler, J. Strobel and G. Saemann-Ischenko, Solid State Comm. 65, 223 (1988).
- 4) K. Atobe and H. Yoshida, Phys. Rev. B36, 7194 (1987).
- 5) A. Umezawa, G. W. Grabtree, J. Z. Liu, H. W. Weber, W. K. Kwok, L. H. Nunez, T. J. Moran, C. H. Sowers and H. Claus, Phys. Rev. B36, 7157 (1987).
- 6) J. R. Cost, J. O. Willis, J. D. Thompson and D. E. Peterson, Phys. Rev. B37, 1567 (1988).

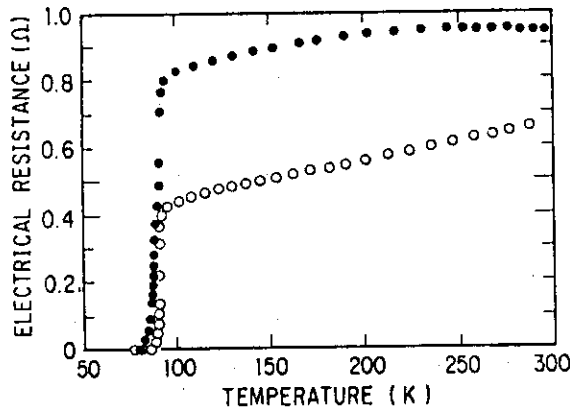


Fig.1 Electrical resistance of YBa<sub>2</sub>Cu<sub>3</sub>O<sub>7-x</sub> before irradiation (open circles) and after O-ion irradiation to the fluence of 1.6 × 10<sup>15</sup>/cm<sup>2</sup> (solid circles).

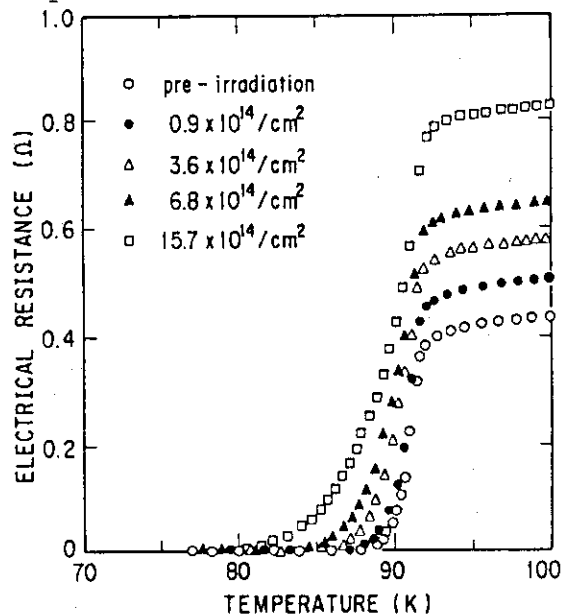


Fig.2 Electrical resistance of YBa<sub>2</sub>Cu<sub>3</sub>O<sub>7-x</sub> around T<sub>c</sub> for several O-ion fluences.

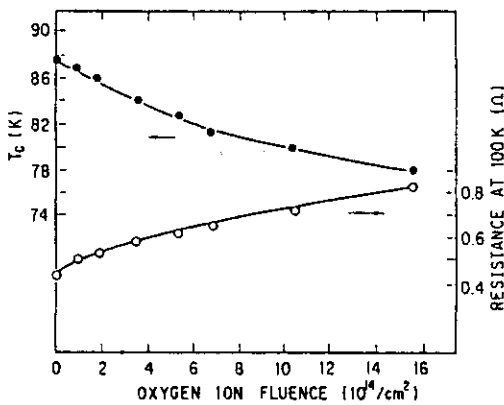


Fig.3 Dependence of  $T_c$  and electrical resistance at 100 K on O-ion fluence.

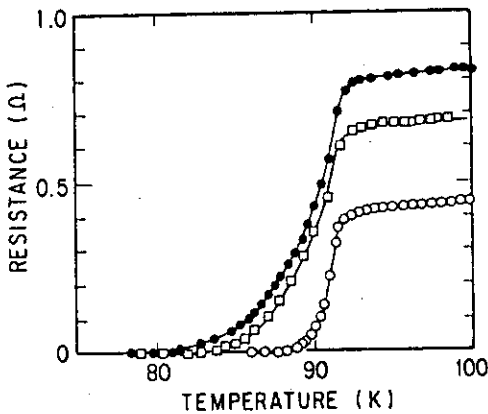


Fig.4 Electrical resistance of  $\text{YBa}_2\text{Cu}_3\text{O}_{7-x}$  around  $T_c$  before irradiation (open circles), after O-ion irradiation to the fluence of  $1.6 \times 10^{15}/\text{cm}^2$  (solid circles) and after subsequent warm-up to 300 K (open squares).

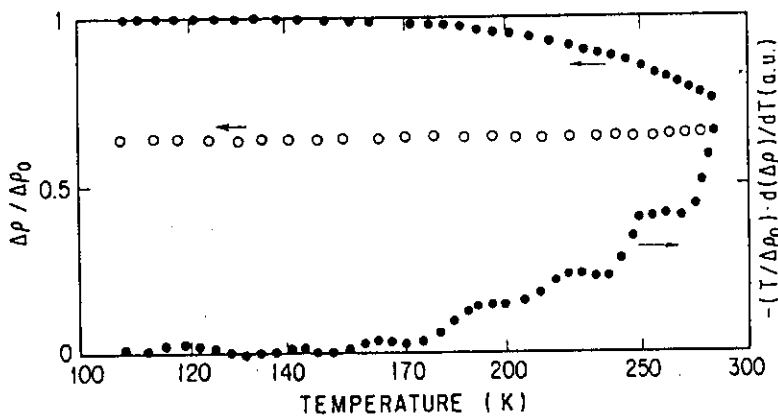


Fig.5 Resistance recovery curves and temperature derivative after O-ion irradiation to the fluence of  $1.6 \times 10^{15}/\text{cm}^2$  (solid circles) and after subsequent warm-up to 300 K (open circles).

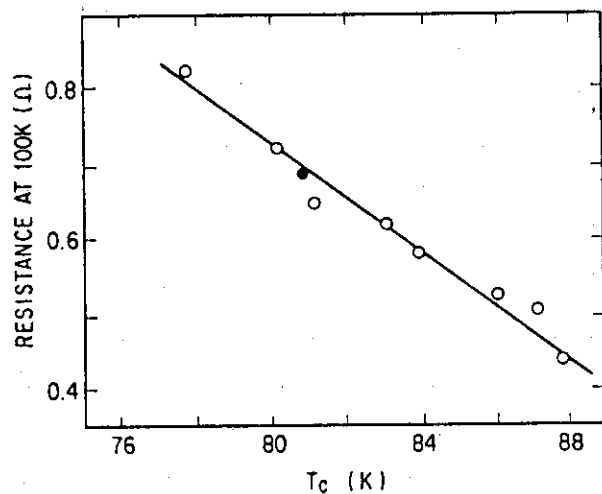


Fig.6 Correlation between  $T_c$  and electrical resistance at 100 K. Solid circle presents the result after warm-up to 300 K.

### 3.12 SURFACE ANALYSIS OF $\text{YBa}_2\text{Cu}_3\text{O}_x$ COMPOUND IRRADIATED WITH 100 MeV BROMINE IONS

Hiroshi NARAMOTO, Yukio KAZUMATA, Mitsuo WATANABE,  
Teruo KATO and Norio MASAKI

Department of Physics, JAERI

#### 1. Introduction

Since the discovery of high temperature superconductivity in oxygen-deficient perovskites<sup>1-2)</sup>, intensive studies have been made to understand their properties and to find out superconducting materials with higher transition temperatures. Along with these fundamental approaches, the trials to control the superconducting properties have started using ion beams<sup>3)</sup> and lasers<sup>4)</sup>. These energetic beams have a potential to modify physical properties of superconductors on a microstructural level. From this point of view, the ion-solid interactions and the radiation effects have become interesting themes even in such complicated compound as these superconductors.

In the present report, are shown briefly the results of surface analysis on  $\text{YBa}_2\text{Cu}_3\text{O}_x$  compound irradiated with 100 MeV bromine ions. The ion irradiation induces the highly insulating layer with the amorphous phase in the limited region of the pellet samples, associated with the compositional change.

#### 2. Experiment

The  $\text{YBa}_2\text{Cu}_3\text{O}_x$  samples were prepared by the standard method of reacting finely ground and thoroughly mixed stoichiometric quantities of  $\text{Y}_2\text{O}_3$ ,  $\text{BaCO}_3$  and  $\text{CuO}$  at 900 C in air. This material was pressed into a disk and sintered at 940 C under flowing oxygen gas and then cooled slowly to room temperature at the constant rate of 30/hr. Before ion irradiation, XDA (X ray Diffraction Analysis) was employed to confirm the formation of superconducting orthorhombic phase.

The sintered samples were irradiated at about 140 K with 100 MeV bromine ions from the JAERI tandem accelerator. The ion beam was scanned two-dimensionally for the uniform irradiation, and the samples received a total fluence of  $1 \times 10^{15}/\text{cm}^2$ . After irradiation, XDA was made both at the irradiated and the virgin surfaces at room temperature. SEM (Scanning

Electron Microscope) examination was also made on the irradiated surface. The sample was cleaved into platelets perpendicular to the surface, and the compositional change was examined along depth with EPMA (Electron Probe Micro-Analysis). For EPMA, crystal spectrometers were used especially to analyse oxygen atoms which play the important role in these compounds.

### 3. Results and discussion

Fig. 1 shows a typical feature of SEM examination on the surface of  $\text{YBa}_2\text{Cu}_3\text{O}_{7-x}$  compound irradiated with 100 MeV bromine ions to a fluence of  $1 \times 10^{15}/\text{cm}^2$ . The definite boundary is observed between the irradiated and virgin regions. The porous surface in the virgin region is turned into smooth one with the formation of blisters, which can be presumably attributed to oxygen gas decomposed through the intense ionization process during high energy ion irradiation. The irradiated surface is highly insulating, and the resistivity amounts to more than 10 Mega-ohms.

Fig. 2 illustrates the results of XDA from the same sample as in shown in Fig. 1. (a) is the x ray diffraction pattern from the unirradiated side of the sample, and most of the peaks originate from the superconducting orthorhombic crystal structure except the extra four peaks. These extra peaks are identified as the peaks from aluminium sample stage as can be seen in the pattern of (c). In the irradiated surface, every peak disappears except the extra peaks, and the formation of amorphous structure is confirmed as shown in (b).

Fig. 3 is a SEM micrograph of cross-sectional area in the irradiated side of the same sample as in Fig. 1. The irradiated layer runs up obliquely from left to right, and the formation of compact layer can be observed, different from the porous structure in the bulk region. The boundary between the observed layer and porous region is not diffused, which is not explained by the thermal effect on a bulk scale. The width of this layer is about 15  $\mu\text{m}$ , and is rather long compared with the projected range.

EPMA was made to determine the depth-distributions of constituent atoms and implants in the amorphous layer as observed in Fig. 3. Electron beam was linearly scanned perpendicular to the amorphous region. Fig. 4 illustrates the relative intensity-change of characteristic x rays from every relevant element as a function of depth. Thickness of the layer determined by SEM is about 15  $\mu\text{m}$ , and is denoted by an arrow in this figure. In the amorphous region, Cu and Ba atoms distribute uniformly along depth with almost no change of contents compared with those in the virgin region

(deeper than 15  $\mu\text{m}$ ). On the contrary, the large amount of decrease is induced for the O and Y atom contents. The distribution of O atom is gradually decreasing function along depth, and is influenced beyond the amorphous region. This feature of O atom distribution can be connected with the decomposition of constituent O atoms and the blister formation on the irradiated surface. The distribution of Y atom indicates the increasing tendency along depth. The signal from implanted Br atoms is so weak, and the x ray intensity detected beyond 15  $\mu\text{m}$  is from the back-ground noise. The Br distribution is a simply decreasing function, different from Bragg peak characteristic for implanted species, which is similar to the regrowth process from substrate after melting.

The present examination suggests a possibility of forming highly insulating region in the superconducting material in a controlled manner like ion beams. The amorphous layer obtained is compact and nonporous, and it may be possible to convert the layer into superconductor with high critical current without the influence of grain boundary.

#### References

- 1) D. Bednorz and K. A. Muller, Z. Phys. B64(1986)189.
- 2) M. K. Wu, J. R. Ashburn, C. J. Torng, P. H. Hor, R. L. Meng, L. Gao, Z. J. Huang, Y. Q. Wang, and C. W. Chu, Phys. Rev. Lett. 58(1987)908.
- 3) For example: G. J. Clark, A.D. Marwick, R. H. Koch, and R. B. Laibowitz, Appl. Phys. Lett. 51(1987)2687.
- 4) For example: K. Murakami, O. Eryu, K. Takita and K. Masuda, Jpn. J. Appl. Phy. 26(1987)93.

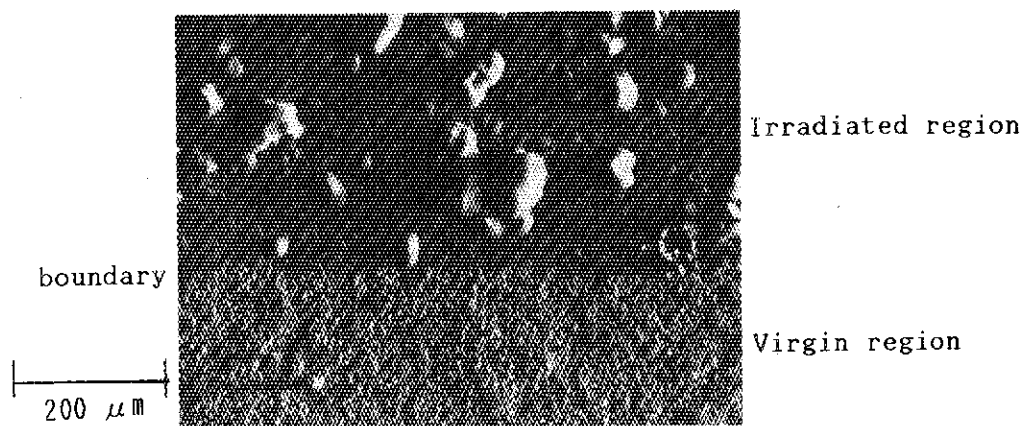


Fig. 1 SEM micrograph of YBa<sub>2</sub>Cu<sub>3</sub>O<sub>x</sub> pellet irradiated at LNT with 100 MeV Br ions to a fluence of  $1 \times 10^{15}/\text{cm}^2$ . Upper for the irradiated region and bottom for virgin one.



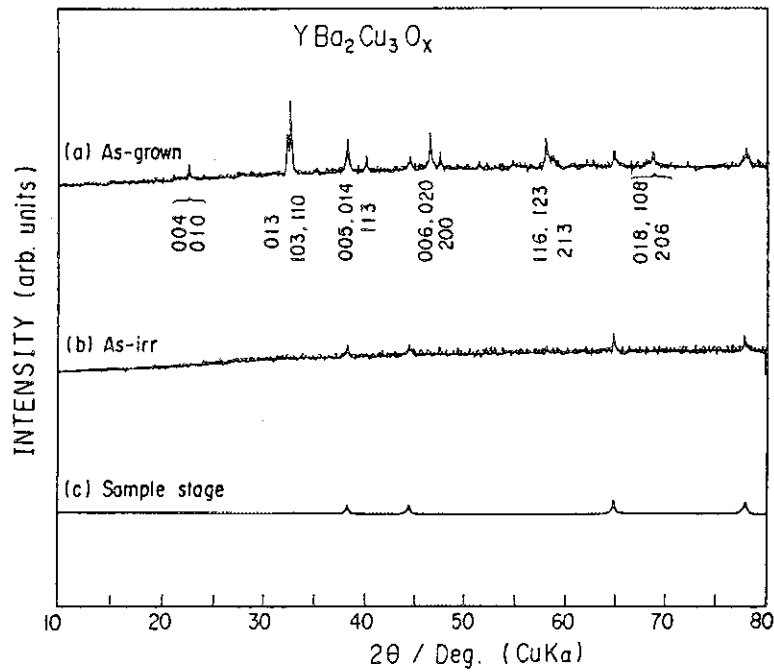


Fig. 2 Diffraction patterns of  $\text{CuK}\alpha$  x rays from a pellet irradiated with the same condition as in Fig. 1. (a), (b) and (c) are from as-grown, as-irradiated and sample stage regions.

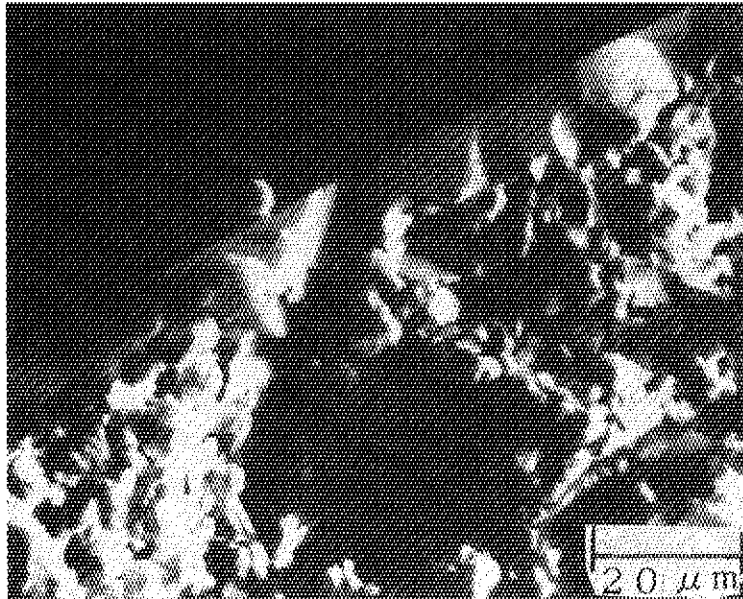


Fig. 3 SEM micrograph of cross-sectional area in a irradiated sample. The upper shiny layer corresponds to the irradiated side. Irradiation condition is the same as in the previous figures.

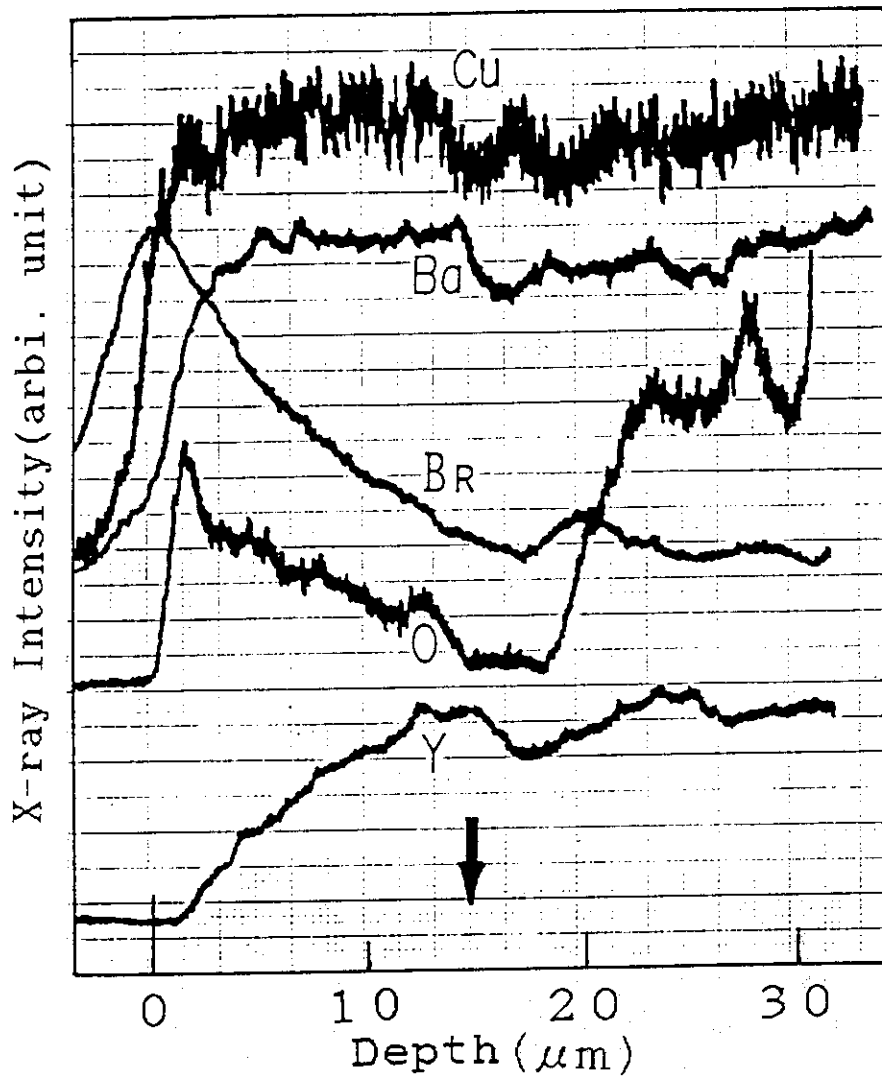


Fig. 4 Depth distributions of relevant constituent elements determined with EPMA. The arrow indicates the calculated projected range.

IV NUCLEAR CHEMISTRY

4.1  $^{12}\text{C}$  INDUCED FISSION OF  $^{233}\text{U}$ ,  $^{235}\text{U}$  AND  $^{238}\text{U}$ 

Sumiko BABA, Kentaro HATA, Yuichiro NAGAME,  
Ming-Jinn Duh\*, Naruto TAKAHASHI\*, Akihiko YOKOYAMA\*  
and Hiroshi BABA\*

Department of Radioisotopes, JAERI,\*Faculty of  
Science, Osaka University

A fundamental knowledge about nuclear fission mechanism can be obtained by the measurement of nuclear charge distribution of the fragments. In particular, the numbers of pre-fission neutron  $\nu_{\text{pre}}$  and post-fission neutron  $\nu_{\text{post}}$  are shown<sup>1)</sup> to be closely related to the charge distribution. They can be analyzed on the basis of the most probable charge  $Z_p$ . The charge distribution is rarely studied in the heavy-ion induced fission in contrast to fairly abundant data available in the light-ion induced fission in the neighborhood of uranium and plutonium. The purpose of the present work is firstly to study the charge distribution of heavier fissioning systems ( $Z \sim 100$ ) and secondly to investigate whether the heavy-ion induced fission is of somewhat different character from the light-ion induced fission as it seems to be the case considering the apparent distinction in the mass distribution for instance.

The most probable charge  $Z_p$  of a given product can be expressed as a function of the mass  $A_F$  and charge  $Z_F$  of the fissioning nucleus, the fragment mass  $A^*$ , and the excitation energy  $E_x$  given to the initial compound nucleus:

$$Z_p = Z_p(A_F, Z_F, A^*, E_x). \quad (1)$$

Among four terms one obtains when  $Z_p$  is differentiated with respect to  $E_x$ <sup>1)</sup>, the derivative  $dZ_p/dE_x$  is taken to be zero because evaporation of charged particles prior to fission can be neglected in the medium excitation. A partial derivative  $(\partial Z_p / \partial E_x)_{A_F, Z_F, A^*}$  can also be dropped since the most probable charge for a given primary fragment mass is expressed to remain constant against the energy change as long as one stays with the same fissioning nucleus. Considering that  $dA_F/dE_x = -d\nu_{\text{pre}}/dE_x$  and  $dA^*/dE_x = d\nu_{\text{post}}/dE_x$

(because  $Z_p$  is observed for a given secondary fragment), one obtains

$$\frac{dZ_p}{dE_x} = -\left(\frac{\partial Z_p}{\partial A_F}\right)_{Z_F, A^*, E_x} \frac{d\nu_{pre}}{dE_x} + \left(\frac{\partial Z_p}{\partial A^*}\right)_{A_F, Z_F, E_x} \frac{d\nu_{post}}{dE_x} \quad (2)$$

Knowing the three quantities  $dZ_p/dE_x$ ,  $(\partial Z/\partial A_F)_{Z_F, A^*, E_x}$  and  $(\partial Z_p/\partial A^*)_{A_F, Z_F, E_x}$  for at least two fissioning nuclei, one can find the energy dependences of the numbers of pre-fission and post-fission neutrons separately by introducing a relation governing the fission neutrons:

$$\nu_{total} = \nu_{pre} + \nu_{post} = E_x/\alpha + \nu_0. \quad (3)$$

Here,  $\alpha$  and  $\nu_0$  are constant numbers.

Three kinds of target were prepared by electrodeposition onto a 26.2  $\mu\text{m}$  Al foil. The thickness is about 1.0 mg/cm<sup>2</sup>. The targets were bombarded with 90 MeV <sup>12</sup>C from the tandem accelerator at JAERI. The incident energy was adjusted so as to give the same excitation energy for the three compound systems by the use of Al degraders with appropriate thicknesses. Targets were sandwiched with Al foils thick enough to catch fission products completely. The long and short bombardments of uranium target were carried out; one for 2 hr and the other for 30 min. After the bombardment the targets were subjected to the non-destructive measurement of  $\gamma$  rays. Antimony, tellurium and iodine were chemically separated from the target and other elements in separate runs. Obtained  $\gamma$ -ray spectra were analyzed to determine the radioactivities of observed nuclides.

In this experiment the cross-sections of fission products for masses between 80 and 151 were obtained. Isobaric triplets were observed for  $A = 132$  with all the targets and for  $A = 129$  with <sup>233</sup>U. Therefore, we could construct the charge dispersion curve to be given by

$$P_A(Z) = Y_A \exp\{-(Z - Z_p)^2/2\sigma^2\}, \quad (4)$$

where  $P_A(Z)$  is the fractional yield of the nuclide with charge  $Z$  in a given mass chain and  $2\sigma^2$  is the width parameter. The dispersion

curve for  $A = 132$  of  $^{238}\text{U}$  is shown in Fig.1 as an example. The deduced values are summarized in Table 1 from which the conclusion that  $\sigma = 1.05 \pm 0.05$  is drawn. The obtained values were significantly larger than that obtained for thermal-neutron induced fission ( $\sigma = 0.69$ ). The most probable charges  $Z_p$  were determined for several mass chains with observed yields of isobaric pairs using thus deduced width of the charge dispersion. The relationship between  $Z_p$  and fission product mass is shown in Fig.2. The values of  $(\partial Z_p / \partial A^*)_{A_F, Z_F, E_x}$  is obtained from the slope of a straight line constructed by plotting  $Z_p$  of a given observed fission system versus mass of the fragment  $A^*$  with a given excitation energy. Their values were the same (0.39) for the three fission systems and practically equal to those of the light-ion induced fission systems. The relationship between  $Z_p$  and compound mass  $A_c$  is shown in Fig.3, which is considered to be equivalent to the fissioning mass dependence. The values of  $(\partial Z_p / \partial A_F)_{Z_F, A^*, E_x}$  ranged between -0.15 and -0.09, which were again considered to lie within the same range of the values obtained in the case of the light-ion induced fission<sup>1)</sup>.

In the succeeding experiments we shall change the bombarding energy to get the remaining  $dZ_p/dE_x$  value and to deduce the neutron systematics for the heavy-ion induced fission in comparison with the thermal-neutron and light-ion induced fission.

#### Reference

- 1) H.Umezawa et. al., Nucl. Phys. A160 (1970) 65.

Table 1 The charge dispersion for  $A = 129$  and 132.

A	Charge dispersion ( $\sigma$ )		
	$^{238}\text{U}$	$^{235}\text{U}$	$^{233}\text{U}$
129			$1.00 \pm 0.05$
132	$0.9 \pm 0.1$ $1.0 \pm 0.1$	$1.10 \pm 0.05$ $1.1 \pm 0.1$	$1.10 \pm 0.05$ $1.10 \pm 0.05$

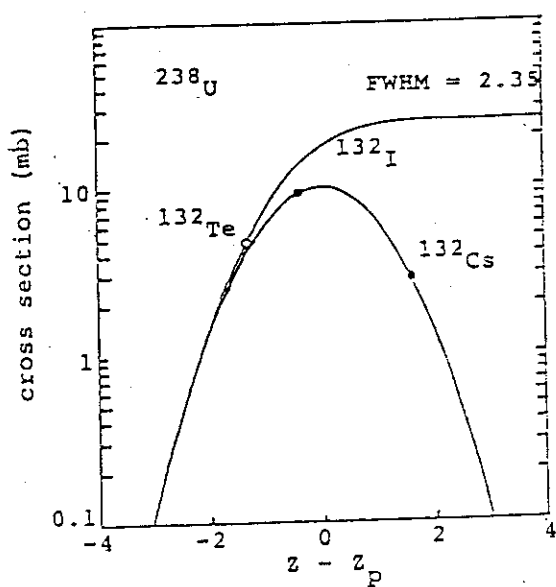


Fig. 1 The charge dispersion curve for  $A = 132$  of  $^{238}\text{U}$ .

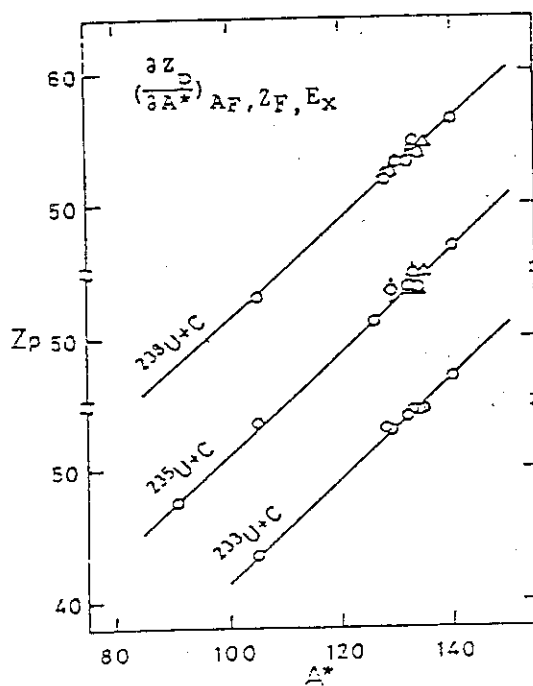


Fig. 2 The relationship between  $z_p$  and  $A^*$ .

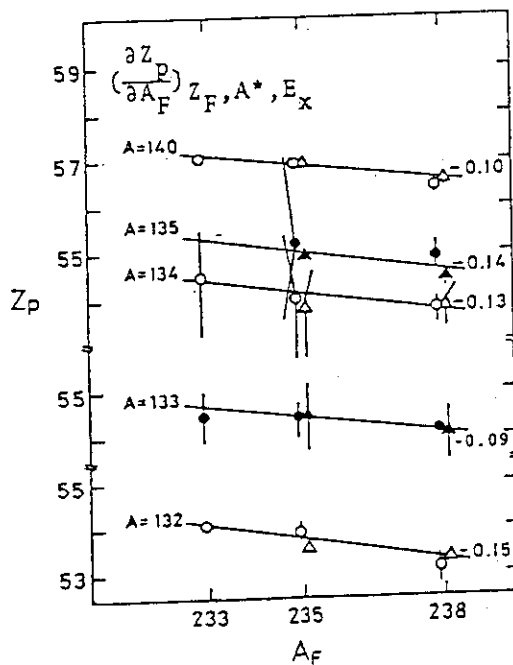


Fig. 3 The relationship between  $z_p$  and  $A_F$ .

4.2 COMPLEX FRAGMENT EMISSION FROM THE COMPOUND NUCLEUS  $^{105}\text{Ag}$ 

Yuichiro NAGAME, Sumiko BABA, Kentaro HATA, Toshiaki SEKINE,  
Hiroshi IKEZOE\*, Kazumi IDENO\*, Shin-ichi ICHIKAWA\*\*,  
Akihiko YOKOYAMA\*\*\* and Yuichi HATSUKAWA\*\*\*\*

Department of Radioisotopes, \*Department of Physics and  
\*\*Department of Chemistry, JAERI, \*\*\*Department of  
Chemistry, Osaka University, \*\*\*\*Department of Chemistry,  
Tokyo Metropolitan University

A generalized treatment of highly excited compound nucleus decay has been proposed by Moretto<sup>1)</sup>. This model predicts that particles of any mass can be emitted from the compound nucleus, that is, the complex fragments intermediate between light particles and symmetric fission fragments are produced in the decay of the compound nucleus. The decay widths for various mass divisions are mainly controlled by the potential energy of the conditional saddle at fixed mass asymmetry<sup>1)</sup>.

In order to study the influence of the angular momentum on this potential energy, we have measured the cross sections of the complex fragments produced in the heavy ion reaction  $^{37}\text{Cl}+^{68}\text{Zn}$ .

The experiments were performed at the JAERI tandem accelerator utilizing 166 MeV  $^{37}\text{Cl}$  beam to bombard a self-supporting enriched target of  $^{68}\text{Zn}$  ( $755 \mu\text{g}/\text{cm}^2$ ). The reaction products were identified with a  $\Delta E$ - $E$  counter telescope consisting of a gas  $\Delta E$  ionization chamber and a Si(Li) position sensitive  $E$  detector.

The complex fragments with  $Z=6$  to 29 have been measured. In the kinetic energy distributions for each fragment  $Z$ , the mean kinetic energies of the relaxed component roughly corresponded to the Coulomb repulsion energy between two touching spheres.

The angular distributions of the relaxed kinetic energy component for the products with  $Z \leq 10$  and  $Z \geq 20$  are essentially flat in  $d\sigma/d\theta_{\text{cm}}$  and the products with  $11 \leq Z \leq 19$  were also flat at the backward angles. These products with  $1/\sin\theta_{\text{cm}}$  angular distribution are considered to be either the products of a long-lived dinuclear system or the decay products from a compound nucleus.

Figure 1 shows the integrated cross section of each fragment  $Z$  over the



flat region in the angular distribution together with the cross sections given by a statistical model calculation<sup>2,3</sup>). As shown in Fig.1, one can see the substantial agreement between the data and the calculation. The results suggest that the lighter fragments ( $Z < 9$ ) are produced by asymmetric mass divisions, while the heavier fragments around  $Z_{CN}/2$  are favorably produced by symmetric mass divisions at higher angular momentum region in the compound nucleus  $^{105}\text{Ag}$ . For better understanding of the angular momentum dependence of the potential energy, measurements of the excitation functions for the complex fragments and of the widths of the mass distributions for the symmetric mass division products are in progress.

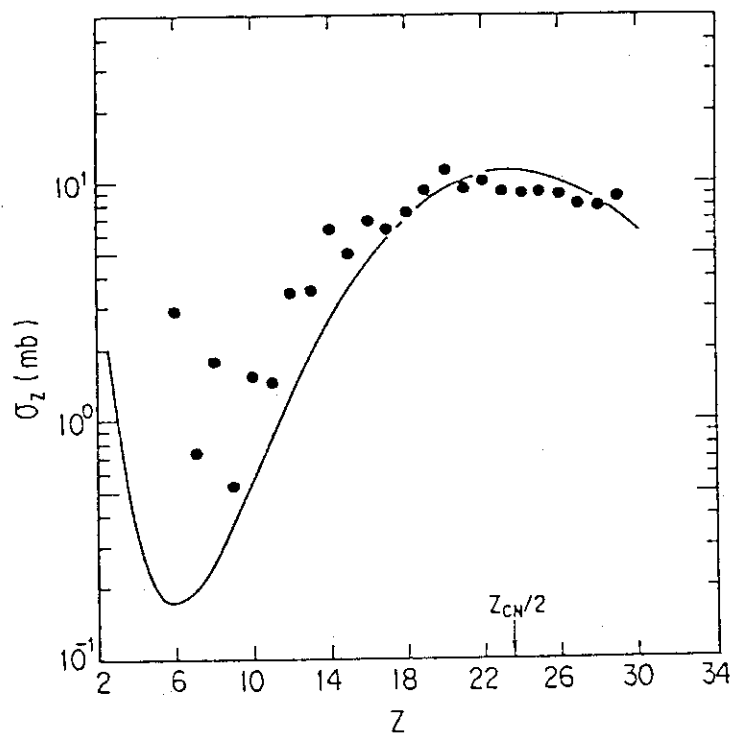


Fig.1 Integrated cross sections over the flat region in the angular distribution. The solid line is the result of the statistical model calculation.

#### References

- 1) L.G.Moretto, Nucl. Phys. A247(1975)211
- 2) L.G.Sobotka et al., Phys. Rev. Lett. 51(1983)2187 and 53(1984)2004
- 3) W.J.Swiatecki, Aust. J. Phys. 36(1983)641

Journal

Itahashi, T., Fukuda, T., Shimoda, T., Fujita, Y., Yamagata, T. and Nagame, Y.  
Mass Spectrometry of  $^{41}\text{Ca}$  with the RCNP Cyclotron  
Nucl. Instrum. & Methods B29(1987)151

Scientific Meetings

Nagame, Y., Magara, M., Hata, K., Ichikawa S., Sekine, T., Baba, S., Ideno, K.,  
Ikezoe, H., Yokoyama A. and Hatsukawa Y.  
Heavy Particle Emission Process In The  $^{37}\text{Cl}+^{68}\text{Zn}$  Heavy Ion Reaction  
The 31th Symposium on Radiochemistry in Fukuoka (Oct. 13-15, 1987)

T

Nagame, Y., Baba, S., Hata, K., Sekine, T., Ichikawa, S., Ikezoe, H., Ideno, K.,  
Yokoyama A. and Hatsukawa Y.  
Large Fragment Emission From The  $^{105}\text{Ag}$  Compound Nucleus  
Annual Meeting of Physical Society of Japan in Kohriyama (Mar. 31- Apr. 3,  
1988)

T

### 4.3 MASS DISTRIBUTIONS OF THE FISSION FRAGMENTS OF $^{233}\text{U}+p$ , $^{237}\text{Np}+p$ AND $^{239}\text{Pu}+p$

Tsutomu Ohtsuki, Keisuke Sueki, Yuichi Hatsukawa,  
Takayuki Kobayashi, Kazuaki Tsukada and Hiromichi Nakahara  
Yuichiro Nagame\* and Nobuo Shinohara\*\*

Department of chemistry, Faculty of Science, Tokyo  
Metropolitan University, \*Department of Radioisotopes, JAERI,

\*\*Department of Chemistry, JAERI

#### Introduction

Although many mass yield curves have been reported for thermal-neutron induced and spontaneous fissions, those for charged particle induced fissions are still scarce. Charged particle induced fissions (especially, proton induced fission and  $\alpha$ -particle induced fission among them) are suitable for the studies of the excitation energy dependence of mass yield curves.

In this work, we have investigated the proton induced fissions of  $^{233}\text{U}$ ,  $^{237}\text{Np}$  and  $^{239}\text{Pu}$ , and determined the mass yields of about thirty masses in the proton energy range of 9-16 MeV  $^{233}\text{U}+p$  and  $^{239}\text{Pu}+p$ , and in 9-32 MeV for  $^{237}\text{Np}+p$ . Shape of the mass yield curves and its excitation energy dependence are discussed mainly on  $^{237}\text{Np}+p$ .

#### Experimental Procedures and Data Analysis

The isotopic compositions of the enriched isotopes of  $^{233}\text{U}$ ,  $^{237}\text{Np}$  and  $^{239}\text{Pu}$  used as targets were found to be over 99% by the  $\alpha$ -spectrometry. They were purified from fission products by the anion exchange method with nitric acid-methanol and dissolved in isopropyl alcohol for electrodeposition on 7  $\text{mg}/\text{cm}^2$  Al foil under the condition of 500 V, 2mA/ $\text{cm}^2$  for 30 minutes with cooling. The efficiency of electrodeposition was over 80% for all these elements. Thickness of each target was determined by the  $\alpha$ -spectrometry to be 100-300  $\mu\text{g}/\text{cm}^2$ . Each target foil was wrapped in Al foil (6  $\text{mg}/\text{cm}^2$ ) thick enough to stop all fission products. And then, six to eight of the wrapped targets were stacked for proton bombardment. Several pieces of 10  $\text{mg}/\text{cm}^2$  Cu foil were inserted into the target stack at appropriate positions to monitor the beam current.

Bombardments were performed at the JAERI tandem accelerator with the

beam current of about  $1 \mu\text{A}$ .

After bombardment, the targets were left standing for about 30 minutes for cooling, and their  $\gamma$ -ray activities were measured directly with a Ge(Li) detector equipped with a 4098 channel pulse height analyzer. The produced nuclides were identified through their characteristic  $\gamma$ -ray energies, and their formation cross sections were evaluated from the observed photo-peak areas and the beam current determined with the Cu-monitor. The reaction cross section data reported by Colle et al.<sup>1)</sup> for protons on Cu were used. The incident proton energy on each target was estimated from the range energy relations reported by C. F. Williamson et al.<sup>2)</sup> and L. C. Northcliffe et al.<sup>3)</sup>.

### Results and Discussion

Mass yields were obtained from the observed cross section of each fission product, for which correction was made, if necessary, for charge distribution assuming a gaussian charge distribution curve with the most probable charge  $Z_p$  of the unchanged charge distribution model. The gaussian width parameter of 0.95 was used as suggested by J. A. McHugh et al.<sup>4)</sup>. The correction was large for  $^{127}\text{Sb}$ ,  $^{129}\text{Sb}$ ,  $^{132}\text{Te}$  and  $^{135}\text{Xe}$ . The mass yield curves of  $^{237}\text{Np}+p$  thus obtained are shown in Figure 1. All mass yield curves were asymmetric as expected. The figure shows that the valley (symmetric region) has a strong energy dependence in comparison with the peak through the outer sides (asymmetric region) of the mass yield curves.

The mass yield curves for  $^{232}\text{Th}+p$ <sup>5)</sup> has been reported to have a broad valley in the symmetric region, but the present results on  $^{233}\text{U}+p$ ,  $^{237}\text{Np}+p$  and  $^{239}\text{Pu}+p$  reveal that the width of the valley becomes narrower as the fissioning mass  $A_f$  becomes heavier. The weighted mean mass of the heavy asymmetric peak varies very slightly over a broad mass range of fissioning nuclide  $A_f$ , whereas that of the light mass peak increases substantially with increasing  $A_f$ . A similar tendency has been also observed for thermal-neutron induced and spontaneous fissions<sup>6)</sup>.

For clear depiction of the incident energy dependence, cross section ratios of several fission products are shown as a function of the incident proton energy in Figure 2. The yield ratios of some of the typical asymmetric mass division products are independent of the incident proton energy as well as those of the symmetric ones. On the other hand, the yield ratios of asymmetric to symmetric products are strongly dependent on the incident

energy. These observations suggest the existence of two distinctly different threshold energies, one for the symmetric and the other for the asymmetric. The products with mass around 112 and mass 126 through 131 seem to have an intermediate energy dependence, and hence it is still an open question whether they belong to symmetric or asymmetric, or rather independent.

#### References

- 1) R. Colle, R. Kishore, and J. B. Cumming, Phys. Rev. C9, (1974)1819.
- 2) C. F. Williamson, J.P. Boujot, and J. Picard, Centre d'Etudes Nucleaires de Saclay Report CEA-R3042, (1966) unpublished.
- 3) L. C. Northcliffe and R. F. Schilling, Nucl. Data A7, (1970)233.
- 4) J. A. MuHugh and M. C. Michel, Phys. Rev. 172, (1968)1160.
- 5) H. Kudo, H. Muramatsu, and H. Nakahara et al. Phys. Rev. C25, (1982)3011.
- 6) H. R. Von Gunten, Actinides Rev. 1, (1969)275.

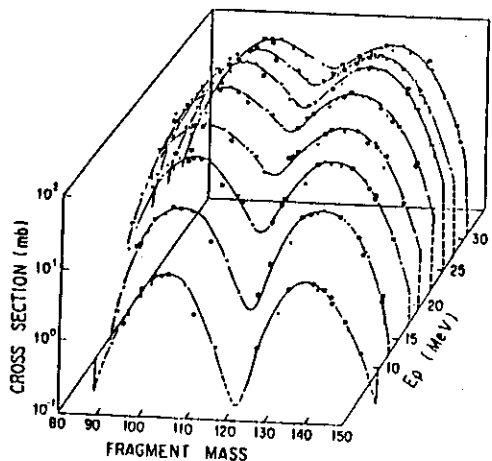


Fig. 1 Mass yield curves measured in proton-induced fission of  $^{237}\text{Np}+p$ .

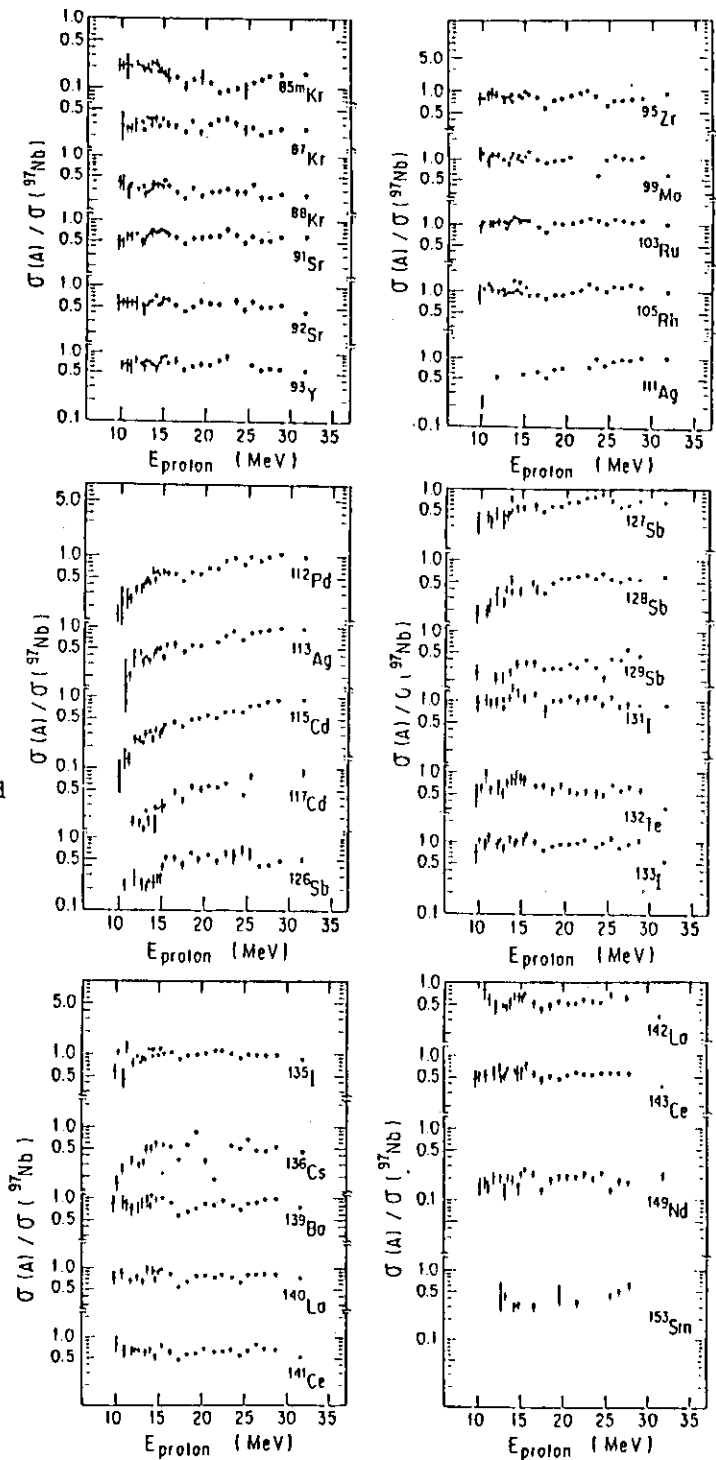


Fig. 2 Cross section ratios  $\sigma(A)/\sigma(^{97}\text{Nb})$  as a function of the incident proton energy.

#### 4.4 EXCITATION FUNCTIONS OF $^{95}\text{Mo}(p,n)$ REACTION FOR THE PRODUCTION OF $^{95m}\text{Tc}$

Mishiroku IZUMO, Takami SORITA, Hiromitsu MATSUOKA, Sumiko BABA, Yuichiro NAGAME and Kentaro HATA

Department of Radioisotopes, JAERI

$^{95m}\text{Tc}$  have relatively longer half-life(61 d) and abundant  $\gamma$ -rays of 204, 582, 835 and 1039 keV. Therefore, it is useful as the tracer for studying the behavior of technetium isotopes in natural environment and for developing new labeled compounds of  $^{99m}\text{Tc}$ (6.02 h) radio-pharmaceuticals. Presently,  $^{95m}\text{Tc}$  is mainly produced by the  $^{\text{nat}}\text{Mo}(p,xn)$  and  $^{93}\text{Nb}(\alpha,2n)$  reactions. The  $^{95}\text{Mo}(p,n)^{95m}\text{Tc}$  reaction on an enriched target would provide the isotope of high purity. Therefore, we have measured the excitation functions for the reactions

$^{95}\text{Mo}(p,n)^{95m}\text{Tc}$  studying the production conditions.

Enriched  $^{95}\text{Mo}$  powder of isotopic abundance 96.47%, obtained from ORNL, was used as target. The powder was suspended in 1% potassium iodide solution and was deposited on aluminum foil(5 mg/cm<sup>2</sup>) by electro-deposition method to prepare thin(2 mg/cm<sup>2</sup>) and heat-stable target.

Stacked-foil technique was applied to measure the excitation functions. In addition to the target foils and Al foils(28 - 128 mg/cm<sup>2</sup>) used as beam-energy degrader, thin copper foils(8 mg/cm<sup>2</sup>) were inserted to monitor energy and intensity of the beam. In the Cu foils,  $^{65}\text{Zn}$  is produced via the  $^{65}\text{Cu}(p,n)$  reaction, for which the excitation function is accurately known<sup>1,2</sup>). Stopping powers of the foils in the stack for protons were calculated using the computer code OSCAR<sup>3</sup>).

The proton bombardments were performed at the JAERI tandem accelerator with an incident energy of 30 MeV. After bombardments, the radioactivities of Tc isotopes in each target-catcher pair were measured by a Ge(Li) detector, the

efficiency of which was calibrated with standard  $\gamma$ -ray sources. The decay of the main  $\gamma$ -rays was followed to establish the half-lives involved and to confirm the identity of the radionuclides.

The measured excitation functions are given in Figure 1. The formation cross sections of  $^{95m}\text{Tc}$  at energies less than 5 MeV were not obtained accurately in the present work. The supplemental work is in progress.

#### References

- 1) R. Colle, R. Kishore and J. B. Cumming: Phys. Rev. C 9  
(1974) 1819.
- 2) F. E. Little and M. C. Lagunas-Solar: Int. J. Appl. Radiat.  
Isot. 34  
(1983) 631
- 3) K. Hata and H. Baba: INDC(NDS)-195/GZ (1988)



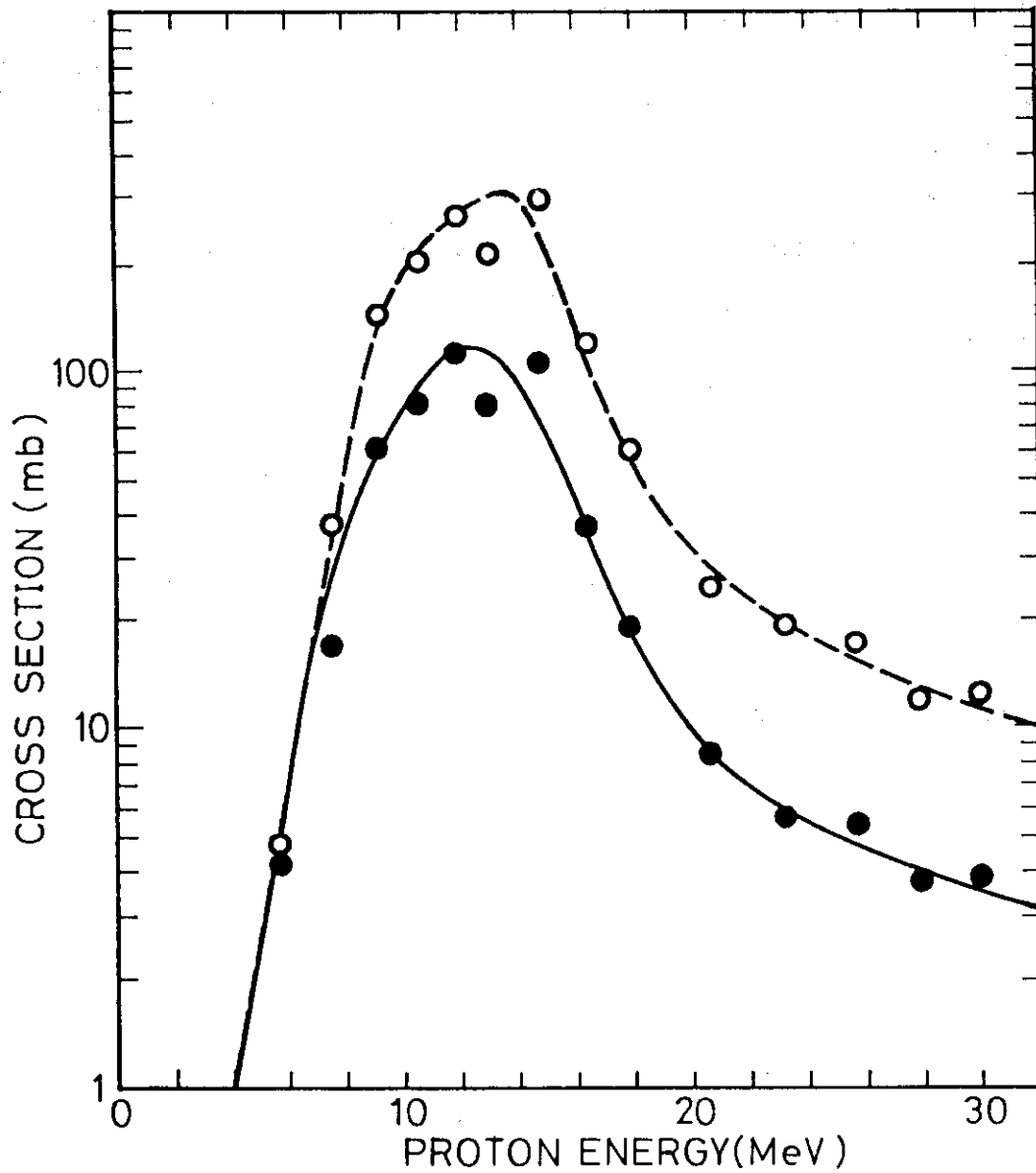


Fig.1. Measured excitation functions for the  $^{95}\text{Mo}(p,n)^{95\text{m}}\text{Tc}$  (closed circles) and  $^{95}\text{qTc}$  (open circles). The curves are drawn to guide the eye.

#### 4.5 Identification of A New Isotope of $^{121}\text{La}$ by Means of Element-Selective Mass Separation

Toshiaki Sekine, Shin-ichi Ichikawa\*, Masumi Oshima\*\*,  
Hideki Iimura\*, Yuichiro Nagame, Kentaro Hata,  
Naruto Takahashi\*\*\* and Akihiko Yokoyama\*\*\*

Department of Radioisotopes, \*Department of Chemistry, \*\*Department of Physics, Japan Atomic Energy Research Institute and \*\*\*Faculty of Science, Osaka University

The isotope  $^{121}\text{La}$ , which is far from the  $\beta$ -stability line and is predicted to lie beyond the proton-drip line<sup>1)</sup>, has been searched for, using an isotope separator on-line to the tandem accelerator of JAERI. In this study a new ion-source technique<sup>2)</sup> which strengthens elemental selectivity in on-line isotope separation was applied.

In the bombardment of an enriched  $^{92}\text{Mo}$  target (3.06 mg/cm<sup>2</sup>) with a 4.7-MeV/u  $^{32}\text{S}$  beam (50 particle nA), La isotopes were produced through (HI,lpxn) channels and ionized in a thermal ion source as the  $\text{LaO}^+$  species rather than as the  $\text{La}^+$  species.<sup>2)</sup> Since Cs and Ba, which are effectively ionized into a metallic ion, were not obtained as a monoxide ion, the Cs and Ba isobars of a La isotope did not come into the  $\text{LaO}^+$  fraction after mass separation. For other elements, we consider that the Ce isobar may be included in the  $\text{LaO}^+$  fraction, because Ce is also obtainable as the species  $\text{CeO}^+$ .<sup>2)</sup> In the nuclear reaction used, however,  $^{121}\text{Ce}$  is expected to be produced in much smaller amount than  $^{121}\text{La}$ : ALICE code<sup>3)</sup> predicts the production cross sections to be 8 mb for  $^{121}\text{La}$  and 0.07 mb for  $^{121}\text{Ce}$ .

After mass separation, we performed  $\gamma$ -singles, X/ $\gamma$ - $\gamma$  coincidence and  $\beta$ - $\gamma$  coincidence measurements, using a tape transport system. For the A=137 ( $^{121}\text{La}^{160+}$ ) fraction, Fig. 1 shows the  $\beta$ -coincident  $\gamma$ -ray spectra observed during a counting period of 12 h; for comparison a spectrum that was previously obtained at A=121 in the bombardment of a Mo target is shown.<sup>4)</sup> In the A=137 spectra, one can notice several  $\gamma$  lines which are much shorter-lived than those of  $^{121}\text{Ba}$  ( $T_{1/2}=30$  s) and  $^{121\text{m},9}\text{Cs}$  ( $T_{1/2}=121$  s, 136 s). As seen from Fig.2, the short-lived activity decays with a half-life of  $5.3\pm 0.2$  s, while the  $\gamma$  lines of

$^{121}\text{Ba}$  and  $^{121\text{m}}\text{Ba}$  show a growth and decay pattern; it appears that the observed time spectra of  $^{121}\text{Ba}$  and  $^{121}\text{Cs}$  are in agreement with the calculated ones to be observed when they are the daughter and the granddaughter, respectively, of the 5.3-s activity. This suggests that the 5.3-s activity is assigned to the decay of  $^{121}\text{La}$  as a precursor of  $^{121}\text{Ba}$ .

The results of the X/ $\gamma$ - $\gamma$  coincidence measurement eliminated the possibility of  $^{121}\text{Ce}$  as the 5.3-s activity and supported the foregoing assignment: Some of the short-lived  $\gamma$  lines proved to coincide with Ba X-rays which are emitted in an electron-capture decay of  $^{121}\text{La}$  or in an internal conversion process associated with a transition in  $^{121}\text{Ba}$ , that is, the daughter of  $^{121}\text{La}$ . From these arguments we have assigned the observed 5.3-s activity to the  $^{121}\text{La}$  decay.

On the basis of the results of the  $\gamma$ - $\gamma$  coincidence measurement, a partial decay scheme of  $^{121}\text{La}$  has been constructed, as shown in Fig.3. For the ground state of  $^{121}\text{Ba}$ , we took the spin and parity  $5/2^+$  given by Eastham et al.<sup>5)</sup> from the laser spectroscopy.

Takahashi et al.<sup>6)</sup> have predicted half-lives of nuclei on the basis of the gross theory of  $\beta$  decay. Their theoretical half-life 5 s for  $^{121}\text{La}$  is in good agreement with our experimental value.

#### References

- 1) M. Beiner and R.J. Lombard, At. Nucl. Data. Tables 17 (1976) 450.
- 2) S. Ichikawa, H. Iimura, M. Oshima, T. Sekine and N. Takahashi, Nucl. Instr. Meth. A., in press.
- 3) M. Blann and J. Bisplinghoff, COO-3494-27 (1975).
- 4) S. Ichikawa, T. Sekine, K. Hata, N. Shinohara and N. Takahashi, JAERI-M 85-104 (1985) 139.
- 5) D.A. Eastham, J.R.H. Smith, J. Groves, D.D. Warner, D.W.L. Tolfree, S.A. Wells, J.A.R. Griffith, D.E. Evance, M.J. Fawcett, I.S. Grant, J. Billowes and P.M. Walker, Proc. Int. Conf. on Nuclei Far From Stability, Lake Rosseau, Canada, Sep. 14, 1987, p.136.
- 6) K. Takahashi, M. Yamada and T. Kondoh, At. Nucl. Data. Tables 12 (1973) 101.

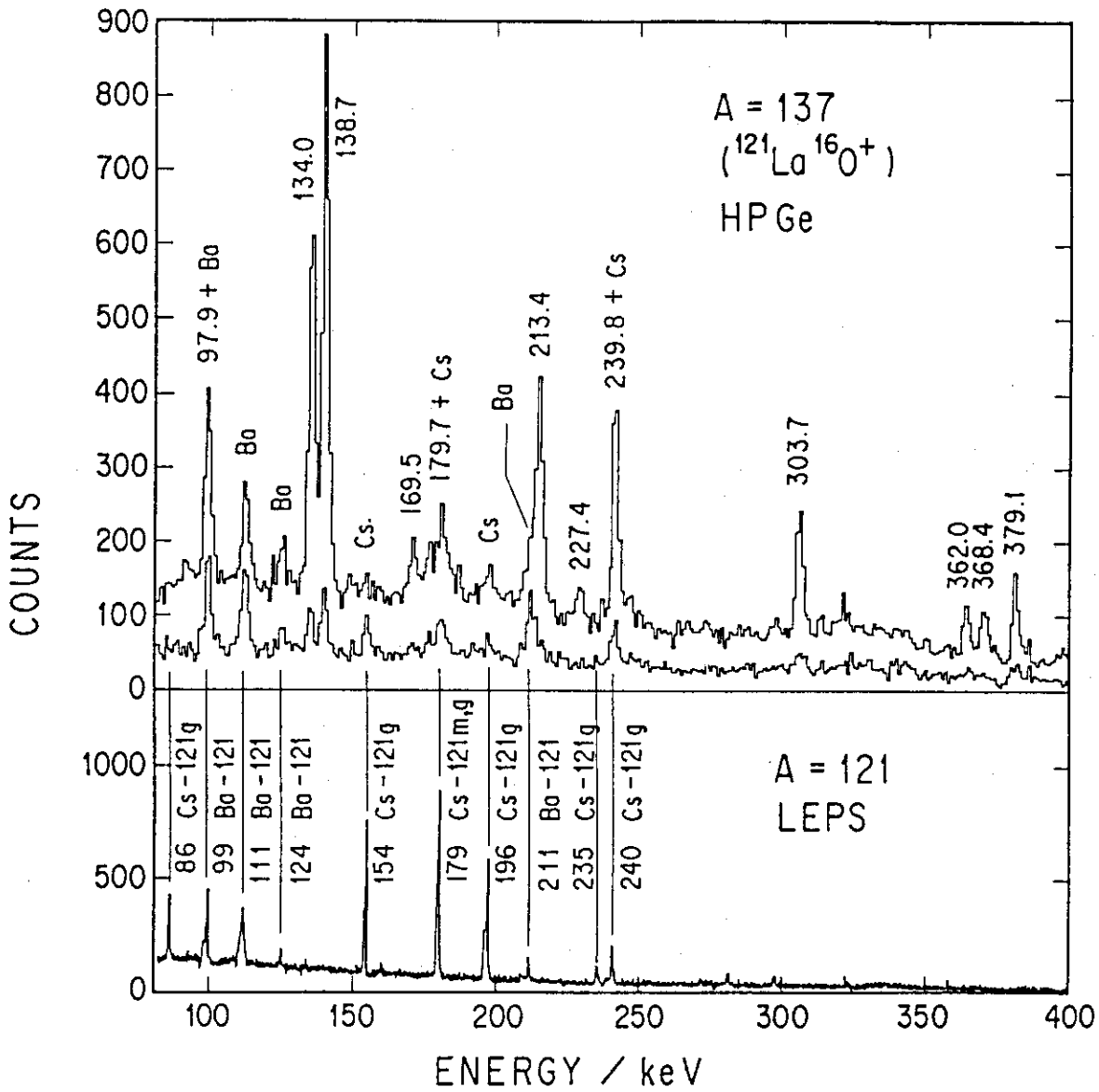


Fig.1  $\beta$ -coincident  $\gamma$ -ray spectra for the A=137 ( $^{121}\text{La}^{16}\text{O}^+$ ) (upper part) in comparison with the A=121 spectrum (lower part) of  $^{121}\text{m,gCs}$  and  $^{121}\text{Ba}$  previously obtained<sup>4)</sup> with a low-energy-photon spectrometer. At the upper part are shown the spectra observed in the first and the last 6 s of the 24-s counting period after the 24-s collection and 1-s tape transportation; peaks marked by their energy (in keV) are assigned to the decay of  $^{121}\text{La}$ .

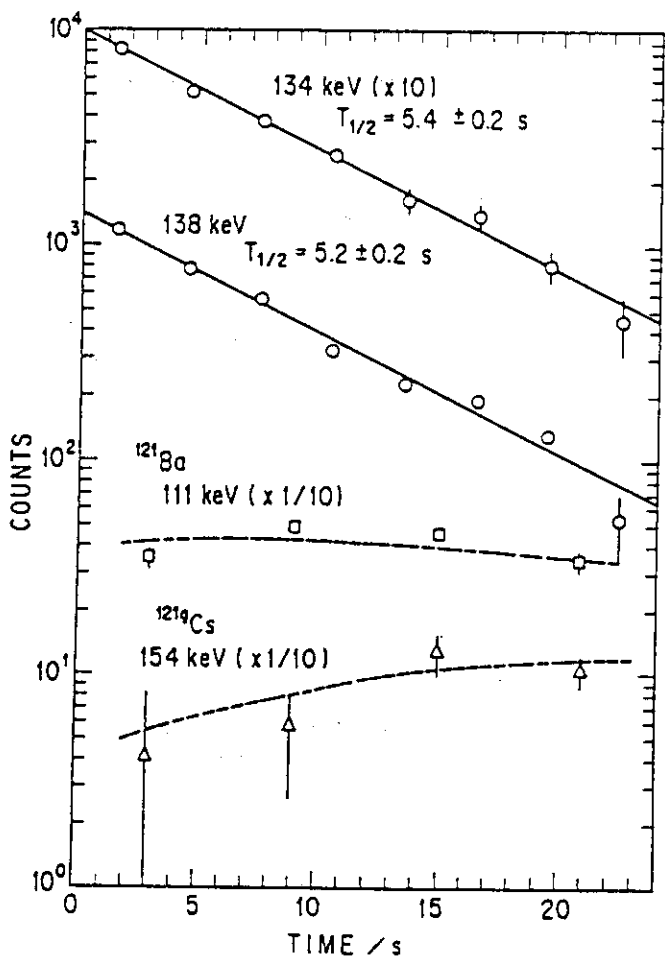


Fig.2 Time spectra of  $\gamma$  lines obtained in the A=137 fraction, using the same data set as for Fig. 1. Broken lines show the calculated time spectra of  $^{121}\text{Ba}$  and  $^{121}\text{Cs}$  to be observed as a daughter and a granddaughter, respectively, of the 5.3-s activity.

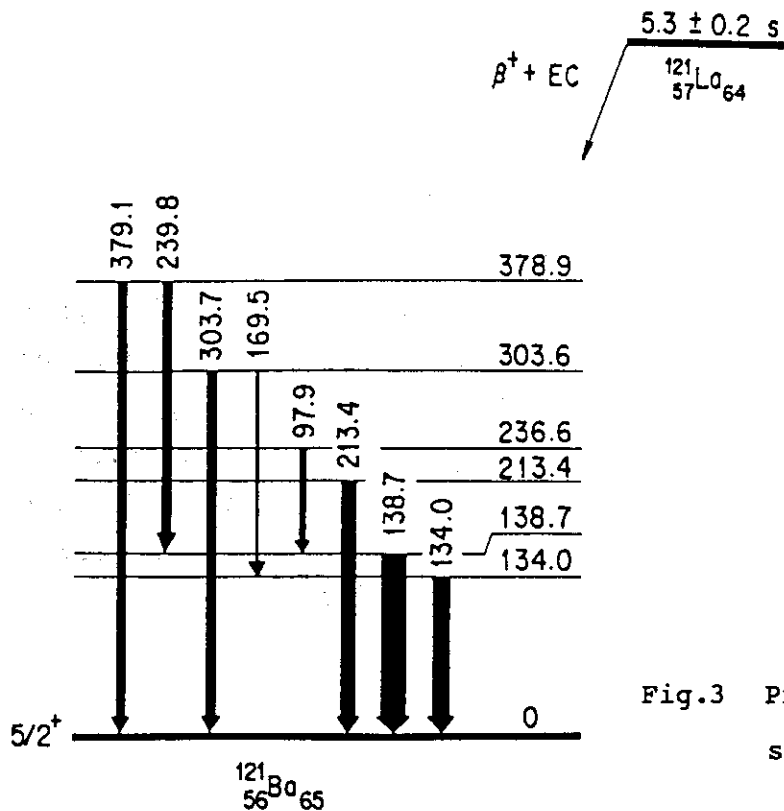


Fig.3 Proposed partial decay scheme of  $^{121}\text{La}$

#### 4.6 Decays of $^{122,124,126}\text{La}$ and $^{128,130}\text{Pr}$ and Properties of the Low-Lying States of Their Daughter Nuclei

Toshiaki Sekine, Hideki Iimura\*, Shin-ichi Ichikawa\*,  
Masumi Oshima\*\*, Kentaro Hata, Yuichiro Nagame,  
Naruto Takahashi\*\*\* and Akihiko Yokoyama\*\*\*

Department of Radioisotopes, \*Department of Chemistry, \*\*Department of Physics, Japan Atomic Energy Research Institute and \*\*\*Faculty of Science, Osaka University

Decays of  $^{122,124,126}\text{La}$  and  $^{128,130}\text{Pr}$  have been studied by means of a combination of heavy-ion reaction and isotope separation on line (ISOL). In this study, we took advantage of an ion-source technique<sup>1)</sup> which uses monoxide-ion formation in a thermal ion source to strengthen elemental selectivity in ISOL for light lanthanoids. In addition to the half-lives and decay schemes of these nuclei, the experimental results gave information on electromagnetic transitions of the low-lying states in their even-even daughter nuclei. These results are compared with the prediction by Puddu et al.<sup>1)</sup> based on the interacting boson model.<sup>2)</sup>

A Mo target ( $4.1 \text{ mg/cm}^2$ ) and a Rh target ( $3.8 \text{ mg/cm}^2$ ) were bombarded with  $^{32}\text{S}$  beams ( $5.0\text{--}6.2 \text{ MeV/u}$ ) to produce neutron deficient isotopes of La and Pr, respectively. As described in Ref.1, La isotopes were mass-separated as  $\text{La}^{160+}$ , being well separated from the Cs and Ba isobars. On the other hand, Pr isotopes were mass-separated as  $\text{Pr}^+$ , because the Ce and La isobars were ionized in a monoxide ion rather than in a metallic ion. Consequently, mass separation was done for the masses 138 ( $^{122}\text{La}^{160+}$ ), 140 ( $^{124}\text{La}^{160+}$ ), 142 ( $^{126}\text{La}^{160+}$ ), 128 and 130. For the mass-separated samples, measurements of  $\gamma$ -singles,  $\gamma$ - $\gamma$  coincidence and  $\beta$ - $\gamma$  coincidence were carried out, using a tape-transport system.

From the  $\gamma$ -ray data, we determined the half-lives of  $^{122,124,126}\text{La}$  and  $^{128,130}\text{Pr}$ , and constructed their decay schemes. The half-lives and the estimated spin-parity values are listed in Table 1 together with the previously-reported ones. The half-lives obtained are more precise in most cases than the previous values. As to the half-life

of  $^{128}\text{Pr}$ , two different values were reported; our experimental value is in agreement with that reported by Bogdanov et al.

In the decay schemes obtained, the levels in the  $\gamma$  band are populated as well as those in the ground band. In addition, populations in the negative parity band were also seen in the decays of  $^{124}\text{La}$  and  $^{126}\text{La}$ . Further, in the decay of  $^{122}\text{La}$ , the  $\gamma$ -band head ( $2_2^+$  level) in  $^{122}\text{Ba}$  was newly identified with a level energy of 940 keV. This energy value is found to be very close to that predicted with IBM.<sup>2)</sup>

From the  $\gamma$ -ray data, we have obtained the branching ratios of electromagnetic transition from  $2_2^+$ ,  $3_1^+$  and  $4_2^+$  states in  $^{122}, ^{124}, ^{126}\text{Ba}$  and  $^{130}\text{Ce}$ . The experimental branching ratios were found to be in good agreement with the theoretical branching ratios calculated with IBM.<sup>2)</sup> Assuming that the observed transitions  $2_2^+ \rightarrow 0_1^+$  and  $2_2^+ \rightarrow 2_1^+$  are a pure E2 transition, we plotted the experimental and the theoretical ratios  $B(E2; 2_2^+ \rightarrow 0_1^+) / B(E2; 2_2^+ \rightarrow 2_1^+)$  in Fig.1. This figure shows that the experimental results support the predicted changes in the structure of the isotopic chains Ba and Ce in addition to Xe.<sup>1,2)</sup>

The authors wish to thank Dr. T. Otsuka of University of Tokyo for supplying us the results of his calculation.

#### References

- 1) S. Ichikawa, H. Iimura, M. Oshima, T. Sekine and N. Takahashi, Nucl. Instr. Meth. A., in press.
- 2) G. Puddu, O. Scholten and T. Otsuka, Nucl. Phys. A348 (1980) 109.
- 3) F. Iachello and A. Arima, "The Interacting Boson Model," Cambridge Univ. Press, Cambridge (1987).

Table 1  
Half-lives and spin-parity values

Nuclide	Present work		Previous work	
	$T_{1/2}$ (s)	$I^\pi$	$T_{1/2}$ (s)	$I^\pi$
$^{122}\text{La}$	$9.6 \pm 1.0$	(3 <sup>+</sup> )	$8.7 \pm 0.7^{\text{a}}$	
$^{124}\text{La}$	$29 \pm 2$	(7)	$29 \pm 3^{\text{b}}$	(6,7) <sup>c)</sup>
$^{126}\text{La}$	$54 \pm 2$	(4)	$60 \pm 18^{\text{d}}$	
$^{128}\text{Pr}$	$2.7 \pm 0.4$	(3 <sup>+</sup> )	$3.2 \pm 0.5^{\text{e}}$	
$^{130}\text{Pr}$	$31 \pm 2$	(4)	$28 \pm 6^{\text{f}}$ $44 \pm 4^{\text{g}}$	

- a) J. M. Nitschke et al., Z. Phys. A316 (1984) 249.
- b) D. D. Bogdanov et al., Nucl. Phys. A307 (1978) 421.
- c) K. Furuno et al., J. Phys. Soc. Japan 56 (1987) 1905.
- d) I. L. Preiss et al., Phys. Rev. 129 (1963) 1284.
- e) P. A. Wilmarth et al., Z. Phys. A321 (1985) 179.
- f) D. D. Bogdanov et al., Nucl. Phys. A275 (1977) 229.
- g) M. Korfelahti et al., Z. Phys. A327 (1987) 231.

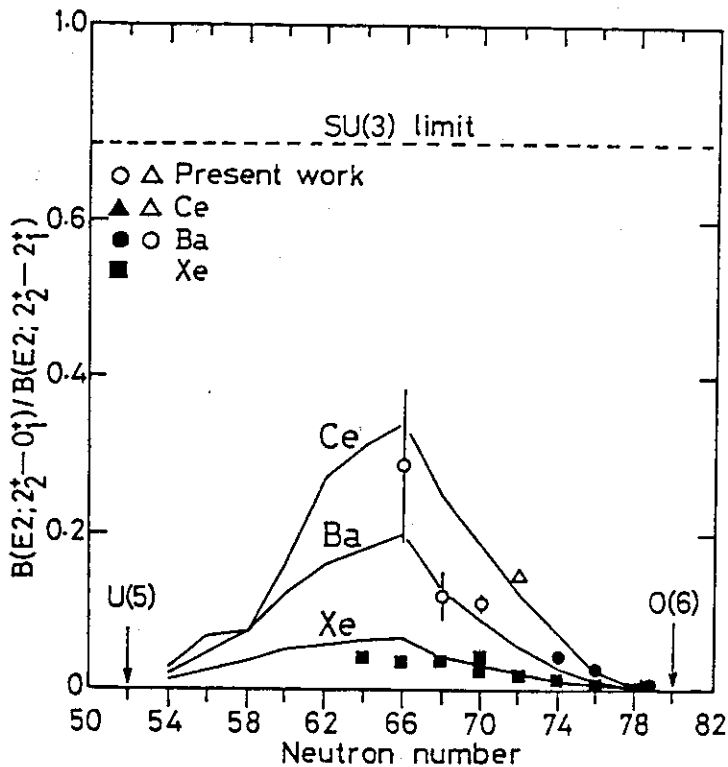


Fig. 1. Comparison between experimental and calculated values of the ratio  $B(E2; 2_2^+ \rightarrow 0_1^+) / B(E2; 2_2^+ \rightarrow 2_1^+)$  in Xe, Ba and Ce. The lines are the calculated values taken from ref. 3) and the solid symbols are the previous experimental values cited in the same reference.



#### 4.7 ISOLATION OF SHORT-LIVED NUCLIDES WITH A HELIUM-JET RECOIL-TRANSPORT SYSTEM AND SISAK

Nobuo SHINOHARA, Shin-ichi ICHIKAWA, Hideki IIMURA,  
 Yoshinori NAKAHARA, Toshio SUZUKI, Shigekazu USUDA,  
 Masaaki MAGARA, Yoshii KOBAYASHI, Akihiko YOKOYAMA\*,  
 Yuichi HATSUKAWA\*\*, Seiichi SHIBATA\*\* and Ichiro FUJIWARA\*\*\*

Department of Chemistry, JAERI,

\* Department of Chemistry, Osaka University,

\*\* Institute for Nuclear Study, University of Tokyo and

\*\*\* School of Economics, Otemon Gakuin University

An on-line chemical separation system has been developed for the purpose of investigating short-lived actinide nuclides. In our previous study, it was found that the transport efficiencies of the fission products differed apparently from that of the evaporation residues produced by the heavy-ion irradiations in the helium-jet recoil-transport system, HJRT, because of their recoil ranges.<sup>1)</sup> Therefore, the recoil chamber connected to the HJRT has been improved to perform quantitative transportation of the evaporation residues. In this paper, some results on isolation of short-lived nuclides with the HJRT and a continuous multistage solvent extraction system, SISAK (Short-lived Isotopes Studied by the AKUFVE-technique), which is coupled with HJRT, are presented.

Figure 1 shows a cross section of the recoil chamber. Using the chamber, the targets of Ag, Ta, Au and U were bombarded with  $^{12}\text{C}$  ions, and the neutron evaporation residues were collected and transferred from the chamber to a tape transport system with the HJRT.<sup>1)</sup> The transport efficiencies of the residues such as I, Au, At and Cf, were measured as given in Table 1. The differences in transport efficiencies among the nuclides might not be ascribed to the characteristics of each element but to unstable operation of HJRT. Figure 2 shows an alpha-ray spectrum of the Cf nuclides measured with the HJRT, where four peaks of alpha rays from  $^{242-244}\text{Cf}$  were observed.

The SISAK is used to make continuous chemical separations for isolating short-lived nuclides according to their nuclear charge  $Z$ .<sup>2)</sup> As a preliminary performance test of SISAK, the iodine nuclides produced by C+Ag reaction

were isolated with a SISAK connected to the HJRT in the three-stage solvent extraction. Figure 3 gives the flow sheet of the SISAK in operation for on-line isolation of iodine: The reaction products collected with aerosol particles in helium gas in the HJRT were transferred to a static mixer, where the carrier gas and sulfuric acid solution were mixed thoroughly. The helium gas was then separated by centrifuge and the liquid was pumped to the chemical separation system. The aqueous solution was then contacted with organic solvent in the static mixer and the mixture was fed into the centrifuge to separate the organic and aqueous solutions. In the first extraction stage, iodine was extracted into the organic solution. It was back extracted to aqueous solution in the second stage, then, purified further by washing the solution with other organic solution in the final extraction stage. After the three-stage extraction, the iodine fraction was measured with a Ge detector. A gamma-ray spectrum of iodine nuclides obtained is shown in Fig. 4, in comparison with a spectrum measured on that with only the HJRT. The nuclides of  $^{117}\text{I}$  (half-life: 2.2 min) and  $^{118\text{m}}\text{I}$  (8.5 min) were well isolated by the system.

The present on-line chemical separation system would be very useful to isolate nuclides with half-lives down to a few seconds and to investigate their decay properties.

The authors wish to thank Messrs. T. Nishiguchi and N. Hamano, Mechanical Engineering Division, JAERI, for their help on preparing the recoil chamber.

#### References

- 1) N. Shinohara et al.: JAERI-M 87-115 (1987) pp.126-128.
- 2) G. Skarnemark et al.: Phys. Scr. 34(6A) (1986) 597.

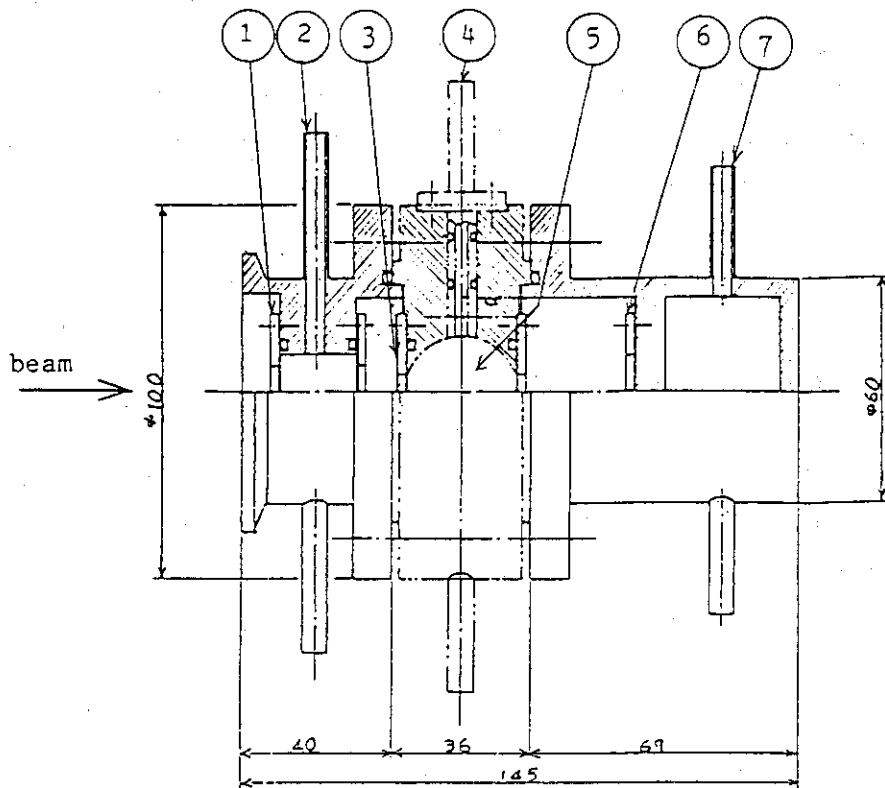


Fig. 1 Cross sectional view of the recoil chamber for the HJRT. The unit in the figure is mm.

- 1: window (5  $\mu\text{m}$  Havar foil), 2: leak tube, 3: target, 4: inlet and outlet of He gas, 5: reaction chamber, 6: beam stopper, 7: inlet and outlet of cooling water.

Table 1 Maximum transport efficiency of the HJRT.

Reaction	Nuclide produced	Efficiency, %
$^{12}\text{C} + \text{nat}_{\text{Ag}}$	$^{117}, ^{118\text{m}}\text{I}$	25
$^{12}\text{C} + ^{181}\text{Ta}$	$^{189\text{m}}\text{Au}$	$76 \pm 14^{\text{a}}$
$^{12}\text{C} + ^{197}\text{Au}$	$^{205}\text{At}$	34
$^{12}\text{C} + ^{238}\text{U}$	$^{245}\text{Cf}$	32

<sup>a</sup> Average and the standard deviation,  $\sigma_{n-1}$  (n=3).

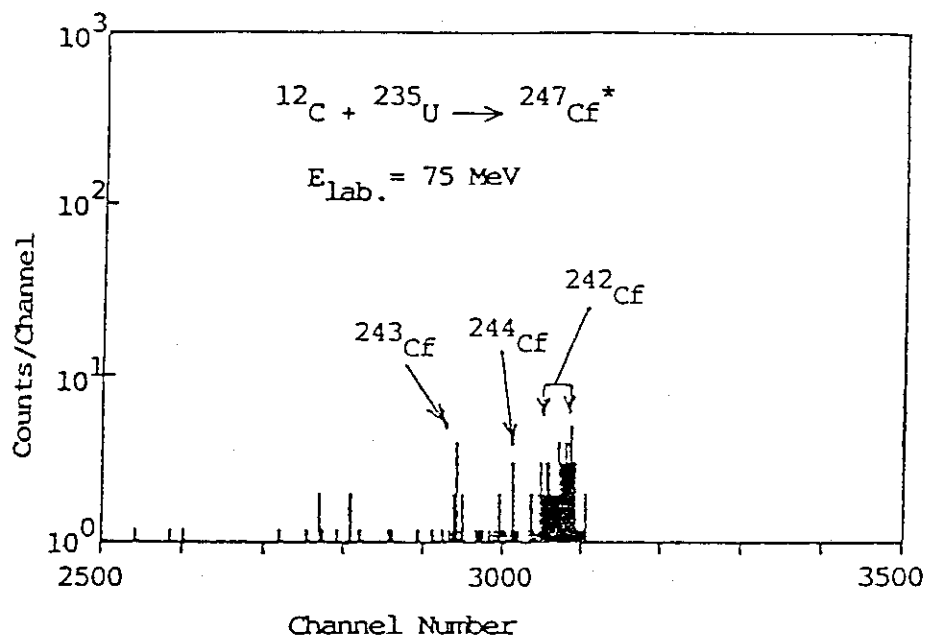


Fig. 2 Alpha-ray spectrum of the californium nuclides collected by the HJRT during 7 hours.

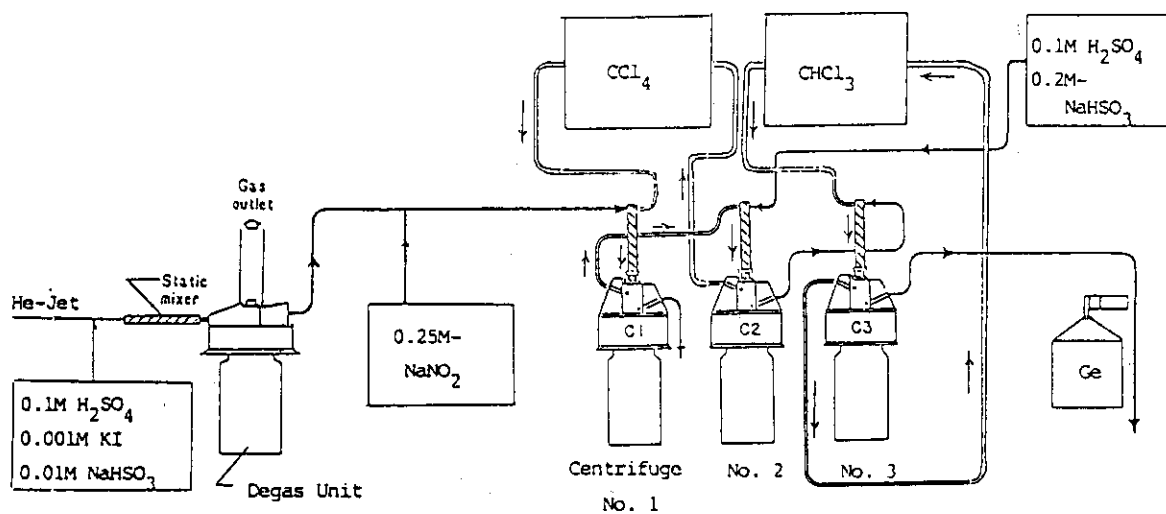


Fig. 3 Flow-sheet of the SISAK system for the on-line isolation of iodine from the products of  $^{12}\text{C} + \text{nat}\text{Ag}$  reaction.

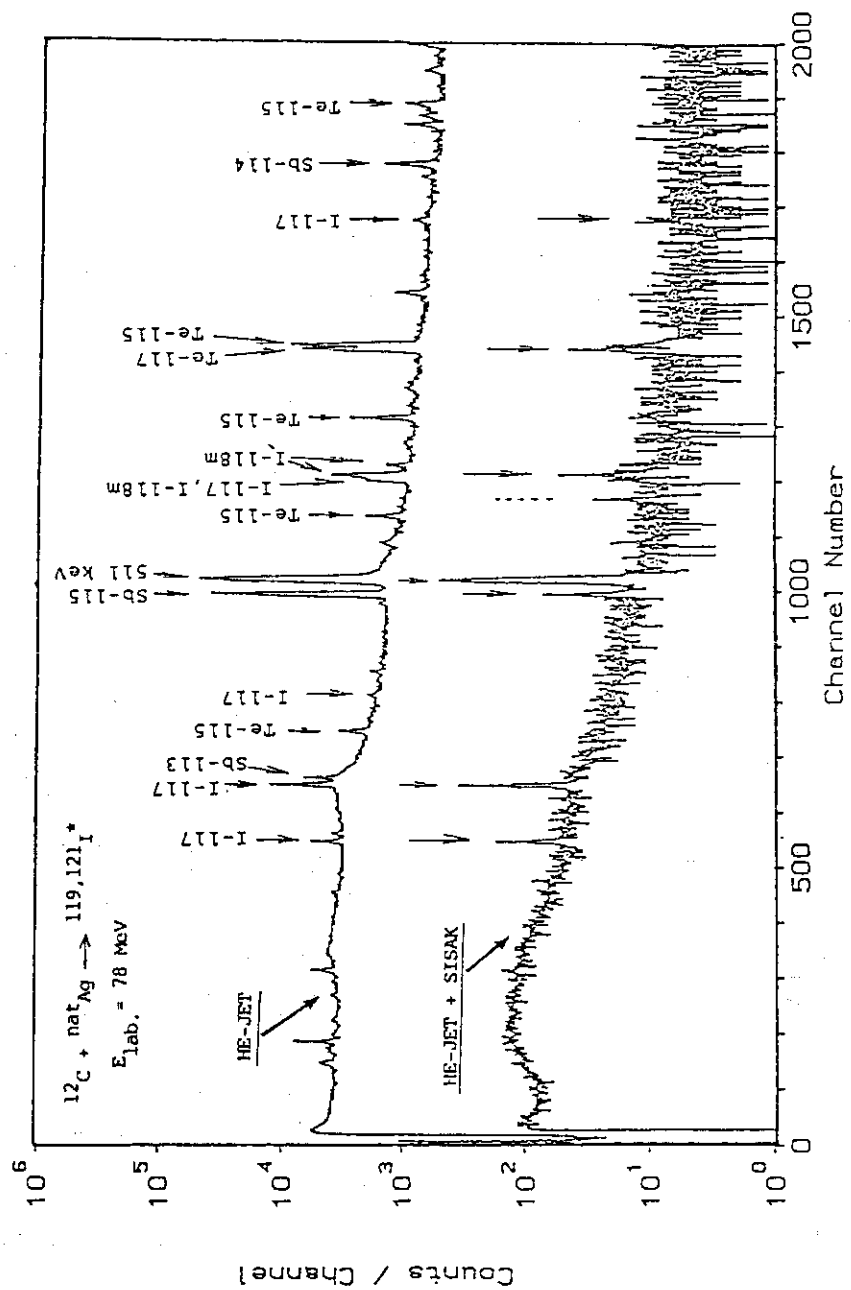


Fig. 4. Gamma-ray spectra of reaction products collected with only the HJRT and of iodine fraction isolated with the HJRT and SISAK.

V NUCLEAR PHYSICS

5.1 NUCLEAR STRUCTURE OF  $^{108}\text{Sn}$ 

Tetsuro ISHII, Mitsuhiro ISHII, Kenichi YANAGIDA\* and Masao OGAWA\*

Department of Physics, JAERI, \*Tokyo Institute of Technology, Yokohama

We have studied the nuclear structure of  $^{108}\text{Sn}$ :  $^{108}\text{Sn}$  nuclei were produced by the reaction  $^{51}\text{V}(^{58}\text{Ni}, 1p2n)$  with a 217 MeV  $^{58}\text{Ni}$  beam from the JAERI tandem accelerator. The  $\gamma$ - $\gamma$  coincidences, the  $\gamma$ -ray angular distributions and  $\gamma$ -ray time spectra have been measured in coincidence with single proton emitted with the help of the Si-Box<sup>1)</sup>. The level scheme has been obtained as shown in fig.1. The  $2^+$ ,  $4^+$  and  $6^+$  states have the typical structure of the particle excitation:  $(\nu g_{7/2})^2$ . Furthermore the  $8^+ \rightarrow 6^+$  and  $12^+ \rightarrow 10^+$  transitions suggest that two more neutron pairs are successively broken as the excitation proceeds. The level scheme of  $^{108}\text{Sn}$  is quite different from those of  $^{110-118}\text{Sn}$  where the excited rotational bands have been observed<sup>2)</sup>. Further investigation is in progress through the lifetime and g-factor measurements.

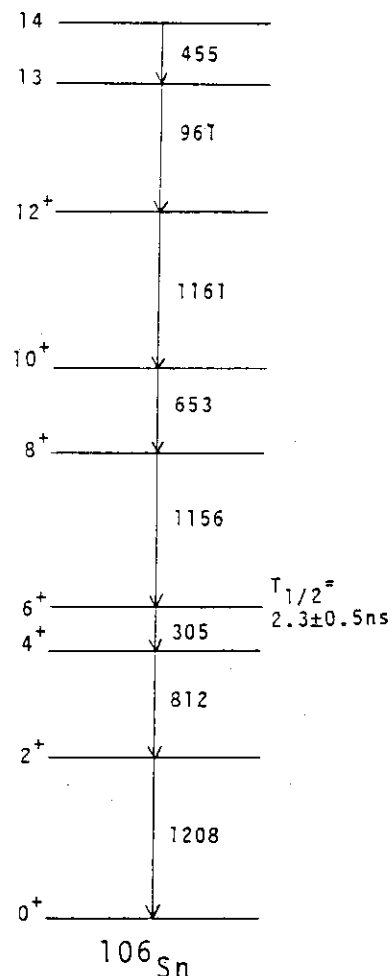


Fig.1 Level scheme of  $^{108}\text{Sn}$ . The transition energies are given in units of keV.

#### References

- 1) M. Ishii et al.: in *Nuclei off the Line of Stability* (ed. R. A. Meyer and D. S. Brenner, A.C.S., Washington D.C., 1986) ch. 75.
- 2) A. Van Poelgeest et al.: *Nucl. Phys.*, **A346** (1980) 70.

5.2 G-FACTOR OF THE  $10^+$  ISOMER IN  $^{134}\text{Nd}$ 

Tetsuro ISHII, Mitsuhiro ISHII, Kenichi YANAGIDA\* and Masao OGAWA\*

Department of Physics, JAERI, \*Tokyo Institute of Technology, Yokohama

In the very light rare earth nuclei the two-quasi proton state:  $(\pi h_{11/2})^2_{10^+}$  and the two-quasi neutron state:  $(\nu h_{11/2})^2_{10^+}$  are excited close to the collective  $10^+$  state. In fact the  $10^+$  state in  $^{138}\text{Sm}$  and the  $10^+_{2}$  state in  $^{128}\text{Ce}$  have turned out to consist of two quasiprotons coupling with collective motion (1,2). Recently we have established the level scheme of  $^{134}\text{Nd}$  including the  $10^+$  isomer with the half lifetime of 13ps as shown in fig.1. The present experiment aimed to investigate the nuclear structure of this isomer.

$^{134}\text{Nd}$  and  $^{132}\text{Nd}$  were produced by the reactions  $^{107}\text{Ag}(^{32}\text{S}, 3p2n)$  and  $^{107}\text{Ag}(^{32}\text{S}, \alpha p2n)$ , respectively, with a 165 MeV  $^{32}\text{S}$  beam from the JAERI tandem accelerator. They were implanted into a cooled  $5\text{mg}/\text{cm}^2$  Gd foil externally magnetized, up( $\uparrow$ ) or down( $\downarrow$ ). The  $\gamma$ -rays emitted from  $^{134}\text{Nd}$  and  $^{132}\text{Nd}$  were sorted with the help of the Si-box<sup>3)</sup>. The  $\gamma$ -ray angular distributions were observed by two Ge detectors placed at  $\pm 55^\circ$  to the direction of the beam. The intensity ratios  $I(\uparrow)/I(\downarrow)$  of the  $\gamma$ -rays involved have been measured for both polarities of the applied magnetic field.

The results are shown in fig. 2. All states in both nuclides inherit almost the same negative precession from some higher excited states which

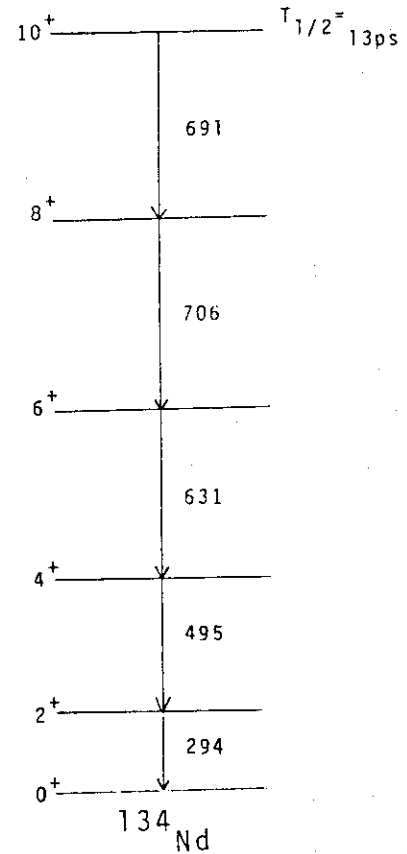


Fig.1 Level scheme of  $^{134}\text{Nd}$ . The transition energies are given in units of keV.



are subject to the transient magnetic field parallel to the applied one. The  $4^+$  state in  $^{132}\text{Nd}$  with the  $g \sim 0.3$  and  $T_{1/2} = 15\text{ps}$  suffers an additional positive precession in the static hyperfine field anti-parallel to the applied one. On the other hand, the  $4^+$  state in  $^{134}\text{Nd}$  fed via the  $10^+$  isomer doesn't show any additional positive precession. This means that the magnitude of  $g$  (the  $10^+$  isomer) is much smaller than that of the  $g$ -factor of the  $4^+$  state in  $^{132}\text{Nd}$ . The present results favor the neutron-like  $10^+$  state.

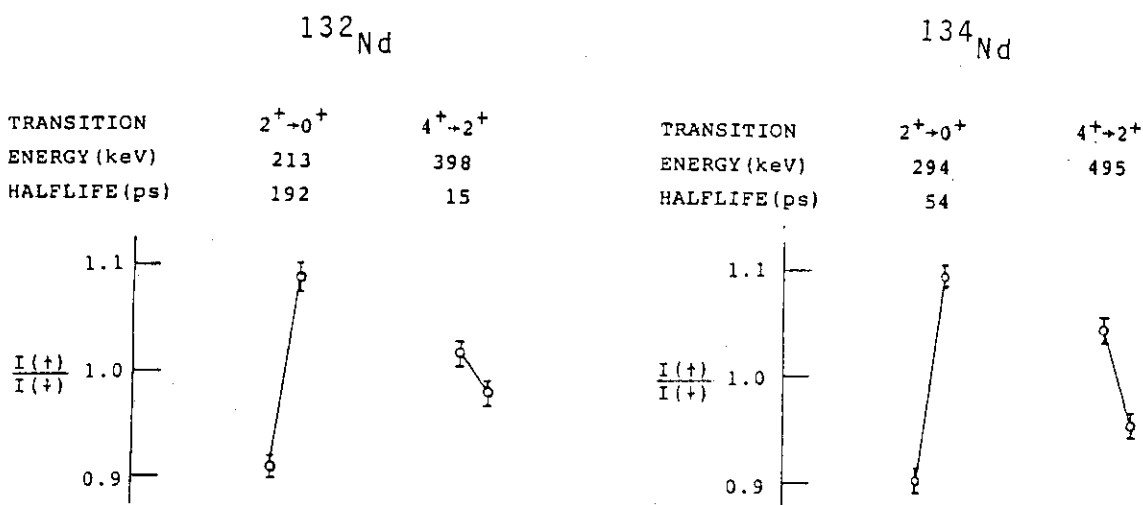


Fig. 2 Intensity ratios  $I(\uparrow)/I(\downarrow)$  of the  $\gamma$ -rays of  $^{132}\text{Nd}$  and  $^{134}\text{Nd}$ . The left(right) point at each transition presents the ratio measured with the Ge detector placed at  $-55^\circ$  ( $+55^\circ$ ) to the beam direction.

References

- 1) M. Ishii et al., Int. Nuclear Physics Conference, Harrogate U.K., 1986
- 2) T. Ishii et al., Int. Conference on Nuclear Structure Through Static and Dynamic Moments, Melbourne, Australia, 1987, Vol2, p93
- 3) M. Ishii et al., in Nuclei off the Line of Stability (ed. R. A. Meyer and D. S. Brenner, A.C.S., Washington D.C., 1986) ch. 75.

### 5.3 ELECTROMAGNETIC TRANSITION PROBABILITIES FOR NATURAL-PARITY ROTATIONAL BANDS IN $^{173}\text{Yb}$ AND $^{157}\text{Gd}$

Masumi OSHIMA, Shin-ichi ICHIKAWA,\* Hideki IIMURA,\* Eisuke MINEHARA, Hideshige KUSAKARI,\*\* Takashi INAMURA\*\*\* and Akira HASHIZUME\*\*\*

Department of Physics, \*Department of Chemistry, JAERI,  
 \*\*Faculty of Education, Chiba University, Yayoi-cho, Chiba  
 260, \*\*\*RIKEN, Wako-shi, Saitama 351-01

Recently the electromagnetic transition probabilities in the rotational bands have been studied extensively.<sup>1-4)</sup> Signature dependence of the reduced transition probabilities which originates from the Coriolis force has been found to provide a sensitive test of the wave functions. Since a strong Coriolis force acts on particles in high-spin orbitals, most experimental and theoretical studies are concerned with the rotational bands based on them. The rotational perturbation in low-spin orbitals have not been studied so well because it is believed to be rather small. However, we have found a quite large signature dependence of the  $B(M1)$  values in  $^{163}\text{Dy}$  whose ground-state rotational band has a dominant  $h_{9/2}$  character.<sup>5)</sup> Furthermore, the phase of the staggering in the  $B(M1)$  has turned out to contradict with the prediction of the single-j model<sup>6)</sup> for  $J = \frac{9}{2}$ , while that in the quasiparticle energy splitting agrees with it. This phenomenon is ascribed to the j-mixing effects for these bands.<sup>5)</sup>

In the present study we have investigated  $^{173}_{70}\text{Yb}_{103}$  and  $^{157}_{64}\text{Gd}_{93}$  nuclei whose ground-state rotational bands have a main component of  $f_{7/2}$ . These nuclei were multiply Coulomb excited with a 250-MeV  $^{58}\text{Ni}$  beam from the tandem accelerator. Information was obtained on high-spin states and their electromagnetic transition probabilities for the ground-state rotational bands.

The  $B(M1; 1 \rightarrow 1-1)$  and  $B(E2; 1 \rightarrow 1-2)$  values for  $^{173}\text{Yb}$  are plotted relative to the predictions of the rigid-rotor model<sup>7)</sup> in Figs. 1 and 2, respectively. An intrinsic quadrupole moment,  $Q_0 = 7.4$  b, and g-factors,  $g_K - g_R = -0.77$ , were assumed for the rigid-rotor-model predictions.<sup>7)</sup> The  $B(M1; 1 \rightarrow 1-1)$  and  $B(E2; 1 \rightarrow 1-2)$  values are close to the predictions and they show almost no signature dependence. This reflects the fact that the rotational perturbation due to the Coriolis force is weak for the

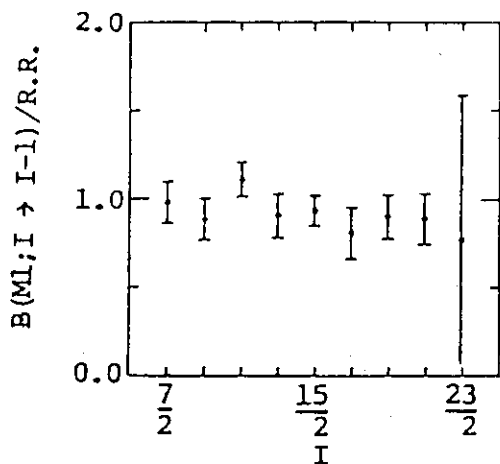


Fig. 1  $B(M1; I \rightarrow I-1)$  values of the ground band of  $^{173}\text{Yb}$  relative to the rigid-rotor-model prediction.

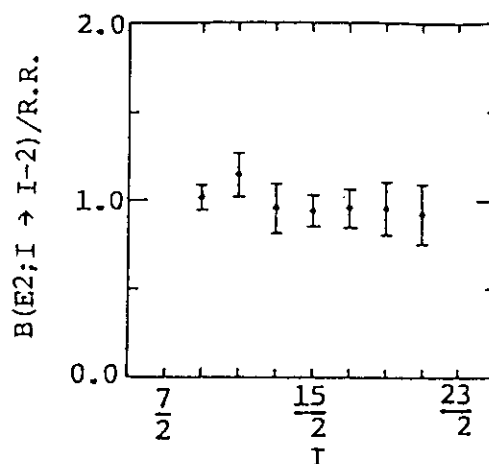
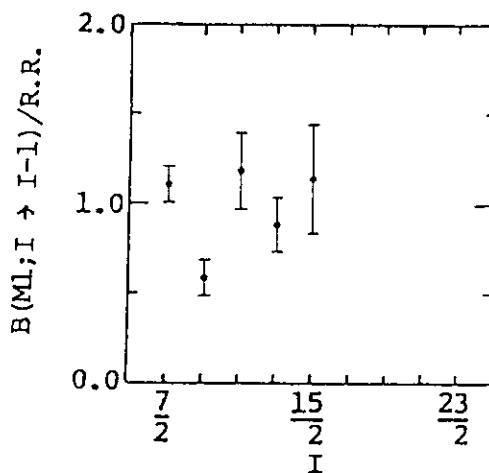


Fig. 2  $B(E2; I \rightarrow I-2)$  values of the ground band of  $^{173}\text{Yb}$  relative to the rigid-rotor-model prediction.

Fig. 3  $B(M1; I \rightarrow I-1)$  values of the ground band of  $^{157}\text{Gd}$  relative to the rigid-rotor-model prediction. The intrinsic quadrupole moment,  $Q_0 = 7.0$  b, was assumed to deduce them from the experimental  $B(M1; I \rightarrow I-1)/B(E2; I \rightarrow I-2)$  ratios.



predominant  $f_{7/2}$  orbital.

A preliminary result for  $^{157}\text{Gd}$  is shown in Fig. 3. Here we adopt  $g_K - g_R = -0.79$  for the rigid-rotor-model prediction. The result reveals a different feature as compared with  $^{173}\text{Yb}$ : Although the amplitude is small as compared with that in the high-spin-orbital bands,<sup>(1-4)</sup> the  $B(M1)$  values show a clear signature dependence (zigzag). The signature dependence is considered to be due to a significant  $\gamma$  deformation in the  $\gamma$ -unstable nuclei with  $N \sim 90$  because the  $\gamma$  deformation (static or dynamic) is closely related to the signature dependence.

It is interesting to see that the single-j model breaks down in  $^{157}\text{Gd}$ . The favored signature is  $r = +i$  for the  $B(M1)$ , while that for the quasiparticle energy is  $r = -i$ . This phase relation agrees with that for  $^{163}\text{Dy}$  where the  $h_{9/2}$  neutron state is the dominant component. In order to

explain the experimental results for  $^{173}\text{Yb}$  and  $^{157}\text{Gd}$ , it is necessary to take account of the  $\gamma$  degrees of freedom and  $J$  mixing. A theoretical study as well as the final analysis for  $^{157}\text{Gd}$  is in progress.

#### References

- 1) M.Oshima, E.Minehara, M.Ishii, T.Inamura and A.Hashizume, Nucl. Phys. A436 (1985) 518
- 2) J.Kownacki, J.D.Garrett, J.J.Gaardhøje, G.B.Hagemann, B.Herskind, S.Jonsson, N.Roy, H.Ryde and W.Walus, Nucl. Phys. A394 (1983) 269
- 3) G.B.Hagemann, J.D.Garrett, B.Herskind, J.Kownacki, B.M.Nyako, P.L.Nolan and J.F.Sharpey-Schafer, Nucl. Phys. A424 (1984) 365
- 4) S.Jonsson, J.Lyttkens, L.Carlen, N.Roy, H.Ryde, W.Walus, J.Kownacki, G.B.Hagemann, J.D.Garrett, B.Herskind and P.O.Tjøm, Nucl. Phys. A422 (1984) 397
- 5) E.Minehara, M.Oshima, S.Kikuchi, T.Inamura, A.Hashizume and H.Kumahara, Phys. Rev. C35 (1987) 858; M.Oshima, E.Minehara, S.Ichikawa, H.Iimura, T.Inamura, A.Hashizume and H.Kusakari, submitted to Phys. Rev. C (1988)
- 6) I.Hamamoto, Phys. Lett. 106B (1981) 281; Proc. Niels Bohr Centennial Conf. on Nuclear Structure, Copenhagen 1985, ed. R.Brogia, G.B.Hagemann and B.Herskind (North-Holland, Amsterdam-London, 1985) p.129
- 7) A.Bohr and B.R.Mottelson, Nuclear Structure Vol. 2 ( Benjamin, New York, 1975 )

5.4 MULTIPLE COULOMB EXCITATION OF  $^{148,150}\text{Nd}$ 

Masumi OSHIMA, Shin-ichi ICHIKAWA,\* Hideki IIMURA,\* Eisuke  
MINEHARA, Hideshige KUSAKARI\*\* Takashi INAMURA,\*\*\* and Akira  
HASHIZUME\*\*\*

Department of Physics, \*Department of Chemistry, JAERI,  
\*\*RIKEN, Wako-shi, Saitama 351-01, \*\*\*Faculty of Education,  
Chiba University, Yayoi-cho, Chiba 260

Although there is no sufficient experimental  $B(E2)$  data in the even-even nuclei with  $N \approx 90$ , the  $B(E2)$  values for the transitions up to the  $6^+$  or  $8^+$  states seem to increase more rapidly with the spin than the rigid-rotor-model predictions ( see, for example, Refs. 1-3 ). In order to check up such an interesting feature, we have done Coulomb excitation experiments on  $^{148,150}\text{Nd}$  with  $N = 88$  and  $90$ . We have measured the  $\gamma$ - $\gamma$  coincidences and  $\gamma$ -ray angular distributions. The new levels with spin 8 in  $^{148}\text{Nd}$  and spin 10 and 12 in  $^{150}\text{Nd}$  were established by the  $\gamma$ - $\gamma$  coincidence measurement. In order to deduce the transition probabilities for the ground-band transitions, we have extracted  $\gamma$ -ray yields from the  $\gamma$ -ray angular-distribution data. Theoretical yields can be calculated by using the multiple-Coulomb-excitation code<sup>4)</sup> by Winther and de Boer which includes the  $E2$  matrix elements between the ground-band members as free parameters. Therefore, the matrix elements can be determined by fitting the experimental yields with the theoretical ones. In a preliminary analysis we have not found so good agreement between our results and the previous values.<sup>1-3)</sup> Further analysis is in progress.

References

- <sup>1</sup> N.Rud et al., Nucl. Phys. A191 (1972) 545.
- <sup>2</sup> H.J.Wollersheim and Th.W.Elze, Nucl. Phys. A278 (1977) 87.
- <sup>3</sup> S.W.Yates et al., Phys. Rev. C17 (1978) 634.
- <sup>4</sup> A.Winther and J.de Boer, "Coulomb Excitation" (Academic Press) p.394.

## 5.5 Quasi-Elastic Scattering for $^{16}\text{O}+^{144,148,152}\text{Sm}$ Near The Coulomb Barrier

Yasuharu SUGIYAMA, Yoshiaki TOMITA, Hiroshi IKEZOE, Kazumi IDENO, Norihisa KATO\*, Tsuyoshi SUGIMITSU\*, Hiroshi FUJITA\*\* and Shigeru KUBONO\*\*\*

Department of Physics, JAERI, \* Department of Physics, Kyushu University,  
\*\* Daiichi College of Pharmaceutical Sciences, \*\*\* INS, University of Tokyo

The large subbarrier fusion cross sections, which reveal a strong isotope dependence for many systems<sup>1)</sup>, attract much interest in heavy-ion reactions near the Coulomb barrier. A number of theoretical models have been so far proposed, connecting the strong transfer channels with the large subbarrier fusion cross sections<sup>1)</sup>. In the  $^{16}\text{O}+^{144,148,150,152,154}\text{Sm}$  systems, a strong isotope dependence of subbarrier fusion cross section has been observed<sup>2,3)</sup>. The effect of the quadrupole deformation has been taken into account in order to explain the isotope dependence.

In this report we describe results of the quasielastic reaction for the  $^{16}\text{O}+^{144,148,152}\text{Sm}$  systems carried out at the JAERI tandem accelerator. The  $^{16}\text{O}$  beam energy was 72 MeV which was about 10% higher than the Coulomb barrier. The energy spectra were measured with an energy resolution of 200 keV by using the heavy-ion spectrograph<sup>4)</sup> "ENMA". The mass number, atomic number, Q-value and atomic charge state  $q$  of a reaction product were determined unambiguously from a measurement of the total energy  $E$ , energy loss  $\delta E$  and momentum  $P$ . Six nuclei  $^{17}\text{O}$ ,  $^{18}\text{O}$ ,  $^{15}\text{N}$ ,  $^{12}\text{C}$ ,  $^{13}\text{C}$  and  $^{14}\text{C}$  were observed in addition to elastically scattered  $^{16}\text{O}$ . Other reaction products could not be identified because of their small yields.

The angular distribution of the elastic scattering for  $^{16}\text{O}+^{144}\text{Sm}$  was measured at the incident energy of 71.4 MeV<sup>5)</sup>. The optical potential parameters which reproduced the data were obtained with the code Ptolemy.

Energy spectra obtained at  $\theta_{\text{lab}}=95^\circ$  from the reactions  $\text{Sm}(^{16}\text{O}, ^{17}\text{O})$  and  $\text{Sm}(^{16}\text{O}, ^{15}\text{N})$  are shown in fig. 1. Angular distributions for the ground state transition of these reactions are shown in fig. 2. In the reaction  $^{152}\text{Sm}(^{16}\text{O}, ^{17}\text{O})^{151}\text{Sm}$  the angular distribution for the energy-integrated cross sections (total) is shown. Absolute values of the reaction cross sections were derived by normalizing the yields to those of the elastic scattering which were measured simultaneously. The absolute value of the

elastic scattering cross sections for  $^{16}\text{O}+^{148,152}\text{Sm}$  was taken from the data by Weber et al<sup>6)</sup>.

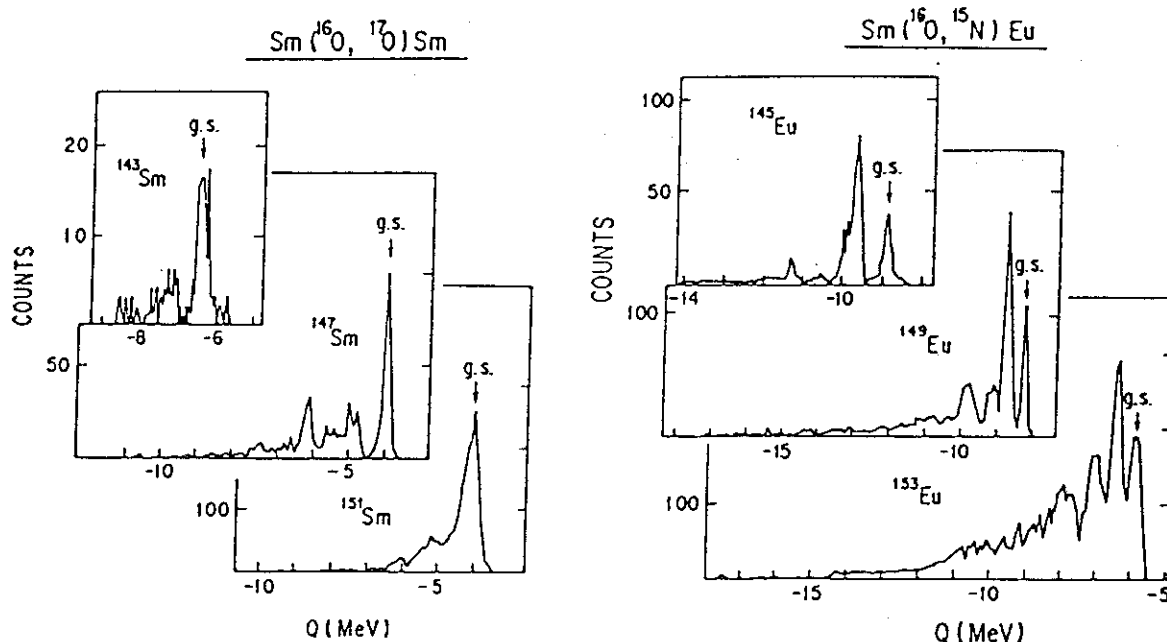


Fig.1 Spectra obtained from the  $(^{16}\text{O}, ^{17}\text{O})$  and  $(^{16}\text{O}, ^{15}\text{N})$  reactions on  $^{144}\text{Sm}$ ,  $^{148}\text{Sm}$  and  $^{152}\text{Sm}$ .

DWBA calculations for one-neutron pickup and one-proton transfer reactions were performed with the code Ptolemy. We used the optical potential parameters which were obtained through the coupled-channel analysis for the elastic scattering<sup>5,7)</sup>. For the spectroscopic factors we used the values obtained by the light-ion induced reactions such as  $(p,d)$ ,  $(d,p)$ ,  $(^3\text{He},d)$  and  $(d,^3\text{He})$  etc. Solid lines in Fig.2 are the results of the DWBA calculations. For the one-neutron pickup reaction  $(^{16}\text{O}, ^{17}\text{O})$ , angular distributions are well explained by the DWBA calculations with a normalization factor  $n=1$ . On the other hand a normalization factor  $n=3.0$  is required for the one-proton transfer  $^{148,152}\text{Sm}(^{16}\text{O}, ^{15}\text{N})$  reaction.

In Table 1 the sum of the measured quasielastic and fusion cross sections at  $E_{\text{lab}}=72$  MeV is compared with the optical-model calculation using parameters which reproduce the elastic scattering data. The optical model calculation reproduces well the total reaction cross sections.

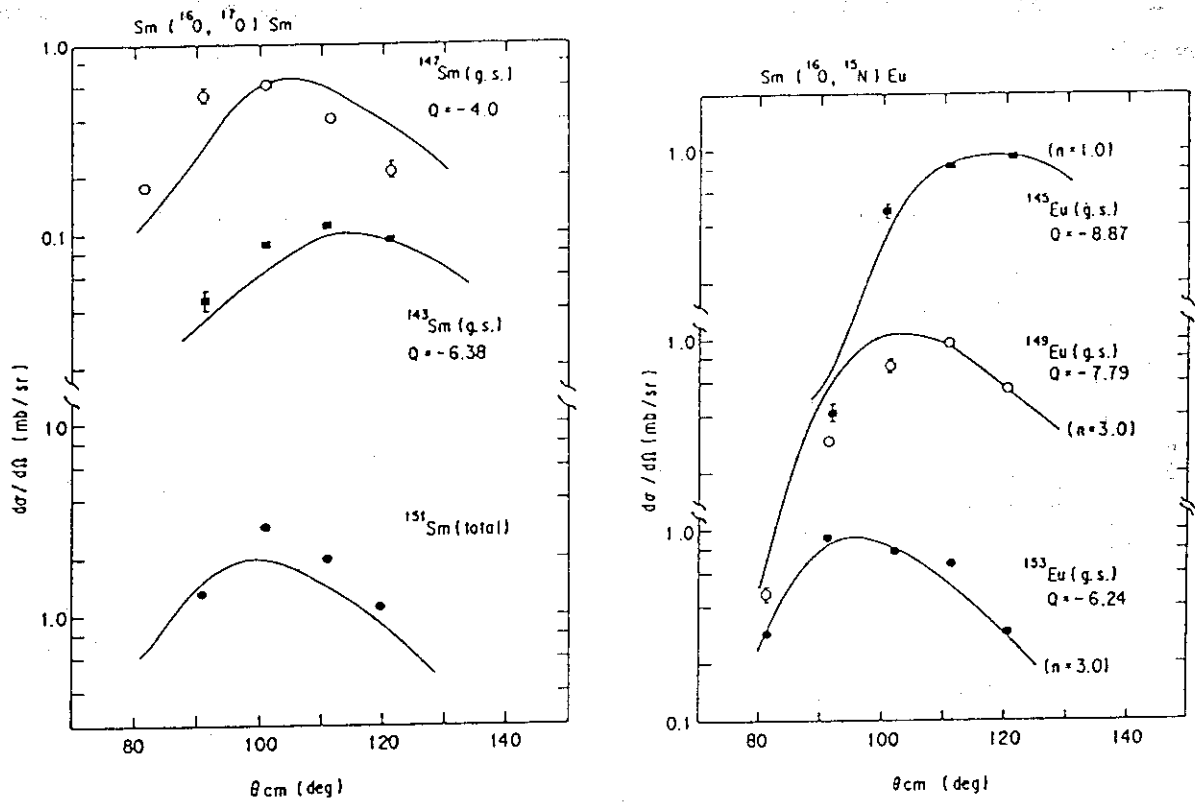


Fig.2 Angular distributions obtained from the (<sup>16</sup>O, <sup>17</sup>O) and (<sup>16</sup>O, <sup>15</sup>N) reactions on <sup>144</sup>Sm, <sup>148</sup>Sm and <sup>152</sup>Sm. Solid lines are DWBA calculations.

Table 1 Measured quasielastic and fusion cross sections at E<sub>lab</sub> = 72 MeV. The sum of measured cross sections are compared with the total reaction cross sections calculated from the optical model.

	target		
	<sup>144</sup> Sm	<sup>148</sup> Sm	<sup>152</sup> Sm
σ <sub>transfer</sub>	34	51	87
σ <sub>fusion</sub>	220	270	330
σ <sub>inelastic</sub>	124	505	1896
Sum	378	826	2313
σ <sub>R</sub> <sup>c</sup>	359	831	2300



References

- 1) S.G. Steadman, ed., Proc. Intern. Conf. on Fusion reaction below the Coulomb barrier, Lecture Notes in Physics, Vol.219 (Springer, Berlin,1985)
- 2) R.G.Stokstad et al., Phys.Rev.C21(1980)2427.
- 3) D.E.Di Gregorio et al., Phys.Lett.B176(1986)322.
- 4) Y.Sugiyama et al., Nucl.Instrum.& Methods 187(1981)25; Z.Phys. A322(1985)579.
- 5) Y.Sugiyama et al., to be published.
- 6) D.J.Weber et al., to be published.
- 7) R.G.Stokstad et al., Phys.Rev. C23(1981)281.

## 5.6 MASS DISTRIBUTIONS OF FISSION FRAGMENTS IN THE $^{19}\text{F} + ^{197}\text{Au}$ REACTION

Hiroshi IKEZOE, Naomoto SHIKAZONO, Yoshiaki TOMITA, Yasuharu SUGIYAMA, kazumi IDENO, Wataru YOKOTA, Yuichiro NAGAME, S.M.LEE\*, Mitsuhiro OGIHARA\*, S.C.JEONG\*, Hideaki FUJIWARA\* and David J.HINDE\*\*

Department of Physics, JAERI, \*Institute of Physics and Tandem Accelerator Center, University of Tsukuba, and \*\*Research Center for Nuclear Physics, Osaka University.

The reaction dynamics of the fission process influences the mass distribution of the fission fragments<sup>1)</sup>. We have previously observed that the mass centroids of the fission fragments produced in the  $^{19}\text{F}$  on  $^{197}\text{Au}$  reaction deviate from the half mass of the compound nucleus. In order to investigate this phenomenon, We have measured the mass distribution by means of a precise mass calibration technique.

A  $450 \mu\text{g}/\text{cm}^2$  thick  $^{197}\text{Au}$  target was bombarded by  $^{19}\text{F}$  beams with beam energies from 100 to 160 MeV. Fission fragments were measured by three time-of-flight (TOF) telescopes. In order to calibrate the absolute mass of the fission fragments, three targets  $^{\text{nat}}\text{Ag}$ ,  $^{\text{nat}}\text{Sb}$  and  $^{\text{nat}}\text{Ba}$  were bombarded with a 200 MeV  $^{81}\text{Br}$  beams. The recoil nuclei and the scattered  $^{81}\text{Br}$  ions were detected by these TOF telescopes at various scattering angles. The  $^{81}\text{Br}$  beam energy and the target masses were chosen so as to make recoil nuclei simulate the fission fragments in mass and energy.

The typical mass distribution corrected for neutron emission is shown in Fig.1. The centroids of the mass distributions are shown in Fig.2 as a function of the mean center-of-mass scattering angle. The present data show a weak but distinct angular dependence of the mass centroids, which increases with bombarding energy. At the highest bombarding energy ( $E_{\text{Lab}} = 160 \text{ MeV}$ ) the mass shift from forward to backward angles amounts to  $\sim 3 \text{ a.m.u.}$ , which is much greater than the systematic uncertainty.

Figure 3 shows the relative angular distributions (normalized to unit at  $\theta_{\text{cm}} = 86.5^\circ$ ) for the two different mass bins at the bombarding energy of 160 MeV. From this figure we can see the enhanced (weakened) yields of the heavy fragments ( $A=118-150 \text{ a.m.u.}$ ) in comparison with those of the

light fragments ( $A=65-97$  a.m.u.) at the forward angles ( at the backward angles). These asymmetric angular distributions of specified fragments have been reported by Keller et al<sup>1)</sup> as evidence of the quasi-fission process.

Previously forward-backward mass centroid shifts have been observed for heavier reaction systems and have been interpreted in the framework of the extra-push model<sup>2)</sup>. According to this model, an "extra-extra push energy" is required for a heavy reaction system to form a compound nucleus inside the true fission saddle point. If the bombarding energy is not so high, a fission-like (quasi-fission) process occurs without a compound nucleus formed inside the saddle-point. In this case the forward-backward mass asymmetry may appear, depending on the reaction time and angular momentum. However the present experiment on the  $^{19}\text{F}$  on  $^{197}\text{Au}$  reaction indicates a different situation: Although according to Back's systematics<sup>3)</sup> the extra-extra push energy is zero, a quasi-fission process as well as a dominant process of compound-fusion fission takes place.

#### References

1. H. Keller, K. Lutzenkirchen, J. V. Kratz, G. Wirth, W. Bruchle, K. Summerer: Z. Phys. A 326, (1987) 313.
2. W. J. Swiatecki: Phys. Scr. 24, (1981) 113.
3. B. B. Back, R. R. Betts, J. E. Gindler, B. D. Wilkins, S. Saini, M. B. Tsang, C. K. Gelbke, W. G. Lynch, M. A. McMahan, P. A. Baisden; Phys. Rev. C32, (1985) 195.
4. S. Cohen, F. Plasil, W. J. Swiatecki: Ann. Phys. (N.Y.) 82, (1974) 557.

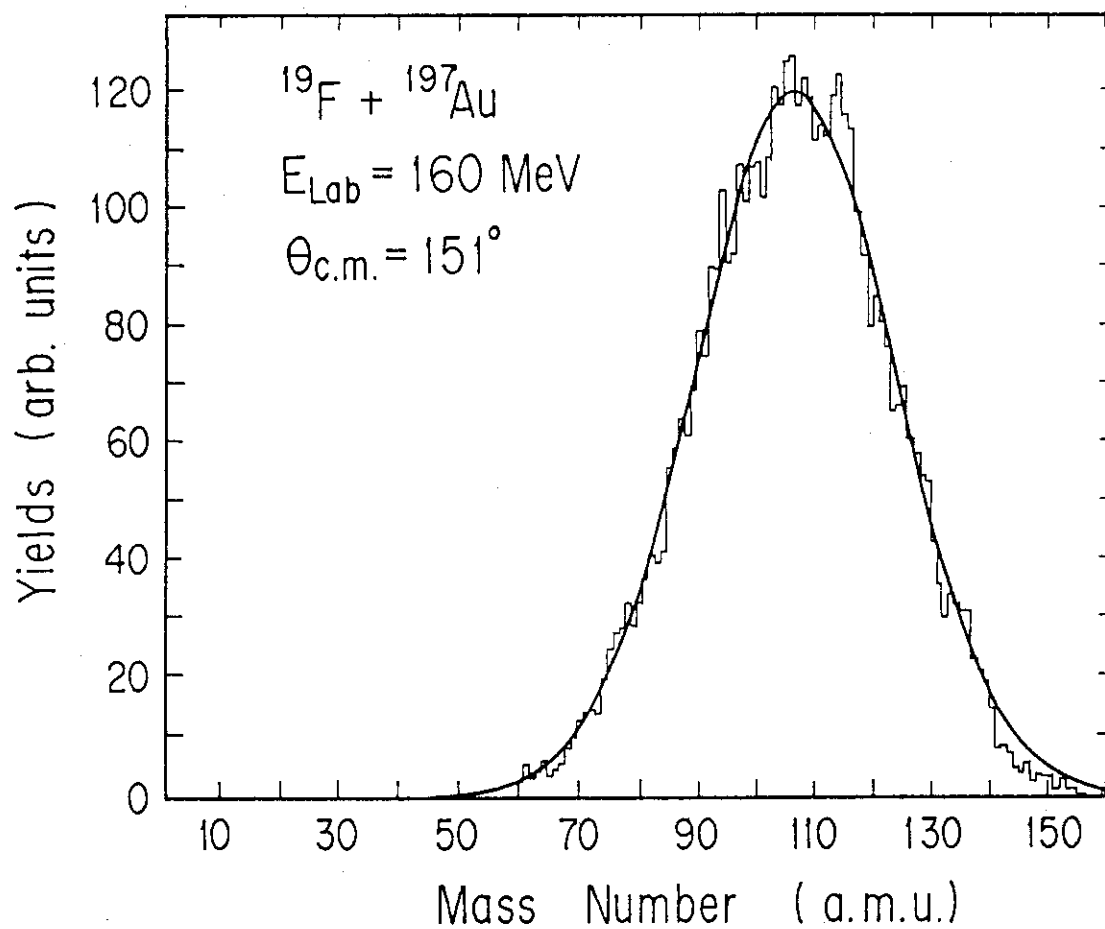


Fig.1 Typical mass distribution of the fission fragments corrected for neutron emission. The solid line is a curve fitted by a gaussian function.

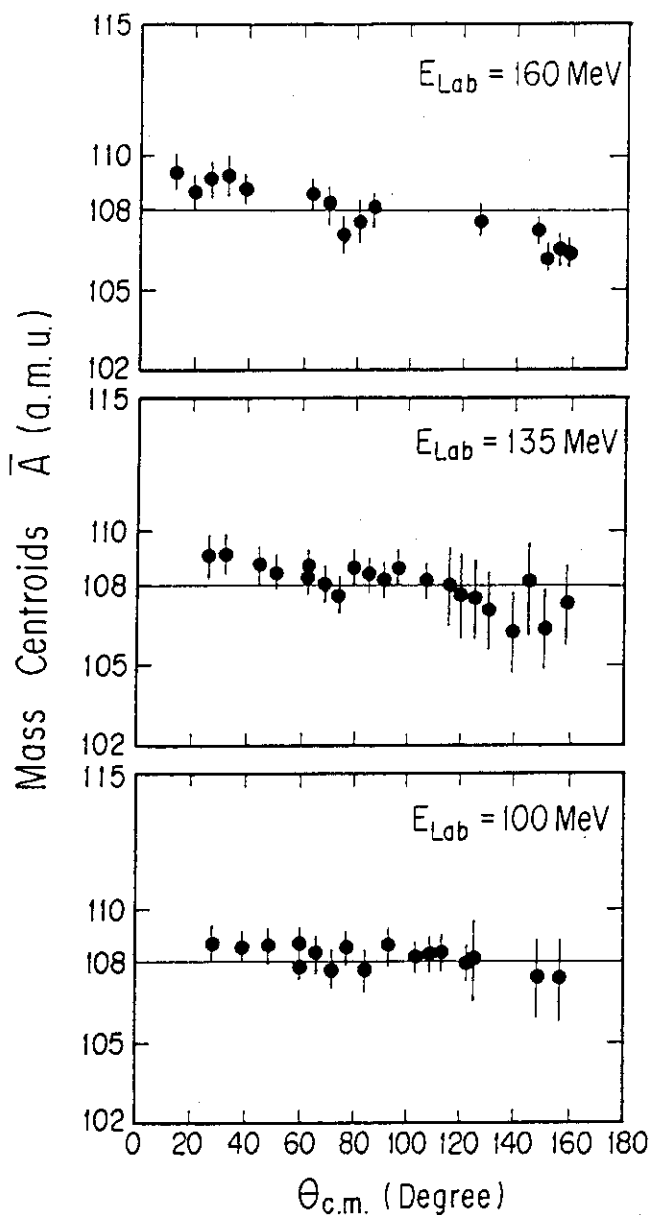


Fig.2 Centroids of the mass distributions of the primary fission fragments at three bombarding energies as a function of the center-of-mass scattering angle. The horizontal line shows the half mass of the compound nucleus.

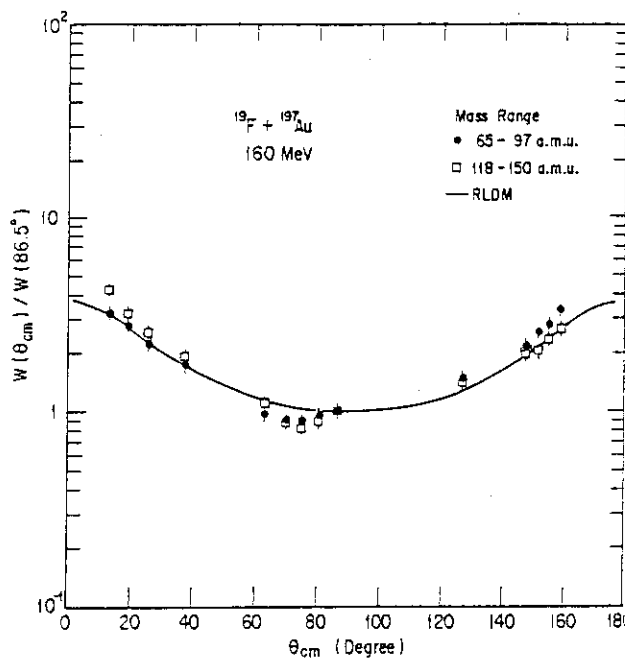


Fig.3 Relative angular distributions of the specified fragments indicated in the figure. Two angular distributions are normalized to unit at  $\theta_{cm} = 86.5^\circ$ . The solid line is calculation of the standard fission theory based on the rotating liquid drop model<sup>4)</sup>.

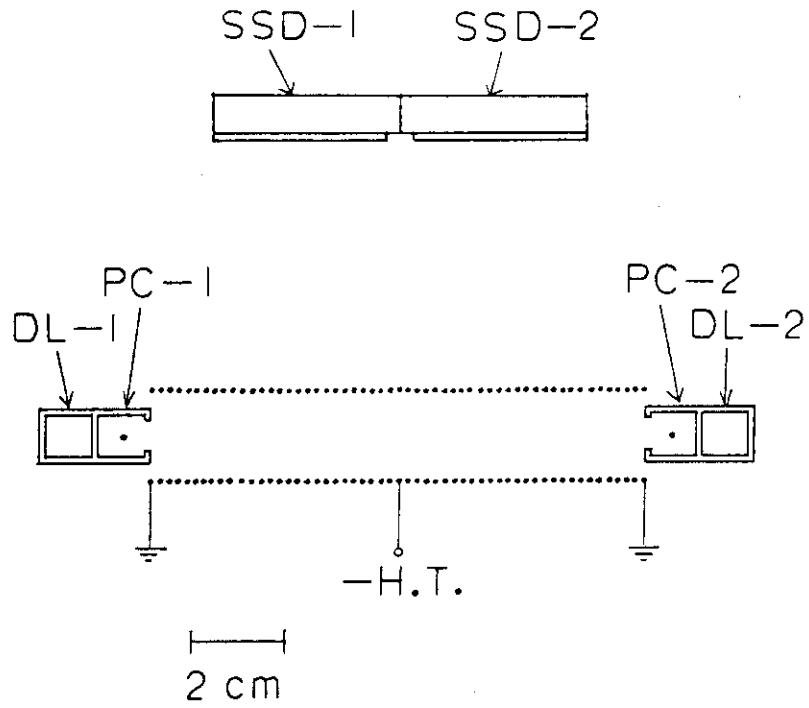
### 5.7 A TWO-DIMENSIONAL POSITION-SENSITIVE DETECTION SYSTEM FOR THE $^8\text{Be}$ NUCLEI FROM HEAVY ION REACTIONS

Kazumi IDENO, Yoshiaki TOMITA, Yasuharu SUGIYAMA,  
Hiroshi IKEZOE, Susumu HANASHIMA and Yuichiro NAGAME\*

Department of Physics, \* Department of Radioisotopes,  
JAERI

In the heavy ion reactions the  $^8\text{Be}$  nuclei are expected to occupy a large part in the production cross sections of light fragments owing to its loosely-bound  $2\alpha$  structure and small  $Q$ -values. They are unstable ( $t_{1/2} \approx 10^{-16}$  sec at ground state) and decay into two  $\alpha$  particles soon after ejected from the composite system. The  $^8\text{Be}$  identification is based on the measurement of spatial and energy correlations between the decaying  $\alpha$  particles<sup>1)</sup>. In the detection system where Si detectors are employed as  $\Delta E$  and  $E$  counters, the size of the  $\Delta E$  counter limits practically the available solid angles. To achieve both large solid angle and good position resolution, we have constructed a two-dimensional position-sensitive detection system<sup>2)</sup> which is composed of paired drift chambers (PDC) as  $\Delta E$  counters and two closely-spaced Si detectors as  $E$  counters.

Fig. 1 shows a schematic diagram of the detection system. All the components are housed in a chamber of  $16 \times 20 \times 20 \text{ cm}^3$  with an entrance window of  $2 \mu\text{m}$  aluminized polyester foil. The PDC has been operated at a pressure of 30 Torr with isobutane gas. The two  $E$  counters have a sensitive area of  $40 \times 40 \text{ mm}^2$  respectively with a separation of 7 mm. The PDC, the components of which are similar in design to the ones described by Breskin et al.<sup>3)</sup>, is symmetrically arranged; each drift region has an active area of  $50 \times 50 \text{ mm}^2$  and its boundary is at the center position of the PDC. The drift region with a width of 20 mm is surrounded by  $50 \mu\text{m}$  tungsten wires with each 2 mm spacing. The proportional counters with a sense wire of  $20 \mu\text{m}$  are placed at the opposite ends of the drift region. To generate the electric field for drifting the electrons horizontally to the proportional counters, a minus high tension ( $V_{\text{DC}}$ ) is applied to the center wire; the end wires at both sides are grounded while the intermediate wires are linked in cascade by a  $1 \text{ M}\Omega$  resistor. To maintain a constant drift velocity ( $v_{\text{DRIFT}}$ ) over the whole drift regions, especially near the boundaries, a high tension of  $V_{\text{DC}} = -1400 \text{ V}$  was applied; in this case,



SSD --- Si(Li) detector                      PC --- Proportional counter  
 DL --- Delay line                              H.T. --- High tension

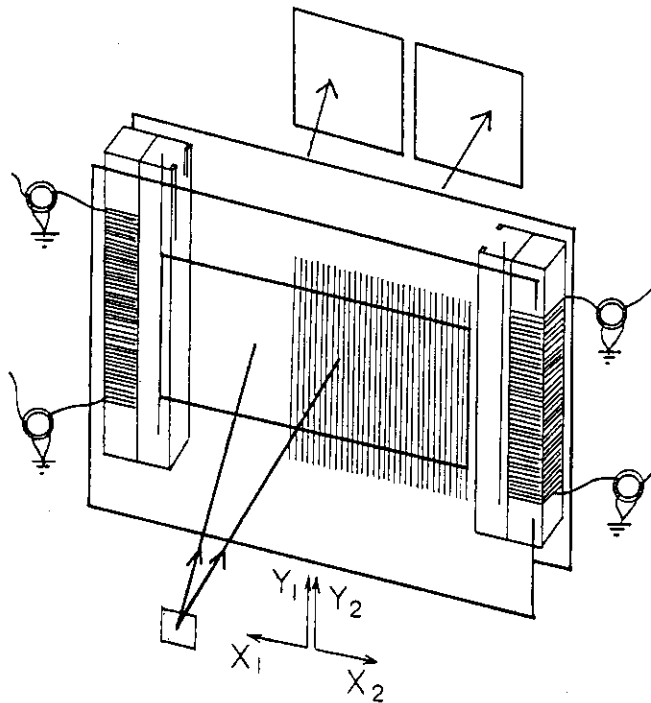
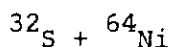


Fig. 1 Schematic diagram of the detection system.

$v_{\text{DRIFT}} = 260$  ns/cm. For the determination of x coordinates for the impinging  $\alpha$  particles on the E counter, we derive a drift time of ionized electrons from a measurement of the time difference between a start signal from the E counter and a stop signal from the sense wire. One side of the cathode planes is made of one surface of a delay line wound on the cubic brass bar. Induced charges caused by the electron avalanches near the sense wire travel through the delay line upwards and downwards and the difference between the arrival times of both signals indicates the position of the avalanches, i.e. Y coordinates. The transmission speed of the signal through the delay line was 52 ns/cm. The position resolution was 0.3 mm in both X and Y directions for the  $^{241}\text{Am}$   $\alpha$  particles and good linearity of the position was attained. For the beam experiments the position resolution is actually determined by the size of the beam spot on the target. For the present system the highest counting rate ( $< 10^4$  counts/sec) is limited by the space charge effect of the proportional counters. In the measurement at forward angles it is necessary to cover the entrance window with a Al or Cu foil to stop the elastically scattered beams.



We have measured the production cross sections of the  $^8\text{Be}_{\text{g.s.}}$  nuclei from the reaction  $^{32}\text{S} + ^{64}\text{Ni}$  at 175 MeV. The target thickness of  $^{64}\text{Ni}$  was  $300 \mu\text{g}/\text{cm}^2$ . The distance between the E detector and the target was 272 mm. The maximum opening angle of the E detector was 8.4 degrees. The half width of the acceptance angle for 40 MeV  $^8\text{Be}_{\text{g.s.}}$  nuclei was 2.2 degrees. Fig. 2 shows a plot of the effective solid angle vs  $^8\text{Be}_{\text{g.s.}}$  kinetic energies. In the measurements at  $\theta_{\text{lab}} = 18 - 35$  degrees the detector window was covered with a  $20 \mu\text{m}$  Cu foil. The proportional counters were operated at a high voltage of 1000 to 1100 V so that sufficient charges were induced on the delay lines to actuate efficiently the Y-coordinate determinations for  $\alpha$  particles with energies up to 100 MeV. We could steadily identify  $\alpha$  particles from protons and other heavier fragments. Fig. 3 shows a plot of the observed momentum distribution of the relative motion between the coincident  $\alpha$  particles. There observed a sharp peak which corresponds to a correlated part R( $\Delta P$ ) determined from the 0.092 MeV Q-value of the  $^8\text{Be}_{\text{g.s.}}$  nucleus. Other contributions at the higher momentum region correspond mostly to the uncorrelated part which was brought about by independently coincident  $\alpha$



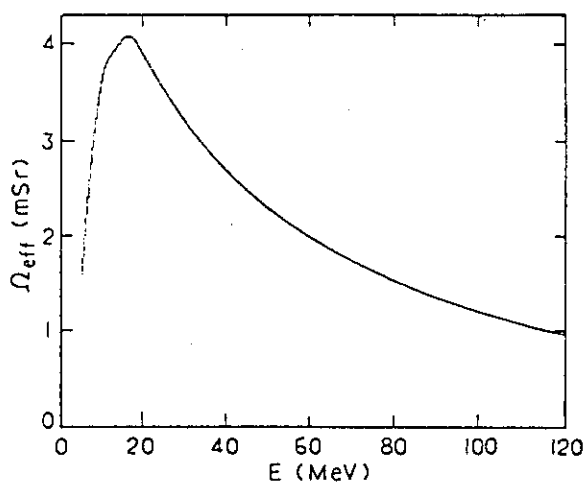


Fig. 2 Effective solid angle as a function of kinetic energies of  ${}^8\text{Be}_{\text{g.s.}}$  nuclei.

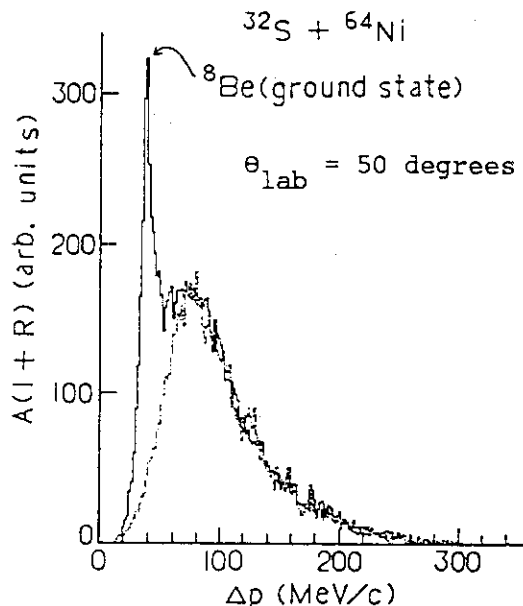


Fig. 3 Momentum distribution of a relative motion between coincident  $\alpha$  particles. The dashed line indicates the contribution from the uncorrelated  $\alpha$  particles.

particles. The yield of the  ${}^8\text{Be}_{\text{g.s.}}$  fragment has been obtained from the distribution of the relative momentum. This unstable nucleus occupies about 80% of the Be fragments emitted at  $\theta_{\text{lab}} = 18 - 50$  degrees. The differential cross section  $d\sigma/d\theta_{\text{c.m.}}$  for  ${}^8\text{Be}_{\text{g.s.}}$  shows a flat pattern. The energy spectra of  ${}^8\text{Be}_{\text{g.s.}}$ , which were obtained by gating the corresponding momentum distributions, are continuous. The observed kinematical behavior of the  ${}^8\text{Be}_{\text{g.s.}}$  fragment is similar to those of other light fragments, the measurement of which was made using a usual Si  $\Delta E$ -E counter telescope. The same feature was also observed for the reaction  ${}^{16}\text{O} + {}^{27}\text{Al}$  at 65 MeV by Brandan et al.<sup>4)</sup>

The present system has worked efficiently in detecting the  ${}^8\text{Be}_{\text{g.s.}}$  fragments with continuous spectra under strong  $\alpha$  backgrounds.

#### References

- 1) G. J. Wozniak et al.: Phys. Rev. C14 (1976) 815.
- 2) K. Ideno et al.: JAERI-M 87-115 (1987).
- 3) A. Breskin et al.: Nucl. Instr. & Methods 148 (1978) 275.
- 4) M. E. Brandan et al.: J. Phys. G12 (1986) 391.

## 5.8 EFFECT OF THE SHELL STRUCTURE ON THE POTENTIAL BARRIER FOR THE SUBBARRIER FUSION REACTIONS

Akira IWAMOTO\* and Noboru TAKIGAWA\*\*

\* Department of Physics, JAERI, \*\* Department of Physics, Tohoku University

The observed values of the subbarrier fusion cross section in heavy-ion reactions are much larger than one-dimensional barrier penetration calculations when both projectile and target are heavy. There is a trend that the enhancement becomes larger as the size of the system becomes larger. Taking into account the intrinsic excitations of the colliding nuclei, the coupled-channels calculation fairly well explains the data for Ni+Ni or for lighter systems. For heavier systems, however, the experimental cross sections are much larger than the calculated ones.

In Ref.1, this problem was attacked by assuming a semiclassical neck-formation mechanism. The formation of the neck part between colliding nuclei lowers the effective barrier, which enhances the fusion cross section. Also Aguiar et al.<sup>2)</sup> have calculated the lowering of the potential in a similar way but more systematically. Their results show that the assumption of neck formation can reproduce the dependence of the fusion cross sections on the size of the colliding systems observed experimentally. Some data, however, deviate much from the systematics of the cross sections as a function of the size of the system. Typical examples are the systems  $^{74}\text{Ge}+^{74}\text{Ge}$  and  $^{40}\text{Ar}+^{154}\text{Sm}$ .<sup>1,2)</sup> The ground state of the nucleus  $^{154}\text{Sm}$  is deformed and it seems to be responsible to the anomaly seen in the latter system. On the other hand, the nucleus  $^{74}\text{Ge}$  is spherical in its ground state and thus it is of interest to inquire what is responsible to the anomaly in the system  $^{74}\text{Ge}+^{74}\text{Ge}$ .

The characteristic of the  $^{74}\text{Ge}+^{74}\text{Ge}$  system is the following. The nucleus  $^{74}\text{Ge}$  is spherical in the ground state but is soft against deformation. The compound system  $^{148}\text{Gd}$  formed by these two lies in the mass region of nuclei which exhibit super-deformed band. Since above mentioned features are caused by the shell structure effect, we investigate the effect of the shell correction energy to the fusion barrier. The potential energy in our model is calculated by the sum of the liquid-drop energy obtained by the Yukawa-plus-exponential model<sup>3)</sup> and the shell

correction energy given by the Strutinsky prescription. We calculated the fusion barrier for the neck-formed configuration <sup>1</sup>).

Calculations including the shell correction energy show only little change of the fusion barrier height. Noticing the fact that the shell correction energy is closely related to the deformation of the nucleus, we also performed the calculation including the freedom of the deformation of two Ge. The barrier height in this model is defined as the maximum value of the potential energy against the center separation of two fragments for given fragments' deformations  $\delta$ .

At deformation  $\delta=0.2$ , the macroscopic contribution lowers the fusion barrier height by 2.3 MeV from the value for the spherical fragments. An addition of the shell energy causes further deformation  $\delta=0.35$  and decrease of the barrier height about 5.1 MeV. As a whole, the fusion barrier height for <sup>74</sup>Ge + <sup>74</sup>Ge system is lowered by 7.4 MeV from the macroscopic barrier height for spherical nuclei. The amount of this reduction of the barrier height is about the same as is required to fit the experimental data.

In order to see the validity of our assertion, we have performed the same kind of calculations for the 6 systems, <sup>40</sup>Ar + <sup>40</sup>Ar, <sup>58</sup>Ni + <sup>58</sup>Ni, <sup>64</sup>Ni + <sup>64</sup>Ni, <sup>80</sup>Se + <sup>80</sup>Se and <sup>90</sup>Zr + <sup>90</sup>Zr. The results are summarized in the table, where  $V_0$ ,  $\Delta V$  and  $V_B$  are the barrier height calculated by using the macroscopic energy for the neck-formed shape at  $\delta=0.0$ , the microscopic correction to  $V_0$  at the optimum value of  $\delta$  and the total barrier, respectively. As is clearly seen in Table 1, the microscopic correction to the barrier height is most significant for <sup>74</sup>Ge + <sup>74</sup>Ge. A fairly large effect is seen also for <sup>80</sup>Se + <sup>80</sup>Se. In these two systems, the optimum deformation is about 0.35. For the other systems, the microscopic effect is not significant. The trend of the barrier height thus obtained is consistent with the systematics of the asymptotic energy shift.

Table 1

SYSTEM	<sup>40</sup> Ca+ <sup>40</sup> Ca	<sup>58</sup> Ni+ <sup>58</sup> Ni	<sup>64</sup> Ni+ <sup>64</sup> Ni	<sup>74</sup> Ge+ <sup>74</sup> Ge	<sup>80</sup> Se+ <sup>80</sup> Se	<sup>90</sup> Zr+ <sup>90</sup> Zr
$V_0$	54.4	94.7	91.5	115.3	127.6	173.2
$\Delta V$	1.7	-1.3	-1.3	-7.4	-4.5	-0.6
$V_B$	56.1	93.4	90.2	107.9	123.1	172.6

The feature of the above mentioned microscopic energy is related to the shell structure of the fragment nucleus as follows. The shell correction energy near the barrier is roughly equal to the sum of the shell correction energies of isolated fragments. In the deformation energies of isolated  $^{74}\text{Ge}$  and  $^{80}\text{Se}$ , the liquid-drop energy rises so rapidly with the deformation that the addition of the shell correction energy causes no significant effect. The situation is quite different in the barrier region where the liquid-drop energy itself decreases as deformation increases. Thus the addition of the shell correction energy, which decreases rapidly with deformation, causes a drastic change in the potential energy. In this respect, the shell structure of the fragment is essentially responsible to the anomaly of the subbarrier fusion cross section. The role of this shell structure becomes remarkable when the freedom of fragment's deformation is taken into account. The structure of the compound nucleus, on the other hand, is not directly related to the change of the barrier height. Therefore no close relation of the existence of the super-deformation and the anomaly of the subbarrier fusion cross section is seen in our calculation.

In summary, the model calculation including the shell correction energy together with the freedom of the deformation can explain the anomalous enhancement of the subbarrier fusion cross section seen in  $^{74}\text{Ge} + ^{74}\text{Ge}$  system. The model also predicts a fairly large enhancement for  $^{80}\text{Se} + ^{80}\text{Se}$  system. It is interesting to measure the subbarrier fusion cross section for this system at much lower energies. In order to calculate the subbarrier fusion cross section more quantitatively, it is necessary to develop a model which takes into account the dynamical aspects of the fusion process.

#### References

- 1) A. Iwamoto and K. Harada: Z.Phys. A326 (1987) 201.
- 2) C.E.Aguiar et al.: Phys.Lett. 201 (1988) 22.
- 3) H.J. Krappe, J.R. Nix and A.J. Sierk: Phys.Rev.C20 (1979) 992.

5.9 ALPHA DECAY IN ACTINIDE NUCLEI  
AND  
THE SPDF BOSON MODEL

Michiaki SUGITA and Takaharu OTSUKA\*

Department of Physics, JAERI, \*Department of  
Physics, University of Tokyo

We have recently proposed an spdf boson model<sup>1)</sup> to describe positive and negative parity bands observed in the actinides. In these nuclei, the negative parity bands appear in excitation energies comparable to those of quadrupole collective states. In such a case, the octupole deformation plays an important role, and strongly couples with the quadrupole deformation. The spdf boson model can provide a unified description of the octupole-quadrupole collective states (see Fig. 1).

The alpha decay width is a sensitive measure of the structure of the quadrupole-octupole collective states. The vibron model<sup>2)</sup> has been successful in describing the alpha decay, but does not have a close or natural connection to the octupole deformation of nuclei. In contrast, the spdf boson model is formulated from the octupole point of view. It is then of great interest to see whether the spdf model can describe the alpha decay or not. We consider the alpha decays of Th isotopes from ground to ground states. We can reproduce them nicely using the constant alpha decay operator (see Fig. 2). It would be quite interesting to investigate the microscopic explanation for this.

References

- 1) T. Otsuka and M. Sugita, to be published in Phys. Lett. B.
- 2) F. Iachello and A. D. Jackson, Phys. Lett. 108B (1982)151;  
H. J. Daley and B. R. Barrett, Nucl. Phys. A449 (1986) 256.

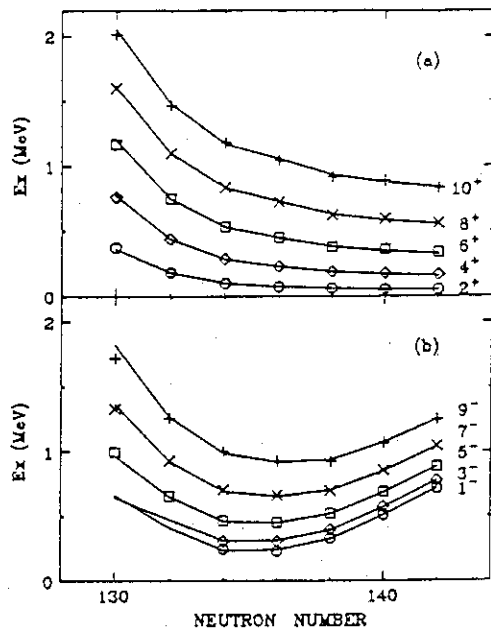


Fig. 1 Experimental (points) and theoretical (lines) energy levels of lowest states of the Th isotopes.

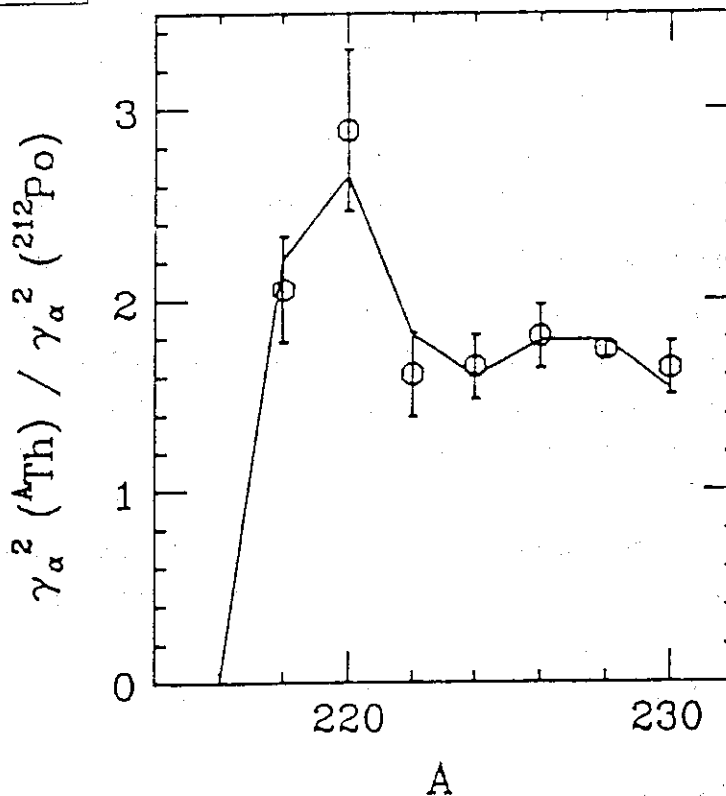


Fig. 2 Experimental (points) and theoretical (lines) relative  $\alpha$  decay widths from the Th to the Ra nuclei.

5.10 PROTON-NEUTRON SDG BOSON MODEL AND SPHERICAL-  
DEFORMED PHASE TRANSITION

Takaharu OTSUKA and Michiaki SUGITA\*

Department of Physics, University of Tokyo,

\*Department of Physics, JAERI.

The spherical-deformed phase transition in nuclei is described in terms of the proton-neutron sdg interacting boson model. The sdg Hamiltonian is formulated as a modeling of the pairing plus quadrupole interaction. The phase transition is reproduced in this framework as a function of the boson number in the Sm isotopes, while all parameters in the Hamiltonian are kept constant at values reasonable from the shell-model point of view. The sd IBM is derived from this model through the renormalization of g boson effects.

## 5.11 DAVYDOV-FILIPPOV LIMIT OF THE IBM

Michiaki SUGITA, Takaharu OTSUKA\*

and

Adrian GELBERG\*\*

Department of Physics, JAERI, \*Department of  
 Physics, University of Tokyo, \*\*Institut fur  
 Kernphysik, University of Koeln, Cologne, West Germany

The  $O(6)$  limit of the interacting boson model (IBM) is studied in connection with the rigid-triaxial-rotor model of Davydov-Filippov, and the gamma-unstable model of Wilets and Jean. The  $I=0$  deformation potential is calculated as a function of axial asymmetry  $\gamma$  by projecting a  $\gamma$  fixed intrinsic state onto the good angular momentum  $I=0$ . Although the projected potential has already been reported to have a minimum at  $\gamma=30^\circ$  for small values of the boson number  $N^1)$ , it is shown to resemble a square well at the classical limit:  $N$  infinite. This indicates that the rigid triaxial wave function differs at infinite  $N$  from the gamma unstable wave function which is the exact solution of the  $O(6)$ . The projected spectrum with  $\gamma=30^\circ$  is found to converge at infinite  $N$  to the Davydov-Filippov spectrum with  $\gamma=30^\circ$ . Thus the Davydov-Filippov limit of the IBM can be introduced as the 'projected' classical limit, although it can no longer be a good approximation to the exact  $O(6)$  solution.

References

- 1) T. Otsuka and M. Sugita, Phys. Rev. Lett. 59 (1987) 1541.



VI NEUTRON PHYSICS

6.1 A PRELIMINARY MEASUREMENT OF THE KINEMATICALLY-COLLIMATED NEUTRON SOURCES USING THE  ${}^1\text{H}({}^{10}\text{B},\text{n}){}^{10}\text{C}$  AND  ${}^1\text{H}({}^{11}\text{B},\text{n}){}^{11}\text{C}$  REACTIONS

Satoshi CHIBA, Kazuo HASEGAWA\*, Motoharu MIZUMOTO,  
and Yoshimaro YAMANOUTI

Department of Physics, JAERI,

\*Faculty of Engineering, Tohoku University

### Introduction

In the fast neutron scattering cross section measurements at the JAERI tandem accelerator facility, the  $\text{D}(\text{d},\text{n}){}^3\text{He}$  reaction has been used as the source neutron producing reaction below neutron energy of 20 MeV<sup>1,2)</sup>. This reaction, however, also produces many lower energy neutrons due to the  $\text{D}(\text{d},\text{np})\text{D}$  break-up reaction, and  ${}^{197}\text{Au}(\text{d},\text{xn})$  reaction from the beam stop made of gold. Therefore, the measurement was restricted to the elastic and inelastic scattering cross sections for some low-lying states with excitation up to 5MeV. Furthermore, these background neutrons, as well as the source neutron itself, are produced at any angles in the laboratory system and hence reduce the S/N ratio of the (n,n') and (n,n'-gamma) measurements, especially at backward angles.

If the source neutrons were produced in endothermic reactions, represented by  $\text{A}(\text{B},\text{n})\text{C}$ , with energy of particle B, say E, satisfying

$$V_G = [2m_B E / (m_A + m_B)^2]^{1/2} > v_n = \{2m_C m_A (E - E_{th}) / [(m_A + m_B)(m_n + m_C)m_n]\}^{1/2},$$

where

$V_G$  denotes velocity of the center-of-mass in the laboratory system,  
 $v_n$  velocity of neutrons in the center of mass system,  $m_x$  the mass of particle x and  $E_{th}$  the threshold energy,

the neutrons will be confined in a forward cone ( $< \theta_{max}$ ) in the Lab. frame. This maximum angle is calculated to be

$$\theta_{max} = \sin^{-1} \{ m_A (m_A + m_B - m_n) (1 - E_{th}/E) / [m_B m_n] \}$$

from a velocity diagram as shown in Fig.1. The  $\theta_{max}$  can be made small if a heavy ion is incident on a light element with an incident energy close to the reaction threshold. In the present study, a preliminary measurement was made for the "kinematically-collimated neutron sources" according to this concept. The  ${}^1\text{H}({}^{10}\text{B},\text{n}){}^{10}\text{C}$  and  ${}^1\text{H}({}^{11}\text{B},\text{n}){}^{11}\text{C}$  reactions were

selected considering the reaction Q-values<sup>3)</sup>, because these reactions are suited to produce neutrons of 10-MeV region at the JAERI tandem, in which neutron cross section data are considerably scarce.

#### Experimental Procedure and Results

The  $^{10}\text{B}$  and  $^{11}\text{B}$  beams of 65 MeV and 61 MeV were provided by the tandem accelerator, respectively. These beams had been chopped and bunched prior to acceleration. A carbon stripper foil (10 micro.g/cm<sup>2</sup>) was used to convert the  $\text{BO}^-$  molecular ions to  $\text{B}^{+4}$  ones in the high voltage terminal. Hydrogen gas (0.2MPa) was employed as the target, with a 5 $\mu\text{m}$  thick Mo entrance window and a 1.5-mm thick gold beam stop. Produced neutrons were detected by an NE213 scintillation detector at 0° with respect to the ion beam. Energies of the neutrons were determined by the time-of-flight (TOF) method. The time spread of the ion beams was 7ns.

In Figs. 2 and 3, the neutron TOF spectra are shown. Some experimental parameters are listed in Table 1 below.

Table 1 Some typical experimental conditions

Accelerated ion	$^{10}\text{B}^{+4}$	$^{11}\text{B}^{+4}$
Negative ion source	NISS	SNICS-2
Beam current on the target (nA)	2.3	80
Energy of Ion beam on the target (MeV)	65	61
Average energy loss in the Mo foil (MeV)	4.4	4.5
Average energy loss in the H <sub>2</sub> gas (MeV)	1.0	1.2
Average energy of Ion beam in the gas (MeV)	59.6	55.3
Energy of produced neutrons (MeV)	10.3	11.3
$\theta_{\text{max}}$ (degree)	26	38
Flight path (m)	1.6	3.6
Time width/ MCA channel (ns/channel)	0.257	0.346

As shown in Fig. 2, neutrons from the  $^1\text{H}(^{10}\text{B},n)^{10}\text{C}$  reaction were shielded by the continuum neutrons produced from the  $^{197}\text{Au}(^{10}\text{B},xn)$  reaction. This result is natural, considering the small cross section of the former reaction, 1.0mb, which was deduced from the "reverse" reaction cross section, i.e., the  $^{10}\text{B}(p,n)$  reaction<sup>4)</sup>.

On the contrary, the  $^1\text{H}(^{11}\text{B},n)^{11}\text{C}$  reaction is about 300mb in this

energy range<sup>5)</sup>, and hence made a clear neutron peak as shown in Fig. 3. A rough estimate of the cross section for this peak gives a value of  $170 \pm 34$  [mb/str]. This value is about twice of that of  $D(d,n)^3\text{He}$  reaction that produces neutrons of same energy<sup>6)</sup>. In this case again, the continuum background neutrons were originated from the  $^{197}\text{Au}(^{11}\text{B},xn)$  reaction from the gold beam stop. The magnitude is, however, small compared with the main peak. Consequently, this reaction has favorable properties as a "clean" neutron source. In the present experimental condition, the neutron flux at a point 10cm from the gas cell was about  $10^5$  [n/cm<sup>2</sup>/s] which might be strong enough for use as a neutron source in some (n,n') and (n,n'-gamma) experiments. The low background of this reaction might also enable us to make such a measurement as detection of more than one neutrons in coincidence, i.e., in the (n,2n) reaction.

In a subsequent work, properties of the  $^1\text{H}(^{11}\text{B},n)^{11}\text{C}$  reaction, e.g., angular distribution of neutrons, excitation function at 0-deg. and spectra of background neutrons, were measured and now under analysis.

#### References

- 1) S. Chiba et al., Jour. Nucl. Sci. Technol. 25, 511(1988).
- 2) M. Mizumoto et al., "Gamma-ray Production Cross Sections of Some Structural and Shielding Materials", Presented at the Int. Conf. Nucl. Data for Science and Technology, May 30 - June 3, 1988, Mito, Japan.
- 3) M. Drosig, Nucl. Instr. Methods, A254, 466(1987).
- 4) L.G. Earwaker et al. Nucl. Phys. 42, 521(1963).
- 5) G.J.F. Legge and I.F. Bubb, Nucl. Phys. 26, 616(1961).
- 6) M. Drosig and O. Schwerer, "Production of Monoenergetic Neutrons Between 0.1 and 23 MeV", in Handbook on Nuclear Activation Data, Apr. 1984, IAEA Technical Report Ser. 278.

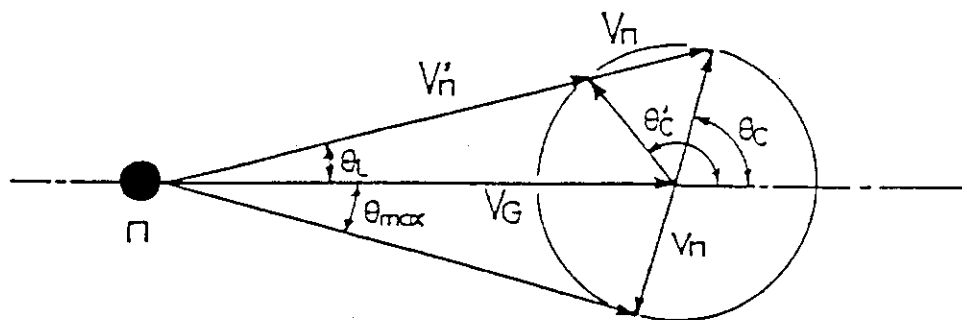


Fig.1 A schematic diagram of the relations among velocities and emission angles in the "kinematically-collimated" neutron source.

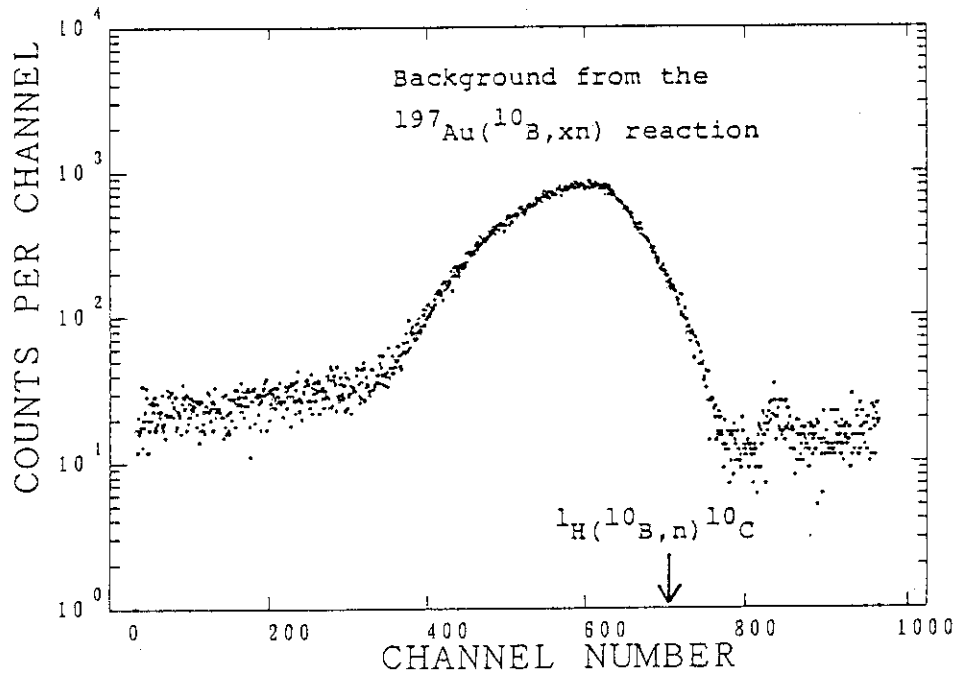


Fig.2 A TOF spectrum measured with 65-MeV  $^{10}\text{B}$  beam.

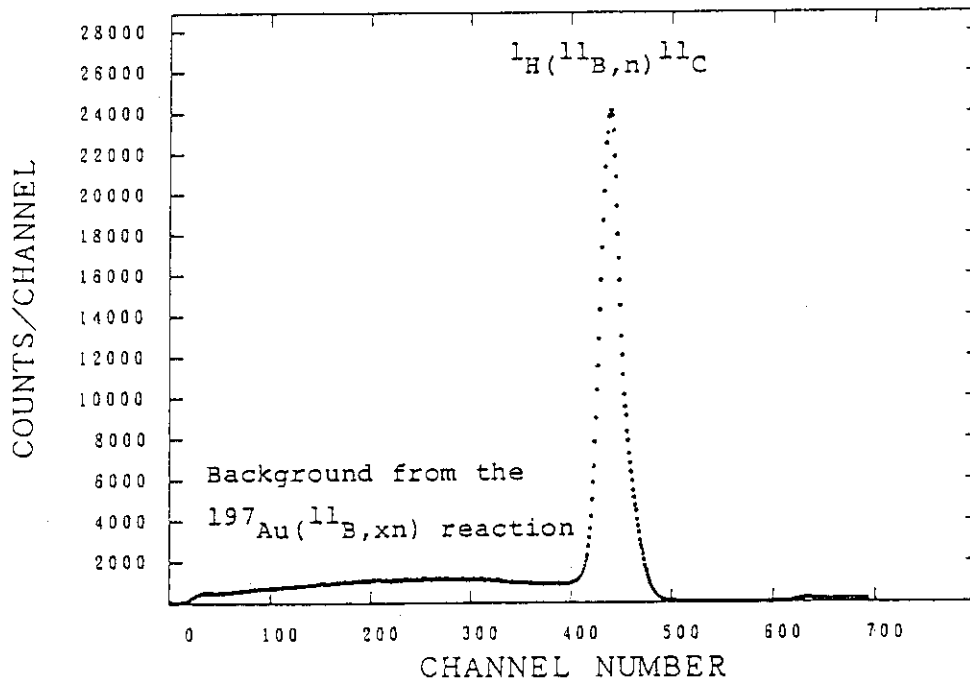


Fig.3 A TOF spectrum measured with 61-MeV  $^{11}\text{B}$  beam.

6.2 SCATTERING OF 13 MeV NEUTRONS FROM  $^{11}\text{B}$ 

Yoshimaro YAMANOUTI, Masayoshi SUGIMOTO, Yutaka FURUTA,  
Motoharu MIZUMOTO, \*Mikio Hyakutake and  
\*\*Thamrong METHASIRI

Department of Physics, JAERI, \*Department of Nuclear  
Engineering, Kyushu University, \*\*Department of Physics,  
Chulalongkorn University

Differential neutron cross sections for elastic and inelastic scattering on  $^{11}\text{B}$  were measured at an incident energy of 13 MeV in order to study the reaction mechanism for the neutron scattering on light odd nuclei. A few measurements of the neutron scattering on  $^{11}\text{B}$  in the energy range above 10 MeV have been made previously. The data available are at neutron energies of 14.1 MeV<sup>1,2)</sup> and 8-14 MeV<sup>3)</sup>. Alder et al have studied the inelastic scattering on the low-lying states of  $^{11}\text{B}$  by using the unified model, which considers two amplitudes, one corresponding to a  $^{12}\text{C}$  core transition and other to a transition of a hole, and have obtained rather good fits to the experimental data<sup>1)</sup>. In this work, particular interest was taken in the collective model analyses taking into account the inelastic compound nuclear contribution.

The measurement was performed with the pulsed beam time-of-flight method. A pulsed beam of deuterons with a repetition rate of 2 MHz and with a burst duration of about 2 nsec was provided by the JAERI tandem electrostatic accelerator. Neutrons were generated by the  $^2\text{H}(d,n)^3\text{He}$  reaction. A scattering sample of granular natural boron packed in a cylindrical aluminum can was used. The neutron detector is a 20 cm in diam by 35 cm thick NE213 liquid scintillator viewed by RCA 8854 photomultiplier tubes at the front and rear scintillator faces. Neutrons were observed by an array of these four neutron detectors for efficient measurements of scattered neutrons.

The resulting differential cross sections were corrected for multiple scattering and flux attenuation in the sample by means of the Monte Carlo method. Differential cross sections were determined for the elastic scattering and the inelastic scattering leading to the excited states at 2.125 MeV( $1/2^-$ ), 4.445 MeV( $5/2^-$ ) and 5.021 MeV( $3/2^-$ ) over the angular range from 20° to 140°.

The neutron time-of-flight spectrum taken at  $50^\circ$  is shown in fig.1.

The elastic scattering data were analyzed by the optical model with the standard form, and the best fit optical potential parameters were searched for. The compound elastic and inelastic cross sections were estimated by using the Hauser-Feshbach formalism. The (n,n'), (n,p), (n,d), (n,t) and (n,alpha) channels were considered for the outgoing channels in the compound nuclear process. The compound cross sections were scaled down by the reduction coefficient<sup>4)</sup> of 0.58 to correct the overestimate for the calculated values. These calculations were performed by means of the code ELIESE-3.

It is of great interest to study to what extent the collective model can describe the light mass nucleus  $^{11}\text{B}$ . Collective model predictions were examined by using the code DWUCK4. In the DWBA calculations the best fit optical potential parameters obtained in the optical model analysis were used. And compound inelastic cross sections were taken into account in the DWBA fits. The result obtained in the DWBA calculation for the  $5/2^-$  state at 4.445 MeV is shown in fig.2.

The experimental cross sections were also analyzed by the coupled-channel theory by using the code ECIS79 to check the nuclear shape of  $^{11}\text{B}$ . In the coupled-channel calculations the  $3/2^-$  ground state and the  $5/2^-$  state at 4.445 MeV were assumed to be the members of the  $K=3/2$  rotational band. Optical potential parameters except the spin orbit term and the quadrupole deformation parameter were adjusted to get the best fit to the experimental cross sections. The results obtained in the coupled-channel calculations are shown in fig.3. The fits to the experimental cross sections are good. The quality of the fit with oblate deformation is nearly equal to that with prolate deformation.

In the present experiment neutron cross sections for elastic and inelastic scattering on  $^{11}\text{B}$  were obtained, and the collective model calculations taking into account the compound nuclear contribution well reproduce the experimental cross sections for the ground  $3/2^-$  and excited  $5/2^-$  states of  $^{11}\text{B}$ .

#### References

- 1) J. C. Alder and B. Vaucher: Nucl. Phys. A147 (1970) 657.
- 2) M. Hyakutake et al: J. Nucl. Sci. Technol. 11 (1974) 407.
- 3) S. G. Glendinning et al: Nucl. Sci. Eng. 80 (1982) 256.
- 4) B. Zwieglinski et al: Nucl. Phys. A209 (1973) 348

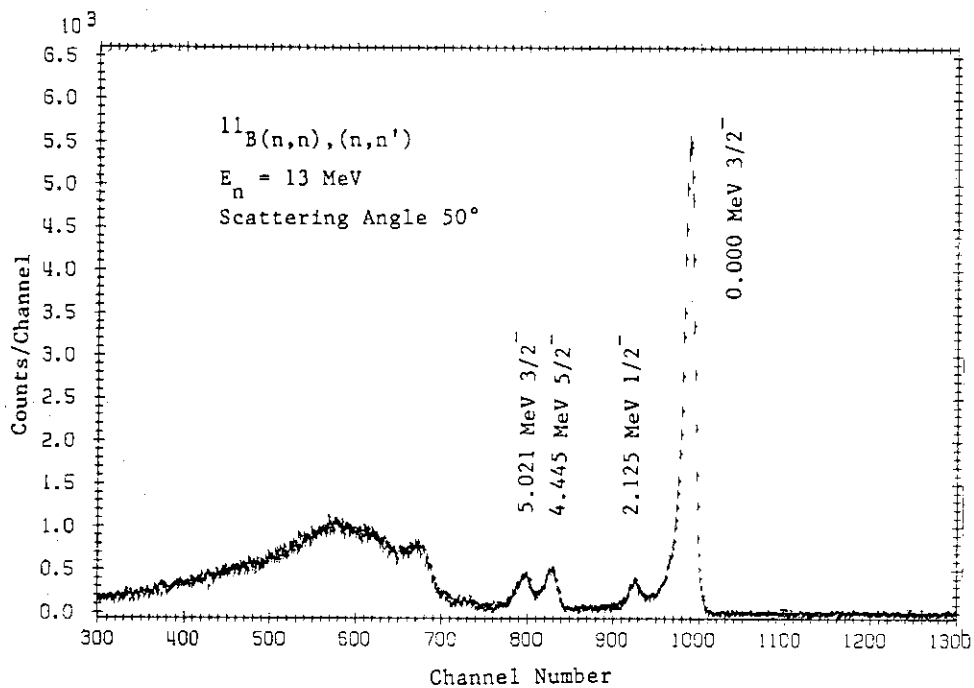


Fig.1 Neutron time-of-flight spectrum taken at  $50^\circ$ .

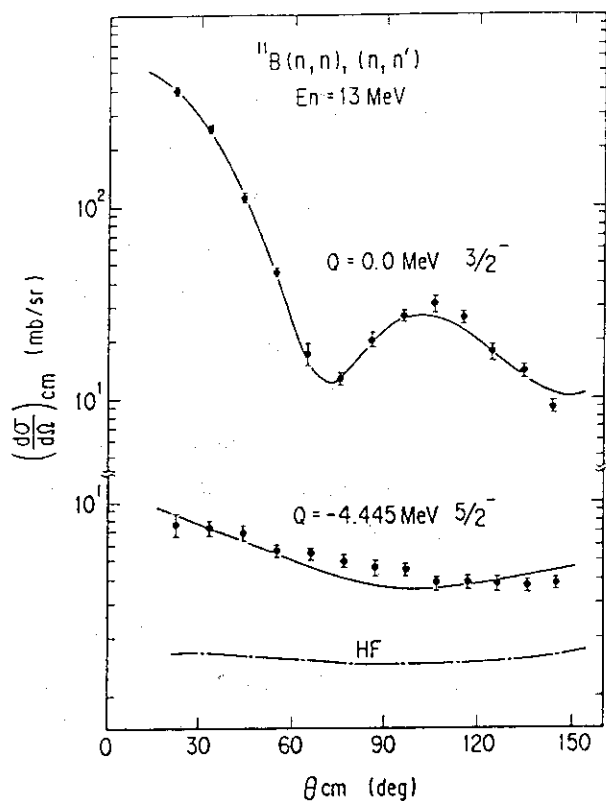


Fig.2 Experimental cross sections, and DWBA and HF predictions for  $^{11}\text{B}$ .

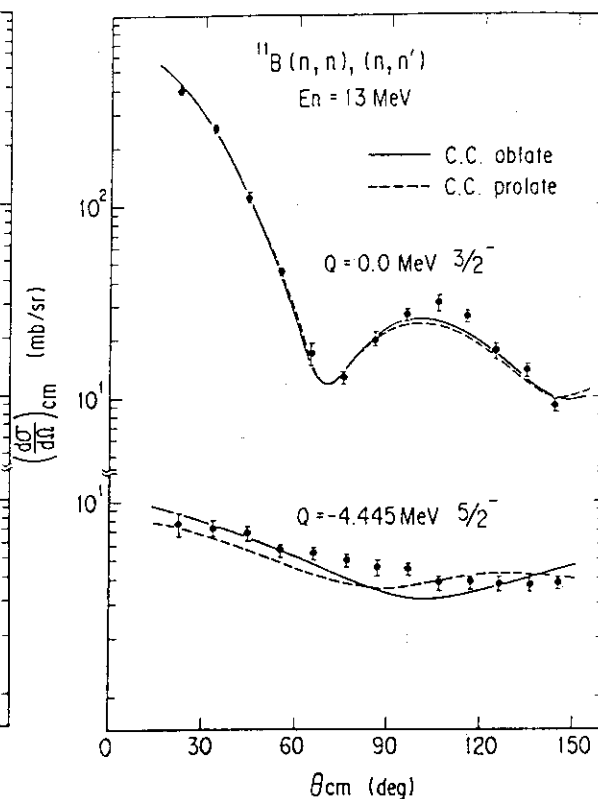


Fig.3 Experimental cross sections and CC predictions for  $^{11}\text{B}$ .



### 6.3 ANALYSIS OF THE NEUTRON SCATTERING CROSS SECTIONS OF $^{118}\text{Sn}$ AT 14.9 AND 18.0 MeV

Satoshi CHIBA,

Department of Physics, JAERI

#### Introduction

Fast neutron scattering cross sections of  $^{118}\text{Sn}$  have been measured using the JAERI tandem neutron time-of-flight spectrometer at the incident neutron energies of 14.9 and 18.0 MeV. Angular distributions for the elastic scattering, and inelastic scattering to the  $2^+$  state ( $Q=-1.23$  MeV) and to the  $3^-$  state ( $Q=-2.32$  MeV) have been obtained<sup>1)</sup>. These results are displayed in Figs. 1, 2 and 3, respectively. In the present study, they have been analyzed theoretically and some parameters have been deduced. This paper describes the method and results of the analysis.

#### Method of the parameter search

The elastic scattering angular distributions have been analyzed by the spherical optical model (SOM) at both energies. The ECIS79 code<sup>2)</sup> was used. The potential was set to be real volume Woods-Saxon + imaginary derivative Woods-Saxon + real Thomas-Fermi type spin-orbit terms. Starting from parameters of Rapaport et al.<sup>3)</sup>, six parameters for the real volume and imaginary surface parts were searched for. The result is listed in Table 1. The broken curves in Fig. 1 show the result of the calculation.

The angular distributions for the inelastic scattering were calculated by the DWBA theory with the DWUCK4 code<sup>4)</sup> using the potential parameters obtained above, and the scaling factors, i.e., the deformation parameters  $\beta_L$ , were determined assuming  $L=2$  and  $L=3$  transitions. Results are listed in Table 2 and shown as the broken curves in Figs. 2 and 3.

The elastic and inelastic scattering cross sections were also fitted by the coupled-channel theory with the ECIS79 code. The harmonic vibrational model was used. The results are listed in Table 1, and shown as the dash-dotted lines in Figs. 1, 2 and 3.

#### Discussion

The deduced deformation parameters and deformation lengths,  $\delta = R \times \beta$  where  $R$  means the real well radius, are compared in Table 2 with other ex-

perimental results. The present results are consistent with the data of Finlay et al.<sup>5,6)</sup> deduced from the same reaction. On the contrary, the quadrupole deformation parameters deduced from the (n,n') reactions are considerably smaller than those from the (p,p') reactions. Therefore, the vibration was proven not purely collective in nature.

According to the Lane model with deformation, the isoscalar deformation length ( $\delta^0$ ) is expressed as

$$\delta^0 = 1/2 \cdot (\delta_{p,p'} + \delta_{n,n'}).$$

From Table 2, this value is calculated to be  $0.704 \pm 0.012$  for L=2. This should be consistent with one deduced from the ( $\alpha, \alpha'$ ) scattering, because  $\alpha$  scattering is entirely isoscalar. This value is really consistent with the data of Baron et al.<sup>7)</sup> listed in Table 2, although their uncertainty is relatively large.

The ratios,  $\beta_{2(p,p')}/\beta_{2(n,n')}$ ,  $\beta_{2(n,n')}/\beta_{2(EM)}$ , and  $\beta_{2(p,p')}/\beta_{2(EM)}$  have been calculated and listed in Table 3. In this table, theoretical values are also listed calculated from the core-polarization theory<sup>8,9)</sup> that expresses these ratios with a  $2 \times 2$  effective charge matrix. Elements of the effective charge matrix were calculated according to the no-parameter and one-parameter schematic models (NPSM, OPSM) and no-parameter and one-parameter Bohr Mottelson models (NPBM, OPBM). Among these four models, the OPSM gives the best results; the ratios are almost consistent in the experimental uncertainties in all quantities.

With regard to the octupole deformation parameters,  $\beta_3$ , there are no differences among the (n,n'), (p,p') and ( $\alpha, \alpha'$ ) results. Although it is expected that the isovector deformation might be larger than the isoscalar one, this result shows that they might be equal in this excitation region.

### References

- 1) S. Chiba et al., JAERI-M 86-112, 155(1986).
- 2) J. Raynal, "Notes on ECIS79", unpublished.
- 3) J. Rapaport et al., Nucl. Phys., A341, 56(1980).
- 4) P. D. Kunz, "DWUCK4", unpublished.
- 5) R. W. Finlay et al., Nucl. Phys. A338, 45(1980).
- 6) R. W. Finlay et al., Nucl. Phys. A344, 257(1980).
- 7) N. Baron et al., Phys. Rev. 146, 861(1966).
- 8) V. R. Brown et al., Phys. Rev. C11, 1298(1975).
- 9) V. A. Madsen et al., Phys. Rev. C12, 1205(1975).

Table 1 Optical potential parameters<sup>\*1</sup>

En (MeV)	model	$V_r$ (MeV)	$r_0$ (fm)	$a$ (fm)	$W_d$ (MeV)	$r_i$ (fm)	$a_i$ (fm)	cpp <sup>*2</sup>
14.9	SOM	48.9	1.17	0.621	7.52	1.15	0.581	6.5
	CC	49.4	1.17	0.621	6.53	1.15	0.581	10.2
18.0	SOM	44.1	1.23	0.712	8.90	1.21	0.506	5.0
	CC	44.5	1.23	0.712	7.88	1.21	0.506	6.1

\*1; the optical potential has the standard form with a real volume term, a surface derivative imaginary term and a real Thomas-Fermi type spin-orbit term. The spin-orbit term was fixed to be  $V_{so}=6.2$  MeV,  $r_{so}=1.01$  and  $a_{so}=0.76$ fm.

\*2; chi-squares per point for the elastic scattering cross sections

Table 2 Quadrupole and Octupole deformation parameters and lengths deduced from various kinds of transition.

Reaction	Reference	Energy	Method	$\beta_2$	$\delta_2$	$\beta_3$	$\delta_3$
(n,n')	Present	average	DWBA	0.115±0.006	0.674±0.035	0.172±0.014	1.01 ±0.08
(n,n')	Finlay+	11.0	DWBA	0.108±0.007	0.636±0.041	0.173±0.029	1.02 ±0.14
(p,p')	Makosfke+	16.0	DWBA	0.134±0.010	0.789±0.059	0.168±0.014	0.989±0.014
(p,p')	Beer+	24.5	DWBA	0.134±0.004	0.743±0.022	0.174±0.110	0.964±0.061
( $\alpha,\alpha'$ )	Baron+	40.0	DWBA	0.10 ±0.02	0.72 ± 0.14	0.15 ±0.03	1.1±0.2
EM	Raman+		Eval <sup>*</sup>	0.111±0.002	0.653±0.012		

\* : Evaluation of Raman et al. from the experimental  $B(E2)^+$  values.

Table 3 Comparison of the ratios of the Quadrupole deformation parameters deduced from different kinds of transition with theory.

Quantity	NPSM	OPSM	NPBM	OPBM	Exp.
$\beta_2(p,p')/\beta_2(n,n')$	1.13	1.10	1.20	1.18	1.14 ± 0.04
$\beta_2(n,n')/\beta_2(EM)$	1.07	1.05	1.06	1.05	1.01 ± 0.03
$\beta_2(p,p')/\beta_2(EM)$	1.20	1.15	1.26	1.24	1.15 ± 0.03

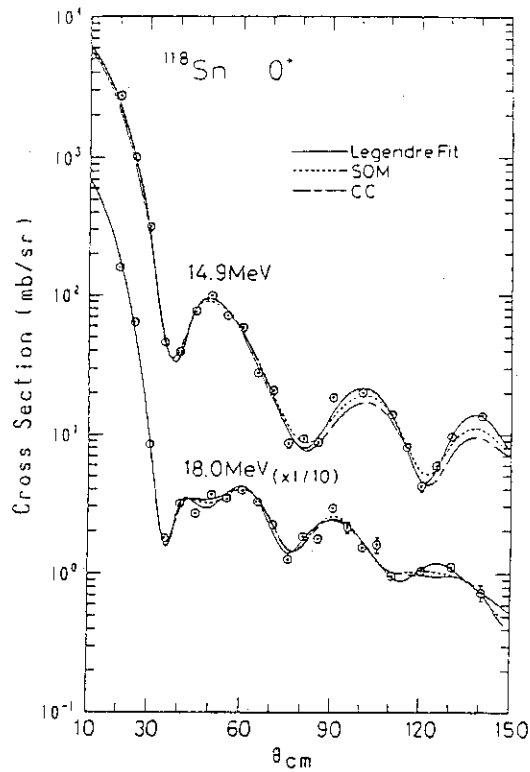


Fig.1 Angular distributions of elastically scattered neutrons from  $^{118}\text{Sn}$ .

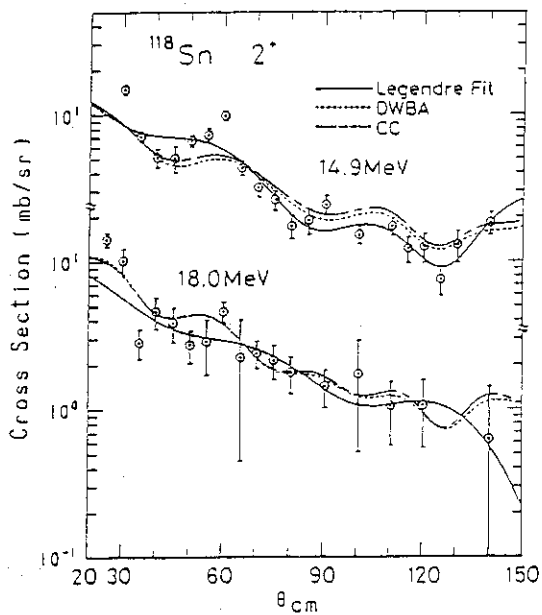


Fig.2 Angular distributions of inelastically scattered neutrons from the first  $2^+$ -state of  $^{118}\text{Sn}$ .

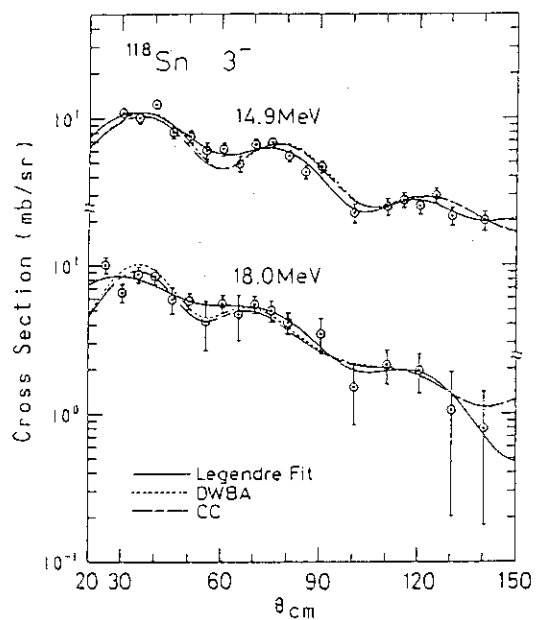


Fig.3 Angular distributions of inelastically scattered neutrons from the  $3^-$ -state of  $^{118}\text{Sn}$ .

## 6.4 MEASUREMENTS OF GAMMA-RAY PRODUCTION CROSS SECTIONS

Kazuo HASEGAWA, Motoharu MIZUMOTO, Satoshi CHIBA,  
 Yoshimaro YAMANOUTI, Masayuki IGASHIRA\*,  
 Toshiro UCHIYAMA\*, Hideo KITAZAWA\*, Manfred DROSG\*\*

Department of Physics, JAERI, \*Research Laboratory for  
 Nuclear Reactors, Tokyo Institute of Technology,

\*\*University of Wien, Austria

### Introduction

Gamma-ray production cross sections are necessary to calculate the radiation shielding and the gamma-ray heating both for fission and fusion reactors. Experimental data measured using monoenergetic neutron sources are scarce especially in the energy range from 5 to 14 MeV, where adequate neutron sources have not been available. Measurements to obtain whole gamma-ray spectra including the continuum part have been carried out mainly with the white neutron source using the electron linear accelerator. Their neutron energy spread, however, was usually very wide due to the low counting statistics especially in the high energy region.

For the evaluation of JENDL-3, the gamma-ray production cross sections for several important nuclei have been newly evaluated. The evaluated results are now being tested with experimental gamma-ray data as well as neutron data.

Our aims in this experiment are to provide accurate gamma-ray production data for structural and shielding materials such as Al, Si, Fe and Pb in the MeV region with higher neutron energy resolution.

### Experiment

The experimental arrangement is shown in Fig. 1. Neutrons were produced in a 3 cm long 0.2 MPa pressurized gas target by the  ${}^2\text{H}(d,n){}^3\text{He}$  reaction. A deuteron beam was extracted from the in-terminal ion source of the JAERI Tandem Accelerator and was accelerated up to 5 MeV to produce neutrons of 7.8 MeV, where the effects of break-up neutrons could be ignored. The average beam current and pulse width were 0.5  $\mu\text{A}$  and 4 ns, respectively, at a 2 MHz repetition rate.

Gamma-ray spectra were measured with a 7.6 cm dia. x 15.2 cm long

NaI(Tl) detector, which was surrounded by a 25.4 cm dia. x 25.4 cm long NaI(Tl) annular detector. These two detectors were operated in an anti-coincidence mode to suppress the Compton backgrounds in the NaI detector. The sample was placed at a distance of 9.8 cm from the neutron target and the gamma-ray detector was located at about 80

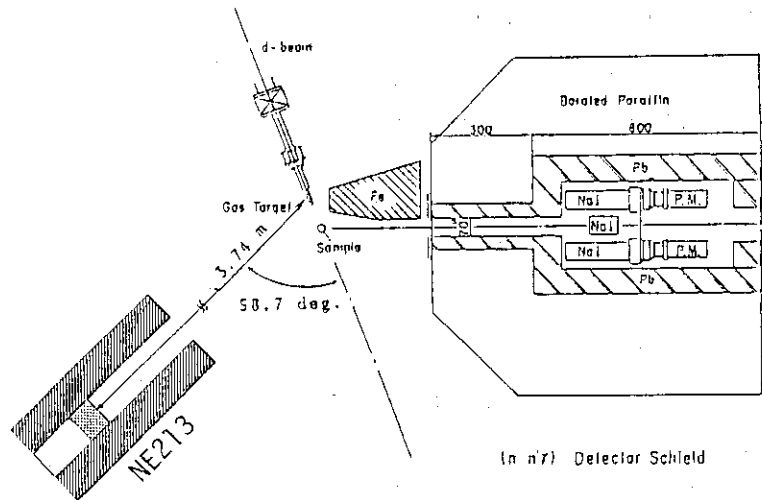


Fig. 1 Experimental arrangement

cm from the sample. The size of all samples was 3cm dia. x 3cm long. Data were taken at a 90 degree in the present experiment.

The neutron spectra were measured at the same time employing a 5 cm dia. x 1.27 cm thick NE213 detector located at a distance of 3.74 m from the neutron source and at an angle of 58.7 degree.

### Analysis

The response function of this anti-Compton NaI detector was determined to obtain absolute gamma-ray yields. The several standard gamma-ray sources such as,  $^{137}\text{Cs}$ ,  $^{60}\text{Co}$ ,  $^{88}\text{Y}$ ,  $^{22}\text{Na}$  and  $^{24}\text{Na}$  were used to examine the response function. The spectra were also obtained for the 4.43 MeV gamma-rays from the  $^{12}\text{C}(n,n')$  reaction and the 6.1 MeV gamma-rays from  $^{16}\text{O}(n,n')$  reaction. After subtracting backgrounds, gamma-ray pulse height spectra were unfolded using the computer program FERDOR<sup>1)</sup>.

In general, a large sample size is needed in order to decrease the uncertainty due to counting statistics of raw data. However, the corrections for absorption and multiple scattering both for neutrons and gamma-rays in the sample become large as the sample size increases. The calculations for these corrections are usually carried out by a Monte Carlo method because analytical solutions are very complicated. Computer codes "MNSCAT" and "COMPCALC" are newly prepared for these calculations. The calculated results are shown in Fig. 2 for Pb. While the correction

factors for Compton scattering are negligible in the high energy region, they become as much as 40 % in the low energy region.

Results

The results are shown in Figs. 3-6, together with the data taken at ORELA<sup>2-5</sup>). The overall agreement of our spectral shapes for all the samples with the ORELA data seems quite good.

The peak areas in the low energy parts of the present results are generally lower than the previous results. This may be partly affected by the difference of the sample size correction methods.

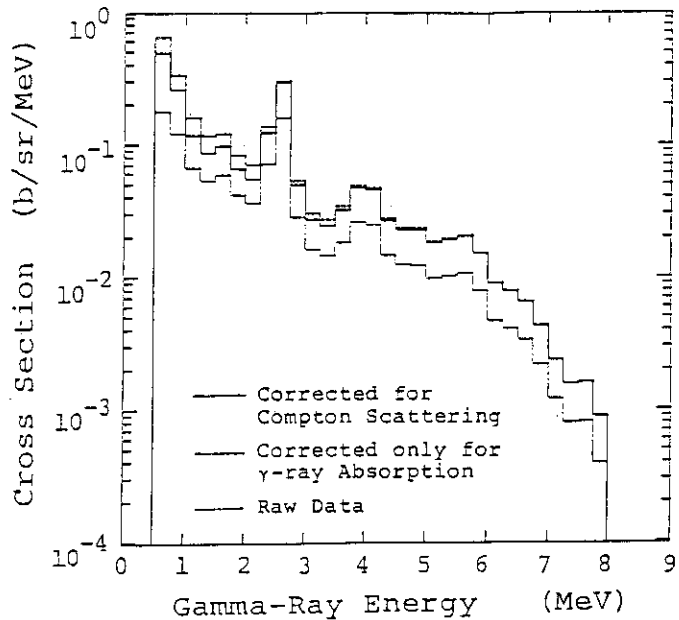


Fig. 2 Sample size corrections for gamma-ray spectrum of Pb

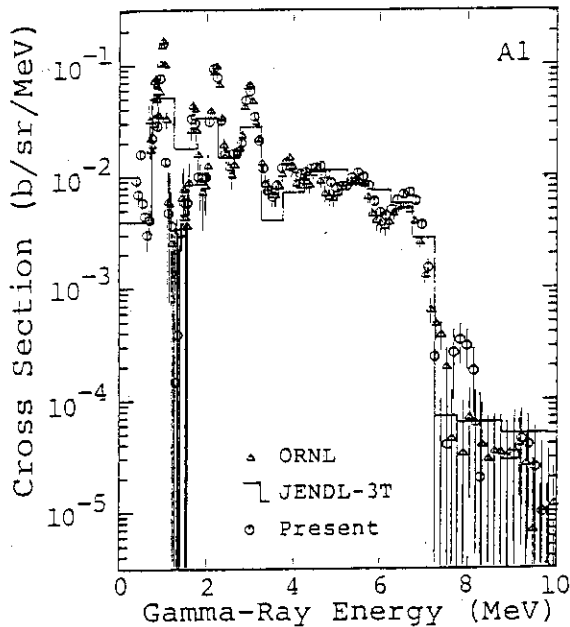


Fig. 3 Comparison of the present results with the data of ORELA and JENDL-3T for Al

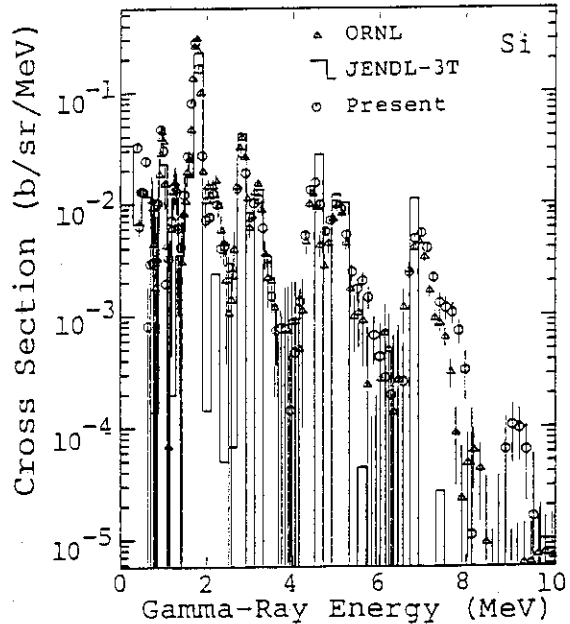


Fig. 4 Comparison of the present results with the data of ORELA and JENDL-3T for Si

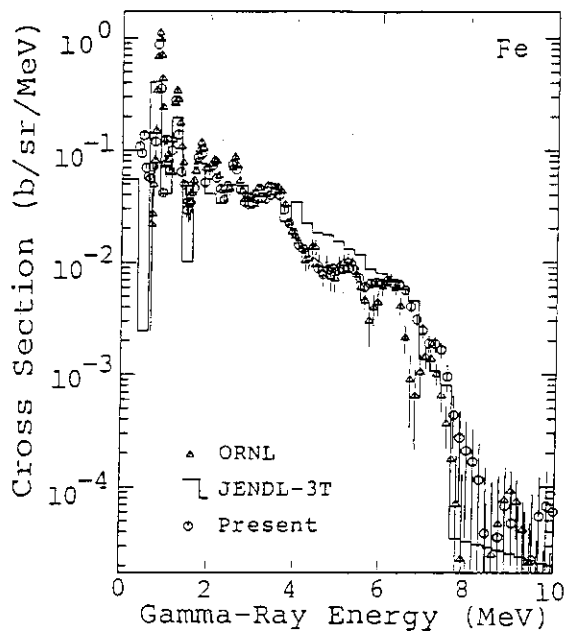


Fig. 5 Comparison of the present results with the data of ORELA and JENDL-3T for Fe

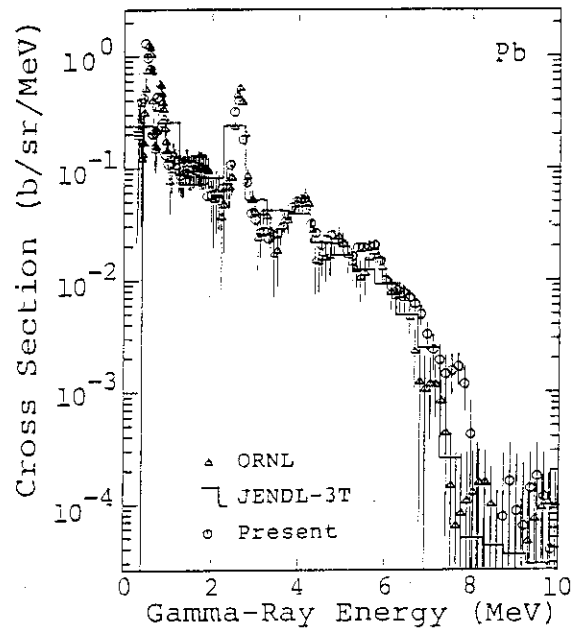


Fig. 6 Comparison of the present results with the data of ORELA and JENDL-3T for Pb

The data stored in JENDL-3T<sup>6)</sup>, were also compared and checked with the present results. Although the energy bin for the evaluations in some cases is too broad, the evaluations represent the present experimental data reasonably well. Data on gamma-rays resulting from these reactions allow evaluators to check the validity of various reaction models to calculate these cross sections.

#### References

1. H. Kendrick and S. M. Sperling, GA-9882 (1970)
2. J. K. Dickens, T. A. Love and G. L. Morgan, ORNL TM-4232 (1973)
3. J. K. Dickens, T. A. Love and G. L. Morgan, ORNL TM-4389 (1973)
4. G. T. Chapman, G. L. Morgan, F. G. Perey, ORNL TM-5416 (1976)
5. G. T. Chapman and G. L. Morgan, ORNL TM-4822 (1975)
6. JENDL Compilation Group (Nuclear Data Center JAERI), JENDL-3T private communication (1988)



6.5 NONDESTRUCTIVE ELEMENTAL ANALYSIS  
BY THE METHOD OF NEUTRON RESONANCE ABSORPTION

Isamu ISHIKAWA, Noboru TACHIKAWA, Makio OHKUBO<sup>\*</sup>  
and Hiroshi TOMINAGA.

Department of Radioisotopes,<sup>\*</sup> Department of Physics, JAERI

INTRODUCTION

The application of neutron resonance absorption to the analysis of material element and element-sensitive radiography was attempted in some laboratories<sup>1,2,3</sup>). We took up recently this technique as a promising one just suitable to the new long-term development program in Japan Atomic Energy Research Institute. Our final goal is to establish a novel technique of element-sensitive computer tomography by using resonance absorption in transmission of epithermal neutrons.

As the first step of the development program, a feasibility study has been made of nondestructive elemental analysis by means of the resonance absorption of pulsed neutrons at a time-of-flight spectrometer of the 120 MeV electron linear accelerator. Some typical elements were analyzed which have large resonance cross sections in ordinary metals, such as cobalt and manganese in stainless steels. Cobalt in a stainless steel is an important element which has to be checked, since in the nuclear industry and related fields it produces a significant amount of residual radioactivity under neutron irradiation. On the other hand, calculations were made to clarify an optimal condition of the analysis and a limit of detection of an element in a general form.

EXPERIMENTAL PROCEDURE

Neutron transmission measurements in a region of epithermal neutrons were carried out on the JAERI Linac time-of-flight spectrometer with a 47m flight path. Pulsed neutrons were generated by bombarding a water-cooled tantalum target by a pulsed electron beam from the Linac. The electron beam energy was 120 MeV, peak current ~2A, pulse width 50ns and repetition rates 150pps. High energy neutrons generated were slowed down with a water moderator in which boron nitride powder was contained to reduce the intensity of hydrogen capture gamma-rays. Neutrons from the moderator were transmit-

ted through a lead gamma-shield, a boron nitride filter, a vacuum flight tube, a collimator of 38mm diameter and a sample to be analyzed, and finally detected with a  $^6\text{Li}$ -glass scintillator of 12.5mm thickness. The time-of-flight spectrum of the transmitted neutrons was measured with a 4096 channel analyzer, with start signals based on the electron beam pulses.

The determination of a specific element in a sample was performed by analyzing the energy and the net peak area of its resonance absorption, with the aid of a modified Atta-Harvey code, using known resonance parameters in a nuclear data file of ENDF/B-V. To confirm the validity of this analysis method, standard samples of steels and aluminum alloys were employed. The analyses of cobalt and so forth in stainless steel samples supplied from different manufacturers were conducted as trial applications.

### RESULTS AND DISCUSSION

The energy spectrum of epithermal neutrons observed without any sample was proportional to  $E^{-0.74} \text{ m}^{-2} \text{ eV}^{-1}$  on the whole, and the total neutron flux per pulse was estimated to be about  $1.2 \times 10^5 \text{ m}^{-2}$  at the position of the detector.

Figure 1 shows examples of neutron time-of-flight spectra for the open beam, and for the beams with SUS304 stainless steel samples of 5mm thickness, containing known amounts of manganese and unknown cobalt. Table 1 shows a result of the analysis of the same samples.

The results of the de-

termination of manganese agreed well with the known values.

In a theoretical approximation, a detection limit of an element to be analyzed, in the unit of weight fraction, is expressed as follows:

$$\Delta\omega = \frac{\Delta C}{\mu_0 \rho l B}, \quad \mu_0 = \frac{\pi}{2} \cdot \frac{\Gamma \sigma_0}{\Delta E} \cdot \frac{N_0}{A}$$

where  $\Delta C$  is the estimation error of net peak area count,  $\rho$  the sample den-

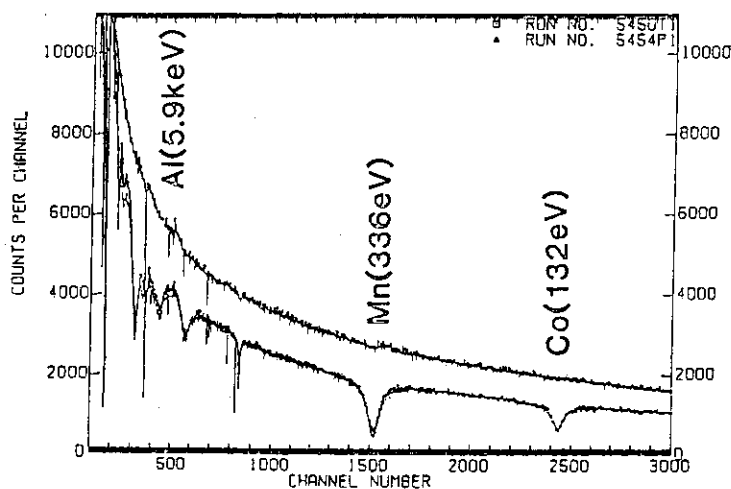


Fig. 1 Neutron time-of-flight spectra.

Table 1 Results of the analysis of manganese and cobalt in SUS304 stainless steel samples.

sample	Mn abundance %		Co abundance %	
	observed	anal.	observed	anal.
A	1.03 ± 0.04	1.07	0.195 ± 0.021	0.178
B	0.85 ± 0.04	0.85	0.232 ± 0.023	0.235
C	1.11 ± 0.05	1.15	0.046 ± 0.016	0.051
D	0.82 ± 0.06	0.84	0.167 ± 0.017	0.161

sity,  $\ell$  the sample thickness,  $B$  the background count in the peak region,  $\Delta E$  the energy width of the peak region used,  $\Gamma$  the total width of the resonance,  $\sigma_0$  the resonance cross section at the peak energy,  $N_0$  is the Avogadro number and  $A$  the atomic weight of the element.

The statistical error of  $\Delta C$  will be roughly  $\sqrt{2B}$  (in  $1\sigma$ ) and  $B = B_0 \exp(-\mu_m \rho \ell)$ ;  $\mu_m$  is the mass attenuation coefficient of the sample matrix at the energy of the resonance. Then, the optimal sample condition to minimize the statistical error comes to  $\mu_m \rho \ell = 2$ , which corresponds to about a thickness of 14mm in the case of the steel samples in Fig.1. The detection limit of cobalt in the steel in that condition is calculated as

$$\Delta \omega \approx \frac{\sqrt{2}}{0.8 \sigma_0 (N_0/A) \rho \ell \sqrt{B}} \approx 1 \times 10^{-5} \text{ (i.e. } \sim 10 \text{ ppm)}$$

where  $\sigma_0 = 1.0 \times 10^4$  barns ( $10^{-28} \text{ m}^{-2}$ ),  $N_0 = 6 \times 10^{23}$ ,  $A = 5.9 \times 10^{-2}$  kg,  $\rho = 8 \times 10^3 \text{ kg} \cdot \text{m}^{-3}$ ,  $\ell = 1.4 \times 10^{-2} \text{ m}$ ,  $B = (e^{-2}/0.5) \times (1 \times 10^3 \text{ counts/channel}) \times (10^2 \text{ channels})$ .

The figures in the above results and discussion show a great possibility of the method of neutron resonance absorption.

#### REFERENCES

- 1) R. A. Schrack, J. W. Behrens, R. G. Johnson and C. D. Bowman  
IEEE Trans. NS-28, 1640 (1981).
- 2) M. G. Strauss, G. H. Lander, R. Brenner and C. T. Roche  
"Proceedings of World Conference on Neutron Radiography" December 7-10, 1981, San Diego, CA.
- 3) R. A. Schrack, Radiation Effects, 95/1-4, 1309 (1986).

## 6.6 CONSTRUCTION OF A STABILIZATION SYSTEM FOR PHOTO-MULTIPLIERS' GAIN USING A REGULATED LIGHT-EMITTING DIODE

Satoshi CHIBA and Fumio HIROKI\*

Department of Physics, JAERI,

\*Department of Engineering Service, JAERI

### Introduction

Scintillation detectors are widely used in many fields of nuclear measurements, combined with photomultiplier tubes (PMT) and register networks. Gain of a photomultiplier tube is, however, not stable against several perturbations loaded on it: changes in counting rate, changes in temperature and fatigue of the tube due to aging, etc. It is difficult to recognize the gain change especially in measurements of neutrons using hydrogenous scintillators, because there are no pronounced structures in the pulse height spectrum of recoil protons.

In the present study, a system was designed and constructed to stabilize the gains of PMTs by using a reference light produced from a light-emitting diode (LED), whose output is also stabilized by an essentially stable and drift-free photo-diode (PD)<sup>1)</sup>.

### Overview of the system

A schematic diagram of the present system is displayed in Fig.1. It consists of two loops: one is to stabilize the light power of an LED using a PD, amplifier and a "LED Stabilizer", the other is one to stabilize the gain of a PMT with a "H.V. Stabilizer", using the regulated LED light. As an example, a combination of RCA8575 PMT, ORTEC 265 base assembly, a green LED HLMP-1540 (YHP) and a PD G1116 (HAMAMATSU) was used in this work.

In the LED stabilization loop, the LED is driven by the LED Stabilizer. This module produces rectangular current pulses of length of 100 to 1000ns, depending on a front panel switch. Output of the LED is extracted by a plastic optical fiber (ESKA Extra) of diameter 1mm, and divided into two portions by an optical divider. Then one branch is used in the LED stabilization loop and the other in the PMT loop. In the LED loop, the branched light is detected by a PD, and converted to a voltage pulse by a charge sensitive pre. amplifier, and it is subsequently amplified to a certain voltage. This pulse is then fed into the LED Sta-

bilizer. If this feedback pulse is less than a reference voltage, the LED Stabilizer will increase the current that drives the LED, and vice versa. In this way, the light output from the LED is stabilized.

In Figs.2 and 3, dependences on the running time and temperature of a non-stabilized and stabilized LED are shown. The output of a non-stabilized LED has a strong dependence on temperature; the output power varies from +20% to -13% in the range from 0 to 50°C. As in Fig. 2, the light power of the LED also drifts depending on time. Note that this property is measured by keeping the temperature of the LED constant. By using the presently constructed system, the LED output can be stabilized to +0.5% as shown in these figures, which will be stable enough for use as a "reference" light.

In the PMT loop, this "regulated" reference light is detected by the PMT concurrently with the scintillation lights made by radiations. Only pulses corresponding to the LED light is selected by a linear gate module, and its output is fed into the H.V. Stabilizer. This module is inserted between the PMT and a high voltage power supply and acts as a "variable resistor". In this module, the input pulse is integrated with a time constant of 3 to 10 sec. and is compared with a reference voltage. If this feedback pulse is smaller than a reference voltage, this module decrease its resistance, i.e., increases the current that is supplied to the breeder resistors of the PMT, and consequently increases its gain, and vice visa. By this loop, the pulse heights that correspond to LED's reference light is kept constant.

In Fig.4, the long term stability of the PMT is shown. It has been obtained by measuring the 1.33-MeV gamma-rays from a  $^{60}\text{Co}$  source by a NaI(Tl) scintillator. For this PMT, there is essentially no drift within 5-days operation even without stabilization. By changes of the counting rate, however, the gain of the non-stabilized PMT changes as much as +15% at  $3 \times 10^4$  [cps] as shown in Fig.5. Gain of the stabilized PMT is, on the contrary, stabilized to -0.9% change at this counting rate, which will be tolerable in actual nuclear measurements. As a conclusion, by using the presently constructed system, the gain of a PMT can be stabilized to +1%, during several-days' operation and counting rate range from 0 to  $3 \times 10^4$  [cps].

#### Reference

- 1) W.L.Reiter and G.Stengel, Nucl. Instr. Methods, 173, 275(1980).

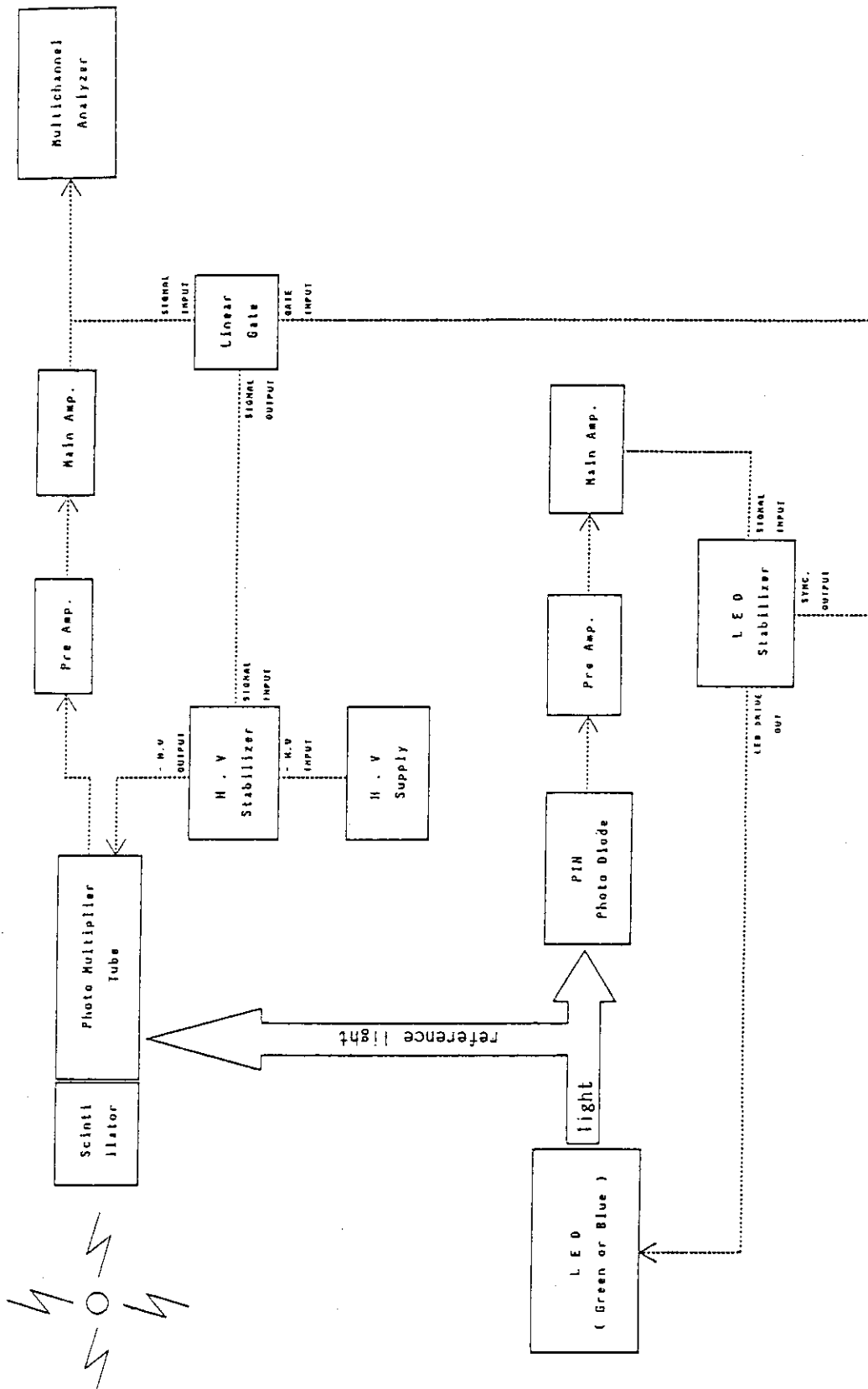


Fig. 1 An overview of the present stabilization system.

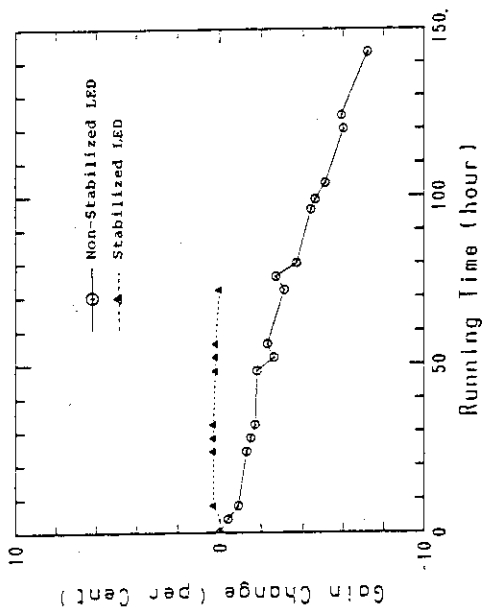


Fig. 2 Dependence of an LED output power on running time.

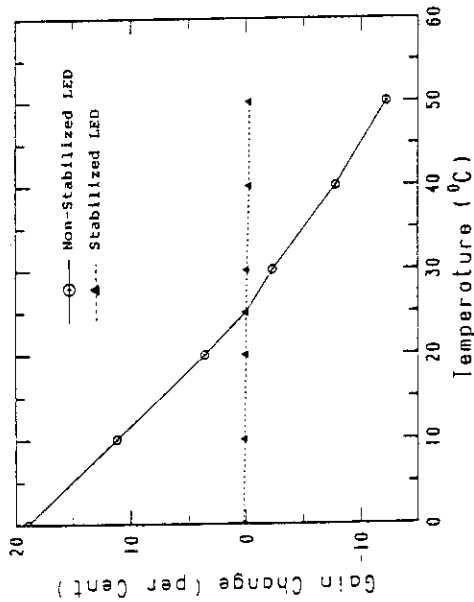


Fig. 3 Dependence of an LED output power on temperature.

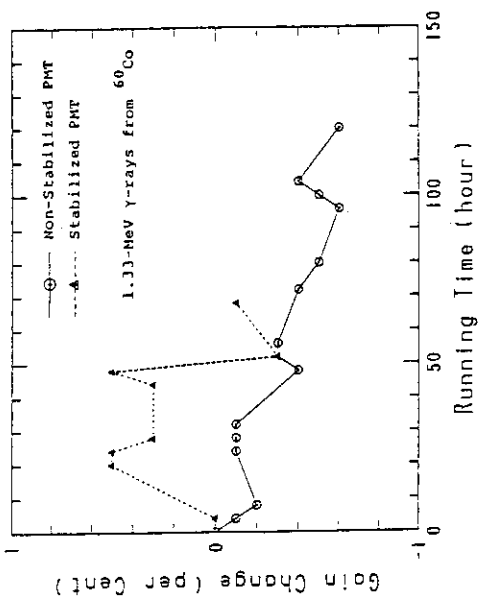


Fig. 4 Dependence of a PMT output on running time.

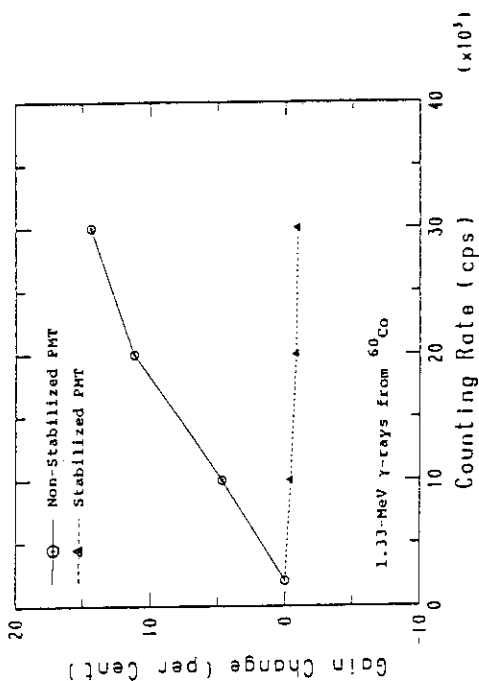


Fig. 5 Dependence of a PMT output on counting rate.

## Ⅵ PUBLICATIONS



Publications in Journals and Proceedings

Aruga, T., Nakata, K. and Takamura, S.  
Computer Simulation of Damage Depth Profiles for 2 - 7.5 MeV/amu  
Heavy Ions Incident on Pure Metals.  
Nucl. Instr. and Meth. B in press.

Awaya, Y., Hino, K., Hitachi, A., Kanai, Y., Kwatsura, K.,  
Kuroki, K., Vogt, H., Yamazaki, Y. and Watanabe, T.  
Photon Angular Distributions of the Relativistic Radiative  
Electron Capture.  
High-Energy Ion-Atom Collisions, edited by D. Berenyi and  
G. Hock (Springer-Verlag, Berlin, 1988) p.185.

Baba, S., Hata, K., Ichikawa, S., Sekine, T., Nagame, Y.,  
Yokoyama, A., Shoji, M., Takahashi, T., Saito, T. and  
Fujiwara, I.  
Evaporation Residue Formation Competing with Fission Process in  
the  $^{197}\text{Au}+^{16}\text{O}$ ,  $^{12}\text{C}$  Reactions and the Fission Barriers at  
Specified J Window.  
Z. Phys. A, in press.

T

Beckerman, M., Auble, R.L., Bertrand, F.E., Blankenship, J.L.,  
Burks, B.L., Fernandes, M.A.G., Glover, C.W., Gross, E.E.,  
Horen, D.J., Sayer, R.O., Satchler, G.R., Shapira, D.,  
Sugiyama, Y. and Varner, R.L.  
Elastic and Inelastic Scattering of  $^{58}\text{Ni}+^{208}\text{Pb}$  at Bombarding  
Energies from 598 to 1011 MeV.  
Phys. Rev. C36 (1987) 657.

T

Chiba, S., Yamanouti, Y., Mizumoto, M., Hyakutake, M. and Iwasaki, S.

Measurement of Fast Neutron Scattering Cross Sections of Li-7 at 11.0 and 13.0 MeV.

J. Nucl. Sci. Technol. 25 (1988) 210.

T

Chiba, S., Yamanouti, Y., Sugimoto, M., Mizumoto, M., Furuta, Y., Hyakutake, M. and Iwasaki, S.

Fast Neutron Scattering Cross Sections of Sn-118 at 14.9 and 18.0 MeV.

J. Nucl. Sci. Technol. 25 (1988) 511.

T

Chiba, S.

Evaluation of the Fusion-Related Neutron Nuclear Data for JENDL-3.

JAERI-M 88-065 (1988) 75.

Fujita, H., Kato, N., Sugimitsu, T. and Sugiyama, Y.  
Three-Body Coupled Channel Analysis of  $^{19}\text{F}+^{12}\text{C}$  and  $^{19}\text{F}+^{16}\text{O}$   
Elastic and Inelastic Scattering.

JAERI-M 88-100 (1988) 90.

T

Ichikawa, S., Iimura, H., Oshima, M., Sekine, T. and Takahashi, T.  
Selective Mass Separation of Light Lanthanoids by Means of Ionization of their Monoxides.

Nucl. Instr. Meth. A., in press.

T

Ichikawa, S.

A High-Temperature Surface-Ionization Ion Source for the JAERI ISOL.

KURRI-TR-291 (1987) 12.

T

Ikezoe, H., Shikazono, N., Tomita, Y., Sugiyama, Y., Ideno, K., Yokota, W., Nagame, Y., Lee, S.M., Ogihara, M., Jeong, S.C., Fujiwara, H., Hinde, D.J.

Mass Distributions of Fission Fragments in the  $^{19}\text{F}+^{197}\text{Au}$  Reaction.

To be published in Z. Phys. A.

T

Ikezoe, H., Shikazono, N., Tomita, Y., Sugiyama, Y., Ideno, K., Yokota, W., Nagame, Y., Lee, S.M., Ogihara, M., Jeong, S.C., Fujiwara, H., Hinde, D.J.

Mass Distributions of Fission Fragments in the  $^{19}\text{F}+^{197}\text{Au}$  Reaction.

Proc. of Riken-IN2P3 Symposium on Heavy-Ion Collisions in Shimoda (1987) p247.

T

Ikezoe, H., Shikazono, N., Tomita, Y., Sugiyama, Y., Ideno, K., Yokota, W., Nagame, Y., Lee, S.M., Ogihara, M., Jeong, S.C., Fujiwara, H., Hinde, D.J.

Mass Distributions of Fission Fragments in the  $^{19}\text{F}+^{197}\text{Au}$  Reaction.

JAERI-M 88-100, p108 (1988).

T

Ishii, T., Ishii, M., Makishima, A., Yanagida, K. and Ogawa, M.  
G-factor of the side band based on the  $10^2+$  state in  $^{126}\text{Ce}$ .

Int. Conference on Nuclear Structure through Static and  
Dynamic Moments, Melbourne, Australia, 1987, Vol.1, p21.

T

Ishii, T., Ishii, M., Yanagida, K. and Ogawa, M., Makishima, A.  
Precession of Rare-earth Nuclei in Ta after Transit through Gd.

Int. Conference on Nuclear Structure through Static and Dynamic  
Moments, Melbourne, Australia, 1987, Vol.1, p22.

T

Ishii, T., Ishii, M., Makishima, A., Yanagida, K. and Ogawa, M.  
G-factor of the side band based on the  $10^2+$  state in  $^{126}\text{Ce}$ .

Int. Conference on Nuclear Structure through Static and Dynamic  
Moments, Melbourne, Australia, 1987, Vol.2, p93.

T

Ishii, K., Sataka, M., Kawatsura, K., Nakai, Y., Ozawa, K.,  
Komaki, K. and Ootuka, A.

Line Identification of Foil-Excited Cl Ion.

JAERI-M 87-134 (1987) 77.

T

Itahashi, T., Fukuda, T., Shimoda, T., Fujita, Y., Yamagata, T.  
and Nagame, Y.

Mass Spectrometry of  $^{41}\text{Ca}$  with the RCNP Cyclotron.

Nucl. Instrum. & Methods B29 (1987) 151.

Iwamoto, A. and Takigawa, N.

On the Subbarrier Fusion of  $^{74}\text{Ge}+^{74}\text{Ge}$ .

JAERI-M 88-100 (1988) 120.

Iwasaki, S., Sugiyama, K., Chiba, S., Yamanouti, Y., Mizomoto, M.  
and Hyakutake, M.

Cross Section Measurement of Pb(n,xn) Reaction at 11 MeV.

JAERI-M 87-115 (1987) 187.

T

Iwase, A., Sasaki, S., Iwata, T. and Nihira, T.

Defect Production and Defect Saturation Behavior in Ni  
Irradiated with Heavy Ions in the Energy Range 84-120 MeV.

J. Nucl. Mater. 154-156 (1988) in press.

Katano, Y., Ohno, H. and Katsuta, H.

Damage Structure in Al<sub>2</sub>O<sub>3</sub> Single Crystal Irradiated with He-ions.

J. Nucl. Mater. 154-156 (1988) in press.

V

Kikuchi, A., Naramoto, H., Ozawa, K. and Kazumata, Y.

Damage Profiles in Alkali Halides Irradiated with High-Energy  
Ions.

Proc. of 6th Int. Conf. on Ion Beam Modification of  
Materials (Nucl. Inst. & Meth. in Phys. Res. B, to be  
published).

T

Kawarasaki, Y., Ohkubo, M., Shikazono, N. and Mashiko, K.

Linac for a Free-Electron-Laser Oscillator: Design Consideration  
on the Injector System.

Proc. of the 12th Meeting on Linac in JAPAN (Aug.24~26, 1987).

Kawarasaki, Y.

Free-Electron Laser: Brief Review and Topics

Proc. of 1987 Seminar on Nuclear Data (Nov.11~13, 1987).

Kawarasaki, Y., Ohkubo, M., Shikazono, N. and Mashiko, K.  
Linac for a Free-Electron-Laser Oscillator; Design Consideration  
on the Injector System.

Proceedings of the 12th Meeting on Linac in JAPAN (1987).

Kawatsura, K., Ootuka, A., Sataka, M., Komaki, K., Sugizaki, Y.,  
Naramoto, H., Ozawa, K., Nakai, Y. and Fujimoto, F.

Radiative Electron Capture in Heavy Ion and He Collisions.

JAERI-M 87-134 (1987) 43.

T

Kawatsura, K., Ootuka, A., Sataka, M., Komaki, K., Naramoto, H.,  
Ozawa, K., Nakai, Y. and Fujimoto, F.

Radiative Electron Capture in Heavy Ion and He Collisions.

Nucl. Instrum. & Methods A262 (1987) 33.

T

Kawatsura, K., Sataka, M., Ootuka, A., Komaki, K., Naramoto, H.,  
Ozawa, K., Nakai, Y. and Fujimoto, F.

Energy and Lifetime Measurements in Highly Ionized Chlorine.

Nucl. Instrum. & Methods A262 (1987) 150.

T

Kikuchi, S. and Takeuchi, S.

A Computer Code 'BEAM' for the Ion Optics Calculation of the  
JAERI Tandem Accelerator System.

JAERI 1308, Nov. 1987.

T

Kitahara, T., Yamaguchi, H., Kawatsura, K., Sataka, M., Ozawa, K.,  
Komaki, K., Ootuka, A. and Fujimoto, F.

Correlation between Charge States and Scattering Angles of 150-  
MeV <sup>37</sup>Cl Ions Exiting from Carbon Foils

Nucl. Instrum. & Methods B33 (1988) 230.

T

Komaki, Y., Ishikawa, N., Sakurai, T. and Iwasaki, M.  
Polyvinylidene Fluoride Microfilter by the  $^{35}\text{Cl}^{9+}$ ,  $^{58}\text{Ni}^{10+}$ , and  
 $^{63}\text{Cu}^{11+}$  Ions Bombardments and Alkali Etching.

to be published in Nuclear Instruments and Methods. (1988).

T

Komaki, Y., Matsumoto, Y., Ishikawa, N. and Sakurai, T.  
Heavy Ion Track Microfilter of Polyimide Film.

Submitted in POLYMER COMMUNICATIONS.

T

Kusakari, H., Oshima, M. and Ono, Y.  
Multiple Coulomb Excitation in the Nd-Sm Region.

JAERI-M Report 88-100 (1988) 4.

T

Mashiko, K., Nobusaka, Y., Shoji, T., Ishizaki, N. and  
Kawarasaki, Y.

Status of the JAERI Linac.

Proceedings of the 12th Meeting on Linac in JAPAN (1987).

Mashiko, K., Nobusaka, Y., Ishizaki, N. and Tayama, H.  
Preliminary Test Experiment for Electron Beam Injection to JSR.  
Proceedings of the Free Electron Laser Workshops (1987).

Mizumoto, M., Sugimoto, M.

Influence of Water Absorption in a Sample for Neutron Capture  
Measurements.

IAEA Specialists' Meeting on the Influence of Target and Sample  
Properties on Nuclear Data Measurements, INDC(NDS)-200/G,MY  
(1988) p39.

Mizumoto, M.

Nuclear Data Evaluation for Medium and Heavy Nuclei.

JAERI-M 88-065 (1988) 29.

Nakahara, H., Ohtsuki, T., Hamajima, Y., and Sueki, K.

Systematic Study of Mass Divisions Mechanism in Low-Energy Nuclear Fission.

Radiochem. Acta 43, 77 (1988).

T

Nakata, K., Takamura, S., Aruga, T. and Kobiyama, M.

Damage Distribution of Heavy Ion Irradiation in Metals studied by Electrical Resistivity.

J. Nucl. Materials 151 (1988) 301.

Naramoto, H., Kawatsura, K., Sataka, M., Sugizaki, Y. and

Nakai, Y., Ozawa, K., Yamaguchi, S., Fujino, Y. and Aoki, M.

Lattice Location of Deuterium in Nb-Mo with Ion Beams.

Nucl. Instrum. & Methods B33 (1988) 595.

T, V

Noda, K., Ishii, Y., Ohno, H., Watanabe, H. and Matsui, H.

Irradiation Defects and Ion Conductivity of Lithium Oxide.

Proc. Sym. on Fabrication and Properties of Lithium Ceramics,

American Ceramic Society, April 26-30, 1987 (Pittsburgh),

"Fabrication and Properties of Lithium Ceramics", Advances in

Ceramics series, ed. I.J. Hastings and G.W. Hollenberg

(American Ceramic Society) in press.

T



Noda, K., Ishii, Y., Matsui, H., Ohno, H., Hirano, S. and Watanabe, H.

Irradiation Damages in Solid Breeder Materials.

J. Nucl. Mater., in press.

T V

Noda, K., Ishii, Y., Matsui, H., Ohno, H. and Watanabe, H.

A study of Tritium Behavior in Lithium Oxide by Ion Conductivity Measurements.

Proc. 1st Int. Sym. on Fusion Nuclear Technology, April 10-15, 1988 (Tokyo), in press.

T

Ootuka, A., Kawatsura, K., Komaki, K., Fujimoto, F., Kouchi, N. and Shibata, H.

Molecular Effects in  $KL^n$  Multiple Ionization of Al for  $H^+$  and  $H_2^+$  Ion Impacts.

Nucl. Instrum. & Methods B33 (1988) 304.

V

Oshima, M., Minehara, E., Ichikawa, S., Iimura, H., Inamura, T., Hashizume, A. and Kusakari, H.

Multiple Coulomb Excitation of  $^{161}\text{Dy}$ .

JAERI-M Report 87-115 (1987) 164.

T

Oshima, M., Minehara, E., Ichikawa, S., Iimura, H., Inamura, T., Hashizume, A. and Kusakari, H.

Rotational Perturbation to the Natural-Parity Rotational Band of  $^{163}\text{Dy}$ .

RIKEN-AF-NP-62 (1987) p.1.

T

Oshima, M., Minehara, E., Ichikawa, S., Iimura, H., Inamura, T., Hashizume, A. and Kusakari, H.

Electromagnetic Transition Probabilities for One-Quasineutron Natural-Parity Rotational Bands.

JAERI-M Report 88-100 (1988) p.10.

T

Oshima, M., Minehara, E., Ichikawa, S., Iimura, H., Inamura, T., Hashizume, A. and Kusakari, H.

Rotational Perturbation to the Natural-Parity Rotational Band of  $^{163}\text{Dy}$ .

To be published in RIKEN Accel. Progr. Rep. 21 (1987).

T

Oshima, M., Minehara, E., Ichikawa, S., Iimura, H., Inamura, T., Hashizume, A., Kusakari, H. and Iwasaki, S.

Signature Dependence of M1 and E2 Transition Probabilities for the  $i_{13/2}$ .

Phys. Rev. C 37 (1988) 2578.

T

Otsuka, T. and M. Sugita

Equivalence between  $\gamma$  Instability and Rigid Triaxiality in Finite Boson System.

Phys. Rev. Lett. 59 (1987) 1541.

Otsuka, T. and Sugita, M.

Dipole Boson in an Extended Interacting Boson Model.

Proceedings of the Sixth Conference on Capture Gamma-ray Spectroscopy held at Leuven, Belgium, from 31 August to 4 September 1987. p.482.

Otsuka, T. and Sugita, M.

Unified Description of Quadrupole-Octupole Collective States.  
Proc. of Int. Conf. on Nucl. Struc. through Static and Dynamic  
Moments, p.44 (Melbourne, 1987).

Sataka, M., Kawatsura, K., Naramoto, H., Sugizaki, Y., Nakai, Y.,  
Ootuka, A., Komaki, K., Fujimoto, F., Ozawa, K. and Ishii, K.  
Lifetime Measurements of Multi-Charged Cl Ion.

JAERI-M 87-134 (1987) 72.

T

Sataka, M., Ozawa, K., Kawatsura, K., Ootuka, A., Komaki, K.,  
Naramoto, H., Fujimoto, F., Nakai, Y. and Ishii, K.

Measurements of Beam-Foil Spectra of Highly Ionized Chlorine  
Ions in the Region of 170 - 260 Å.

J. Phys. Soc. Jpn. 57 (1988) in press.

T

Schutz, Y., Baktash, C., Lee, I.Y., Halbert, M.L., Hensley, D.C.,  
Johnson, N.R., Oshima, M., Ribas, R., Lisle, J.C., Honkanen, K.,  
Sarantites, D.G., Larabee, A.J. and Saladin, J.X.

Search for Superdeformed Shapes in  $^{144}\text{Gd}$ .

Oak Ridge National Laboratory Report ORNL-6420 (1987) 70.

T

Sekine, T., Ichikawa, S., Oshima, M., Iimura, H., Nagame, Y.,  
Hata, K., Takahashi, N. and Yokoyama, A.

Identification of A New Isotope of  $^{121}\text{La}$  by Means of Element-  
Selective Mass Separation.

Z. Phys. A., in press.

T

Sekine, T., Hata, K., Nagame, Y., Ichikawa, S., Iimura, H., Oshima, M., Takahashi, N. and Yokoyama, A.  
Identification of the New Isotope  $^{121}\text{La}$  and Decay Spectroscopy of  $^{122,124,126}\text{La}$  and  $^{128,130}\text{Pr}$  by Means of Selective Mass Separation.

JAERI-M 88-100 (1988) 45.

T

Shinohara, N.

Study of Transuranium Elements by Using JAERI Tandem Accelerator. Proceedings of the 4th Specialist Research Meeting on Measurements of Short-lived Isotopes, KURRI-TR-303 (1988) pp.49-53.

T

Sugita, M.

A Unified Description of  $K\pi=0+$  and  $K\pi=0-$  Bands from Octupole Vibrational to Octupole Deformed Nuclei. Proceedings of the symposium, whose title is "Structure of Rotating Nuclei", held at Institute for Nuclear Study of the University of Tokyo from 24 to 26 Aug. 1987. Genshikaku Kenkyu Vol. 33 (1988) No. 1 p.49.

Sugiyama, Y., Tomita, Y., Ikezoe, H., Ideno, K., Kato, N., Sugimitsu, T., Fujita, H. and Kubono, S.

Quasi-Elastic Scattering Near The Coulomb Barrier:  $^{16}\text{O}+$   $^{144,148,152}\text{Sm}$ .

JAERI-M 88-100 (1988) 117.

T

Takahiro, K., Nakajima, H., Yamaguchi, S., Fujino, Y. and Naramoto, H. Retention and Release of Deuterium Implanted into VCx(x=0.44-0.95).

Proc. of 12th Int. Conf. on Atomic Collision in Solids (Nucl. inst. & Meth. in Phys. Res. B33 (1988) 734.

V

Takeuchi, S.

Status of Work on Superconducting Quarter Wave Resonators at JAERI.

Proc. of The Third Workshop on RF Superconductivity, Argonne, 1987, ANL-PHY-88-1,2 (1988) 429.

Takeuchi, S.

Superconducting Heavy Ion Booster proposed for the JAERI Tandem.

Proc. of Symposium of North Eastern Accelerator Personnel, Florida, 1987 (World Scientific, Singapore, New Jersey and Hongkong, 1988) pp333-342.

Tomimitsu, H.

XDT-Observation of Silicon Single Crystals Irradiated with Energetic Heavy Ions.

Acta Crystallogr. A43 (1987) Suppl. C207.

T

Yamaguchi, S., Fujino, Y., Naramoto, H. and Ozawa, K.

Recovery of Carbon-Implanted Silicon and Germanium.

Proc. on 6th Int. Conf. on Ion Beam Modification of Materials (Nucl. Inst. & Meth. in Phys. Res. B, to be published).

V

Contributions to Scientific and Technical Meetings

Aruga, T., Nakata, K. and Takamura, S.

Computer Simulation of Damage Depth Profiles for 2 - 7.5 MeV/amu Heavy Ions Incident on Pure Metals.

12th International Conference on Atomic Collisions in Solids in Okayama. (Oct. 12-16, 1987).

Awaya, Y., Hino, K., Hitachi, A., Kanai, Y., Kawatsura, K., Kuroki, K., Yamazaki, Y. and Watanabe, T.

Photon Angular Distributions of the Relativistic Radiative Electron Capture.

3rd Workshop on High-Energy Ion-Atom Collisions in Debrecen, Hungary. (Aug. 3-5, 1987).

Chiba, S.

Evaluation of the neutron nuclear data of  $^{10}\text{B}$ .

Autumn Meeting of Atomic Energy Society of Japan in Sapporo. (Oct. 2-4, 1987).

Chiba, S., Baba, M., Kikuchi, T., Ishikawa, M., Hirakawa, N. and Sugiyama, K.

Measurement of DDX of  $^6\text{Li}$  at 18.0 MeV

Annual Meeting of Atomic Energy Society of Japan in Tokyo. (Apr. 4-6, 1988).

Chiba, S., Baba, M., Kikuchi, T., Ishikawa, M., Hirakawa, N. and Sugiyama, K.

Measurement of Neutron-Induced Neutron-Producing Cross Sections of  $^6\text{Li}$  and  $^7\text{Li}$  at 18.0 MeV.

International Conference of Nuclear Data for Science and Technology in Mito. (May 30 - June 3, 1988).

Iimura, H., Ichikawa, S., Sekine, T., Oshima, M. and Takahashi, N.  
Decays of  $^{122}\text{La}$ ,  $^{124}\text{La}$  and  $^{126}\text{La}$ .

Autumn Meeting of the Japan Physical Society in Utunomiya.  
(Sept. 30-Oct. 3, 1987).

T

Ichikawa, S., Iimura, H., Sekine, T., Oshima, M. and Takahashi, N.  
Decay of  $^{121}\text{La}$ .

Autumn Meeting of the Japan Physical Society in Utunomiya.  
(Sept. 30-Oct. 3, 1987).

T

Ichikawa, S., Sekine, T., Oshima, M., Iimura, H. and Takahashi, N.  
On-Line Mass Separation of the Monoxide Ions in the Light Rare-earth Region.

The 31st Symposium on Radiochemistry in Fukuoka. (Oct. 13-15, 1987).

T

Duh, M., Takahashi, N., Yokoyama, A., Baba, H., Baba, S.,  
Hata, K. and Nagame, Y.

$^{12}\text{C}$  induced Fission of  $^{233}\text{U}$ ,  $^{235}\text{U}$  and  $^{238}\text{U}$ .

The 31-st Symposium on Radiochemistry (Oct. 13-15, 1987 in Fukuoka).

T

Hasegawa, K., Mizumoto, M., Yamanouti, Y., Chiba, S.,  
Kawarasaki, Y.

Measurements of Gamma-ray Spectrum from Silicon.

Autumn Meeting of the Atomic Energy Society of Japan in Sapporo  
(Oct. 2-4, 1987).

T

Hasegawa, K., Drosch, M., Mizumoto, M., Chiba S.  
Development of Monte-Carlo Codes for Sample-Size Effects.  
Annual Meeting of the Atomic Energy Society of Japan in Tokyo  
(Apr. 4-6, 1988)

T

Ideno, K., Tomita, Y., Sugiyama, Y., Ikezoe, H., Hanashima, S.  
and Nagame, Y.  
Detection of  $^8\text{Be}$  nuclei from the Reaction  $^{32}\text{S} + ^{64}\text{Ni}$  at 180 MeV.  
Autumn Meeting of Japan Phys. Soc. in Utsunomiya (Oct. 1987).

T

Ishii, K., Sataka, M., Kawatsura, K., Kubo, H., Nakai, Y.,  
Ozawa, K., Ootuka, A., Komaki, K. and Fujimoto, F.  
Beam-Foil Spectroscopy of Carbon-Foil-Excited Chlorine Ions.  
12th International Conference on Atomic Collisions in Solids in  
Okayama (Oct. 12-16, 1987).

T

Ishii, T., Ishii, M., Yanagida, K. and Ogawa, M.  
Hyperfine Interaction of Rare-earth Nuclei in Gd Host.  
Autumn Meeting of Physical Society of Japan, Utsunomiya (Sept.  
26-29, 1987).

T

Ishii, Y., Ishii, M., Yanagida, K. and Ogawa  
Survey of  $^{132}\text{Sm}$ .  
Spring Meeting of Physical Society of Japan in Koriyama (Mar.  
31-Apr. 3 1988).

T



Ishii, T., Ishii, M., Yanagida, K. and Ogawa, M.  
G-factor of the  $10^+$  Isomer in  $^{134}\text{Nd}$ .

Spring Meeting of Physical Society of Japan in Koriyama (Mar.  
31-Apr. 3, 1988).

T

Ishii, Y., Noda, K., Watanabe, H.

Volume Change of Lithium Oxide by Oxygen Ion Irradiation.  
Autumn Meeting of Atomic Energy Society of Japan in Sapporo  
(Oct. 2-4, 1987).

T

Iwamoto, A.

Deformation of Projectile and Target in Subbarrier Fusion  
Reactions.  
RIFP Symposium on Cluster Structure in Highly Excited State  
and the Heavy-Ion Reactions (May 11-14, 1987).

Iwamoto, A., Yamaji, S., Tonozuka, I. and Harada, K.  
On the Alpha Decay of  $^{211}\text{Po}$ .

RCNP Symposium on Cluster Aspects in Nuclear Structure and in  
Nuclear Reactions (Dec. 14-17, 1987).

Iwamoto, A.

Heavy-Ion Fusion Reaction and the Two-Center Shell Model.  
INS Symposium on Dynamics of the Direct Reaction in Heavy-Ion  
Scattering (Mar. 18, 1988).

Iwase, A.

Ion-Irradiation Damage in FCC Metals.  
Autumn Meeting of Physical Society of Japan in Sendai (Sept. 28,  
1987).

Iwase, A., Sasaki, S., Iwata, T. and Nihira, T.  
Defect Production and Defect Saturation Behavior in Ni Irradiated  
with Heavy Ions in the Energy Range 84-120 MeV.  
International Conference on Fusion Reactor Materials (ICFRM-3)  
in Karlsruhe (Oct. 4-8, 1987).

Iwata, T. and Iwase, A.  
Damage Production and Annealing in Ion-Irradiated FCC Metals.  
Workshop on "The Effects of Recoil Energy Spectrum and Nuclear  
Transmutation on the Evolution of the Microstructure" in Lugano,  
Switzerland (Mar. 24-29, 1988).

Iwase, A., Iwata, T., Sasaki, S. and Nihira, T.  
PKA Energy Dependence of Damage Production and Damage Structure  
in FCC Metals Irradiated with Energetic Ions.  
Spring Meeting of Physical Society of Japan in Koriyama (Apr. 3,  
1988).

Kawarasaki, Y., Ohkubo, M., Mashiko, K. and Shikazono, N.  
FEL Program at JAERI.  
9th International FEL Conference, Williamsburg, VA.  
(Sept. 17, 1987)

Kitahara, T., Yamaguchi, H., Kawatsura, K., Sataka, M.,  
Ozawa, K., Komaki, K., Ootuka, A. and Fujimoto, F.  
Correlation between Charge States and Scattering Angles of 150-  
MeV Cl Ion Exciting from Carbon Foils.  
12th International Conference on Atomic Collisions in Okayama  
(Oct. 12-16, 1987).

T

Komaki, K., Kawatsura, K., Ootuka, A., Fujimoto, F., Sataka, M.,  
Naramoto, H., Sugizaki, Y., Nakai, Y. and Ozawa, K.

Energy Spectra and Lifetime Measurements of X-Rays from Foil  
Excited Highly Charged Ion.

12th International Conference on Atomic Collisions in Solids in  
Okayama (Oct. 12-16, 1987)

T

Kusakari, H. and Oshima, M.

Electromagnetic Properties of Atomic Nuclei

INS Symposium on Nuclear Physics at High-Spin States in Tokyo  
(Aug. 20-22, 1987).

T

Maeta, H., Larson, B.C., and Lewis, J.

X-ray Diffuse Scattering of Ion Irradiated Copper Crystal.  
Autumn Meeting of Physical Society of Japan (Koriyama).

Magara, M., Shinohara, N., Usuda, S., Ichikawa, S., Suzuki, T.,  
Iimura, H., Nagame, Y., Kobayashi, Y., Yamamoto, T.,  
Hatsukawa, Y., Horiguchi, T., Shibata, S., Fujiwara, I.

Decay of  $^{245}\text{Cf}$  (II).

The 31-st Symposium on Radiochemistry in Fukuoka, (Oct. 13-15,  
1987).

T

Miyahara, K., Okazaki, Y., Mochizuki, M., Hosoi, Y. and  
Kayano, H.

Microstructure and Mechanical Properties of Alpha Particle  
Irradiated Fe-12%Cr-30%Mn Alloy.

Third International Conference on Fusion Reactor Materials, in  
Karlsruhe, F.G. Germany (Oct. 4-8, 1987).

Mizumoto, M.

Neutron Cross Section Evaluation of Lead for JENDL-3.  
Annual Meeting of the Atomic Energy Society of Japan in Tokyo  
(Apr. 4-6, 1988).

Mizumoto, M., Hasegawa, K., Chiba, S., Yamanouti, Y.,  
Kawarasaki, Y., Igashira, M., Uchiyama, T., Kitazawa, H.,  
Drosg, M.

Gamma-ray Production Cross Sections of Some Structural and  
Shielding Materials.

International Conference of Nuclear Data for Science and  
Technology in Mito (May 30 - Jun. 3, 1988)

T

Nagame, Y., Magara, M., Hata, K., Ichikawa S., Sekine, T.,  
Baba, S., Ideno, K., Ikezoe, H., Yokoyama A. and Hatsukawa Y.  
Heavy Particle Emission Process in The  $^{37}\text{Cl}+^{68}\text{Zn}$  Heavy Ion.  
Reaction The 31th Symposium on Radiochemistry in Fukuoka  
(Oct. 13-15, 1987)

T

Nagame, Y., Baba, S., Hata, K., Sekine, T., Ichikawa, S.,  
Ikezoe, H., Ideno, K., Yokoyama, A. and Hatsukawa, Y.  
Heavy Particle Emission from the  $^{105}\text{Ag}$  Compound Nucleus.  
Annual Meeting of Physical Society of Japan in Koriyama  
(Mar. 31 - Apr. 3, 1988)

T

Nagame, Y., Baba, S., Hata, K., Sekine, T., Ichikawa, S.,  
Ikezoe, H., Ideno, K., Yokoyama, A., Hatsukawa, Y. and Magara, M.  
Large Fragment Emission from the  $^{105}\text{Ag}$  Compound Nucleus.  
Joint Seminar on Heavy-Ion Nuclear Physics and Nuclear Chemistry  
in the Energy Region of Tandem Accelerator (III) in Tokai  
(Jan. 7-9, 1988).

T

Nakata, K., Takamura, S., Kobiyama, M. and Aruga, T.  
Damage Profiles in Metals Irradiated by Heavy Ions.  
Spring Meeting of Japan Institute of Metals in Tokyo (Apr. 1-3,  
1987).

T

Naramoto, H., Kawatsura, K., Sataka, M., Sugizaki, Y., Nakai, Y.,  
Ozawa, K., Yamaguchi, S., Fujino, Y. and Aoki, M.  
Lattice Location of Deuterium in Nb-Mo with Ion Beams.  
12th International Conference on Atomic Collisions in Solids in  
Okayama (Oct. 12-16, 1987)

T, V

Naramoto, H., Kazumata, Y., White, C.W., McHargue, C.J.,  
Williams, J.M. and Appleton, B.R.  
Ion Beam Analysis of Ion-Implanted and Thermal-Treated  $\alpha$ -Al<sub>2</sub>O<sub>3</sub>.  
Spring Meeting of Japan Institute of Metals in Tokyo (Apr.1-3,  
1987).

V

Naramoto, H., Kawatsura, K., Sataka, M., Sugizaki, Y.,  
Nakai, Y., and Kazumata, Y.  
Material Analysis with Energetic Heavy Ions  
Fall Meeting of Japan Society of Powder and Powder Metallurgy  
in Kyoto (Nov. 10-13, 1987).

T

Naramoto, H., Kazumata, Y., Watanabe, M., Kato, T., and  
Masaki, N.  
Surface Analysis of Ion-Irradiated YBa<sub>2</sub>Cu<sub>3</sub>O<sub>x</sub> Compound I.  
Spring Meeting of Japan Institute of Metals in Narashino  
(Mar. 31-Apr. 2, 1988).

T

Noda, K., Ishii, Y., Ohno, H., Watanabe, H. and Matsui, H.  
Irradiation Defects and Ion Conductivity of Lithium Oxide.  
Sym. on Fabrication and Properties of Lithium Ceramics,  
American Ceramic Society in Pittsburgh (Apr. 26-30, 1987).

T

Noda, K., Ishii, Y., Matsui, H., Horiki, M. and Watanabe, H.  
Radiation Effect on Ion Conductivity of  $\text{Li}_2\text{O}$ .  
Autumn Meeting of Atomic Energy Society of Japan in Sapporo  
(Oct. 2-4, 1987).

T

Noda, K., Ishii, Y., Matsui, H., Ohno, H., Hirano, S. and  
Watanabe, H.  
Irradiation Damage in Solid Breeder Materials.  
3rd Int. Conf. on Fusion Reactor Materials in Karlsruhe (Oct.  
4-8, 1987).

T V

Noda, K., Ishii, Y., Matsui, H., Ohno, H. and Watanabe, H.  
A Study of Tritium Behavior in Lithium Oxide by Ion Conductivity  
Measurements.  
1st Int. Sym. on Fusion Nuclear Technology in Tokyo (Apr. 10-15,  
1988).

T

Ohtsuki, T., Sueki, K., Hatsukawa, Y., Nakahara, H.,  
Shinohara, N., Nagame, Y.  
Low-Energy Nuclear Fissions of Actinide Elements.  
Spring Meeting of Japan Physical Society in Koriyama  
(Apr., 1-3, 1988).

T

Ohtsuki, T., Sueki K., Hatsukawa, Y., Nakahara, H.,  
Shinohara, N., Nagame, Y.

Low Energy Nuclear Fission of Actinide Elements.

5th International Conference on Clustering Aspects in Nuclear  
and Subnuclear Systems.

(Jul. 25-19, 1988).

T

Ootuka, A., Kawatsura, K., Komaki, K., Fujimoto, F., Kouchi, N.  
and Shibata, H.

Molecular Effects in Al  $K\alpha$  Satellite Yields for  $H^+$  and  $H_2^+$  Ion  
Impacts.

12th International Conference on Atomic Collisions in Solids in  
Okayama (Oct. 12-16, 1987).

V

Oshima, M., Minehara, E., Ichikawa, S., Iimura, H., Inamura, T.,  
Hashizume, A. and Kusakari, H.

Multiple Coulomb Excitation of  $^{173}\text{Yb}$ .

Autumn Meeting of Physical Society of Japan in Utsunomiya  
(Sept. 27-Oct. 3, 1987).

T

Sekine, T., Hata, K., Nagame, Y., Ichikawa, S., Iimura, H.,  
Oshima, M., Takahashi, N. and Yokoyama, A.

Decays of Neutron Deficient Isotopes of La and Pr.

The 31st Symposium on Radiochemistry in Fukuoka, (Oct. 13-15,  
1987).

T

Sugiyama, Y., Tomita, Y., Ikezoe, H., Ideno, K., Kato, N.,  
Sugimitsu, T., Fujita, H. and Kubono, S.

Quasi-Elastic Scattering for  $^{16}\text{O}+^{144,148,152}\text{Sm}$ .

Autumn Meeting of the Physical Society of Japan in Utsunomiya  
(Oct. 1987).

T

Sugiyama, Y.

Direct Reaction Induced by Heavy-Ion at Tandem Energy Region.  
Symposium on Direct Reaction and its Dynamics in Heavy-Ion  
Induced Reactions, INS, University of Tokyo (Mar. 18, 1988).

T

Sugizaki, Y., Sataka, M., Kawatsura, K. and Nakai, Y.  
Time-of-Flight Measurement of Multiple Ionization Cross Section  
in Heavy Ion-Ne Collision.

Annual Meeting of the Physical Society of Japan in Koriyama  
(March 31 - Apr. 3, 1988).

V

Takeuchi, S., Ishii, T., Ikezoe, H. and Ohkubo, M.  
Development of JAERI-Tandem Superconducting Booster.  
Proc. of The 12 the Linear Acc. Meeting in Japan, Tokai (1987).

Takeuchi, S.

Superconducting Resonators for Heavy Ion Booster at JAERI.  
Third Japan China Joint Symposium, Wako (Nov. 18-20, 1987).

Yamanouti, Y., Sugimoto, M., Furuta, Y., Mizumoto, M.,  
Hyakutake, M. and Methasiri, T.

Elastic and Inelastic Scattering of 13 MeV Neutrons from  $^{11}\text{B}$ .  
Autumn Meeting of the Atomic Energy Society of Japan in Sapporo  
(Oct. 2-4, 1987).

T

Yamanouti, Y., Sugimoto, M., Furuta, Y., Mizumoto, M.,  
Hyakutake, M. and Methasiri, T.

$^{11}\text{B}(n,n)$  and  $(n,n')$  Reactions at 13 MeV.

Annual Meeting of the Physical Society of Japan in Kohriyama  
(Mar. 31 - Apr. 3, 1988).

T



## VIII PERSONNEL AND COMMITTEES

(April 1987 - March 1988)

## (1) Personnel

## Department of Physics

Naomoto	Shikazono	Director
Yoichi	Suto	Administrative Manager

## Accelerators Division

Scientific Staff	Chiaki	Kobayashi*
	Shiro	Kikuchi
	Suehiro	Takeuchi
	Eisuke	Minehara
	Susumu	Hanashima
Technical Staff (Tandem, V.D.G.)	Isao	Ohuchi
	Yutaka	Sato
	Tadashi	Yoshida
	Susumu	Kanda
	Katsuzo	Horie
	Satoshi	Tajima
	Yoshihiro	Tsukihashi
	Shinichi	Abe
	Shuhei	Kanazawa
	Technical Staff (Linac)	Katuo
Yukio		Nobusaka
Tokio		Shoji
Nobuhiro		Ishizaki
Hidekazu		Tayama

## Nuclear Physics Laboratory

Scientific Staff	Mitsuhiko	Ishii***
------------------	-----------	----------

\* Head, Accelerators Division

\*\* Leader, Technical Staff

\*\*\* Head, Nuclear Physics Laboratory

## Nuclear Physics Laboratory (continued)

Scientific Staff	Yoshiaki	Tomita
	Yasuharu	Sugiyama
	Akira	Iwamoto
	Kazumi	Ideno
	Hiroshi	Ikezoe
	Masumi	Ohshima
	Tetsuro	Ishii
	Michiaki	Sugita

## Linac Laboratory

Scientific Staff	Yuuki	Kawarasaki*
	Makio	Ohkubo
	Motoharu	Mizumoto
	Yoshimaro	Yamanouchi
	Masayoshi	Sugimoto
	Satoshi	Chiba

## Solid State Physics Laboratory I

Scientific Staff	Yukio	Kazumata**
	Hiroshi	Naramoto
	Hiroshi	Tomimitsu
	Shigemi	Sasaki

## Solid State Physics Laboratory II

Scientific Staff	Tadao	Iwata***
	Saburo	Takamura
	Hiroshi	Maeta
	Mitsuo	Watanabe
	Teruo	Kato
	Akihiro	Iwase
	Terufumi	Yokota

\* Head, Linac Laboratory

\*\* Head, Solid State Physics Laboratory I

\*\*\* Head, Solid State Physics Laboratory II

Solid State Physics Laboratory III

Scientific Staff Masanobu Sakamoto

Atomic and Molecular Physics Laboratory

Scientific Staff Yohta Nakai\*  
 Kiyoshi Kawatsura  
 Masao Sataka  
 Yasuaki Sugizaki

Department of Chemistry

Nuclear Chemistry Laboratory

Scientific Staff Tadashi Yamamoto\*\* (To September 1987)  
 Michio Hoshi\*\* (From October 1987)  
 Shin-ichi Ichikawa  
 Nobuo Shinohara  
 Hidenori Iimura  
 Yoshii Kobayashi

Analytical Chemistry Laboratory

Scientific Staff Yuji Baba  
 Toshio Suzuki

Physical Chemistry Laboratory

Scientific Staff Mutsuhide Komaki  
 Jiro Ishikawa

Solid State Chemistry Laboratory

Scientific Staff Kazuhiko Izui\*\*\*  
 Shin-ichi Ohno  
 Teikichi Sasaki  
 Shigemi Furuno  
 Takeshi Soga  
 Katsutoshi Furukawa  
 Kiichi Hojou

\* Head, Atomic and Molecular Physics Laboratory

\*\* Head, Nuclear Chemistry Laboratory

\*\*\* Head, Solid State Chemistry Laboratory

Department of Radioisotope Production

Production Development Division

Scientific Staff	Sumiko	Baba
	Hiromitsu	Matsuoka
	Kentaro	Hata
	Toshiaki	Sekine
	Yuichiro	Nagame
	Takami	Sorita
	Mishiroku	Izumo

Department of Fuels and Materials Research

Physical Metallurgy Laboratory

Scientific Staff	Akimichi	Hishinuma*
	Takeo	Aruga
	Shozo	Hamada
	Tomotsugu	Sawai
	Kenji	Suzuki
	Katsumaro	Fukai

Fuel Property Laboratory

Scientific Staff	Hitoshi	Watanabe**
	Kenji	Noda
	Yoshinobu	Ishii

Function Materials Laboratory

Scientific Staff	Hideo	Ohno***
	Takanori	Nagasaki
	Yoshio	Katano

Department of Reactor Engineering

Reactor Instrumentation Laboratory

Scientific Staff	Eiji	Sakai (To January 1988)
------------------	------	-------------------------

\* Head, Physical Metallurgy Laboratory

\*\* Head, Fuel Property Laboratory

\*\*\* Head, Function Materials Laboratory

Department of Health Physics

Technical Staff	Shoji	Izawa*
	Toshihiro	Miyamoto
	Katsunori	Sawahata

\* Chief of Radiation Control Group, Department of Health Physics

## (2) Tandem Steering Committee

(Chairman)	Kazumi	Iwamoto	(Deputy Director General, Tokai Research Establishment)
	Yoshihiko	Kaneko	(Deputy Director, Department of Reactor Engineering)
	Tatuo	Kondo	(Director, Department of Fuels and Materials Research)
	Naomoto	Shikazono	(Director, Department of Physics)
	Enzo	Tachikawa	(Director, Department of Chemistry)
	Masatoshi	Tanaka	(Director, Department of Thermonuclear Fusion Research)
	Eiji	Shikata	(Director, Department of Radioisotopes)
(Secretary)	Chiaki	Kobayashi	(Head, Accelerators Division)
(Secretary)	Yoichi	Suto	(Administrative Manager, Department of Physics)

## (3) Tandem Consultative Committee

(Chairman)	Toyojiro	Fuketa	(Director General, Tokai Research Establishment)
(Vice Chairman)	Kazumi	Iwamoto	(Deputy Director General, Tokai Research Establishment)
(Vice Chairman)	Naomoto	Shikazono	(Director, Department of Physics)
	Hiromichi	Kamitsubo	(Principal Scientist, Institute of Physical and Chemical Research)
	Kōji	Nakai	(Professor, National Laboratory for High Energy Physics)
	Hiroyasu	Ejiri	(Professor, Osaka University)
	Shiori	Ishino	(Professor, University of Tokyo)
	Hiroyuki	Tawara	(Associate Professor, Institute of Plasma Physics, Nagoya University)
	Kohzoh	Masuda	(Professor, University of Tsukuba)
	Shiro	Iwata	(Professor, Kyoto University)
	Ichiro	Fujiwara	(Professor, Otemon Gakuin University)
	Kenji	Sumita	(Professor, Osaka University)
	Naohiro	Hirakawa	(Professor, Tohoku University)
(Secretary)	Chiaki	Kobayashi	(Head, Accelerators Division)
(Secretary)	Yoichi	Suto	(Administrative Manager, Department of Physics)



## (4) Tandem Program Advisory Committee

(Chairman)	Naomoto	Shikazono	(Director, Department of Physics)
	Hirokazu	Umezawa	(Deputy Director, Department of Radioisotopes)
	Shoji	Izawa	(Chief, Radiation Control Group, Department of Health Physics)
	Hitoshi	Watanabe	(Head, Fuel Property Laboratory, Department of Fuels and Materials Research)
	Tadashi	Yamamoto	(Head, Nuclear Chemistry Laboratory, Department of Chemistry)
	Yohta	Nakai	(Head, Atomic and Molecular Physics Laboratory, Department of Physics)
	Mitsuhiko	Ishii	(Head, Nuclear Physics Laboratory, Department of Physics)
	Yuuki	Kawarasaki	(Head, Linac Laboratory, Department of Physics)
	Chiaki	Kobayashi	(Head, Accelerators Division, Department of Physics)

Ⅸ CO-OPERATIVE RESEARCHES

Title	Co-Operation Institution
2.2 Radiative Electron Capture in Heavy Ion and H <sub>2</sub> Collisions	College of General Education, The University of Tokyo*
2.3 X-Ray Emission from Foil-Excited Silicon Beams	College of General Education, The University of Tokyo*
2.4 Beam-Foil Spectra of Chlorine Ions in High Energy Region (V)	Department of Engineering Science, Kyoto University; College of General Education, The University of Tokyo*
3.1 Radiation Annealing in Nickel and Copper by 100 MeV Iodine Irradiation	Faculty of Engineering, Ibaraki University*
3.2 Depth Dependence of Isochronal Annealing Process in Fe Irradiated by Cl Ions	Faculty of Engineering, Ibaraki University*
3.4 Microstructure and Mechanical Properties of Ion Irradiated Fe-12%Cr-15 to 30%Mn Alloys	Faculty of Engineering, Nagoya University*
3.6 Effect of Irradiation Damage on Ion Conductivity of Li <sub>2</sub> O	Faculty of Engineering, Nagoya University*
3.7 Irradiation Damage Studies of Ceramic Materials	Faculty of Engineering, Nagoya University*
3.8 Effect of Heavy Ion Irradiation on Negative Thermal Expansion in Gap Single Crystal	Faculty of Engineering, Tamagawa University*; College of Liberal Arts and Sciences, Okayama University*
4.1 <sup>12</sup> C Induced Fission of <sup>233</sup> U, <sup>235</sup> U and <sup>238</sup> U	Faculty of Science, Osaka University*
4.2 Complex Fragment Emission from the Compound Nucleus <sup>105</sup> Ag	Faculty of Science, Osaka University*; Faculty of Science, Tokyo Metropolitan University

- |     |   |  |
|-----|---|--|
| 4.3 | Mass Distributions of the Fission Fragments of $^{233}\text{U}+p$ , $^{237}\text{Np}+p$ and $^{239}\text{Pu}+p$               | Faculty of Science, Tokyo Metropolitan University                      |
| 4.5 | Identification of A New Isotope of $^{121}\text{La}$ by Means of Element-Selective Mass Separation                            | Faculty of Science, Osaka University*                                  |
| 4.6 | Decays of $^{122,124,126}\text{La}$ and $^{128,130}\text{Pr}$ and Properties of the Low Lying States of Their Daughter Nuclei | Faculty of Science, Osaka University*                                  |
| 4.7 | Isolation of Short-Lived Nuclides with a Helium-Jet Recoil-Transport System and SISAK   | Faculty of Science, The University of Tokyo; Otomon Gakuin University* |
| 5.1 | Nuclear Structure of $\text{Sn}^{106}$  | Tokyo Institute of Technology*   |
| 5.2 | G-factor of the $10^+$ Isomer in $\text{Nd}^{134}$  | Tokyo Institute of Technology*   |
| 5.3 | Electromagnetic Transition Probabilities for Natural-Parity Rotational Bands in $^{173}\text{Yb}$ and $^{157}\text{Gb}$       | The Institute of Physical and Chemical Research                        |
| 5.4 | Multiple Coulomb Excitation of $^{148,150}\text{Nd}$  | The Institute of Physical and Chemical Research                        |
| 5.5 | Quasi-Elastic Scattering for $^{16}\text{O}+$ $^{144,148,152}\text{Sm}$ Near The Coulomb Barrier                              | Kyushu University*; INS, University of Tokyo                           |
| 5.8 | Effect of the Shell Structure on the Potential Barrier for the Subbarrier Fusion Reaction                                     | Department of Physics, Tohoku University                               |
| 6.2 | Scattering of 13 MeV Neutrons from $^{11}\text{B}$ .  | Kyushu University*; Faculty of Engineering                             |

6.4 Measurements of Gamma-Ray      Tokyo Institute of  
Production Cross Sections      Technology\*

\* Travel Expenses are supplied by JAERI